Increasing Accuracy in Powder Diffraction

Oxana Magdysyuk

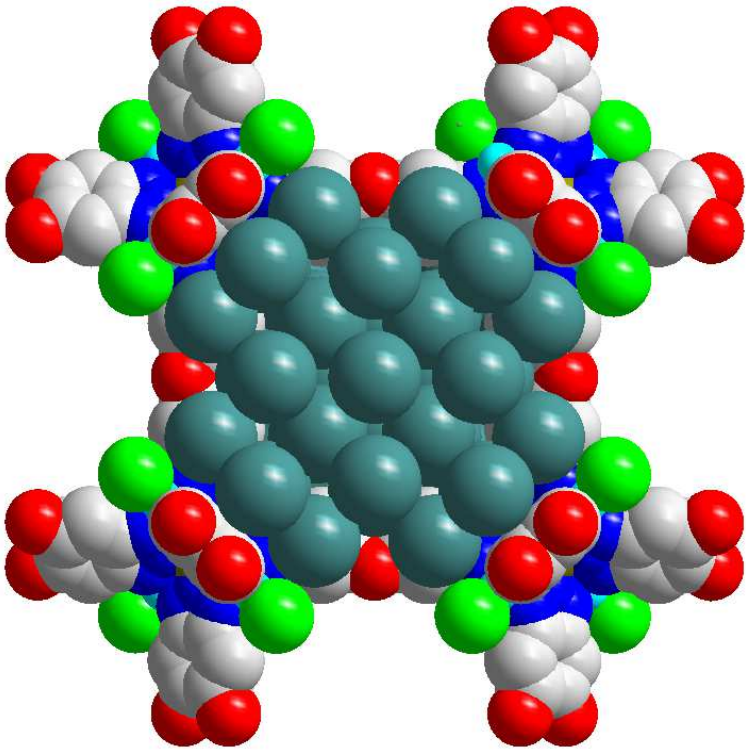

Increasing Accuracy in Powder Diffraction

Von der Fakultät Chemie der Universität Stuttgart zur Erlangung der Würde eines Doktors der Naturwissenschaften (Dr. rer. nat.) genehmigte Abhandlung

Vorgelegt von

Oxana Magdysyuk

aus Nefteyugansk, Russland

Hauptberichter:	Prof. Dr. R. E. Dinnebier
Mitberichter:	Prof. Dr. Th. Schleid
Mitprüfer:	Prof. Dr. F. Gießelmann

Tag der mündlichen Prüfung: 03.06.2014

Max-Planck-Institut für Festkörperforschung, Stuttgart

2014

Table of Contents

1. Introduction

X-ray single crystal crystallography allows precise determination of crystal structures (Ladd & Palmer, 2013) and in some cases even analysis of the electron charge density distribution due to chemical bonding by the multipole formalism (Gatti & Macchi, 2012). On the other site, synthesis of single crystals of sufficient quality can be very complicated or even impossible. Often single crystals of industrially important materials are highly twinned or mosaic. In some cases single crystals possess completely different properties than the corresponding bulk powder due to modification of the in-pores structure during specific growing procedure (Kazin *et al.*, 2003) or crystals can be destroyed during first-order phase transitions. In all these cases the only alternative to extract structural information is the method of powder diffraction.

Powder diffraction data contain reduced information in comparison to single crystal diffraction data due to the projection of the three-dimensional reciprocal space onto the one dimensional 2θ-axis and the resulting accidental and intrinsic peak overlap. Thus, the accuracy of structural information from powder diffraction data critically depends on the quality of the powder diffraction data and on sophisticated methods for data analysis. Different methods for the analysis of the crystal structure of materials from powder diffraction data have been developed over the last 50 years. They include the constant development of laboratory and synchrotron diffractometers (Dinnebier & Billinge, 2008) as well as improvement of data analysis techniques, *e.g.* development of methods for indexing, structure solution, and refinement from powder diffraction data (Pecharsky & Zavalij, 2003; Dinnebier & Billinge, 2008), complementary use of electron microscopy (McCusker & Baerlocher, 2008, 2013; Xie *et al.*, 2008, 2011), methods for analysis of amorphous and low-crystalline materials by pair distribution function and X-ray absorption spectroscopy (Egami & Billinge, 2003; Koningsberger, 1988), microstructural analysis of bulk material (Mittemeijer & Welzel, 2012), analysis of accurate electron density distribution from powder diffraction data (Dinnebier *et al.*, 1999; Samy *et al.*, 2010; Buchter *et al.*, 2011), and methods for qualitative and quantitative description of structural phase transitions (Carpenter *et al.*, 1998a; Campbell *et al.*, 2006; Stinton & Evans, 2007). Increasing the accuracy in powder diffraction is a challenging task including the development of both, instruments and data analysis. The focus of the presented thesis lies in the development of advanced data analysis methods using the method of maximum

entropy (Chapter II and IV) and parametric refinement of *in situ* X-ray powder diffraction data (Chapter III).

Chapter II deals with increasing accuracy of the reconstructed electron density distribution from powder diffraction data, which is of great interest in structure solution and refinement as well as in the analysis of fine details of the electron density distribution, the key feature for the understanding of structure-property relations. Conventional Fourier synthesis strongly depends on the resolution of experimental powder diffraction data and was shown to be not applicable to the analysis of fine features of electron density from conventional laboratory and synchrotron X-ray powder diffraction data with a typical resolution of $\sin\theta/\lambda \approx 0.6\text{-}0.8$ Å^{-1} (de Vries *et al.*, 1994; Roversi *et al.*, 1998; Mondal *et al.*, 2012). To overcome the limitations of Fourier synthesis, the maximum entropy method (MEM) was introduced in the field of crystallography. The MEM allows the maximization of the information extracted from intrinsically limited and/or noisy experimental X–ray powder diffraction data. This can be achieved by applying different improvements for data treatment procedure, which are not available in Fourier synthesis: procrystal electron density for known part of the crystal structure based on the analytical Fourier transform (Zheludev *et al.*, 1995; Papoular *et al.*, 2002, van Smaalen *et al.*, 2003), several possibilities of incorporation of experimentally measured amplitudes of structure factors by changing their order or weighting schemes (de Vries *et al.*, 1994; Palatinus & van Smaalen, 2002), decreasing the model biasing for the extraction of individual intensities from a group of overlapping reflections through the application of *G*-constraints (Sakata *et al.*, 1990), prior-derived F_{PD}-constraints for approximation of the non-measured high-angle structure factors (Palatinus & van Smaalen, 2005), etc. It has been demonstrated that the maximum entropy method (MEM) can be successfully used with powder diffraction data for localization of missing atoms with high occupancies in incomplete crystal structures (Takata, 2008), for revealing the true nature of structural disorder (Dinnebier *et al.*, 1999; Samy *et al.*, 2010) and for determination of integrated atomic charges (Buchter *et al.*, 2011).

On the other hand, the capability of the MEM to locate missing atoms with low occupancies was not explored. This holds in particular true in case of commonly used high-resolution laboratory X-ray powder diffraction data. In the present study, the MEM is used to locate very small amounts of intercalated metal atoms (Cu, Ni, Zn) in incomplete crystal structures of apatites, and to determine their electron density distribution (Magdysyuk *et al.*,

2012). Also the intercalation of noble gas atoms in metal-organic frameworks ZIF-8 and MFU-4*l* was investigated by conventional laboratory X-ray powder diffraction methods and by MEM (Soleimani-Dorcheh *et al.*, 2012; Chapter IV).

Another important problem, considered in Chapter II, is the determination of the accurate electron density distribution and of ionic charges from low-temperature X-ray powder diffraction data. The MEM was successfully applied to single crystal X-ray diffraction data and showed results which are comparable to a traditional multipole refinement (Hofmann *et al.*, 2007; Netzel *et al.*, 2008). But the multipole refinement is not applicable to powder diffraction data even in the case of high resolution diffraction data of a simple cubic crystal structure of diamond (Svendsen *et al.*, 2010). Nevertheless, the determination of the electron density distribution from powder diffraction data would be an interesting alternative in case single crystals are lacking. So far, only one successful example of using MEM for the determination of the charge density distribution was reported for the low-temperature modification of $LiBD_4$, which consists only of light elements (Buchter *et al.*, 2011).

For the first time the applicability of MEM to reconstruct the electron density of heavy-atoms compounds was investigated in the presented work for the low-temperature crystal structures of $BaZnF_4$ and $BaMgF_4$.

A new approach for the advanced analysis of structural phase transitions is considered in Chapter III. The development of fast area detectors during last years provided the possibility for fast acquisition of X-ray powder diffraction data upon changing temperature and pressure, making it necessary to improve the methods for analyzing large amounts of data. One of the most promising methods for this propose is parametric refinement (Stinton & Evans, 2007), which allows simultaneous refinement of up to thousands of data sets with the possibility to apply physical models during the refinement. In additional, the combination of parametric refinement with the distortion mode approach (Campbell *et al.*, 2006) opens great opportunities for the improvement of description and analysis of structural phase transitions (Campbell *et al.*, 2007). Distortion modes are based on the group-theoretical approach and are used to describe the deviation of the low-symmetry structure from the high-symmetry parent structure in terms of the distortion of a high-symmetry structure by atomic displacement/ordering (structural distortion) and by lattice distortion (strain). The coupling between strain and structural distortion (which can be quantified by an order parameter) is critical for the description of the evolution of

material and was previously analyzed based on the results of sequential refinements (Carpenter *et al.*, 1998a; Carpenter & Salje, 1998b). This sequential approach does not always allow to unambiguously determine the type of coupling between strain and order parameter (Tan *et al.*, 2012).

In the presented PhD thesis for the first time, parametric refinement was successfully applied to obtain precise information about the type of coupling between strain and order parameter for temperature-dependent structural phase transitions in $LuF[SeO_3]$ and Sr_2CoOsO_6. Parametric refinement was used to test several possible models of coupling between strain and order parameter and to validate the best one (Magdysyuk *et al.*, 2014). For this propose, the theory for coupling between strain and order parameter was further developed for the case of biquadratic coupling between strain and order parameter with explicit temperature dependence of strain.

Chapter IV reportes advanced investigations of noble gas adsorption in different metal-organic frameworks CPO-27-Ni, CPO-27-Mg, ZIF-8, Zn-MFU-4*l*, and Cu-MFU-4*l* by state of the art high-resolution laboratory and synchrotron powder X-ray diffraction, revealing the key factors, which determins the adsorption of noble gases by MOFs.

1.1. References.

Buchter, F.; Lodziana, Z.; Remhof, A.; Mauron, Ph.; Friedrichs, O.; Borgschulte, A.; Züttel, A.; Filinchuk, Y.; Palatinus, L. (2011). *Experimental charge density of $LiBD_4$ from maximum entropy method. Phys. Rev.* **B86**, 064107.

Campbell, B.J.; Stokes, H.T.; Tanner, D.E.; Hatch, D.M. (2006). *ISODISPLACE: a web-based tool for exploring structural distortions. J. Appl. Cryst.* **39**, 607–614.

Campbell, B.J.; Evans, J.S.O.; Perselli, F.; Stokes, H.T. (2007). *Rietveld refinement of structural distortion-mode amplitudes. IUCr Computing Commission Newsletter.* **8**, 81–95.

Carpenter, M.A.; Salje, E.K.H.; Graeme-Barber, A. (1998a). *Spontaneous strain as a determinant of thermodynamic properties for phase transitions in minerals. Eur. J. Mineral.* **10**, 621–691.

Carpenter, M.A.; Salje, E.K.H. (1998b). *Elastic anomalies in minerals due to structural phase transition. Eur. J. Mineral.* **10**, 693–812.

Dinnebier, R. E.; Schneider, M.; van Smaalen, S.; Olbrich, F.; Behrens, U. (1999). *Disorder determined by high-resolution powder diffraction: structure of pentamethylcyclopentadienyllithium*. *Acta Cryst.* B**55**, 35–44.

Dinnebier, R.E.; Billinge, S.J.L. (2008). *Powder diffraction: theory and practice.* 582 p. The Royal Society of Chemistry, Cambridge, UK.

Egami, T.; Billinge, S.J.L. (2003). *Underneath the Bragg Peaks: Structural Analysis of Complex Materials*. Pergamon Press, Elsevier, Oxford, England.

Gatti, C.; Macchi, P. (2012). *Modern Charge-Density Analysis.* 783 p. Springer, New York, USA.

Hofmann, A.; Kalinowski, R.; Luger, P.; van Smaalen, S. (2007). *Accurate charge density of the tripeptide Ala-Pro-Ala with the maximum entropy method (MEM): influence of data resolution. Acta Cryst.* B**63**, 633–643.

Kazin, P.E.; Karpov, A.S.; Jansen, M.; Nuss, J.; Tretyakov, Yu.D. (2003). *Crystal structure and properties of strontium phosphate apatite with oxocuprate ions in hexagonal channels. Z. Anorg. Allg. Chem.* **629**, 344–352.

Koningsberger, D.C. (1988). *X-ray absorption: principles, applications, techniques of EXAFS, SEXAFS and XANES.* 673 p. Wiley, New York, USA.

Ladd, M.; Palmer, R. (2013). *Structure determination by X-ray crystallography.* 756 p. Springer, New York, USA.

Magdysyuk, O.V.; Dinnebier; R.E.; van Smaalen, S.; Zykin, M.A.; Kazin, P.E.; Jansen, M. (2012). *Reconstructions of electron density by the Maximum Entropy Method from X-ray powder diffraction data based on incomplete and complete crystal structure models: a case study of apatites with different intercalated metal atoms. Z. Kristallog.* **227**, 321–333.

Magdysyuk, O.V.; Mueller, M.; Dinnebier; R.E.; Lipp, C.; Schleid, Th. (2014) *Parameterization of the coupling between strain and order parameter for $LuF[SeO_3]$. J. Appl. Cryst.* **47**, 701-711.

McCusker, L.B.; Baerlocher, Ch. (2008). *Using electron microscopy to complement X-ray powder diffraction data to solve complex crystal structures, Chem. Commun.* 1439–1451.

McCusker, L.B.; Baerlocher, Ch. (2013). *Electron crystallography as a complement to X-ray powder diffraction techniques. Z. Kristallogr.* **228**, 1–10.

Mittemeijer, E.J.; Welzel, U. (2012). *Modern diffraction methods.* Willey, Germany.

Mondal, S.; Prathapa, S.J.; van Smaalen, S. (2012). *Experimental dynamic electron densities of multipole models at different temperatures. Acta Cryst.* A**68**, 568–581.

Netzel, J.; Hofmann, A.; van Smaalen, S. (2008). *Accurate charge density of a-glycine by the maximum entropy method. CrystEngComm.* **10**, 335–343.

Palatinus, L.; van Smaalen, S. (2002), *The Generalized F-constraint in the Maximum Entropy Method: a study on simulated data, Acta Crystallogr.* A**58**, 559–567.

Palatinus, L.; van Smaalen, S. (2005). *The prior-derived F constraints in the maximum entropy method. Acta Cryst.* A**61**, 363–372.

Papoular, R.J.; Collin, G.; Colsont, D.; Viallet, V. (2002). *Direct Imaging Of Fractional Oxygen O_δ In Hg-based High-T_c Superconductors. AIP Conf. Proc.* **617**, 204–226.

Pecharsky, V.K.; Zavalij, P.Y. (2003). *Fundamentals of powder diffraction and structural characterization of materials.* 713 p. Springer, New York, USA.

Roversi, P.; Irwin, J.J.; Bricogne, G. (1998). *Accurate Charge-Density Studies as an Extension of Bayesian Crystal Structure Determination. Acta Cryst.* A**54**, 971–996.

Sakata, M.; Mori, R.; Kumazawa, S.; Takata, M.; Toraya, H. (1990). *Electron-Density Distribution from X-ray Powder Data by Use of Profile Fits and the Maximum-Entropy Method. J. Appl. Cryst.* **23**, 526–534.

Samy, A.; Dinnebier, R. E.; van Smaalen, S.; Jansen, M. (2010). *Maximum entropy method and charge flipping, a powerful combination to visualize the true nature of structural disorder from in situ X-ray powder diffraction data. Acta Cryst.* **B66**, 184–195.

van Smaalen, S.; Palatinus, L.; Schneider, M. (2003). *The maximum entropy method in superspace. Acta Cryst.* **A59**, 459 – 469.

Soleimani-Dorcheh, A.; Dinnebier, R.E.; Kuc, A.; Magdysyuk, O.V.; Adams, F.; Denysenko, D.; Heine, Th.; Volkmer, D.; Donner, W.; Hirscher, M. (2012). *Novel characterization of the adsorption sites in large pore metal–organic frameworks: combination of X-ray powder diffraction and thermal desorption spectroscopy. PCCP*. **14**, 12892–12897.

Stinton, G.W.; Evans, J.S.O. (2007). *Parametric Rietveld refinement. J. Appl. Cryst.* **40**, 87–95.

Svendsen, H.; Overgaard, J.; Busselez, R.; Arnaud, B.; Rabiller, P.; Kurita, A.; Nishibori, E.; Sakata, M.; Takata, M.; Iversen, B.B. (2010). *Multipole electron-density modelling of synchrotron powder diffraction data: the case of diamond. Acta Cryst.* A66, 458–469.

Takata, M. (2008). *The MEM/Rietveld method with nano-applications – accurate charge-density studies of nano-structured materials by synchrotron-radiation powder diffraction. Acta Cryst.* A**64**, 232–245.

Tan, T.-Y.; Kennedy, B.J.; Zhou, Q.; Ling, C.D.; Miiler, W.; Howard, C.J.; Carpenter, M.A.; Knight, K.S. (2012). *Impact of Jahn-Teller active* Mn^{3+} *on strain effects and phase transitions in* $Sr_{0.65}Pr_{0.35}MnO_3$. *Phys. Rev. B.* **85**, 104107.

de Vries, R. Y.; Briels, W. J.; Feil, D. (1994). *Novel treatment of the experimental data in the application of the maximum-entropy method to the determination of the electron-density distribution from X-ray experiments. Acta Cryst.* **A50**, 383–391.

Xie, D.; Baerlocher, Ch.; McCusker, L.B. (2008). *Combining precession electron diffraction data with X-ray powder diffraction data to facilitate structure solution, J. Appl. crystallogr.* **41**, 1115–1121.

Xie, D.; Baerlocher, Ch.; McCusker, L.B. (2011). *Using phases retrieved from two-dimensional projections to facilitate structure solution from X-ray powder diffraction data. J. Appl. crystallogr.* **44**, 1023–1032.

Zheludev, A.; Papoular, R.J.; Ressouche, E.; Schweizer, J. (1995). *A Non-Uniform Reference Model for Maximum-Entropy Density Reconstruction from Diffraction Data. Acta Cryst.* A**51**, 450**–**455.

Chapter 2

Application of the maximum entropy method (MEM) to powder diffraction data

2.1. Introduction

Conventional Fourier synthesis is the most commonly used method for localization of missing atoms in crystal structures from powder diffraction data. A "perfect" Fourier map would require a complete set of structure factors up to a resolution of at least $\sin\theta/\lambda = 5.0$ Å^{-1} (de Vries *et al.*, 1994; Roversi *et al.*, 1998; Mondal *et al.*, 2012). This resolution is far beyond any realistic experimental resolution (the resolution of powder diffraction data measured on laboratory instruments is generally limited to $[\sin(\theta)/\lambda]_{max} \approx 0.6$ A^{-1} for CuKα-radiation). Another limiting factor of powder diffraction is intrinsic and accidental peak overlap due to the projection of the three-dimensional reciprocal space onto the one dimensional 2θ axis (Fig. 2.1). A strong disadvantage of the Fourier synthesis for electron density reconstruction is the inability to incorporate additional information about the density map, like positivity of the electron density. As a result, the Fourier transform is affected by series termination errors (e.g., spurious peaks of positive electron densities that do not correspond to atoms in the structure and unphysical local minima with negative densities).

The concept of entropy of a map of strictly positive values goes back to Shannon (1948a, 1948b). Maximizing the entropy of a map has become a powerful tool for reconstruction of nuclear and electron density distributions from intrinsically limited and/or noisy experimental X-ray powder diffraction data.

The concept of informational entropy was introduced in the field of crystallography to handle series termination effects in Fourier maps. Series termination effects are much less pronounced in MEM-optimized electron density maps than in Fourier maps obtained with the same data. It has been demonstrated that MEM can be successfully used with powder diffraction data for localization of missing atoms with high occupancies in incomplete crystal structures (Papoular *et al.*, 1995; Ikeda *et al.*, 1998; Kitaura *et al.*, 2002; Matsuda *et al.*, 2005), for revealing the nature of structural disorder (Dinnebier *et al.*, 1999; Samy *et al.*, 2010) and for determination of integrated atomic charges (Buchter *et al.*, 2011). On the other hand, the capability of the MEM to locate missing atoms with low occupancies and to reconstruct their

accurate electron density distribution is not fully investigated. This holds in particular true in case of commonly used high-resolution laboratory X-ray powder diffraction data.

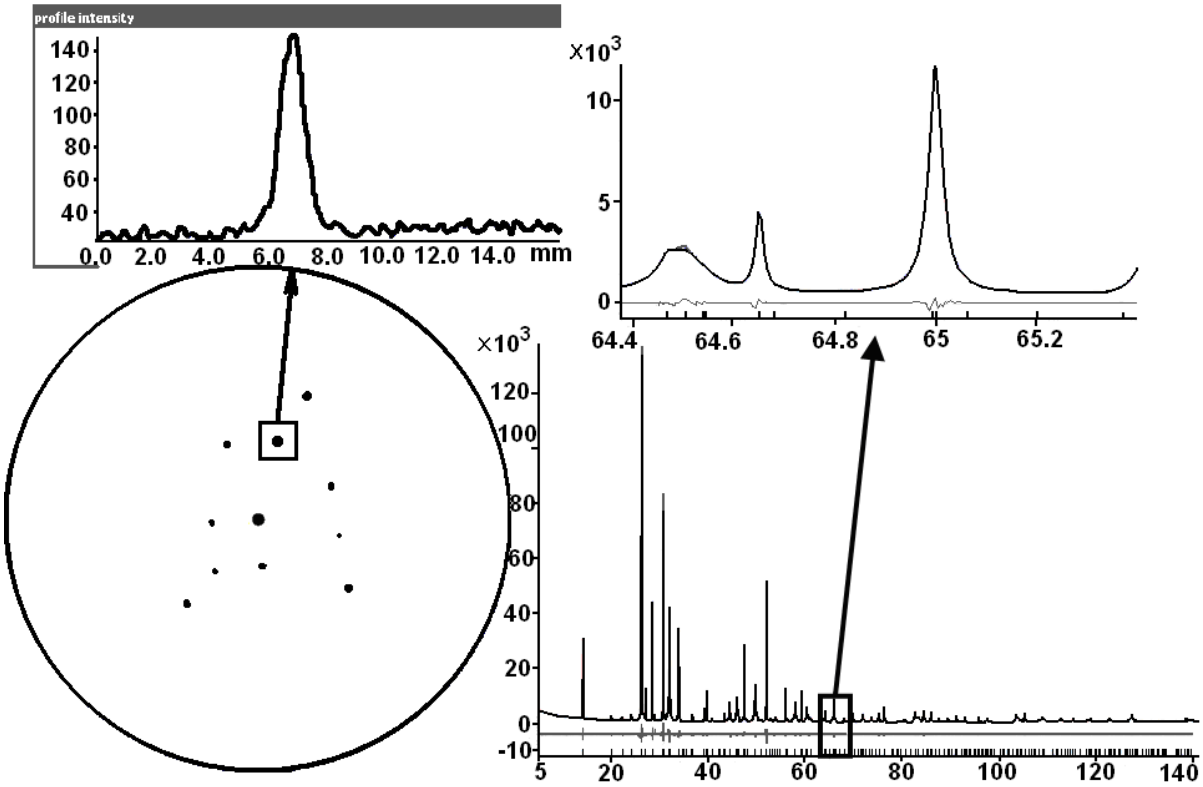

Figure 2.1. X-ray single crystal and powder diffraction data of Pb_3O_4. The powder diffraction pattern includes systematically and accidentally overlapping reflections.

2.2. Basics of application of MEM to powder diffraction data.

In the MEM, the unit cell (with lattice parameters *a*, *b*, and *c*) is divided into a grid of $N_{pix} = N_a \times N_b \times N_c$ pixels. The entropy of the system is defined as:

$$S = -\sum_{i=1}^{Npix}\left\{-\rho_i + \rho_i^{prior} + \rho_i \log\frac{\rho_i}{\rho_i^{prior}}\right\} \qquad (1.1)$$

considering the density ρ_i of pixel *i* and the prior density ρ_i^{prior}. The prior density ρ_i^{prior} can be used for the introduction of prior information that is available about the system. The prior density can represent any desirable distribution of the available electrons over the unit cell. The prior density can be also a constant function, thus called a flat or uniform prior. In the present study either the density of the independent spherical atom model (ISAM) of the structure obtained after Rietveld refinement (procrystal density), or a uniform (flat) prior were employed.

The ρ_i are adjusted so that S is maximized under the constraints of normalization of the density and constraints representing the diffraction data.

The normalization of the electron density $\{\rho_i\}$ over the unit cell to the expected number of electrons, N_{el}, in the unit cell of volume V_{UC}:

$$C_N = N_{el} - \frac{V_{UC}}{N_{pix}} \sum_{i=1}^{Npix} \rho_i = 0 \qquad (1.2)$$

The experimental data for the electron density reconstruction are represented by the observed structure factors (so-called F-constraints)

$$C_F = -\chi^2_{aim} + \frac{1}{N_F} \sum_{i=1}^{N_F} \omega_i \left(\frac{\left| F_{obs}(\vec{\mathrm{H}}_i) - F_{MEM}(\vec{\mathrm{H}}_i) \right|}{\sigma(\vec{\mathrm{H}}_i)} \right)^2 = 0 \qquad (1.3)$$

where N_F is the number of observed structure factors $F_{obs}(\vec{\mathrm{H}}_i)$ with standard uncertainties $\sigma(\vec{\mathrm{H}}_i)$; $F_{MEM}(\vec{\mathrm{H}}_i)$ is obtained by discrete Fourier transform of the current estimate of the charge density $\{\rho_i\}$. The standard version of the MEM employs $\omega_i = 1$ and $\chi^2_{aim} = 1$.

Integrated intensities of individual Bragg reflections can be determined by powder diffraction for resolved reflections as well as for reflections with little overlap, employing one of the decomposition techniques for powder diffraction data. For reflections with severe overlapping, only the sum of intensities of group of reflections can be measured. When the crystal structure is at least partially known, the calculated intensities of all individual reflections are available from the current structural model. These calculated intensities can be used to divide the total intensity of the peak into contributions of all overlapping reflections proportional to their calculated intensities (Rietveld, 1967, 1969). This procedure results into strong bias by the (incomplete) model of the intensities and phases of individual reflections. A Le Bail fit (Le Bail *et al.*, 1988) assigns the intensities for overlapping reflections based only on the quality of refinement (intensities are varied as independent variables to minimize the least-square function), regardless if this assignment is meaningful. For fully overlapping reflections the total intensity of the peak will be equally divided between all contributed reflections.

Fig. 2.2 presents an example of decomposition of the intensities of overlapping reflections into individual reflections by a Le Bail fit (without structural model) and by a Rietveld refinement (with structural model) for $K_2C_2O_4$ (Samy *et al.*, 2010; Dinnebier *et al.*, 2005).

Careful consideration of the Rietveld and Le Bail plots shows strong differences between peak fitting at $2\theta = 37.57^{o}$. Two reflections at $2\theta = 37.57^{o}$ are fully overlapped, and the Le Bail fit assigns equal intensities to both reflections. The Rietveld refinement assigns all experimental intensity to one Bragg reflection and zero intensity to the other, because the calculated structure factor of the latter is zero.

Any technique of decomposition of integrated intensities for a group of overlapping reflections into individual intensities of single reflections decreases the accuracy of the reconstructed electron density distribution due to the possible bias by the model used for decomposition of integrated intensities of the group. These uncertainties can be avoided by the use of so-called *G*-constraints based on the integrated intensities of groups of overlapping reflections (Sakata *et al.*, 1990).

G-constraints are based on N_G groups of overlapping reflections. Group *i* has contributions of N_G^i reflections, resulting in a "group amplitude" G^i equal to the square root of the integrated intensity and related to the structure factor amplitudes through:

$$G^i = \sqrt{\sum_{j=1}^{N_G^i}\left(\frac{m_j}{\sum m_j}\left|F(\vec{\mathrm{H}}_j)\right|^2\right)} \qquad (1.4)$$

where m_j is the point-group multiplicity of reflection *j*. The summation runs over the symmetry-independent structure factors contributing to group *i*. The standard uncertainty of the group amplitude G^i follows as:

$$\sigma(G^i) = \frac{1}{G^i}\sqrt{\sum_{j=1}^{N_G^i}\left(\frac{m_j}{\sum m_k}\left|F(\vec{\mathrm{H}}_j)\right|\sigma(F_j)\right)^2} \qquad (1.5)$$

The group amplitudes can be used in the *G*-constraint in a way similar to the *F*-constraint (eq. 1.3):

$$C_G = -\chi^2_{aim}(G) + \frac{1}{N_G}\sum_{i=1}^{N_G}\left(\frac{G^i_{obs} - G^i_{MEM}}{\sigma(G^i_{obs})}\right)^2 \qquad (1.6)$$

where G^i_{obs} and $\sigma(G^i_{obs})$ are the group amplitude and standard uncertainty as obtained from the experiment and G^i_{MEM} is computed from $F_{MEM}(\vec{\mathrm{H}}_j)$ according to eq. 1.4.

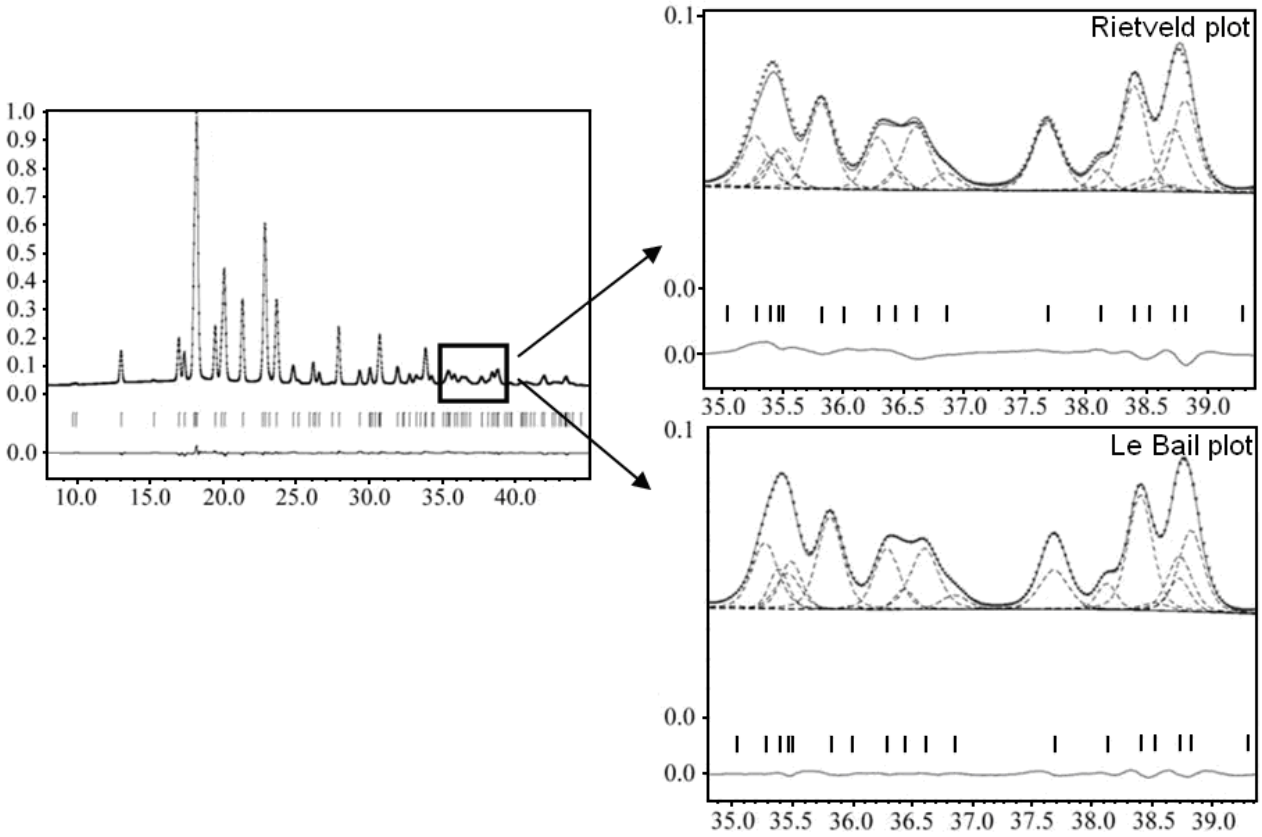

Figure 2.2. Dividing of the total intensity of overlapping reflections into the contributions of individual reflections by Rietveld refinement (with structural model) and by Le Bail fit (without structural model) for powder diffraction data of $K_2C_2O_4$ (adapted Fig. 3 from Samy *et al.*, 2010).

2.3. Application of MEM for reconstruction of electron density of apatites from X-ray powder diffraction data

2.3.1. Background information

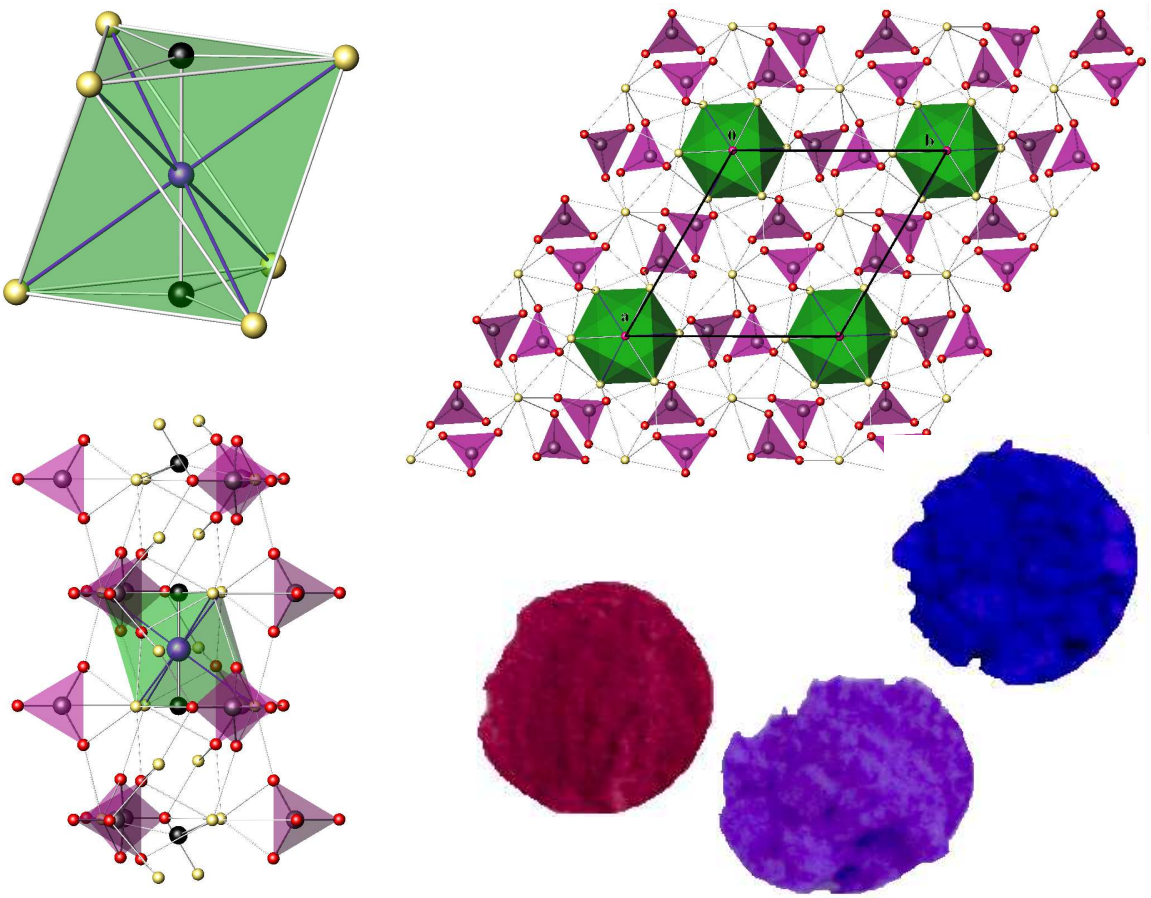

Figure 2.3. Crystal structure of investigated hydroxy-apatites of general formula $Sr_5(PO_4)_3OH_{x-\delta}$ with intercalated oxygen-metal-oxygen linear units in the channels (inside of green polyhedra). These apatites are used as inorganic pigment because of their bright color.

The unique physical properties of apatites make them attractive for a variety of practical applications: catalysis, bone replacement, inorganic pigments, solid-oxide fuel cells (White & ZhiLi, 2003; Fukuda *et al.*, 2012; Wopenka & Pasteris, 2005; Karpov *et al.*, 2003; Kazin *et al.*, 2003, 2007, 2008, 2012, 2014). Sr-apatites with intercalated copper atoms are used as non-toxic inorganic pigments in industrial production (patents: Kazin *et al.*, 2002; 2004), and the development of new inorganic apatite-based pigments are subject of ongoing basic investigations (Kazin *et al.*, 2014). The latter requires deep understanding of the chemical process of apatite synthesis and relation between color and structural changes. It is important to

note, that single crystals of apatites with intercalated atoms are colorless in contrast to powdered samples (Kazin *et al.*, 2003), thus the growing of single crystals results in substances with different properties, and possibly, different in-channel structure.

Apatites with general formula $A_5(BO_4)X$ (sg. $P6_3/m$) are comprised of BO_4 tetrahedra (pink tetrahedra in Fig. 2.3), cations A (yellow atoms in Fig. 2.3) are located in two symmetry independent positions (between BO_4 tetrahedra and along the one-dimensional channels), and anion X is located in the channel formed by A cations (Fig. 2.3). The $A(1)$ cation (surrounded by BO_4 tetrahedra) is described by being coordinated by nine oxygen atoms (6 of them are closer to $A(1)$), while the $A(2)$ cation (along one-dimensional channels) is coordinated by seven oxygen atoms and one X atom. The location of the large anion X in position (0,0,0) instead of (0, 0, ¼) often results into a decrease of the symmetry of the crystal structure of apatite (White & ZhiLi, 2003). Often anion X is displaced from its position and statistically occupies two closely located symmetry-equivalent positions.

Synthesis and physical properties of all apatites, investigated in this work, were previously described by Karpov *et al.* (2003) and Kazin *et al.* (2003, 2007, 2008, 2012, 2014).

In the present study, the MEM was used to locate the intercalated metal atoms (Cu, Ni, Zn) in the incomplete crystal structures of apatites, and to determine their electron density distribution. The localization of missing atoms using either Fourier synthesis or MEM is based on the Rietveld refinement of the initial incomplete crystal structure model. Alternatively, amplitudes of structure factors extracted after a Le Bail fit were used for MEM calculations of centrosymmetric crystal structures. For non-centrosymmetric structures problems arise in dividing intensities between real and imaginary parts and in assigning phases.

2.3.2. X-ray powder diffraction investigation of apatites

X–ray powder diffraction data of hydroxyl-apatites $Sr_5(PO_4)_3Ni_{0.2}OH_{0.8-\delta}$ (sample SrA(0.2Ni)) and $Sr_5(PO_4)_3Zn_{0.15}OH_{0.85-\delta}$ (sample SrA(0.15Zn)) with intercalated nickel and zinc atoms were collected at room-temperature on a laboratory powder diffractometer STOE (Cu–$K\alpha_1$ radiation from a primary Ge(111) monochromator; position sensitive detector Mythen-Dectris with 12^o opening) in Debye-Scherrer geometry.

X–ray powder diffraction data of all hydroxyapatite compounds with intercalated copper atoms, hydroxy-apatite, and peroxyhydroxy-apatite were collected at room-temperature on a

laboratory powder diffractometer D8–Advance (Cu–Kα_1 radiation from a primary Ge(111) monochromator; Linx-Eye position–sensitive detector with 3.5^o 2θ opening) in Bragg-Brentano geometry.

X–ray powder diffraction data of one series of Sr–apatites ($Sr_5(PO_4)_3Cu_{0.1}OH_{0.9-\delta}$, different content of peroxide δ) were also measured at room-temperature at the high-resolution powder diffractometer I11 at Diamond (Parker *et al.*, 2011; Thompson *et al.*, 2011; Thompson *et al.*, 2009). The wavelength was determined to be 0.8264(3) Å from a silicon standard. The samples were contained in sealed 0.5-mm lithium borate glass capillaries and were rotated around θ in order to improve randomization of the crystallites. The diffracted beam was detected with 45 MAC detectors.

All series of investigated apatites are summarized in Table 2.1.

The program TOPAS 4.1 (Coelho, 2007) was used for extraction of intensities after whole powder pattern fitting (WPPF) according to the Rietveld or Le Bail method. The fundamental-parameter approach to line profile analysis (Cheary & Coelho, 1992), implemented in Topas 4.1, allows to describe accurately line profile shapes across a large 2θ range, with all refined parameter values having physical meaning. In the conventional mathematical approach to fitting, the refined numerical parameters are mainly phenomenological, which can be responsible for an erroneous assigning of intensities in groups of overlapping reflections in the latter approach. Crystallographic and refinement data for all samples at ambient conditions are given in Appendix 1, Tables A1-A4. Experimental and calculated profiles for typical Rietveld refinements and Le Bail fits are given in Figs. 2.4 and 2.5.

Table 2.1. Different series of investigated hydroxyl-apatites.

Sample	Molecular formula
Sr–hydroxyapatites (SrA) without fluorine atoms with different content of intercalated copper atoms	
SrA(0.3Cu-2)	$Sr_5(PO_4)_3Cu_{0.3}OH_{0.7-\delta}$
SrA(0.25Cu)	$Sr_5(PO_4)_3Cu_{0.25}OH_{0.75-\delta}$
SrA(0.125Cu)	$Sr_5(PO_4)_3Cu_{0.125}OH_{0.875-\delta}$
SrA(0.1Cu-2)	$Sr_5(PO_4)_3Cu_{0.1}OH_{0.9-\delta}$
SrA(0.05Cu)	$Sr_5(PO_4)_3Cu_{0.05}OH_{0.95-\delta}$
Ca–hydroxyapatites (CaA) without fluorine atoms with different content of intercalated copper atoms	
CaA(0.3Cu)	$Ca_5(PO_4)_3Cu_{0.3}OH_{0.7-\delta}$
CaA(0.1Cu)	$Ca_5(PO_4)_3Cu_{0.1}OH_{0.9-\delta}$
Ca– and Sr–hydroxyapatites (CaA and SrA) with in-channel fluorine atoms and with different content of intercalated copper atoms	
CaA(0.1Cu_0.5F)	$Ca_5(PO_4)_3Cu_{0.1}O_{0.5}H_{0.4-\delta}F_{0.5}$
CaA(0.05Cu_0.5F)	$Ca_5(PO_4)_3Cu_{0.05}O_{0.5}H_{0.45-\delta}F_{0.5}$
CaA(0.02Cu_0.5F)	$Ca_5(PO_4)_3Cu_{0.02}O_{0.5}H_{0.48-\delta}F_{0.5}$
CaA(0.01Cu_0.5F)	$Ca_5(PO_4)_3Cu_{0.01}O_{0.5}H_{0.49-\delta}F_{0.5}$
SrA(0.05Cu_0.5F)	$Sr_5(PO_4)_3Cu_{0.05}O_{0.5}H_{0.45-\delta}F_{0.5}$
Sr–hydroxyapatites (SrA) with intercalated copper atoms of occupancy 0.1 and different content of peroxide and copper ions in higher oxidation state	
SrA(0.1Cu-1), $\delta = 0.038$	$Sr_5(PO_4)_3Cu_{0.1}OH_{0.9-\delta}$
SrA(0.1Cu-2), $\delta = 0.10$	$Sr_5(PO_4)_3Cu_{0.1}OH_{0.9-\delta}$
SrA(0.1Cu-3), $\delta = 0.26$	$Sr_5(PO_4)_3Cu_{0.1}OH_{0.9-\delta}$
SrA(0.1Cu-4), $\delta > 0.26$	$Sr_5(PO_4)_3Cu_{0.1}OH_{0.9-\delta}$
Sr–hydroxyapatites (SrA) with intercalated copper atoms of occupancy 0.3 and different content of peroxide and copper ions in higher oxidation state	
SrA(0.3Cu-1), $\delta = 0.022$	$Sr_5(PO_4)_3Cu_{0.3}OH_{0.7-\delta}$
SrA(0.3Cu-2), $\delta = 0.104$	$Sr_5(PO_4)_3Cu_{0.3}OH_{0.7-\delta}$
SrA(0.3Cu-3), $\delta = 0.29$	$Sr_5(PO_4)_3Cu_{0.3}OH_{0.7-\delta}$
Sr–hydroxyapatites (SrA) with intercalated nickel atoms of occupancy 0.2 and with intercalated zinc atoms of occupancy 0.15	
SrA(0.2Ni)	$Sr_5(PO_4)_3Ni_{0.2}OH_{0.8-\delta}$
SrA(0.15Zn)	$Sr_5(PO_4)_3Zn_{0.15}OH_{0.85-\delta}$

Parameter δ corresponds to the presence of peroxide ions O_2^{2-} (equivalent to ½ δ) and/or copper in the oxidation state above +1 (equivalent to $\frac{\delta}{n-1}$, n – the copper oxidation state).

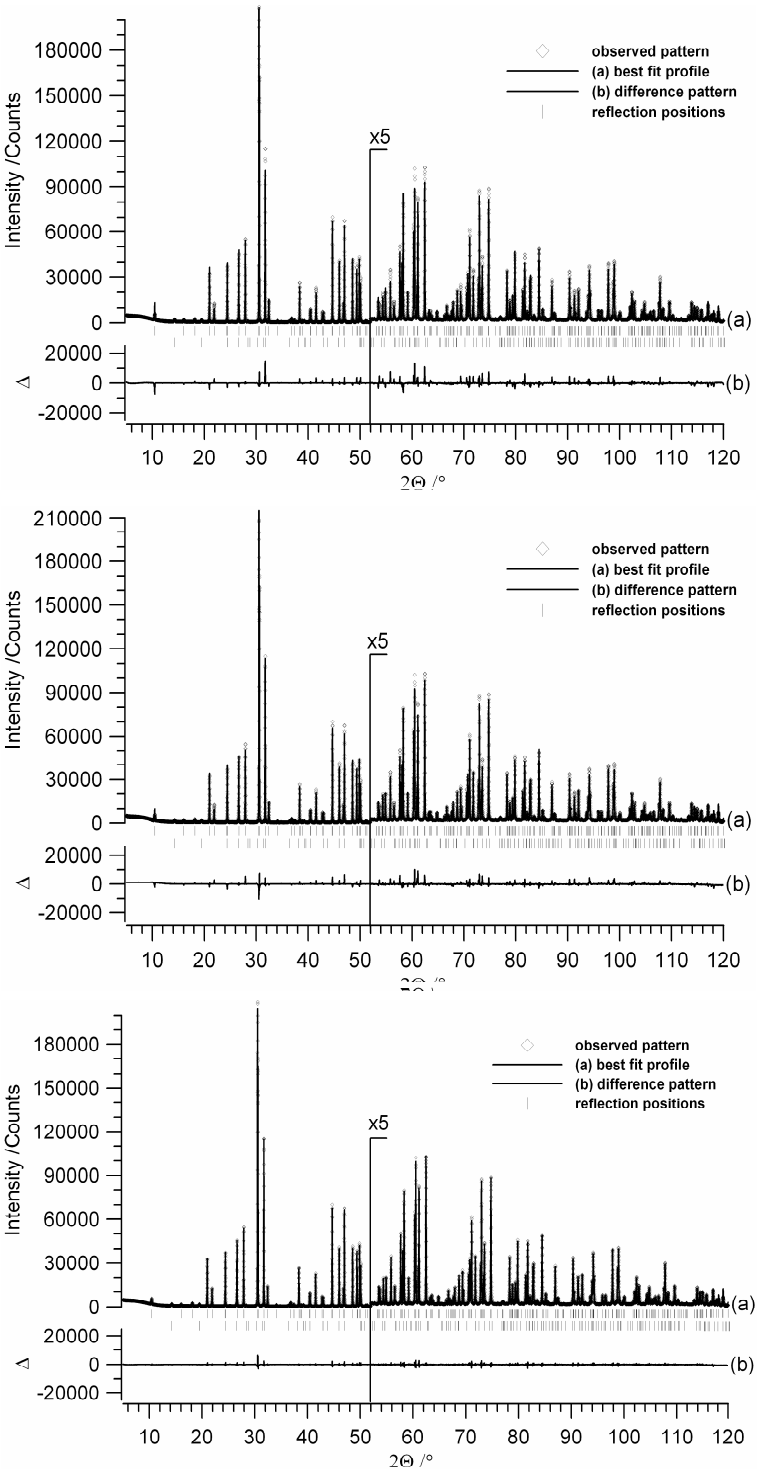

Figure 2.4. Rietveld plots of laboratory X-ray powder diffraction data of apatite $Sr_5(PO_4)_3Cu_{0.1}OH_{0.9-\delta}$ (sample SrA(0.1Cu-2), $\delta = 0.10$) without copper atoms (top), with copper atoms included (middle) and Le Bail fit (bottom). $Sr(OH)_2 \cdot H_2O$ was refined as second phase (2 weight %).

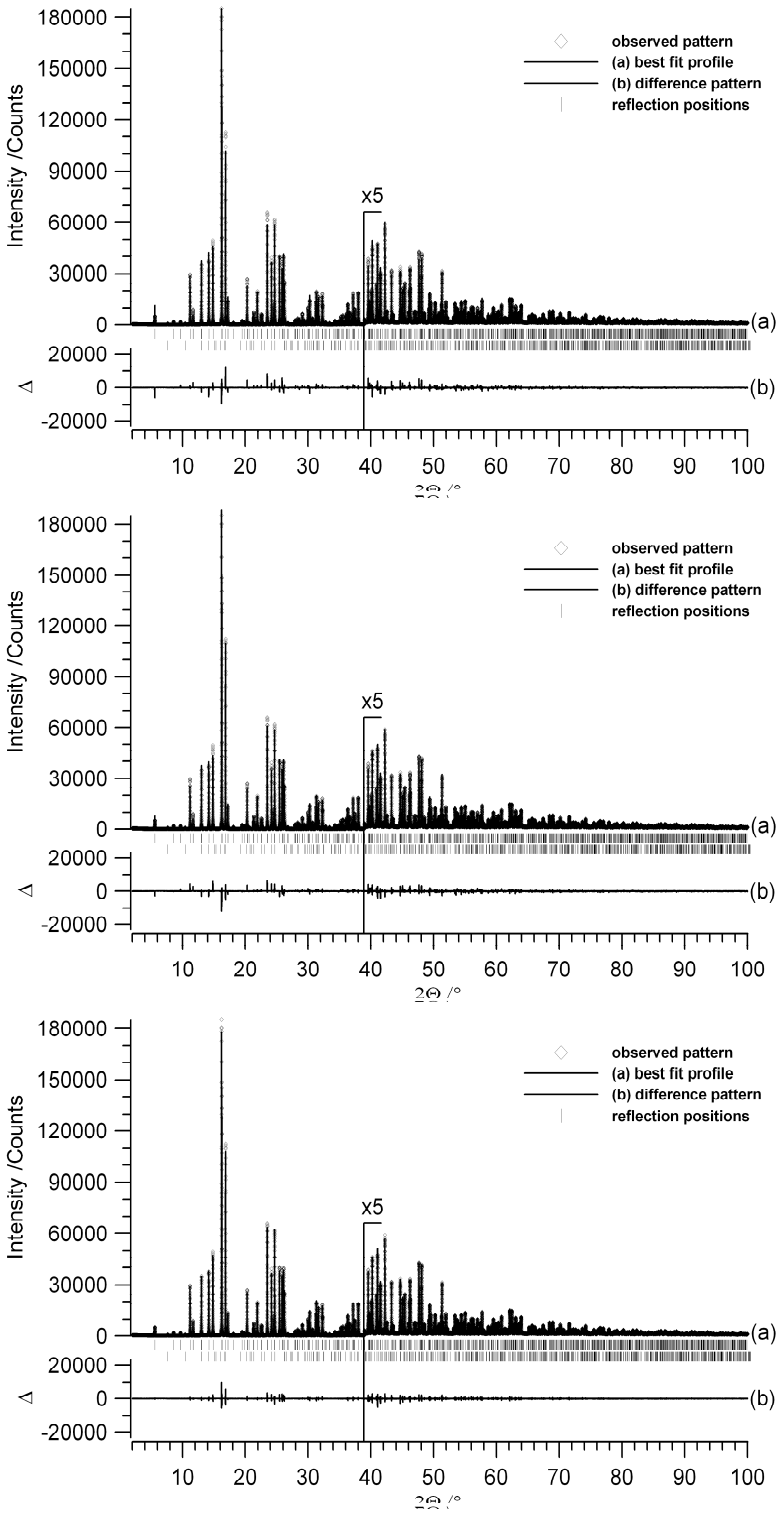

Figure 2.5. Rietveld plots of synchrotron X-ray powder diffraction data of apatite $Sr_5(PO_4)_3Cu_{0.1}OH_{0.9-\delta}$ (sample SrA(0.1Cu-2), $\delta = 0.10$) without copper atoms (top), with copper atoms included (middle) and Le Bail fit (bottom). $Sr(OH)_2 \cdot H_2O$ was refined as second phase (2 weight %).

2.3.3. MEM calculations of electron density of apatites

All MEM calculations were performed with the computer program BayMEM (van Smaalen *et al.*, 2003), employing the Sakata–Sato algorithm (Sakata & Sato, 1990). Details about the maximum-entropy calculations are given in Appendix 1, Tables A5-A12. The maximal resolution $\sin\theta/\lambda$ for laboratory X-ray powder diffraction data was 0.55 $Å^{-1}$. Synchrotron data could be measured up to higher resolution, and three different data sets with resolutions $\sin\theta/\lambda$ = 0.55 $Å^{-1}$, $\sin\theta/\lambda$ = 0.65 $Å^{-1}$, and $\sin\theta/\lambda$ = 0.93 $Å^{-1}$ were chosen for comparison of MEM calculations from synchrotron and laboratory powder diffraction data. Optimal values for the Lagrange multiplier λ were obtained by trial and error; an automated adjustment of λ during iterations was not possible due to an increase of the constraints values for several cycles of the iteration. In the MEM calculations, the total number of electrons in the unit cell was given as a constant. The number of electrons for all missing atoms was included in the calculations.

Special attention was given to the value of the stopping criterion χ^2_{aim}. Historically the MEM uses χ^2_{aim} = 1 as stopping criterion. Applying this stopping criterion to the present work resulted either in non-fitting of a significant amount of electron density or overfitting. Therefore, the stopping criterion was modified according to the procedure described in Hofmann *et al.* (2007) in order to avoid under- and overfitting of the electron density. The value of χ^2_{aim} depended strongly on the occupancy of missing atoms, on the presence of other atoms in the hexagonal channel, on the type of the prior density (procrystal density or flat prior), on the type of constraints (F_{obs}, F_{obs}+G, F_{LeBail}+G) used for the MEM calculations, and on the resolution $\sin\theta/\lambda$ of X-ray powder diffraction data.

Atomic charges, densities, and volumes were determined by applying the Bader analysis for atoms in molecules (Bader, 1990) to the MEM reconstructed electron density distribution, using the program EDMA (Palatinus *et al.*, 2012) with partition mode “on-grid”.

The determination of the electron density of in-channel atoms consists of two parts: localization of the intercalated atoms in the crystal structure (chapter 2.3.4) and determination of their electron density distribution (chapter 2.3.5)

2.3.4. Localization of intercalated atoms in apatites by MEM from X-ray powder diffraction data

Originally, the MEM was introduced in crystallography as a method for localizing missing atoms in complicated cases (reviewed by Takata, 2008), where Fourier maps could not provide unambiguous results. Although it was shown, that MEM calculations can be performed based on several different types of constraints (Samy *et al.*, 2010), MEM calculations for localizaton of missing atoms were performed only based on F_{obs} – constraints (Takata, 2008).

In the present work, the possibilities and limitations of the MEM for localization of missing intercalated metal atoms in apatites with intercalated copper, nickel and zinc metal atoms based on applying different types of constraints: F_{obs}, F_{obs}+G, and F_{LeBail}+G were investigated. The concentration of metal atoms is quite low in all samples, thus the Fourier method turned out to be inappropriate.

For all investigated compounds, conventional Fourier maps based on F_{obs} (phases of the structure factors are calculated from the best incomplete model) contain a lot of spurious peaks with high electron density, making it impossible to locate the intercalated metal atoms unambiguously. Using difference-Fourier maps, copper atoms with fractional occupancies of 0.3, 0.125 and 0.1 could be located (Fig. 2.6), while for compounds with lower concentrations of 0.05, 0.02 and 0.01 all difference-Fourier maps contained spurious peaks higher than the peaks at the presumed copper positions (Fig. 2.7).

MEM maps based on F_{obs}–, F_{obs}+G– and F_{LeBail}+G–constraints allowed unambiguous localization of copper atoms with occupancies down to 0.05, which corresponds to approximately 1.4 electrons per site. The occupancy of 0.02 for copper atoms corresponds to approximately 0.6 electrons per atomic position. The localization of atoms with such low occupancy is usually impossible even from single crystal data. The presence of copper atoms with occupancy 0.02 and 0.01 in the channels could thus only be concluded based on the change in color and physical properties. Fig. 2.8 presents the general scheme of filling of channels of apatites with different types of in-channel atoms. Figs. 2.9–2.20 show the results of localization of missing metal atoms in the hexagonal channels of apatites using MEM maps.

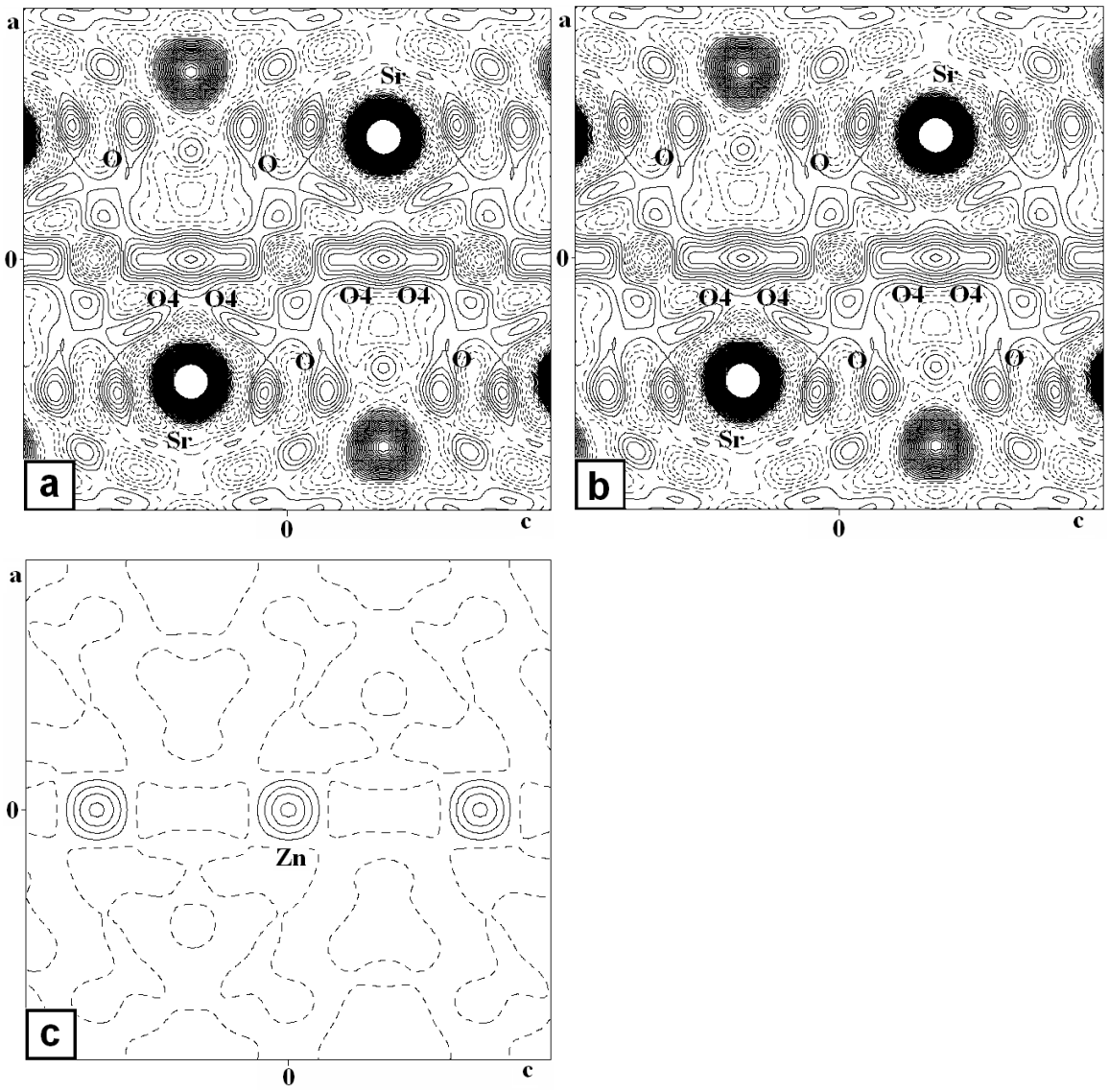

Figure 2.6. Two-dimensional Fourier electron-density maps at *y=0* of apatite $Sr_5(PO_4)_3Zn_{0.15}OH_{0.85-\delta}$ (sample SrA(0.15Zn)).

Contour levels: from 1 to 50 e/Å^3, step 1 e/Å^3. High-resolution laboratory X-ray powder diffraction data.

a) based on F_{calc}
b) based on F_{obs}
c) based on F_{diff}

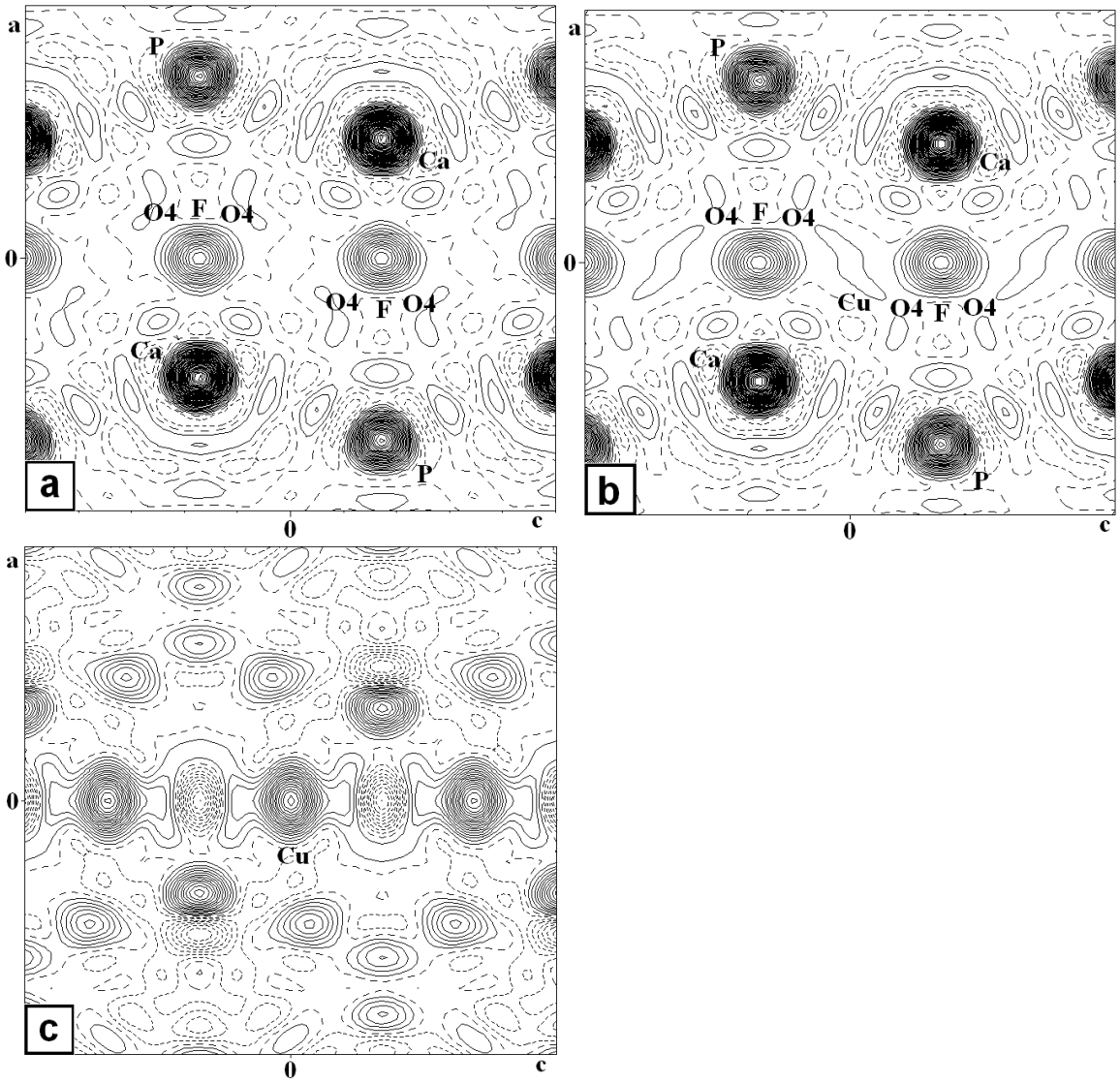

Figure 2.7. Two-dimensional Fourier electron-density maps at *y=0* of apatite $Ca_5(PO_4)_3Cu_{0.05}OH_{0.9-\delta}F_{0.5}$ (sample CaA(0.05Cu_0.5F)).

Contour levels: from 1 to 50 e/Å^3, step 1 e/Å^3. High-resolution laboratory X-ray powder diffraction data.

a) based on F_{calc}
b) based on F_{obs}
c) based on F_{diff}

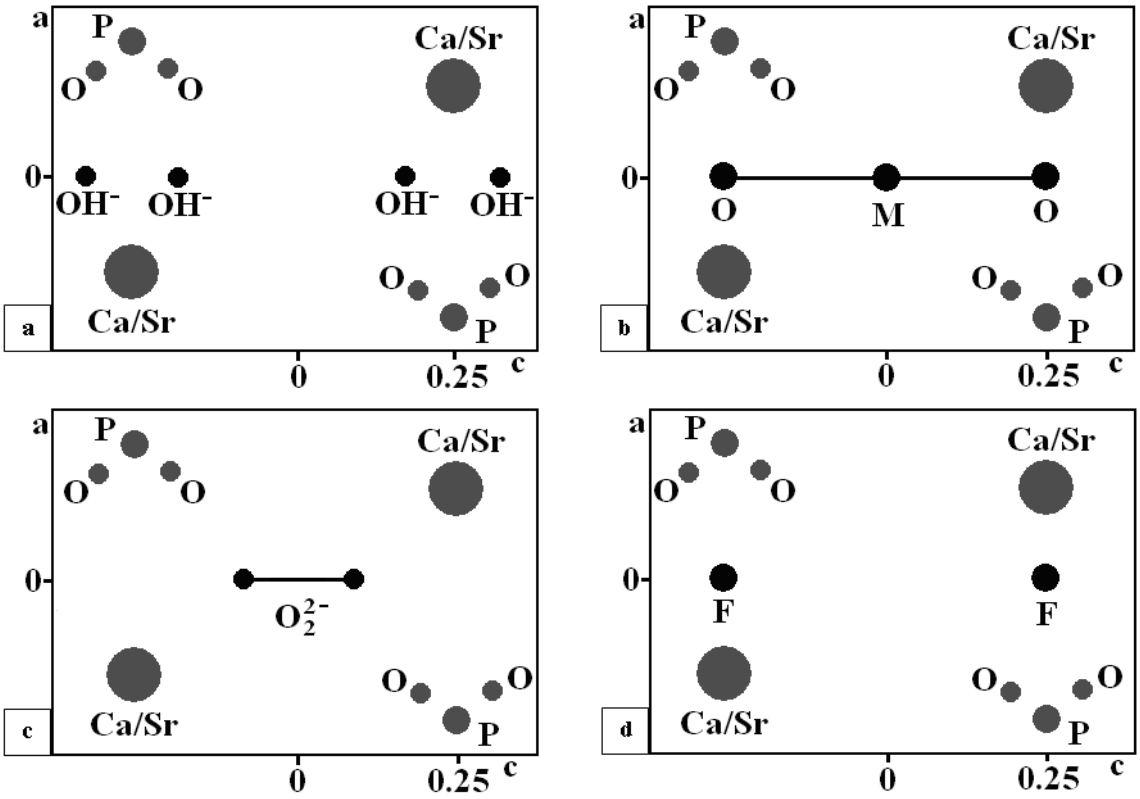

Figure 2.8. Schemes of filling of channels in investigated apatites. M – different intercalated metal atoms.

a) scheme of channel in hydroxyapatite (Sudarsanan *et al.*, 1972)

b) scheme of channel in apatite with intercalated metal atoms (Karpov *et al.*, 2003)

c) scheme of channel in hydroxyapatite with peroxide atoms (Kazin *et al.*, 2012)

d) scheme of channel in apatite with fluorine atoms (Rodriguez-Lorenzo *et al.*, 2003)

a) MEM calculations based on F_{obs}–constraints from high-resolution laboratory X-ray powder diffraction data

MEM calculations based on the observed structure factors F_{obs} from Rietveld refinement and flat prior density were successfully applied for localization of atoms from high-resolution synchrotron data (Papoular *et al.*, 1995; Ikeda *et al.*, 1998; Kitaura *et al.*, 2002; Matsuda *et al.*, 2005).

In this work, the MEM was applied for localization of missing atoms with low occupancy in the incomplete crystal structure of apatite from high-resolution laboratory X-ray powder diffraction data (resolution $\sin\theta/\lambda = 0.55$ Å^{-1}). This method worked well down to an occupancy

of copper atoms of 0.05 (Figs. 2.9-2.17). In contrast to the standard procedure (Takata, 2008), the MEM calculations based on F_{obs}–constraints were performed not only with a flat prior density, but also with a procrystal density in form of the independent spherical atomic model (ISAM) from the best Rietveld refinement of the corresponding incomplete structure (without intercalated metal atoms).

It was found that different factors influence the value of the electron density of the localized metal atoms in the channels of apatites: type of the prior electron density and location of other atoms in the channels near positions of intercalated metal atoms. In fluorine containing Ca–apatites the electron density of the located copper atoms was higher if the procrystal density for known atoms was used (Figs. 2.9-2.10). In fluorine free Ca– and Sr–apatites the electron density of the located copper atoms was the same or higher when a flat prior was used (Figs. 2.11-2.17). A possible explanation of this effect is a redistribution of the electron density in the channels during MEM calculations: fluorine atoms can accumulate electron density from nearby copper atoms, especially when flat prior density is used.

Almost all MEM maps based on F_{obs}–constraints with procrystal density for known atoms and with flat prior contained noise: the density of the strongest noise peak was 4-15 times smaller than the density of the located metal atom. In the case of powder diffraction data, electron density maps based on F_{obs}–constraints are strongly biased by the model, because the calculated structure factors of the model are used to decompose the overlapping reflections into contributions of individual reflections. At the same time the number of overlapping reflections is large for all investigated apatites (Appendix 1, Tables A5-A12). Due to the incomplete initial model, individual intensities between overlapping reflections as well as phases of weak reflections can be falsely assigned.

b) MEM calculations based on F_{obs}+G–constraints from high-resolution laboratory X-ray powder diffraction data

To decrease the model bias of the MEM reconstructed electron density, G–constraints for overlapping reflections were used together with observed structure factors extracted after Rietveld refinement of the incomplete structures (Samy *et al.*, 2010).

The MEM maps based on F_{obs}+G–constraints were more successful for localization of missing intercalated copper atoms than the MEM maps based on F_{obs}–constraints alone due to the better treatment of the intensities of strongly overlapping reflections (Figs. 2.9-2.17). In this

case it was necessary to use the procrystal electron density for all known atoms, because of the reduced information content of group intensities as compared to individual reflections. The localization of missing copper atoms in fluorine containing Ca–apatites was again complicated by the presence of fluorine atoms, with the located copper atom showing a lower value of electron density as compared to fluorine free Ca–apatite.

In Sr–apatite without fluorine atoms the atom O4 is a superposition of the electron density of the oxygen atom from the hydroxide group and the oxygen atom bonded to the copper atom (the latter is located at position (0, 0, 0.25), (Kazin *et al.*, 2003). The Rietveld refinement of the incomplete structure (without intercalated copper atoms) caused the displacement of O4 towards the position of Cu (0, 0, 0). In Sr–apatite SrA(0.1Cu-3) and especially in SrA(0.1Cu-4) this displacement is stronger than in Sr–apatite SrA(0.1Cu-1) due to the presence of a large amount of peroxide molecules near the position (0, 0, 0) (Kazin *et al.*, 2012). As a result, the refined O4 position can be also considered as a superposition of the electron densities of copper atoms and O_2^{2-} molecules. The presence of a large amount of peroxide molecules near the copper position in SrA(0.1Cu-3) and SrA(0.1Cu-4) causes elongation and redistribution of the electron density near the copper atom. The located copper atom in SrA(0.1Cu-1) shows a higher value of the electron density than in SrA(0.1Cu-3) and SrA(0.1Cu-4) (1.3 and 2 times, respectively).

c) MEM calculations based on F_{LeBail}+G–constraints from high-resolution laboratory X-ray powder diffraction data

Another possible combination of the structure factors for the MEM calculations of centrosymmetric crystal structures is the combination of the amplitudes of the structure factors from a Le Bail fit with calculated phases for resolved reflections: F_{LeBail}+G (Samy *et al.*, 2010).

The MEM maps based on F_{LeBail}+G–constraints were the most successful among all MEM maps calculated for localization of missing intercalated metal atoms (Figs. 2.9-2.17). The amplitudes of the structure factors extracted after the Le Bail fits were scaled according to the absolute scale factor of the Rietveld refinement of the corresponding incomplete structure (without intercalated metal atoms). From this Rietveld refinement the procrystal density was created for known atoms as ISAM. The Le Bail fit allows extractraction of amplitudes of the structure factors without bias from a structure model. The amplitudes of the structure factors after Le Bail fit can be used in the MEM calculations only with G–constraints for groups of

overlapping reflections. The corresponding esd's were taken from the MEM calculations based on F_{obs}+G–constraints.

The results of the MEM calculations based on F_{LeBail}+G–constraints are excellent for both, Ca– and Sr–apatite without fluorine atoms in the channels and Ca-apatite with fluorine atoms in the channels. Nevertheless, the localization of the copper atoms with extremely low occupancy of 0.02 and 0.01 was not successful.

Two interesting examples for localization of missing metal atoms are the Sr–apatites with intercalated Ni and Zn atoms (Figs. 2.16-2.17). A prominent feature of the powder diffraction data of these samples is the strong overlapping of the reflections in comparison to copper containing Sr– and Ca–apatites, which is caused by the change of the lattice parameters of the unit cell. The powder pattern of SrA(0.2Ni) apatite has at least 37 resolved reflections, while SrA(0.15Zn) apatite has only 18 (Appendix 1, Table A9). For both samples all four MEM maps were successful in localization of missing Ni and Zn atoms and the main features of the MEM maps were the same as in the case of Sr–apatite with missing copper atoms.

d) MEM calculations from high-resolution synchrotron X-ray powder diffraction data

MEM calculations based on F_{obs}–, F_{obs}+G–, and F_{LeBail}+G–constraints were performed for samples SrA(0.1Cu-1), SrA(0.1Cu-3), and SrA(0.1Cu-4). Three different values of resolution $\sin\theta/\lambda = 0.55$ Å^{-1}, $\sin\theta/\lambda = 0.65$ Å^{-1}, and $\sin\theta/\lambda = 0.93$ Å^{-1} were considered (Figs. 2.18-2.20). All tendencies observed for laboratory X-ray powder diffraction data were confirmed. For all MEM maps based on F_{obs}–, F_{obs}+G–, and F_{LeBail}+G–constraints with procrystal density for known atoms, the located copper atoms in SrA(0.1Cu-1) had a higher value of the electron density than in SrA(0.1Cu-3) and SrA(0.1Cu-4). In addition, the localization of missing atom was better when G–constraints were used for overlapping reflections. The highest values of the electron density of missing intercalated atoms were obtained in case of MEM maps based on F_{LeBail}+G–constraints and this value almost coincided with the value of the electron density of copper atoms for MEM calculations with intercalated copper atoms. The differences are caused by different scale factors: the localization of missing atoms based on F_{LeBail}+G–constraints was performed with the scale factor from Rietveld refinement of the incomplete structure. Additionally, anomalous scattering was not taken into account.

For all MEM maps based on F_{obs}–, F_{obs}+G–, and F_{LeBail}+G–constraints with procrystal density for known atoms, strong distortion of the electron density was detected near the copper

atom. This distortion increased with increasing content of peroxide in the investigated samples and was located close to the position of the peroxide atoms. For sample SrA(0.1Cu-4) with highest content of peroxide a splitting of the copper position on the MEM map based on F_{LeBail}+G–constraints at low resolution $\sin\theta/\lambda = 0.65$ Å^{-1} was detected (Fig. 2.20b), possibly caused by the presence of peroxide atoms near the copper atom and the corresponding accumulation of the electron density from the copper atom. The MEM map based on F_{LeBail}+G–constraints at high resolution $\sin\theta/\lambda = 0.93$ Å^{-1} two positions were detected near the copper atom for sample SrA(0.1Cu-4) (Fig. 2.20c), which are close to the position of the peroxide molecule (Kazin *et al.*, 2012). But the high level of noise did not allow unambiguous interpretation: the wavelength was close to the absorption edge of Sr leading to fluorescence, and the size of crystallites of this sample is more then 2 times lower than for all other samples. As a result, at high angles the peak-background ratio is low. In addition, at highest diffraction angles the reflections are very broad and the correlation between peak profile and background is quite strong. Consequently, the intensities at high angles were extracted with high uncertainty.

The electron density distribution at resolution $\sin\theta/\lambda = 0.55$ Å^{-1} from synchrotron data (Figs. 2.18a, 2.19a, 2.20a) is similar to the electron density distribution with the same resolution from laboratory data (Figs. 2.12-2.14), but the value of the electron density of the position of the in-channel atoms is higher in case of synchrotron data. With increasing the resolution from $\sin\theta/\lambda = 0.55$ Å^{-1} to $\sin\theta/\lambda = 0.93$ Å^{-1} for synchrotron powder data (Figs. 2.18c, 2.19c, 2.20c), the value of the electron density of the located copper atoms is increased for all MEM maps.

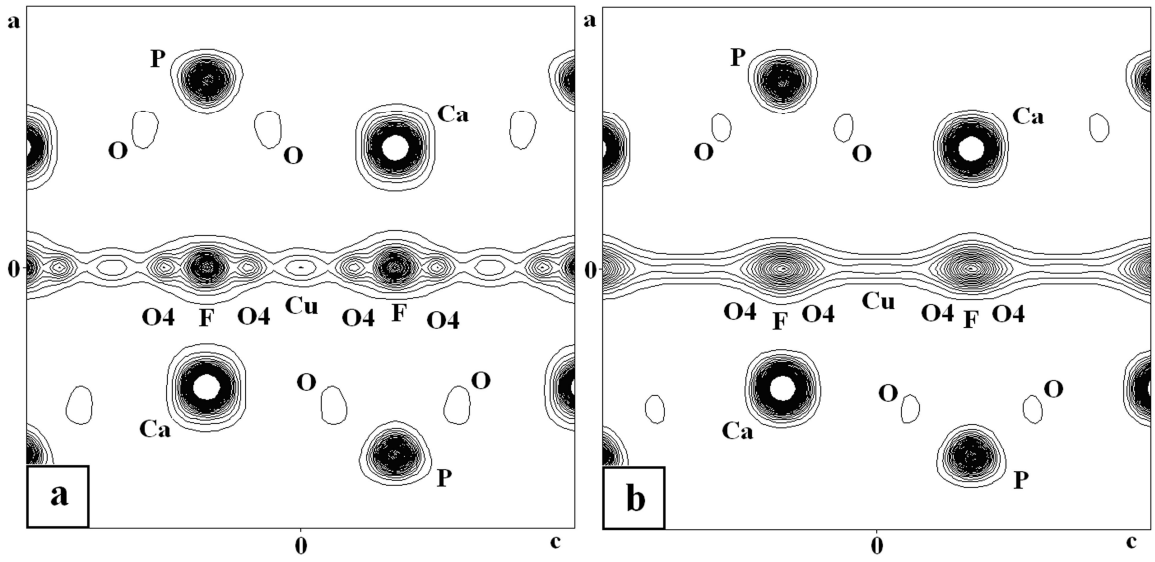

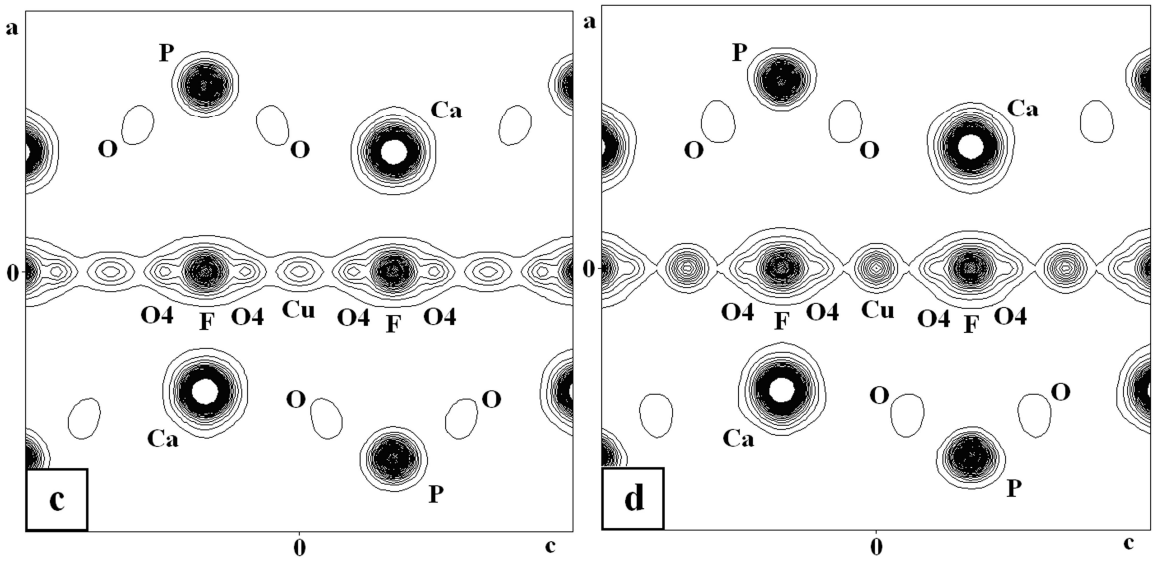

Figure 2.9. Two-dimensional electron-density maps at *y=0* of apatite $Ca_5(PO_4)_3Cu_{0.1}O_{0.5}H_{0.4-\delta}F_{0.5}$ (sample CaA(0.1Cu_0.5F)).

Contour levels: from 1 to 50 e/Å^3, step 1 e/Å^3. High-resolution laboratory X-ray powder diffraction data.

a) based on F_{obs} (with procrystal density for known atoms)

b) based on F_{obs} (with flat prior)

c) based on $F_{obs}+G$ (with procrystal density for known atoms)

d) based on $F_{LeBail}+G$ (with procrystal density for known atoms)

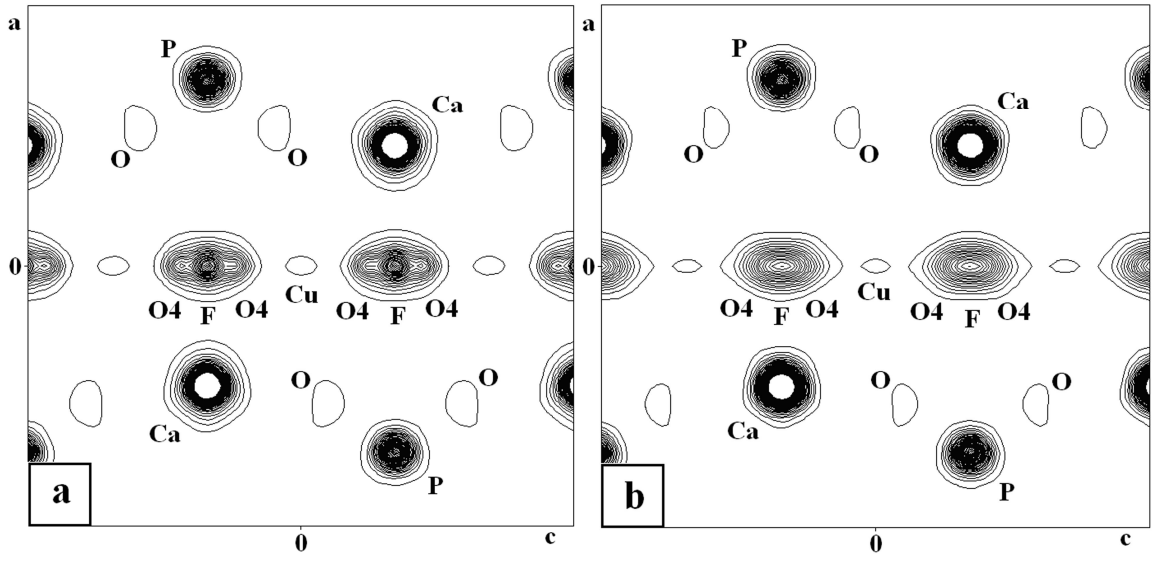

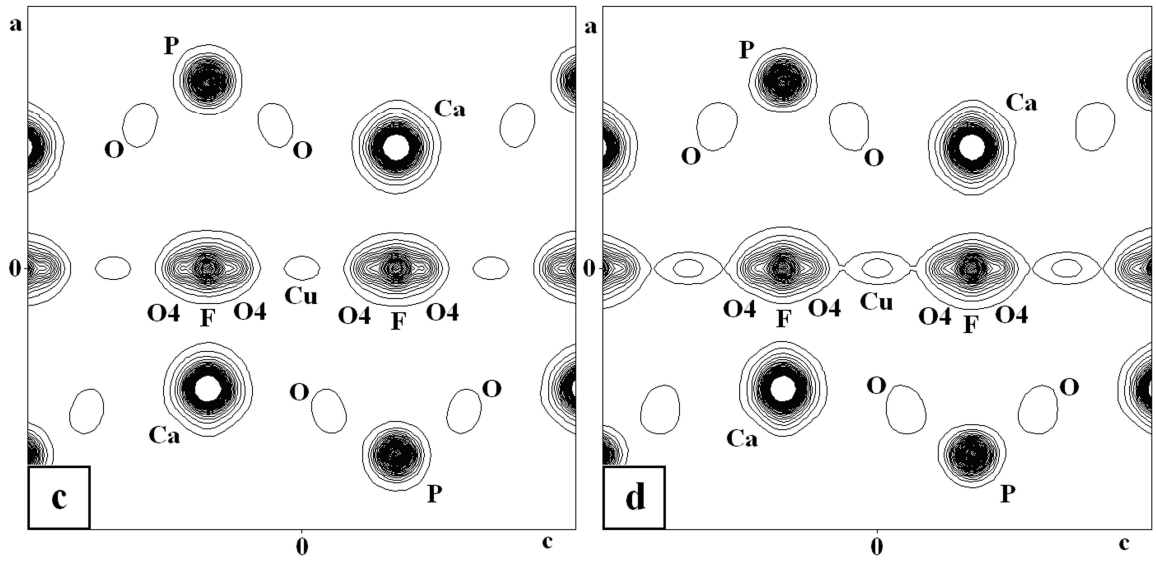

Figure 2.10. Two-dimensional electron-density maps at *y=0* of apatite $Ca_5(PO_4)_3Cu_{0.05}O_{0.5}H_{0.45-\delta}F_{0.5}$ (sample CaA(0.05Cu_0.5F)). Contour levels: from 1 to 50 e/Å^3, step 1 e/Å^3. High-resolution laboratory X-ray powder diffraction data.

a) based on F_{obs} (with procrystal density for known atoms)

b) based on F_{obs} (with flat prior)

c) based on $F_{obs}+G$ (with procrystal density for known atoms)

d) based on $F_{LeBail}+G$ (with procrystal density for known atoms)

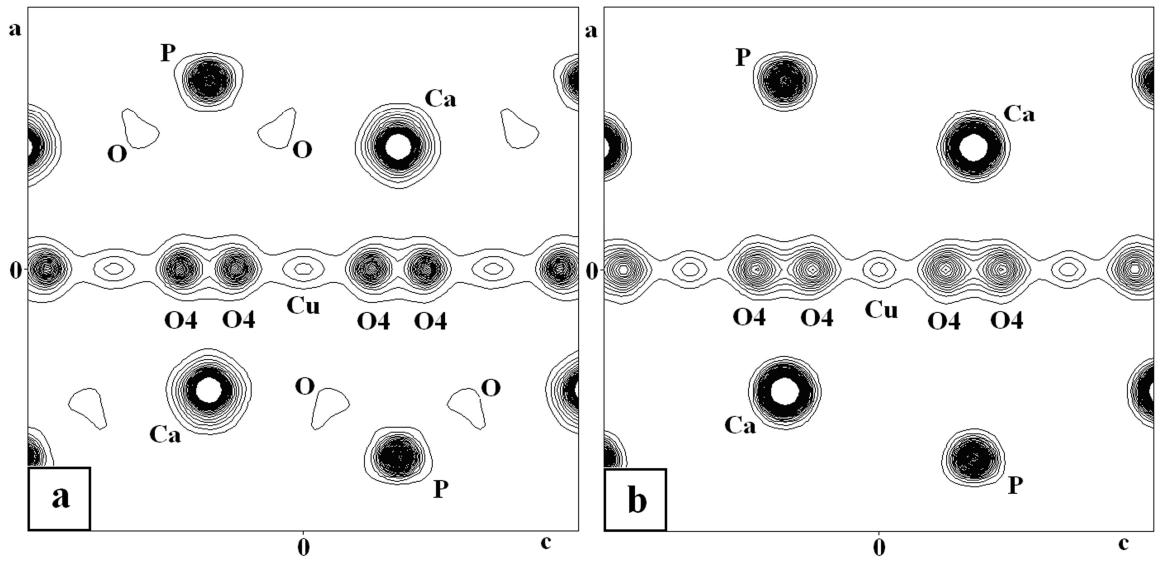

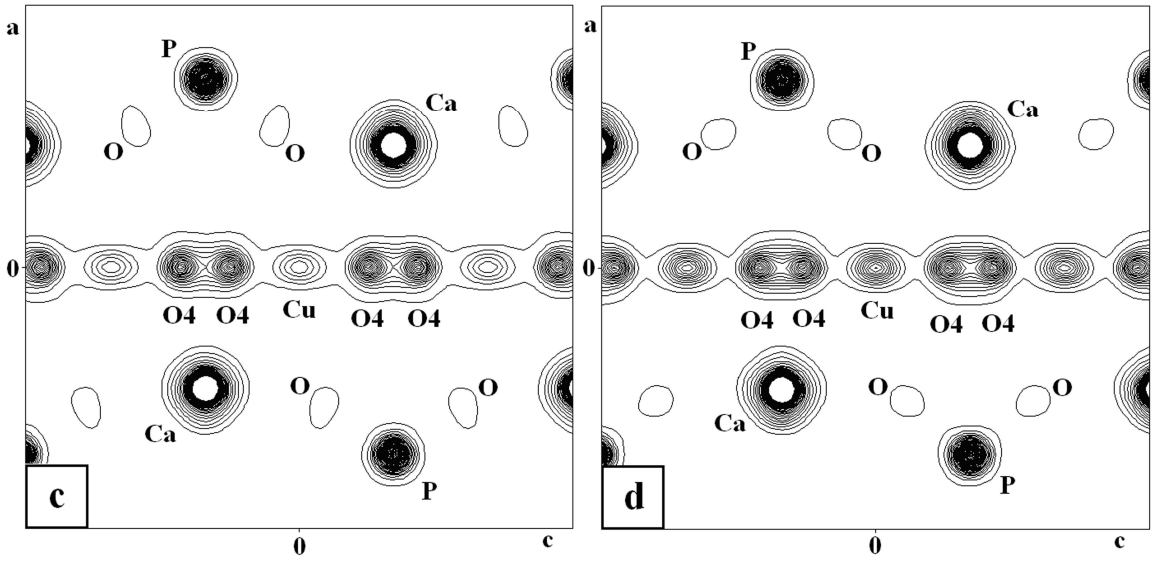

Figure 2.11. Two-dimensional electron-density maps at *y=0* of apatite $Ca_5(PO_4)_3Cu_{0.1}OH_{0.9-\delta}$ (sample CaA(0.1Cu)). Contour levels: from 1 to 50 e/Å^3, step 1 e/Å^3. High-resolution laboratory X-ray powder diffraction data.

a) based on F_{obs} (with procrystal density for known atoms)

b) based on F_{obs} (with flat prior)

c) based on $F_{obs}+G$ (with procrystal density for known atoms)

d) based on $F_{LeBail}+G$ (with procrystal density for known atoms)

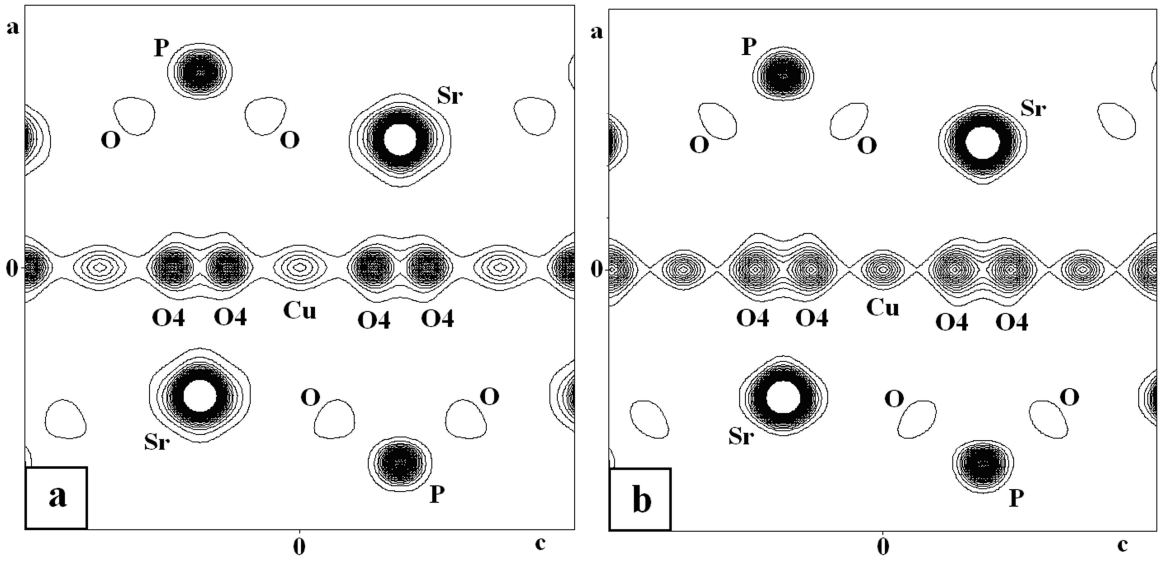

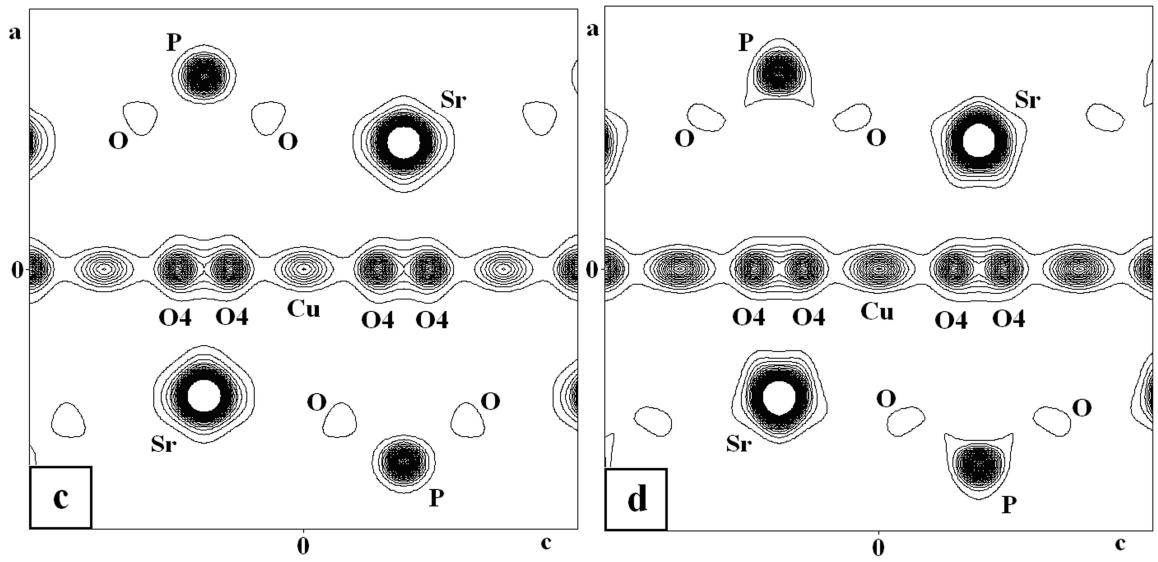

Figure 2.12. Two-dimensional electron-density maps at *y=0* of apatite $Sr_5(PO_4)_3Cu_{0.1}OH_{0.9-\delta}$ (sample SrA(0.1Cu-1)). Contour levels: from 1 to 50 e/Å^3, step 1 e/Å^3. High-resolution laboratory X-ray powder diffraction data.

a) based on F_{obs} (with procrystal density for known atoms)

b) based on F_{obs} (with flat prior)

c) based on $F_{obs}+G$ (with procrystal density for known atoms)

d) based on $F_{LeBail}+G$ (with procrystal density for known atoms)

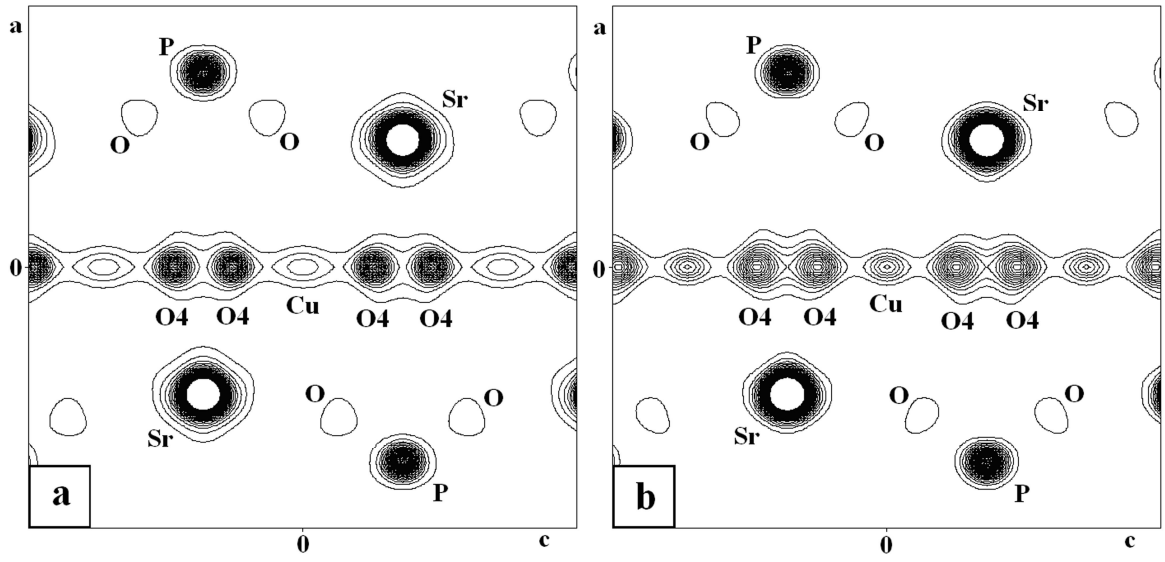

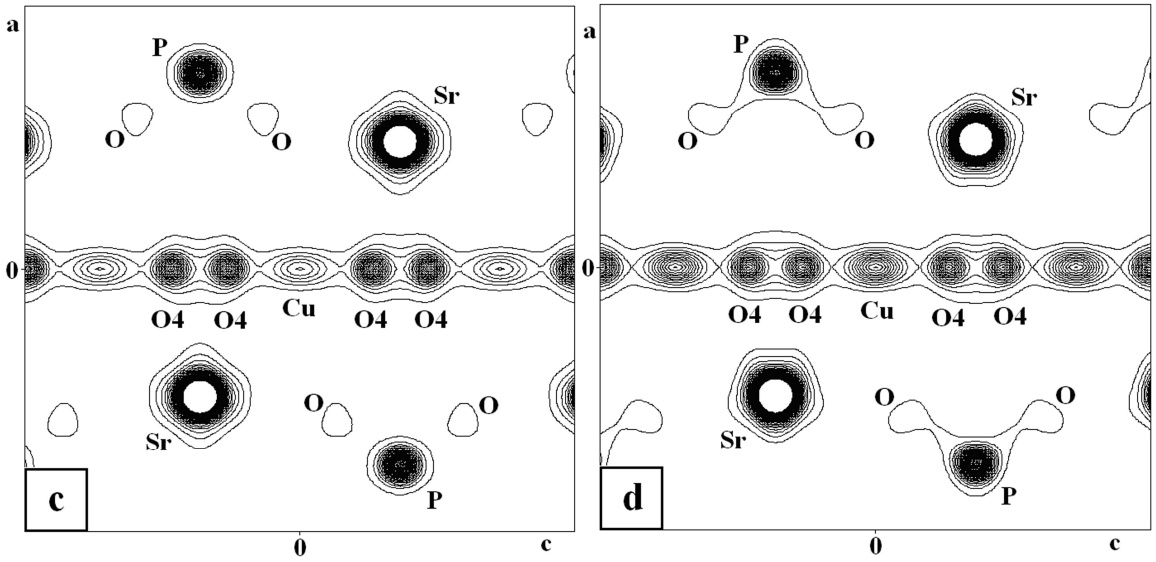

Figure 2.13. Two-dimensional electron-density maps at *y=0* of apatite $Sr_5(PO_4)_3Cu_{0.1}OH_{0.9-\delta}$ (sample SrA(0.1Cu-3)). Contour levels: from 1 to 50 e/Å^3, step 1 e/Å^3. High-resolution laboratory X-ray powder diffraction data.

a) based on F_{obs} (with procrystal density for known atoms)

b) based on F_{obs} (with flat prior)

c) based on $F_{obs}+G$ (with procrystal density for known atoms)

d) based on $F_{LeBail}+G$ (with procrystal density for known atoms)

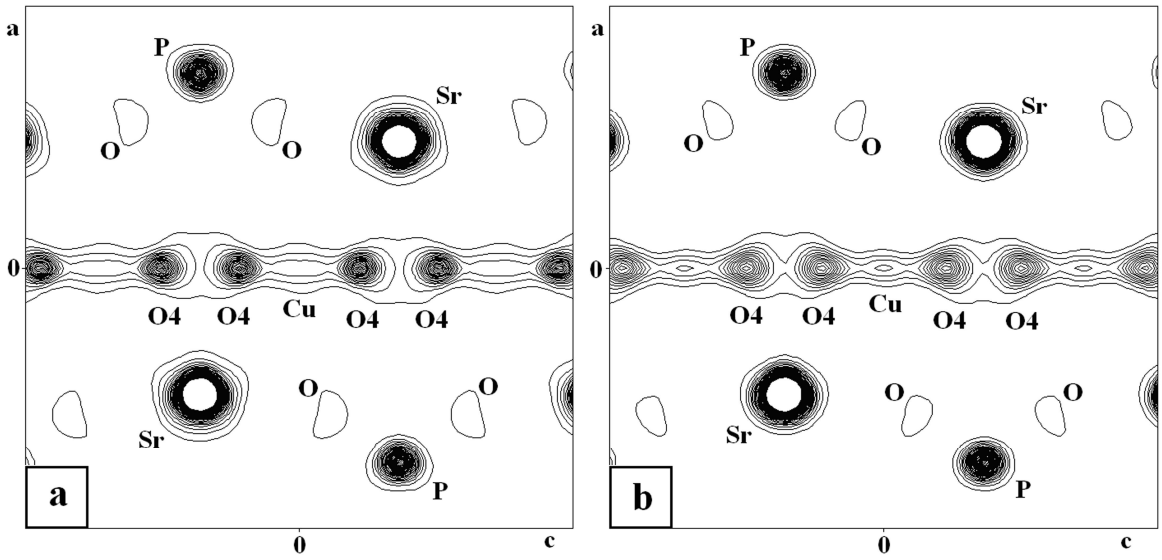

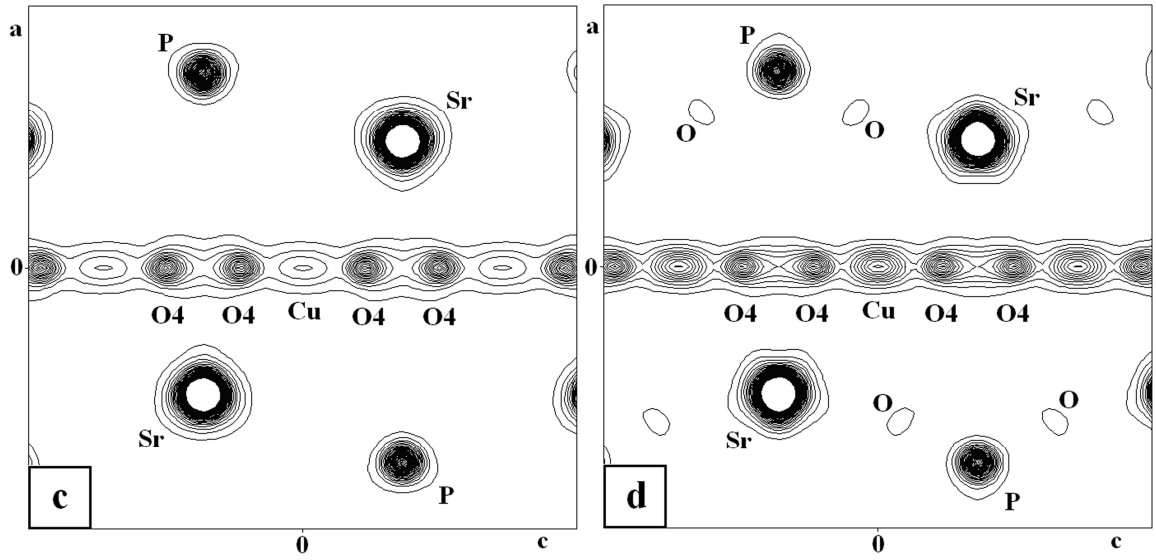

Figure 2.14. Two-dimensional electron-density maps at *y=0* of apatite $Sr_5(PO_4)_3Cu_{0.1}OH_{0.9-\delta}$ (sample SrA(0.1Cu-4)). Contour levels: from 1 to 50 e/Å^3, step 1 e/Å^3. High-resolution laboratory X-ray powder diffraction data.

a) based on F_{obs} (with procrystal density for known atoms)

b) based on F_{obs} (with flat prior)

c) based on F_{obs}+G (with procrystal density for known atoms)

d) based on F_{LeBail}+G (with procrystal density for known atoms)

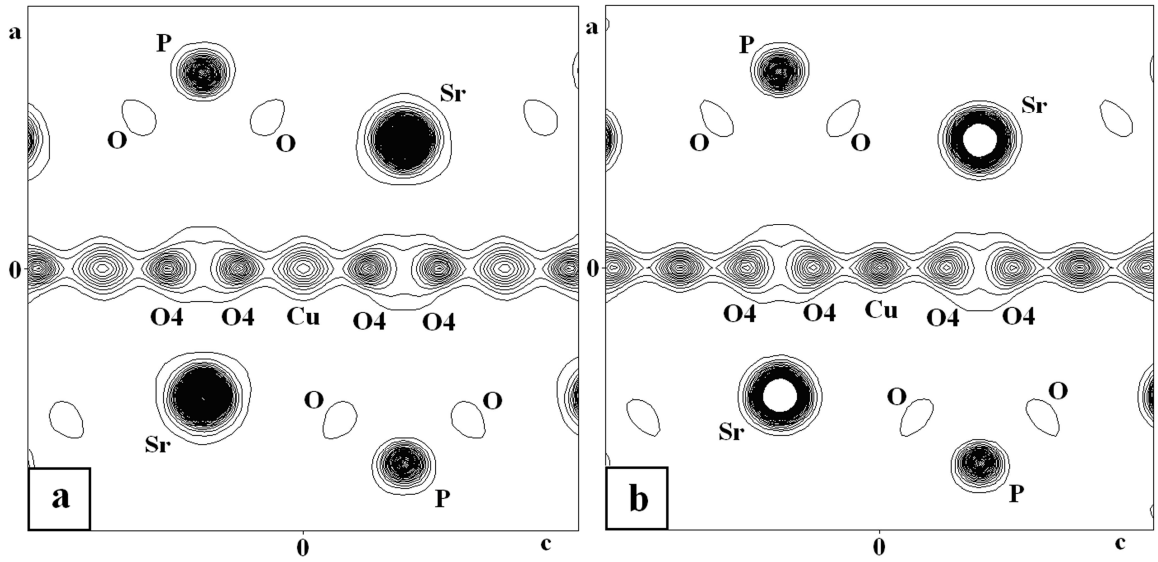

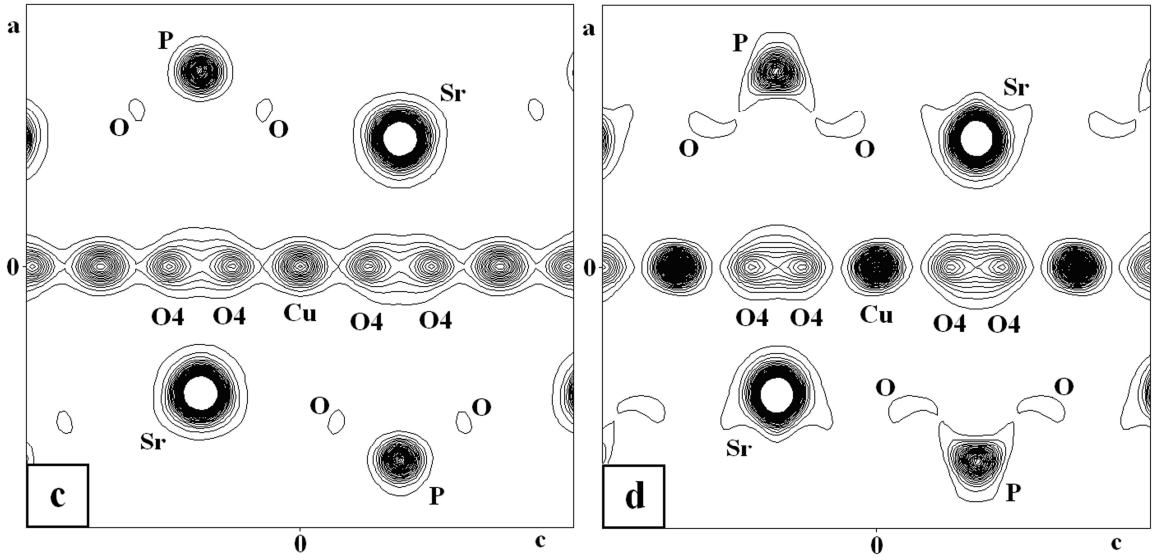

Figure 2.15. Two-dimensional electron-density maps at *y=0* of the apatite $Sr_5(PO_4)_3Cu_{0.25}OH_{0.75-\delta}$ (sample SrA(0.25Cu)). Contour levels: from 1 to 50 e/Å^3, step 1 e/Å^3. High-resolution laboratory X-ray powder diffraction data.

a) based on F_{obs} (with procrystal density for known atoms)

b) based on F_{obs} (with flat prior)

c) based on $F_{obs}+G$ (with procrystal density for known atoms)

d) based on $F_{LeBail}+G$ (with procrystal density for known atoms)

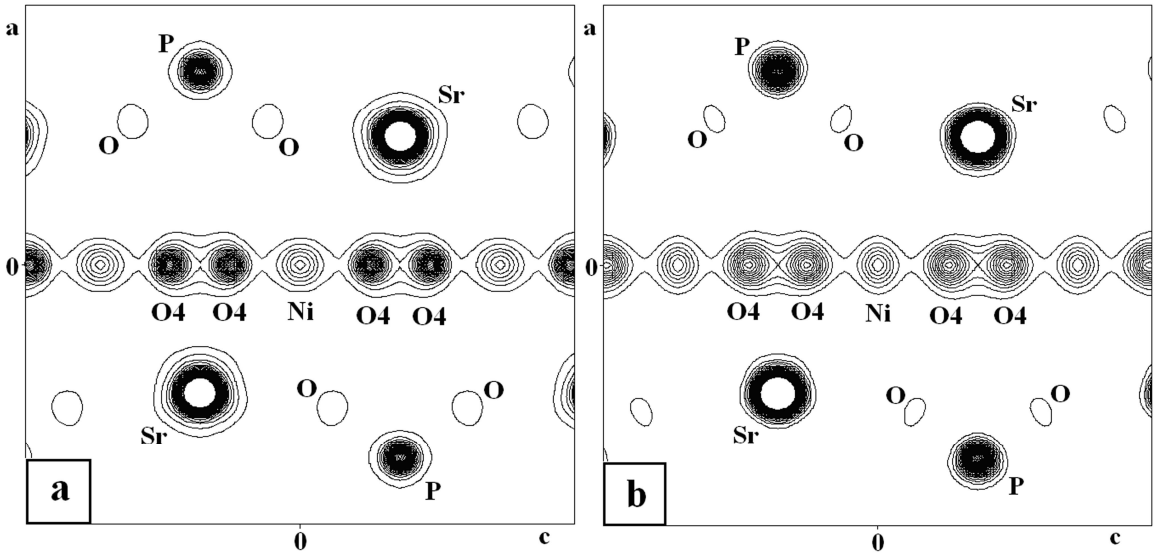

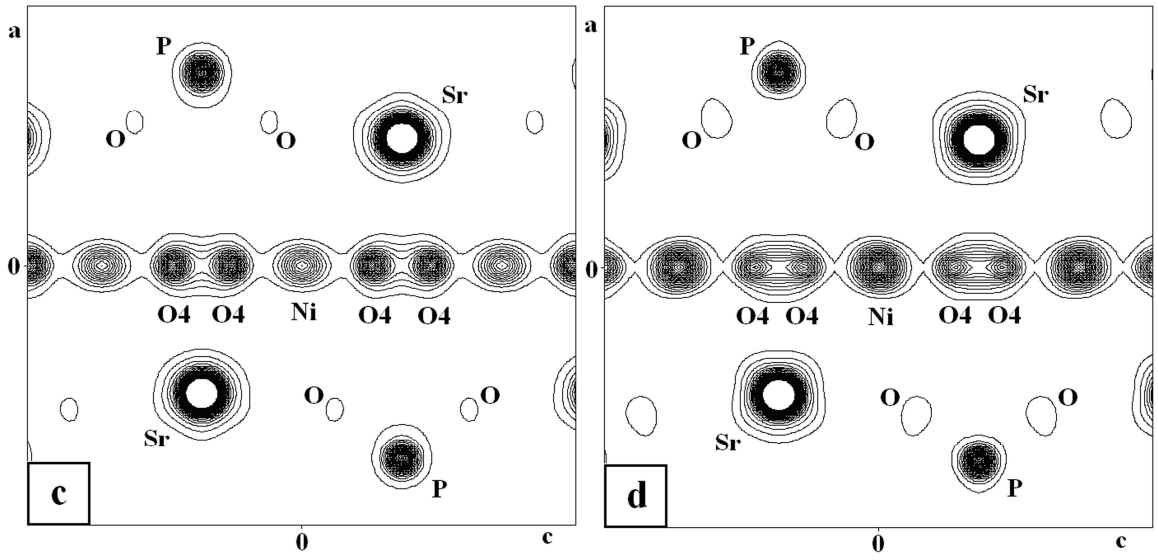

Figure 2.16. Two-dimensional electron-density maps at *y=0* of apatite $Sr_5(PO_4)_3Ni_{0.2}OH_{0.8-\delta}$ (sample SrA(0.2Ni)). Contour levels: from 1 to 50 e/Å^3, step 1 e/Å^3. High-resolution laboratory X-ray powder diffraction data.

a) based on F_{obs} (with procrystal density for known atoms)

b) based on F_{obs} (with flat prior)

c) based on F_{obs}+G (with procrystal density for known atoms)

d) based on F_{LeBail}+G (with procrystal density for known atoms)

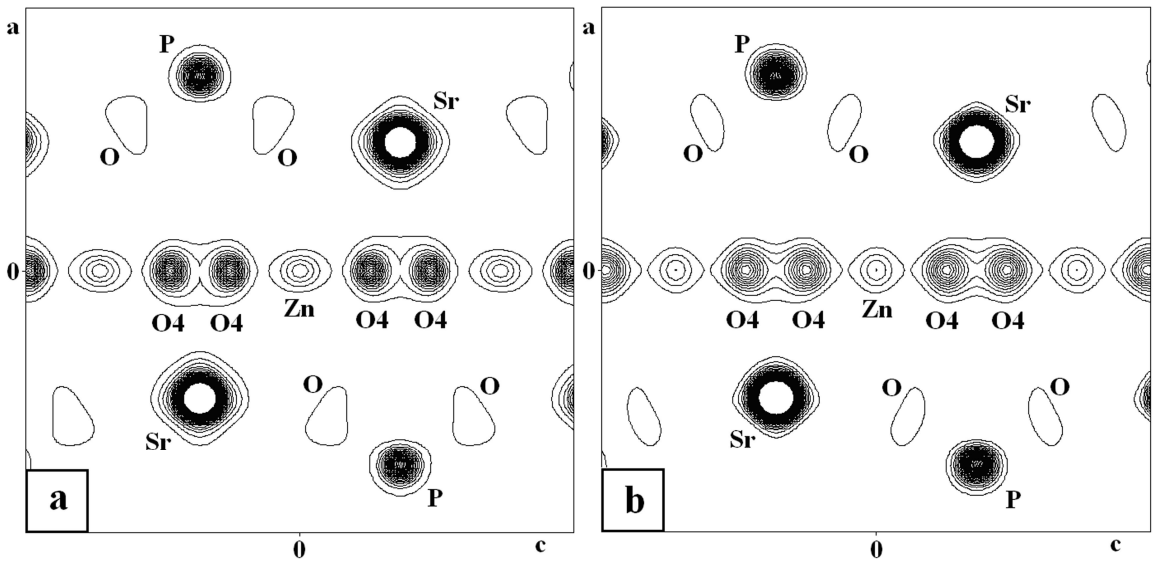

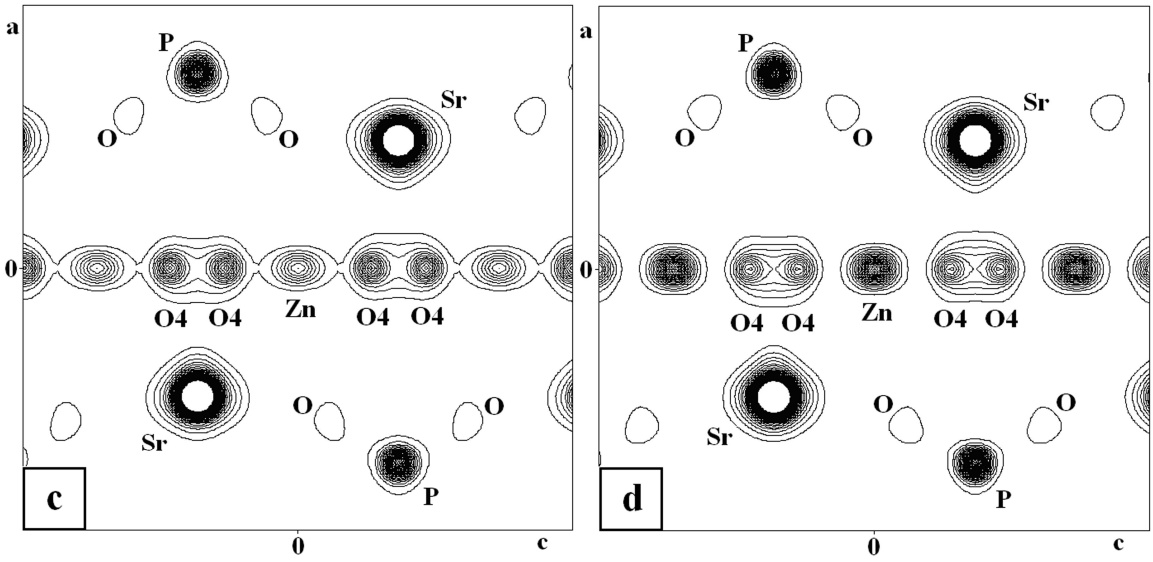

Figure 2.17. Two-dimensional electron-density maps at *y=0* of apatite $Sr_5(PO_4)_3Zn_{0.15}OH_{0.85-\delta}$ (sample SrA(0.15Zn)). Contour levels: from 1 to 50 e/Å^3, step 1 e/Å^3. High-resolution laboratory X-ray powder diffraction data.

a) based on F_{obs} (with procrystal density for known atoms)

b) based on F_{obs} (with flat prior)

c) based on F_{obs}+G (with procrystal density for known atoms)

d) based on F_{LeBail}+G (with procrystal density for known atoms)

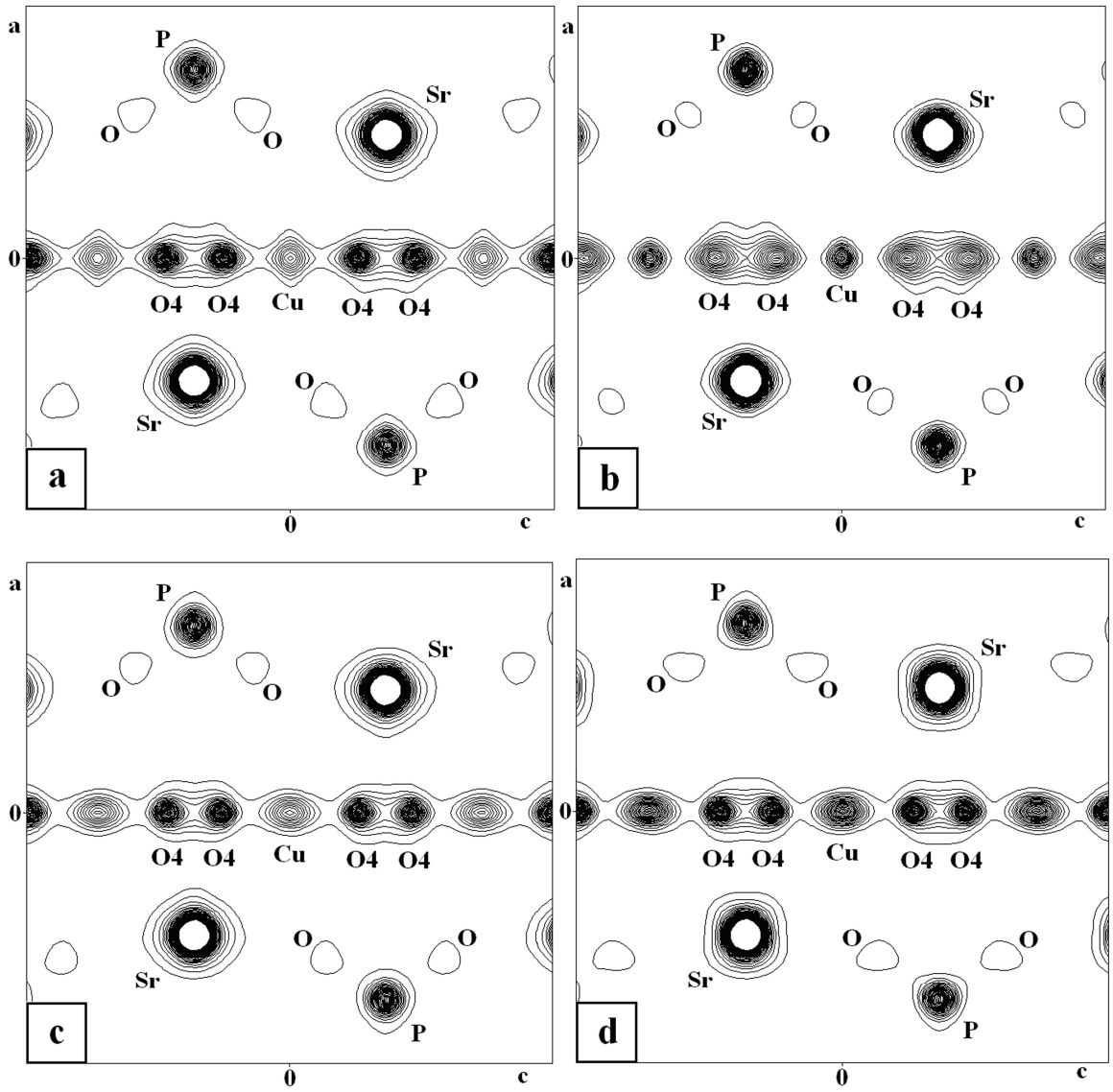

Figure 2.18a. Two-dimensional electron-density maps at *y=0* of apatite $Sr_5(PO_4)_3Cu_{0.1}OH_{0.9-\delta}$ (sample SrA(0.1Cu-1), $\delta = 0.038$). Contour levels: from 1 to 50 e/Å^3, step 1 e/Å^3. High-resolution synchrotron X-ray powder diffraction data with $\sin\theta/\lambda = 0.55$ Å^{-1}.

a) based on F_{obs} (with procrystal density for known atoms)

b) based on F_{obs} (with flat prior)

c) based on $F_{obs}+G$ (with procrystal density for known atoms)

d) based on $F_{LeBail}+G$ (with procrystal density for known atoms)

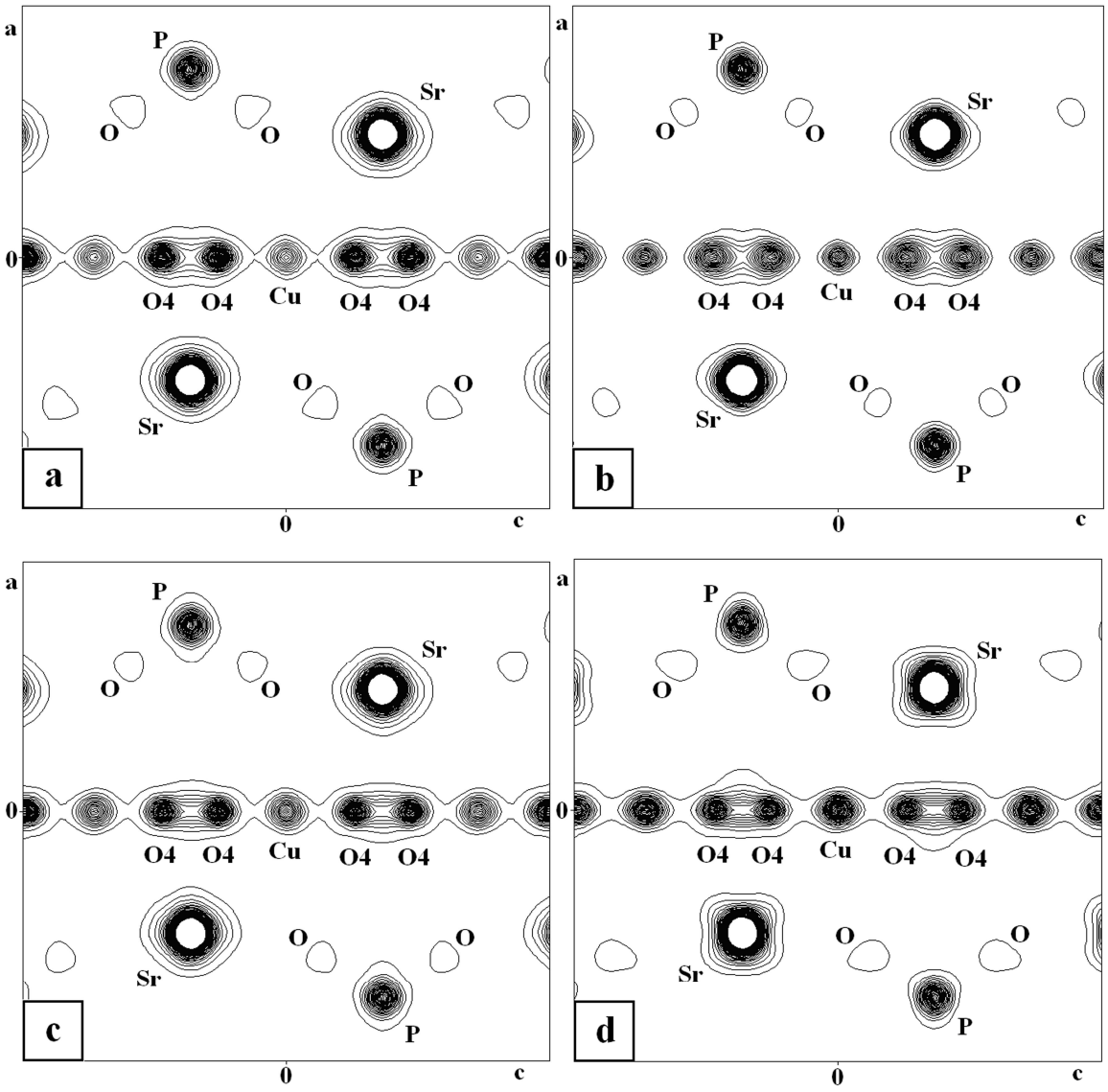

Figure 2.18b. Two-dimensional electron-density maps at *y=0* of apatite $Sr_5(PO_4)_3Cu_{0.1}OH_{0.9-\delta}$ (sample SrA(0.1Cu-1), $\delta = 0.038$). Contour levels: from 1 to 50 e/Å^3, step 1 e/Å^3. High-resolution synchrotron X-ray powder diffraction data with $\sin\theta/\lambda = 0.65$ Å^{-1}.

a) based on F_{obs} (with procrystal density for known atoms)

b) based on F_{obs} (with flat prior)

c) based on $F_{obs}+G$ (with procrystal density for known atoms)

d) based on $F_{LeBail}+G$ (with procrystal density for known atoms)

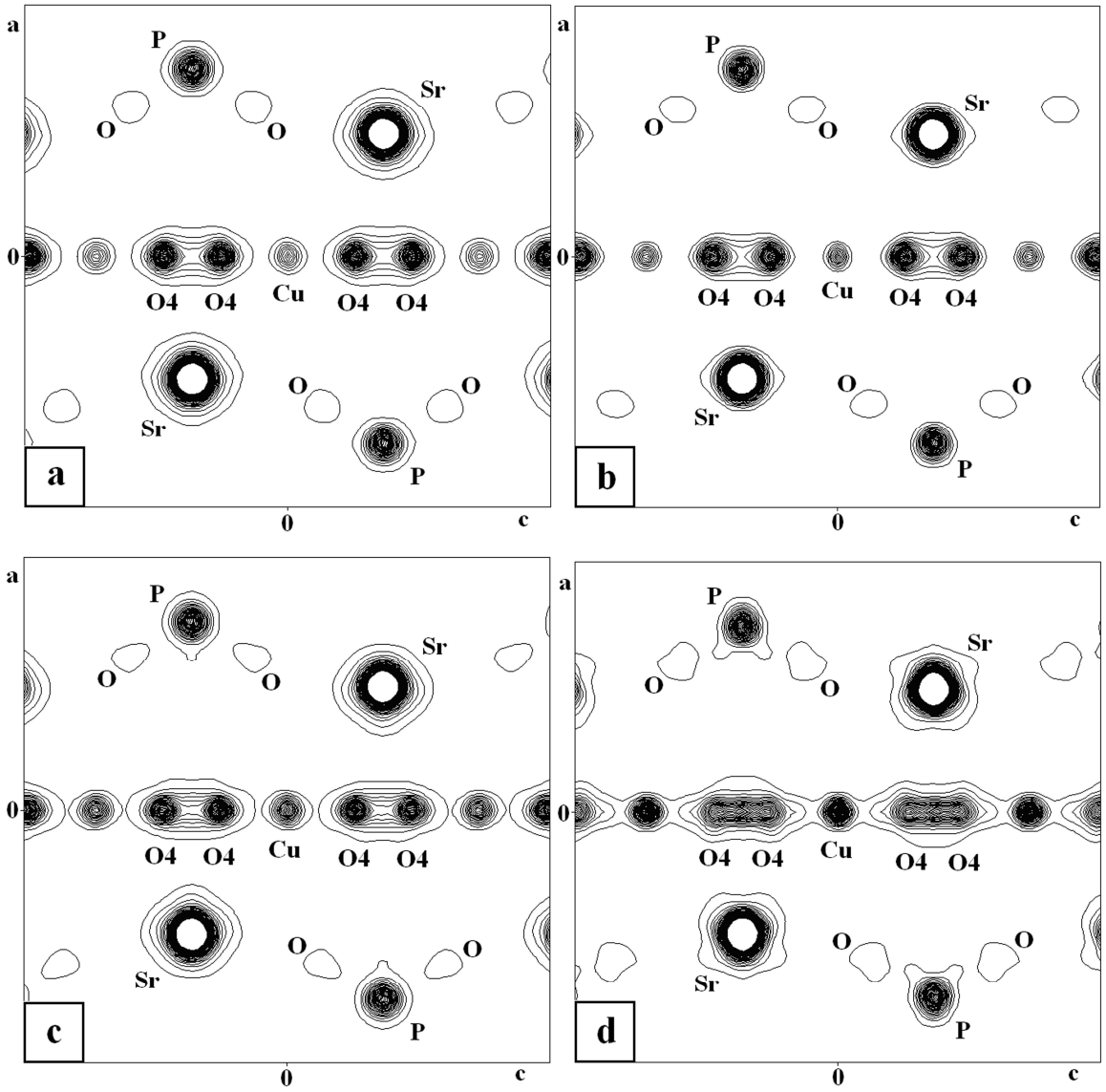

Figure 2.18c. Two-dimensional electron-density maps at *y=0* of apatite $Sr_5(PO_4)_3Cu_{0.1}OH_{0.9-\delta}$ (sample SrA(0.1Cu-1), $\delta = 0.038$). Contour levels: from 1 to 50 e/Å^3, step 1 e/Å^3. High-resolution synchrotron X-ray powder diffraction data with $\sin\theta/\lambda = 0.93$ Å^{-1}.

a) based on F_{obs} (with procrystal density for known atoms)

b) based on F_{obs} (with flat prior)

c) based on $F_{obs}+G$ (with procrystal density for known atoms)

d) based on $F_{LeBail}+G$ (with procrystal density for known atoms)

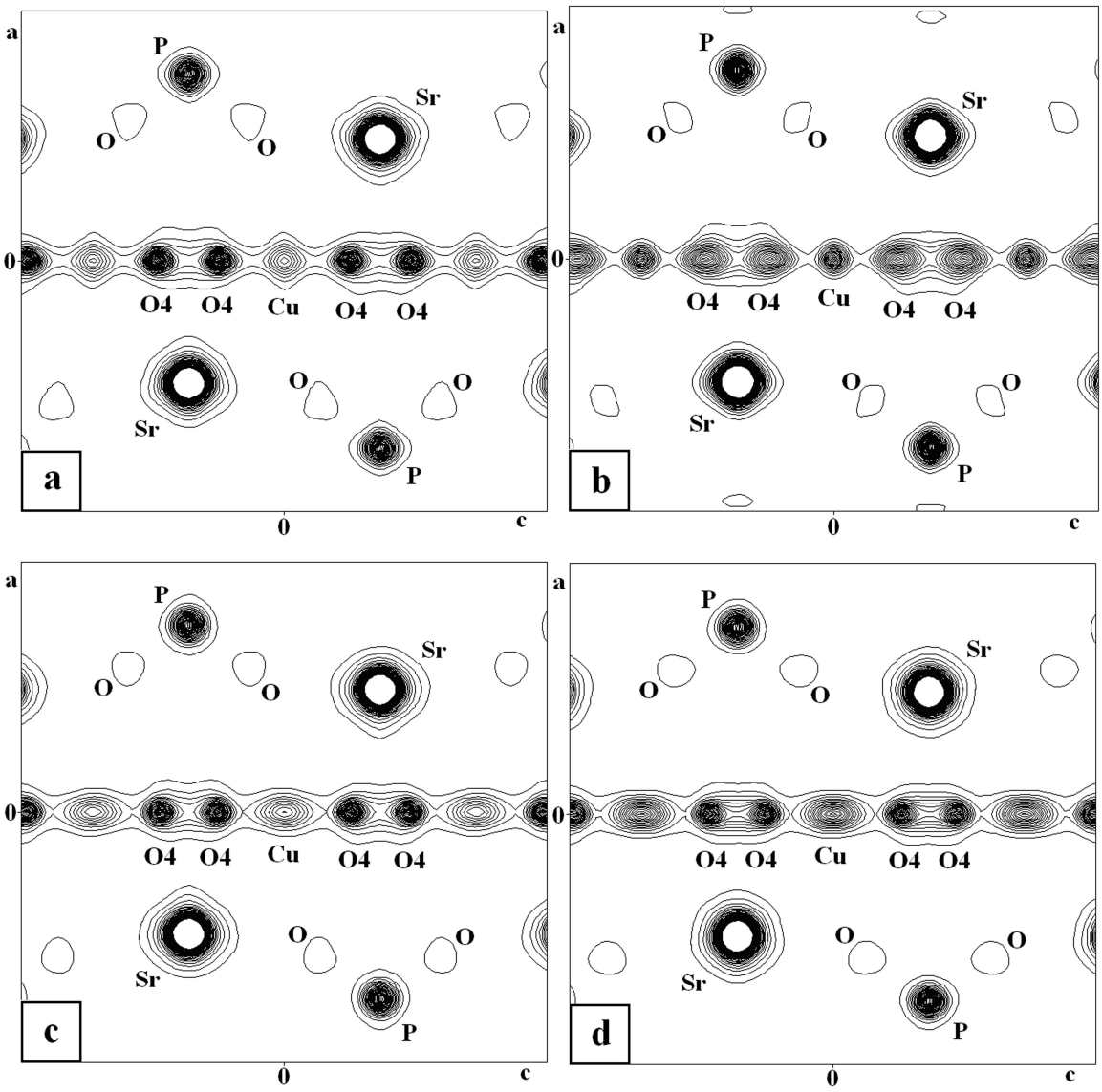

Figure 2.19a. Two-dimensional electron-density maps at *y=0* of apatite $Sr_5(PO_4)_3Cu_{0.1}OH_{0.9-\delta}$ (sample SrA(0.1Cu-3), $\delta = 0.26$). Contour levels: from 1 to 50 e/Å^3, step 1 e/Å^3. High-resolution synchrotron X-ray powder diffraction data with $\sin\theta/\lambda = 0.55$ Å^{-1}.

a) based on F_{obs} (with procrystal density for known atoms)

b) based on F_{obs} (with flat prior)

c) based on $F_{obs}+G$ (with procrystal density for known atoms)

d) based on $F_{LeBail}+G$ (with procrystal density for known atoms)

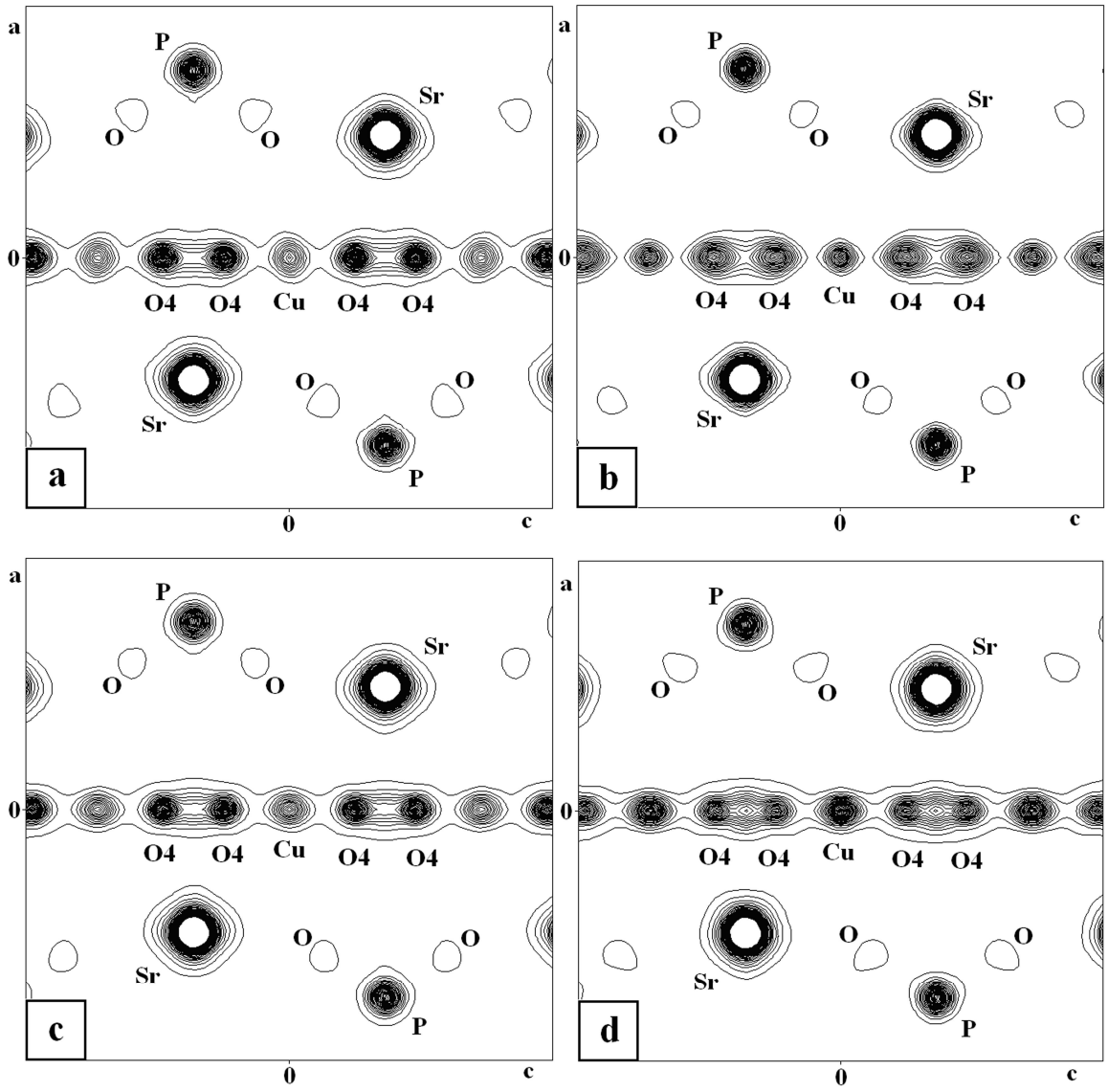

Figure 2.19b. Two-dimensional electron-density maps at *y=0* of apatite $Sr_5(PO_4)_3Cu_{0.1}OH_{0.9-\delta}$ (sample SrA(0.1Cu-3), $\delta = 0.26$). Contour levels: from 1 to 50 e/Å^3, step 1 e/Å^3. High-resolution synchrotron X-ray powder diffraction data with $\sin\theta/\lambda = 0.65$ Å^{-1}.

a) based on F_{obs} (with procrystal density for known atoms)

b) based on F_{obs} (with flat prior)

c) based on $F_{obs}+G$ (with procrystal density for known atoms)

d) based on $F_{LeBail}+G$ (with procrystal density for known atoms)

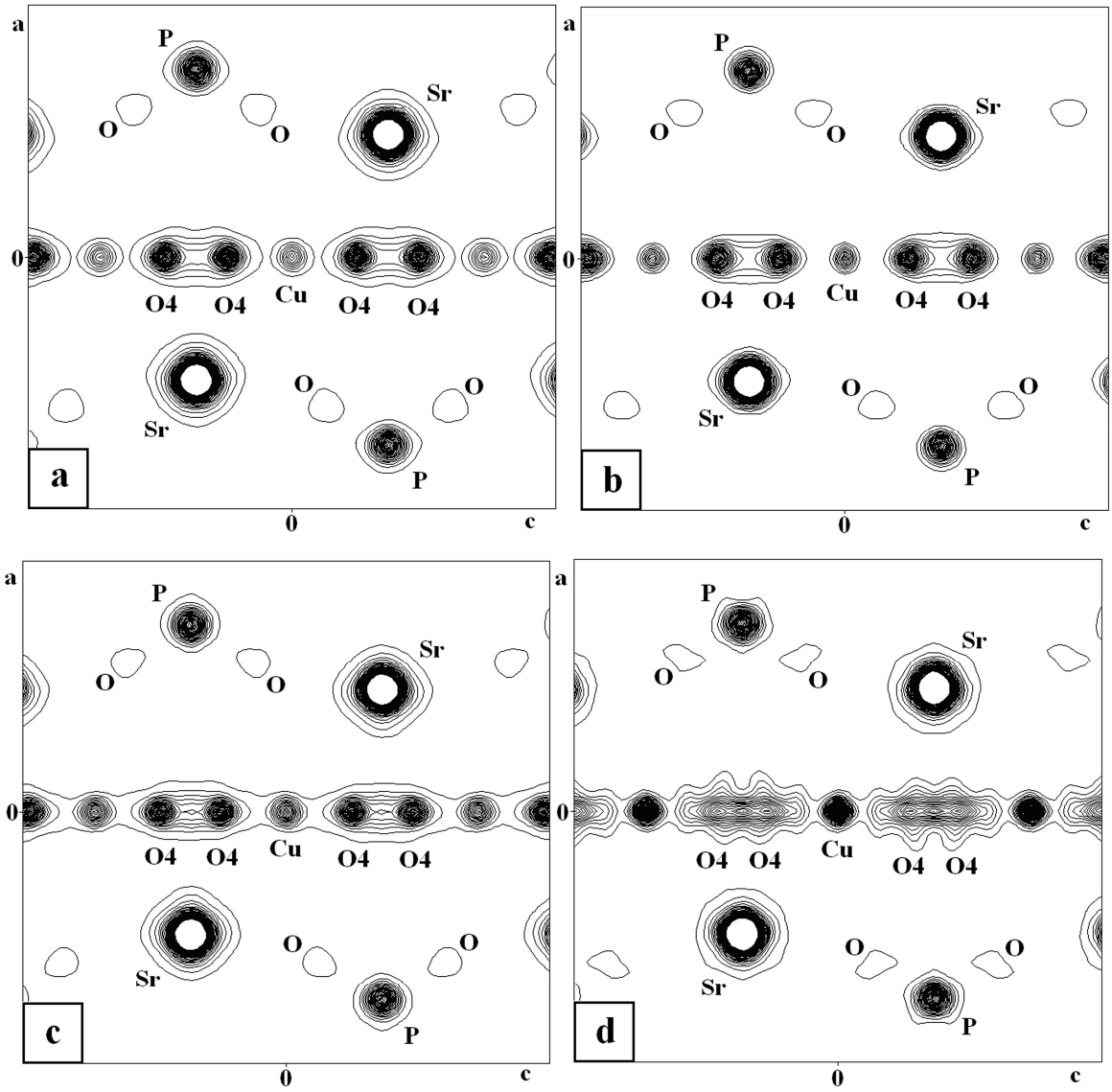

Figure 2.19c. Two-dimensional electron-density maps at *y=0* of apatite $Sr_5(PO_4)_3Cu_{0.1}OH_{0.9-\delta}$ (sample SrA(0.1Cu-3), $\delta = 0.26$). Contour levels: from 1 to 50 e/Å^3, step 1 e/Å^3. High-resolution synchrotron X-ray powder diffraction data with $\sin\theta/\lambda = 0.93$ Å^{-1}.

a) based on F_{obs} (with procrystal density for known atoms)

b) based on F_{obs} (with flat prior)

c) based on $F_{obs}+G$ (with procrystal density for known atoms)

d) based on $F_{LeBail}+G$ (with procrystal density for known atoms)

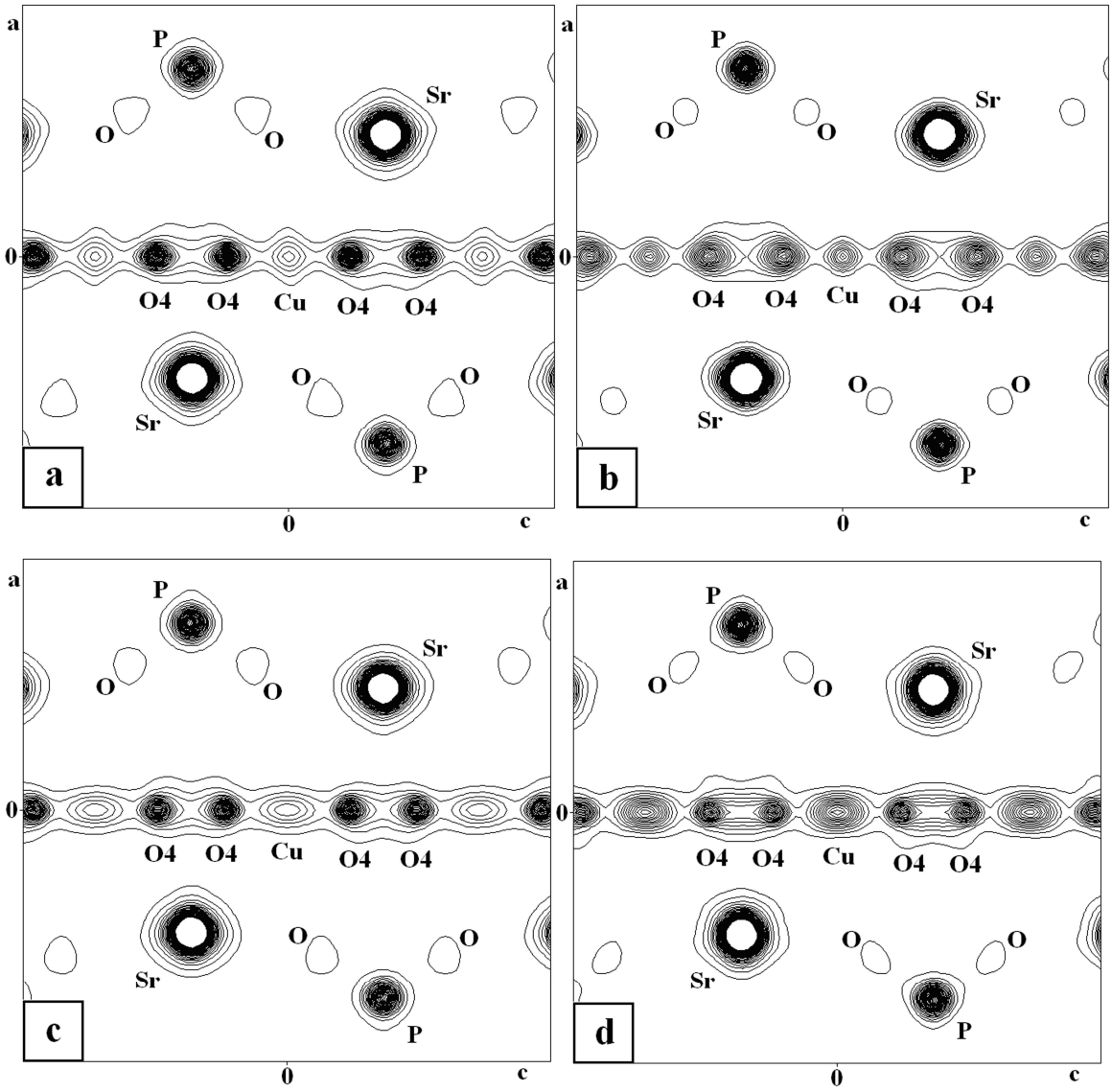

Figure 2.20a. Two-dimensional electron-density maps at *y=0* of apatite $Sr_5(PO_4)_3Cu_{0.1}OH_{0.9-\delta}$ (sample SrA(0.1Cu-4), $\delta > 0.26$). Contour levels: from 1 to 50 e/Å^3, step 1 e/Å^3. High-resolution synchrotron X-ray powder diffraction data with $\sin\theta/\lambda = 0.55$ Å^{-1}.

a) based on F_{obs} (with procrystal density for known atoms)

b) based on F_{obs} (with flat prior)

c) based on $F_{obs}+G$ (with procrystal density for known atoms)

d) based on $F_{LeBail}+G$ (with procrystal density for known atoms)

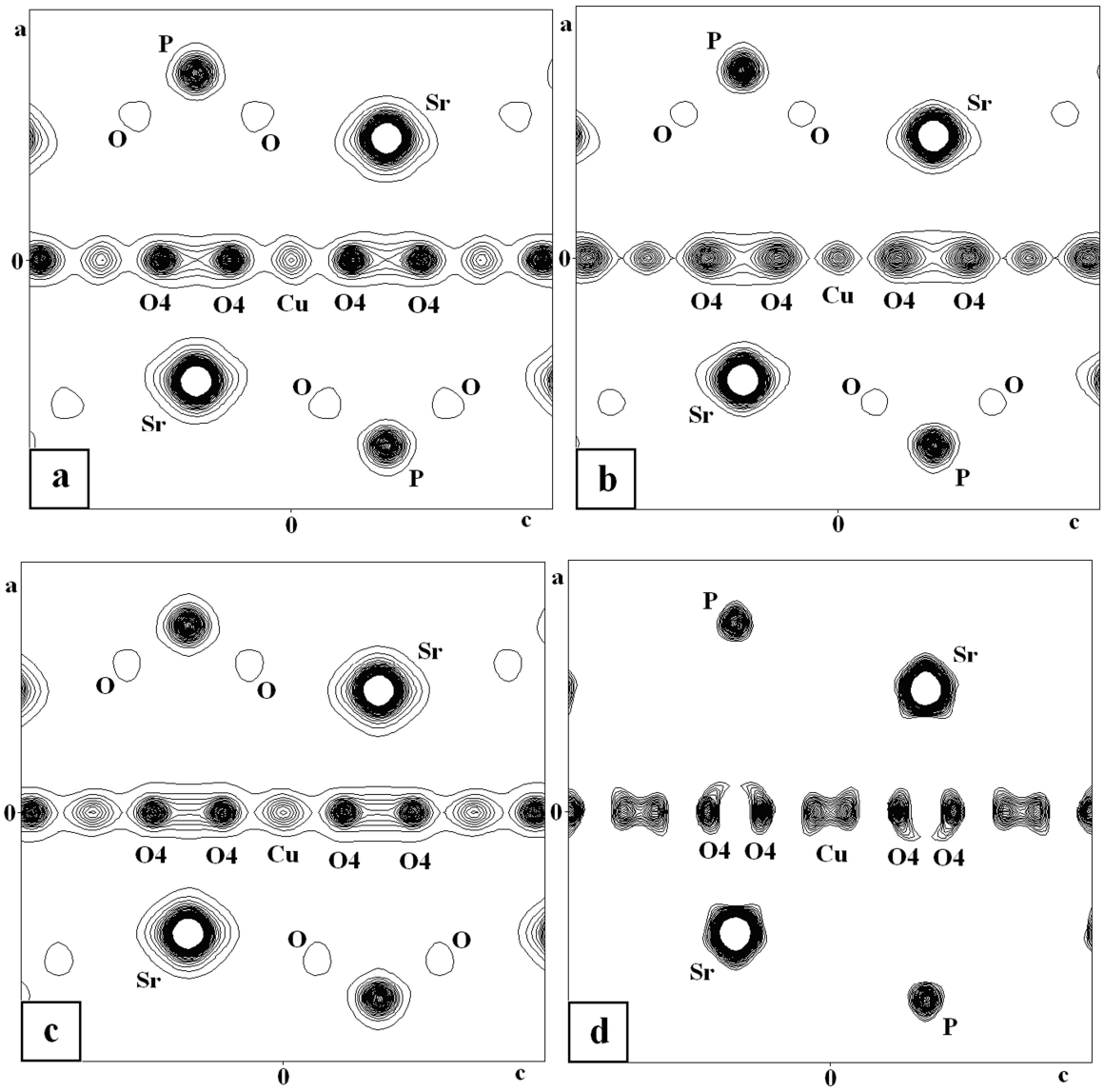

Figure 2.20b. Two-dimensional electron-density maps at *y=0* of apatite $Sr_5(PO_4)_3Cu_{0.1}OH_{0.9-\delta}$ (sample SrA(0.1Cu-4), $\delta > 0.26$). Contour levels: from 1 to 50 (from 3 to 50 – case d) e/Å^3, step 1 e/Å^3. High-resolution synchrotron X-ray powder diffraction data with $\sin\theta/\lambda = 0.65$ Å^{-1}.

a) based on F_{obs} (with procrystal density for known atoms)

b) based on F_{obs} (with flat prior)

c) based on $F_{obs}+G$ (with procrystal density for known atoms)

d) based on $F_{LeBail}+G$ (with procrystal density for known atoms)

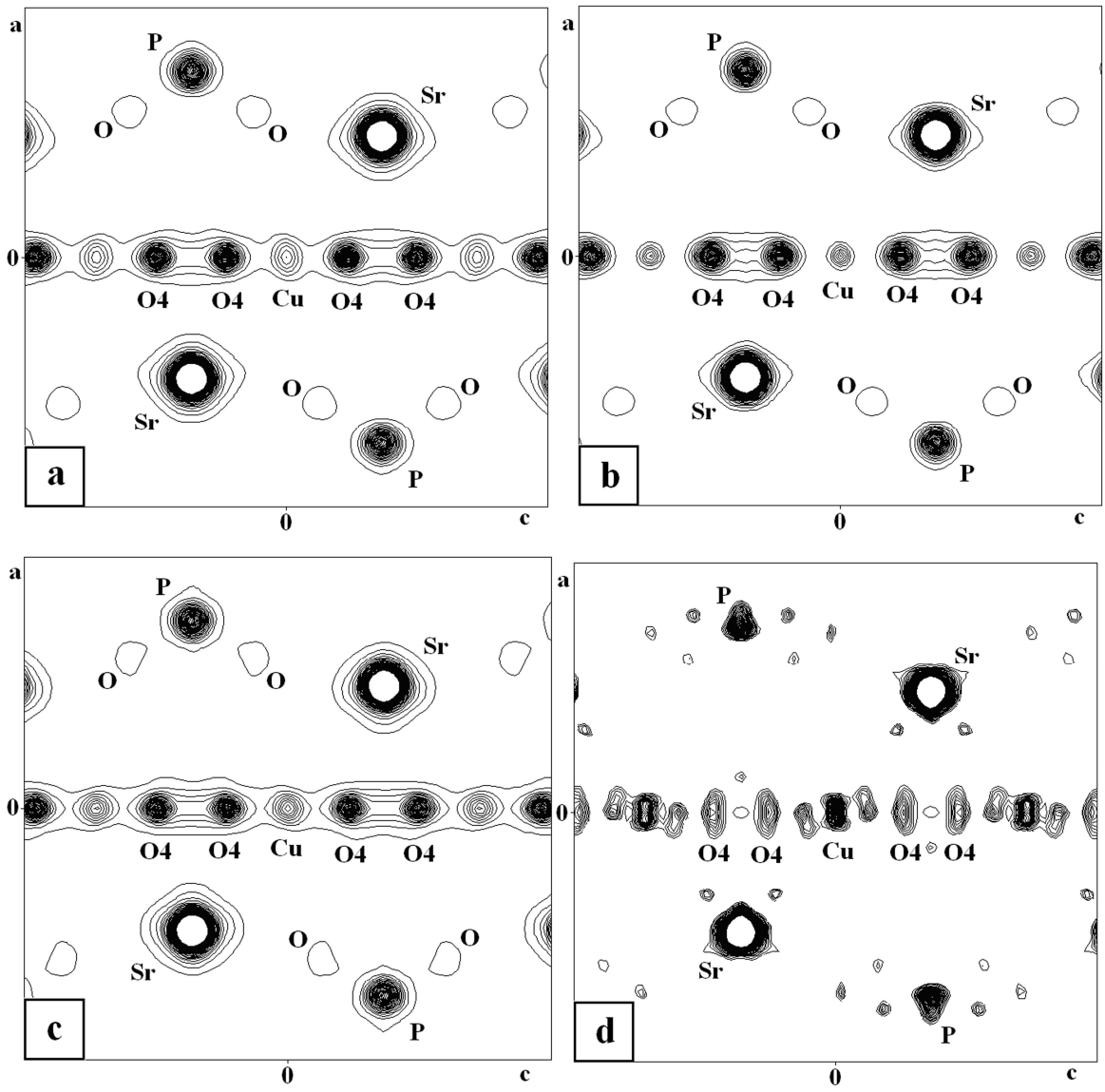

Figure 2.20c. Two-dimensional electron-density maps at *y=0* of apatite $Sr_5(PO_4)_3Cu_{0.1}OH_{0.9-\delta}$ (sample SrA(0.1Cu-4), $\delta > 0.26$). Contour levels: from 1 to 50 (from 3 to 50 – case d) e/Å^3, step 1 e/Å^3. High-resolution synchrotron X-ray powder diffraction data with $\sin\theta/\lambda = 0.93$ Å^{-1}.

a) based on F_{obs} (with procrystal density for known atoms)

b) based on F_{obs} (with flat prior)

c) based on $F_{obs}+G$ (with procrystal density for known atoms)

d) based on $F_{LeBail}+G$ (with procrystal density for known atoms)

2.3.5. Determination of electron density distribution of intercalated atoms in apatites by MEM from X-ray powder diffraction data

After all missing intercalated atoms were located in the crystal structure of apatites, the next problem was the determination of the accurate electron density distribution of the intercalated atoms, especially in the low-density region (including redistribution of the electron density due to bonding). Fourier synthesis cannot be applied for the determination of the accurate electron density distribution of in-channel atoms in apatites (Figs. 2.21-2.23), so MEM was used as an alternative method. The advantage of MEM reconstructed electron density based on F_{obs}–constraints was shown for many examples of intercalated atoms with high occupancy (Takata, 2008). In the present study we investigated the case of low occupancy of intercalated atoms, and compared the distribution of the electron density calculated based on F_{obs}– and F_{obs}+G–constraints.

Using the MEM for reconstruction of the accurate electron densities from powder diffraction data requires the use of a procrystal density as a prior for all atoms in the crystal structure (de Vries *et al.*, 1994; Zheludev *et al.*, 1995). The procrystal electron density for MEM calculations in the present case was created from the best Rietveld refinement of the crystal structure with all intercalated atoms included. Since the MEM reconstructed electron density map based on F_{obs}–constraints leads to a model bias in the reconstructed density (Samy *et al.*, 2010; Buchter *et al.*, 2011), a combination of F_{obs}– and G–constraints was used to receive the least bias by the model MEM reconstructed electron density.

In the present work, the experimental determination of the accurate electron density distribution based on the combination of F_{obs}– and G–constraints (with procrystal density for the complete structure) for a series of apatites with intercalated metal atoms is reported.

The MEM reconstructed electron density maps of Sr–apatites without fluorine atoms and with different content of intercalated copper atoms allow to draw conclusions about the isotropic distribution of the electron densities of the intercalated copper atoms with positional occupancies in the range of 0.05–0.3 (Fig. 2.24). In accordance with single crystal investigations of Sr–apatite without hydroxide groups in the channels (Kazin *et al.*, 2003), the electron density distribution of the copper atoms at (0, 0, 0) is almost isotropic and the oxygen atoms connected with copper atoms are located exactly at position (0, 0, 1/4). In all investigated powder samples

the position of O4 presents the superposition of the electron density of the oxygen atom from the hydroxide group OH^- and the oxygen atom bonded with the copper atom. As a result, this position is shifted from the position (0, 0, 1/4). Increasing the content of the hydroxide groups in the channel (it is the same as decreasing the content of oxygen atoms bonded with copper atoms due to the decrease of the amount of copper atoms) causes the shift of the O4 position towards the position of hydroxide molecules in pure hydroxyapatite (Kazin *et al.*, 2003).

The electron density distribution of the intercalated copper atoms in Ca–apatites without fluorine atoms with different content of intercalated copper atoms is almost isotropic (Fig. 2.25) in agreement with single crystal data (Karpov *et al.*, 2003).

In all Ca–apatites with fluorine atoms and with different content of intercalated Cu–atoms (Fig. 2.26) the O4 position is close to the position of the fluorine atom (0, 0, 1/4). The integration of the resulting electron density distribution based on the independent atom model did not allow integration of the electron density of the O4 atom independently from the fluorine atom. The change of the electron density distribution of the O4 and fluorine atoms in dependence on the content of the copper atoms is weak. In Sr–apatite with fluorine atom the position of O4 is far from the fluorine atom and the electron density of the O4 atom can be integrated independently from the fluorine atom (Fig. 2.26).

Figs. 2.27-2.29 show a clear distortion of the electron density (indicated by arrows) near the copper atoms from high-resolution laboratory and synchrotron X-ray powder diffraction data in Sr–apatites with intercalated copper atoms with positional occupancies of 0.1 and 0.3 due to different content of peroxide molecules which are located near the copper atoms (Kazin *et al.*, 2012). The tendency of distortion is the same for both, laboratory and synchrotron powder diffraction data (Figs. 2.27, 2.29); some differences are caused by the different resolution $\sin\theta/\lambda$ of X-ray powder diffraction data and different instrumental peak profile. The distortion of the electron density near copper atoms as obtained from synchrotron X-ray powder diffraction data is similar to the distortion of the electron density near copper atoms from laboratory X-ray powder diffraction data with lower resolution $\sin\theta/\lambda$ (Fig. 2.29).

The MEM reconstructed distributions of the electron density of intercalated Zn and Ni atoms in Sr–apatites with intercalated Zn and Ni atoms are also isotropic (Fig. 2.30).

Another interesting example is the reconstruction of the electron density distribution in peroxy-apatites. The peroxide ions substitute the hydroxide ions only partially, making it

difficult to locate both atoms unambiguously form powder diffraction data. The distribution of the electron density in the channels was found to be different for hydroxyl-apatite (Fig. 2.31a) and peroxyhydroxy-apatite (Fig. 2.31b). Peroxyhydroxy-apatite includes two different positions of oxygen atoms in the channels with different values of the electron density, O5 and O6. Position O6 with lower electron density corresponds to the position of hydroxide atom O4 in hydroxyapatite. Position O5 with higher value of the electron density corresponds to the oxygen atom of the peroxide molecule and its value of the electron density almost 7 times exceeds the value of the electron density of the hydroxide oxygen O6.

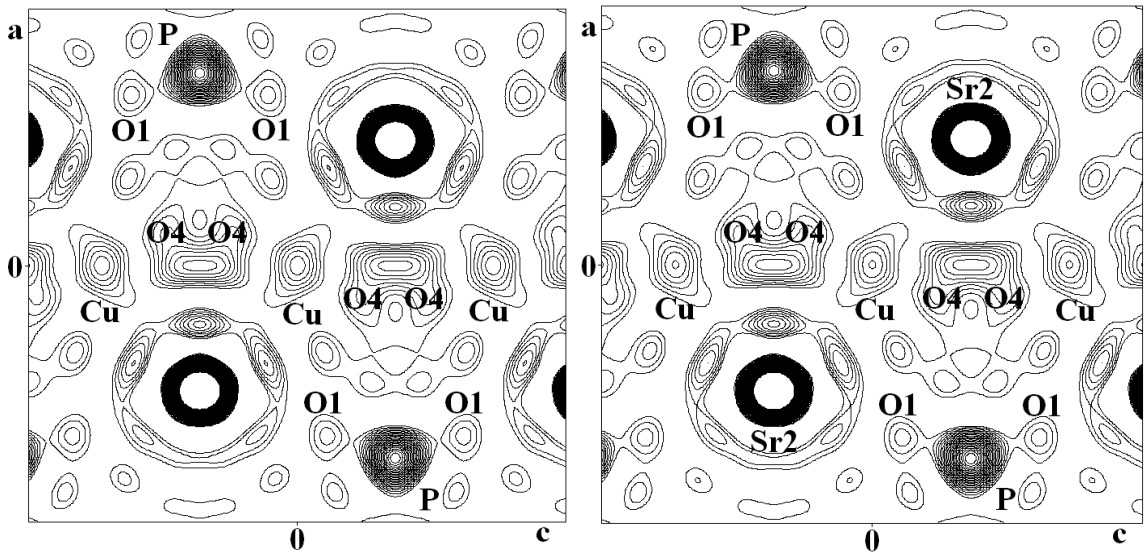

Figure 2.21. Two-dimensional Fourier electron-density maps at *y=0* of apatite $Sr_5(PO_4)_3Cu_{0.1}OH_{0.9-\delta}$ (sample SrA(0.1Cu-1)). Contour levels: from 1 to 50 e/Å^3, step 1 e/Å^3. High-resolution laboratory X-ray powder diffraction data, $\sin\theta/\lambda = 0.55$ Å^{-1}. Left: based on F_{calc}–constraints; right: based on F_{obs}–constraints.

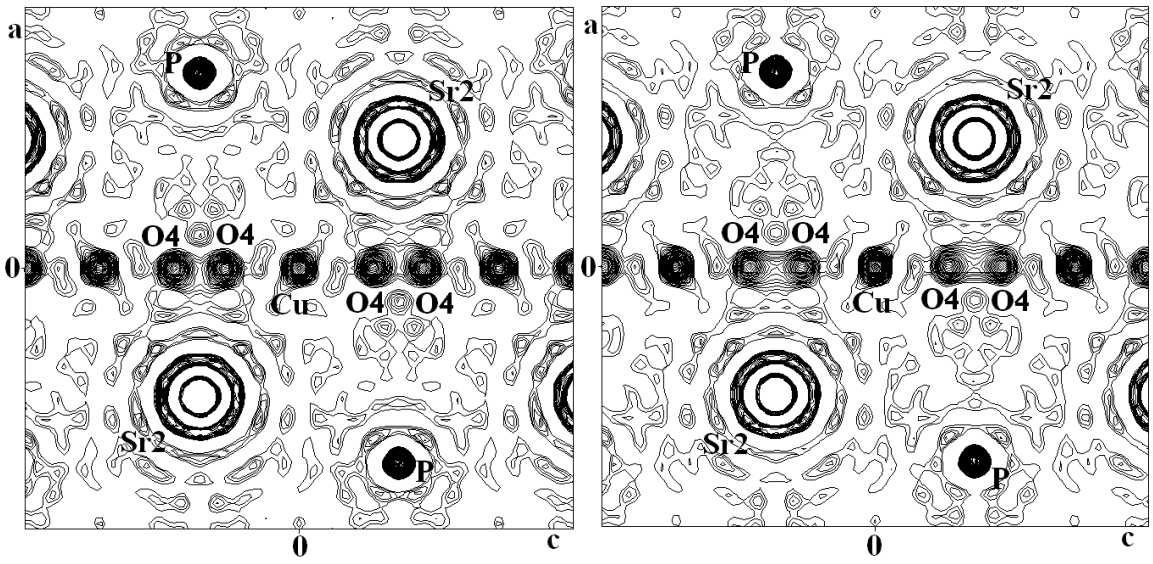

Figure 2.22. Two-dimensional Fourier electron-density maps at *y=0* of apatite $Sr_5(PO_4)_3Cu_{0.1}OH_{0.9-\delta}$ (sample SrA(0.1Cu-1)). Contour levels: from 1 to 50 e/Å^3, step 1 e/Å^3. High-resolution synchrotron X-ray powder diffraction data, $\sin\theta/\lambda = 0.93$ Å^{-1}. Left: based on F_{calc}–constraints; right: based on F_{obs}–constraints.

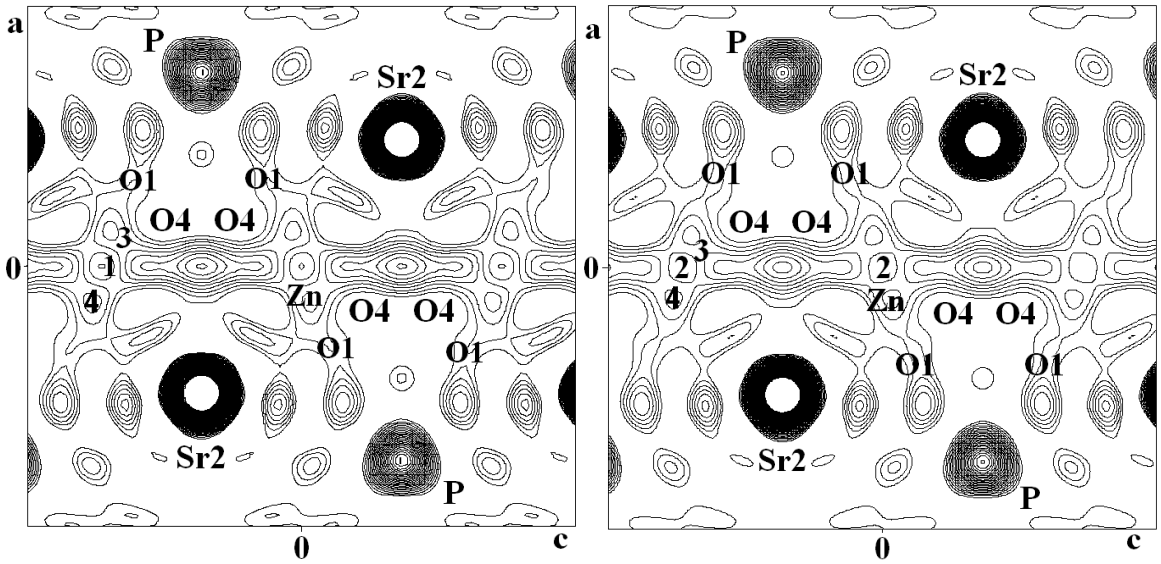

Figure 2.23. Two-dimensional Fourier electron-density maps at *y=0* of apatite $Sr_5(PO_4)_3Zn_{0.15}OH_{0.85-\delta}$ (sample SrA(0.15Zn)). Contour levels: from 1 to 50 e/Å^3, step 1 e/Å^3. High-resolution laboratory X-ray powder diffraction data. Left: based on F_{calc}–constraints; right: based on F_{obs}–constraints.

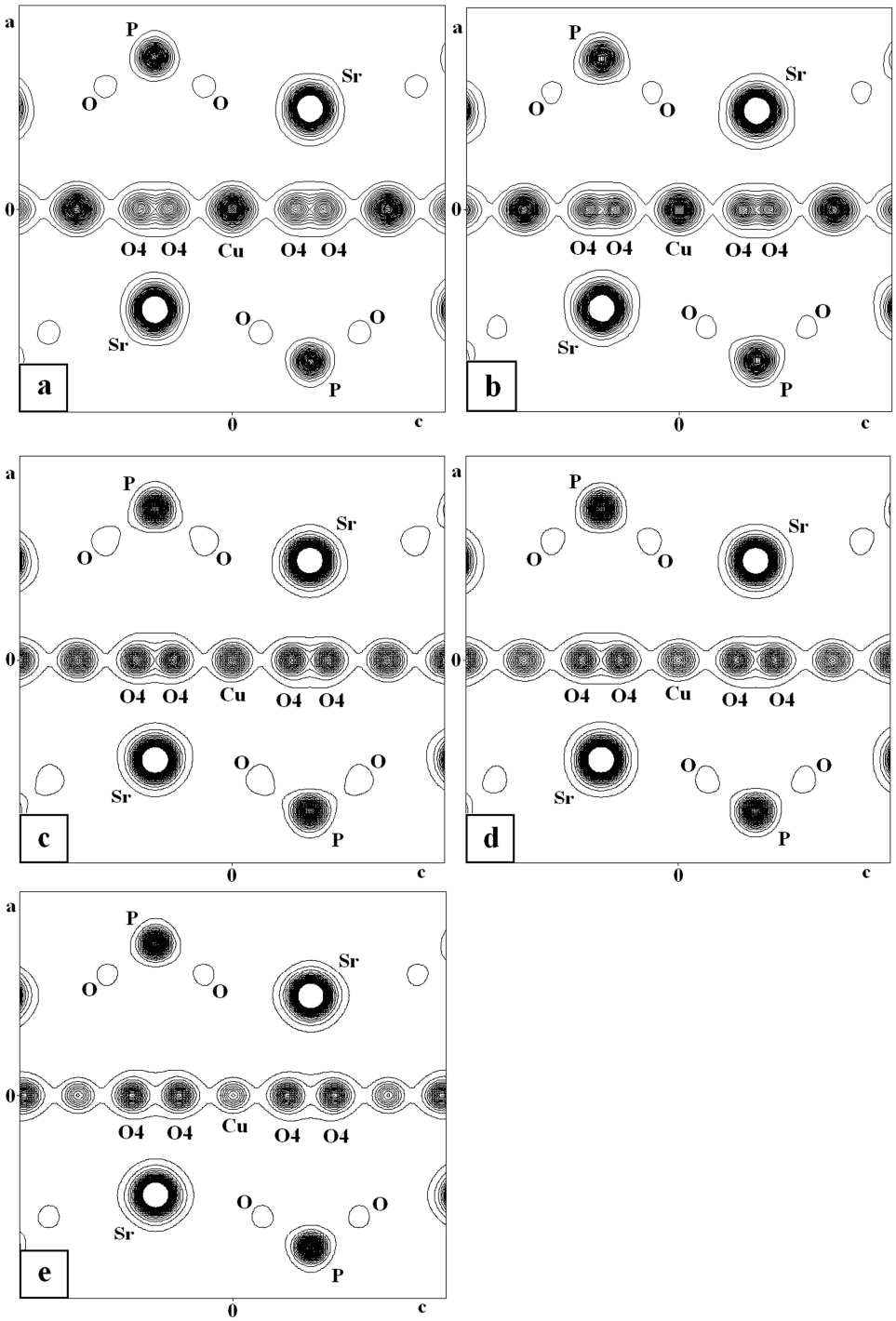

Figure 2.24. Two-dimensional electron-density maps based on F_{obs}+G–constraints (with procrystal density for complete structure) at $y=0$ of Sr–apatites with different content of intercalated copper atoms. Contour levels: from 1 to 50 e/Å^3, step 1 e/Å^3. High-resolution laboratory X-ray powder diffraction data.
a) $Sr_5(PO_4)_3Cu_{0.3}OH_{0.7-\delta}$ (sample SrA(0.3Cu-2)),
b) $Sr_5(PO_4)_3Cu_{0.25}OH_{0.75-\delta}$ (sample SrA(0.25Cu)),
c) $Sr_5(PO_4)_3Cu_{0.125}OH_{0.875-\delta}$ (sample SrA(0.125Cu)),
d) $Sr_5(PO_4)_3Cu_{0.1}OH_{0.9-\delta}$ (sample SrA(0.1Cu-2)),
e) $Sr_5(PO_4)_3Cu_{0.05}OH_{0.95-\delta}$ (sample SrA(0.05Cu)).

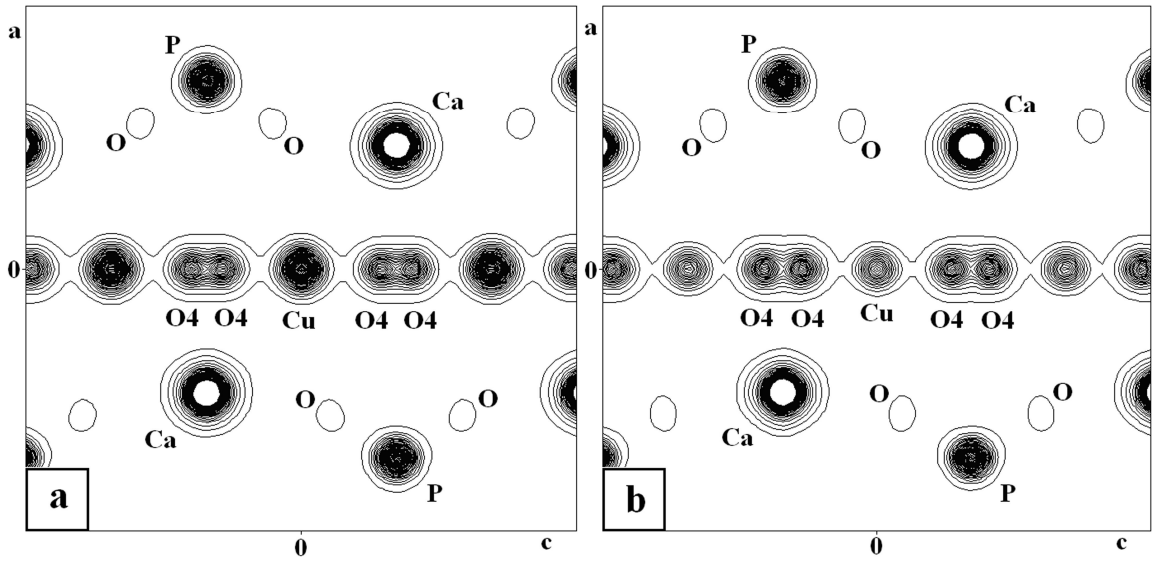

Figure 2.25. Two-dimensional electron-density maps based on F_{obs}+G–constraints (with procrystal density for complete structure) at *y=0* of Ca–apatites:

a) $Ca_5(PO_4)_3Cu_{0.3}OH_{0.7-\delta}$ (sample CaA(0.3Cu))

b) $Ca_5(PO_4)_3Cu_{0.1}OH_{0.9-\delta}$ (sample CaA(0.1Cu)).

Contour levels: from 1 to 50 e/Å^3, step 1 e/Å^3. High-resolution laboratory X-ray powder diffraction data.

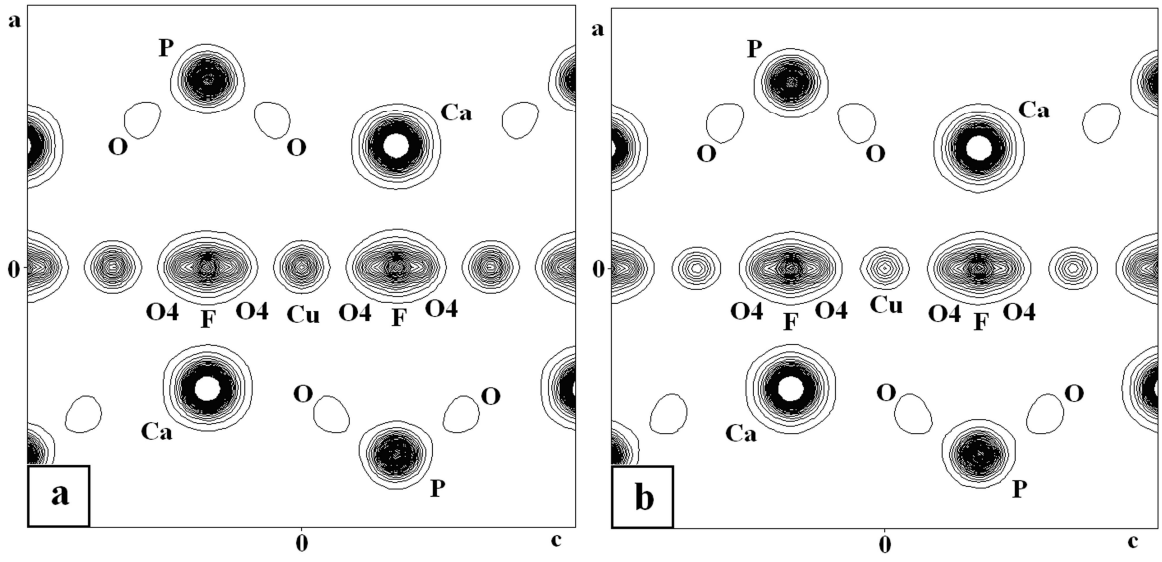

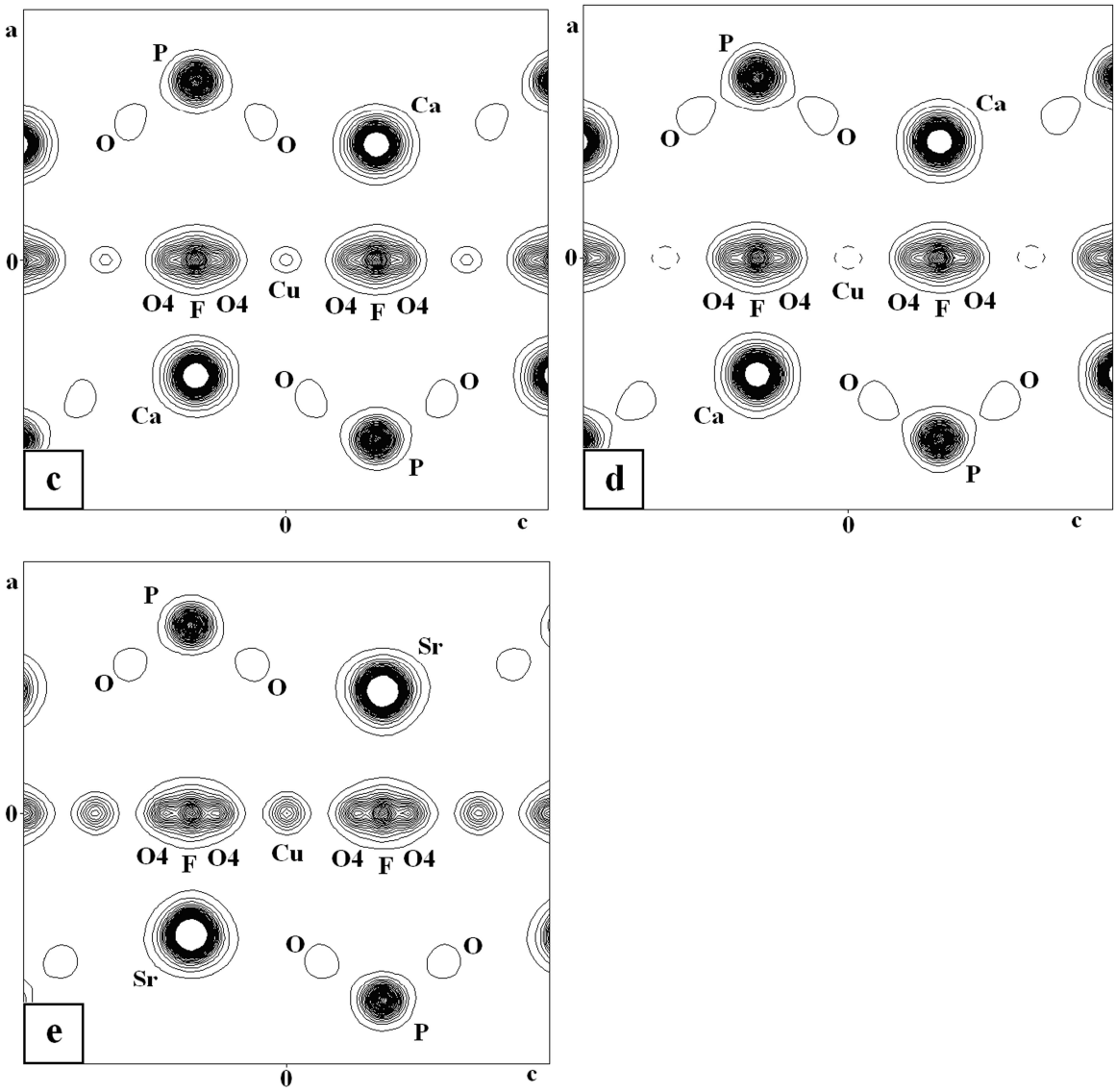

Figure 2.26. Two-dimensional electron-density maps based on F_{obs}+G–constraints (with procrystal density for complete structure) at *y=0* of apatites:

a) $Ca_5(PO_4)_3Cu_{0.1}O_{0.5}H_{0.4-\delta}F_{0.5}$ (sample CaA(0.1Cu_0.5F)),

b) $Ca_5(PO_4)_3Cu_{0.05}O_{0.5}H_{0.45-\delta}F_{0.5}$ (sample CaA(0.05Cu_0.5F)),

c) $Ca_5(PO_4)_3Cu_{0.02}O_{0.5}H_{0.48-\delta}F_{0.5}$ (sample CaA(0.02Cu_0.5F)),

d) $Ca_5(PO_4)_3Cu_{0.01}O_{0.5}H_{0.49-\delta}F_{0.5}$ (sample CaA(0.01Cu_0.5F)),

e) $Sr_5(PO_4)_3Cu_{0.05}O_{0.5}H_{0.45-\delta}F_{0.5}$ (sample SrA(0.05Cu_0.5F)).

Contour levels: from 1 to 50 e/Å^3, step 1 e/Å^3. High-resolution laboratory X-ray powder diffraction data. Dotted line – contour lever at 0.5 e/Å^3.

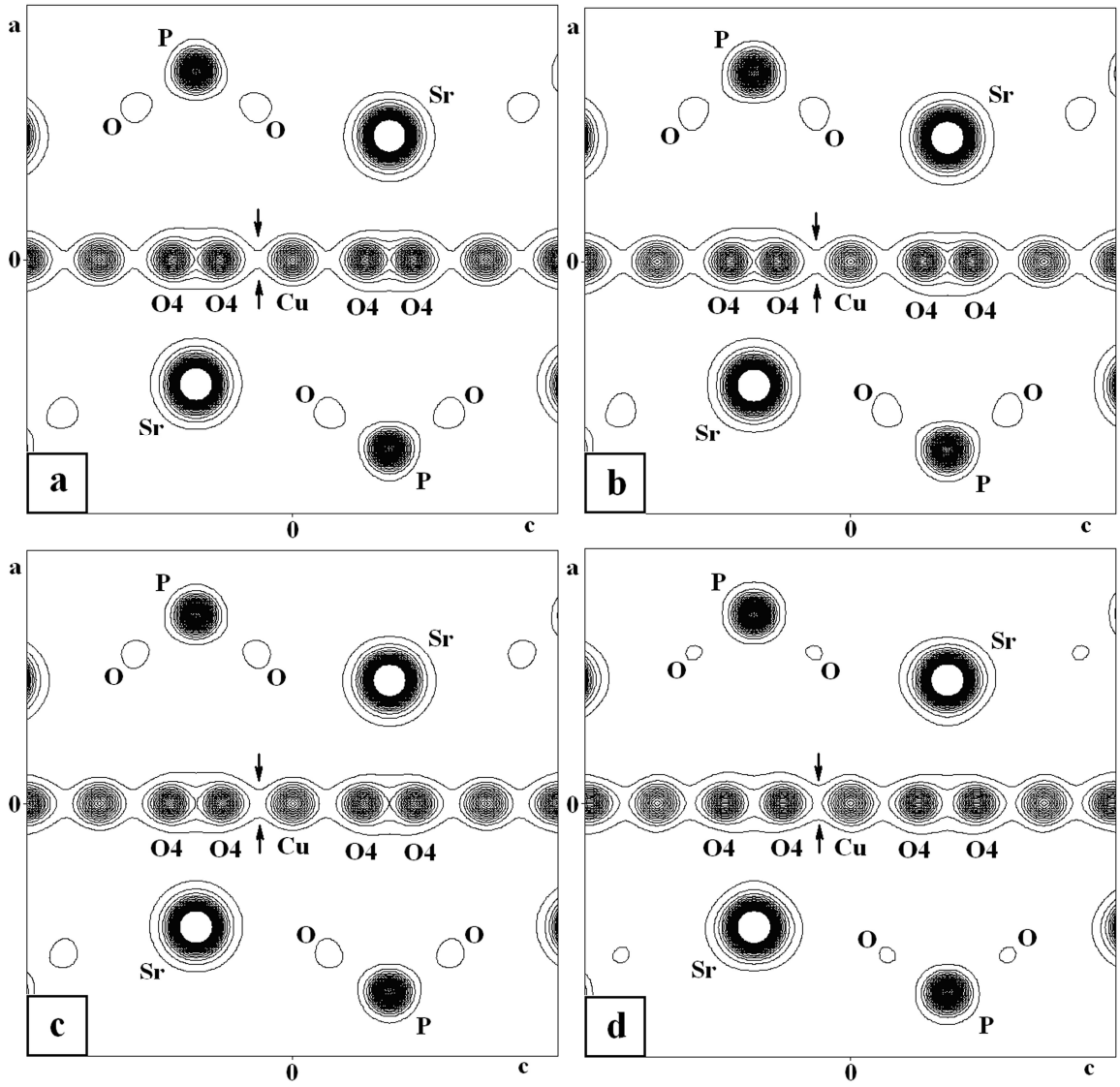

Figure 2.27a. Two-dimensional electron-density maps based on F_{obs}+G–constraints (with procrystal density for complete structure) at $y=0$ of apatites $Sr_5(PO_4)_3Cu_{0.1}OH_{0.9-\delta}$ with different content δ of peroxide and copper ions in higher oxidation state. Contour levels: from 1 to 50 e/Å^3, step 1 e/Å^3. High-resolution laboratory X-ray powder diffraction data. Arrows show the distortion of the electron density near the copper atom.

a) $Sr_5(PO_4)_3Cu_{0.1}OH_{0.9-\delta}$ (sample SrA(0.1Cu-1), δ = 0.038)

b) $Sr_5(PO_4)_3Cu_{0.1}OH_{0.9-\delta}$ (sample SrA(0.1Cu-2), δ = 0.10)

c) $Sr_5(PO_4)_3Cu_{0.1}OH_{0.9-\delta}$ (sample SrA(0.1Cu-3), δ = 0.26)

d) $Sr_5(PO_4)_3Cu_{0.1}OH_{0.9-\delta}$ (sample SrA(0.1Cu-4), δ > 0.26)

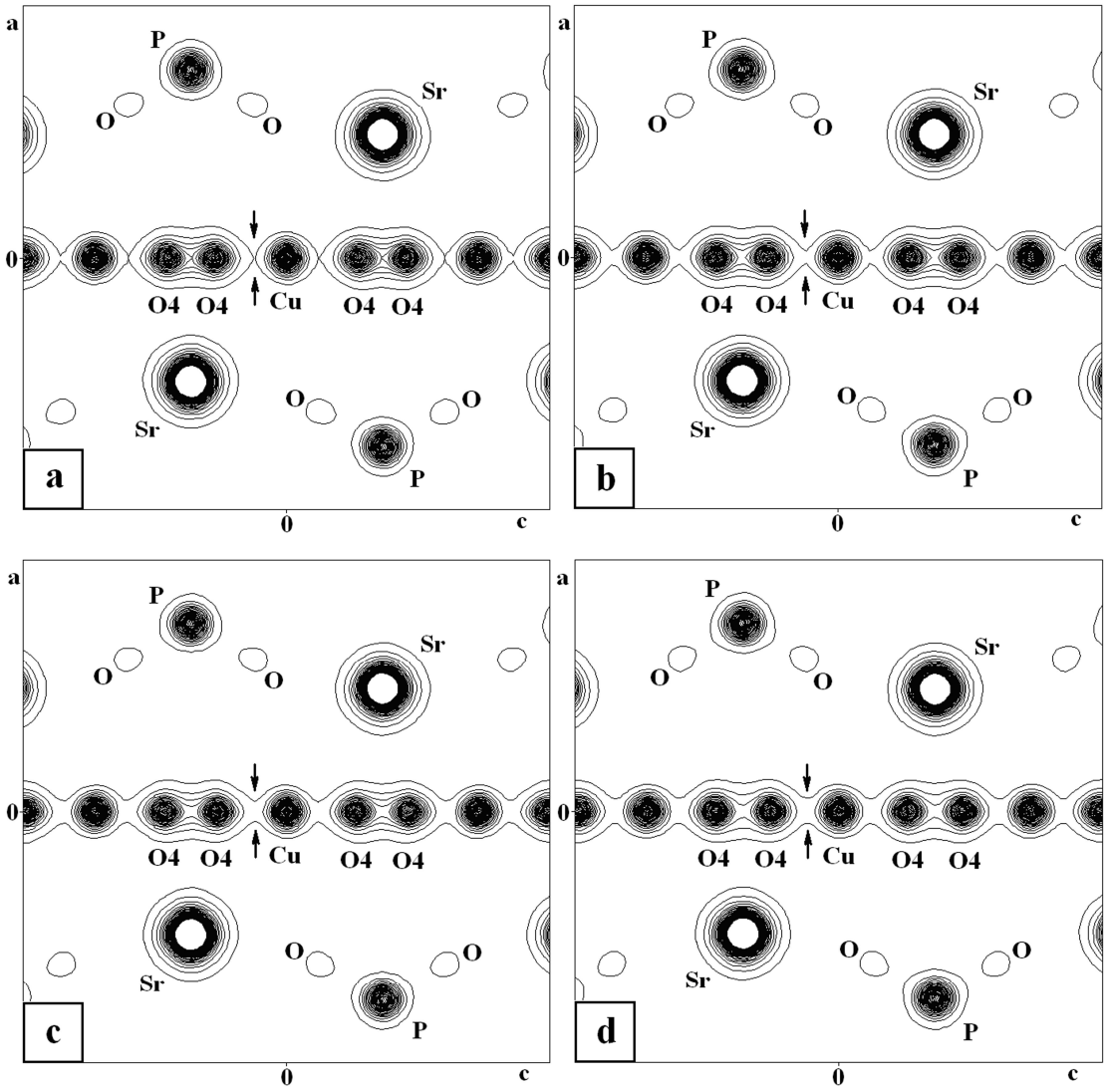

Figure 2.27b. Two-dimensional electron-density maps based on F_{obs}+G–constraints (with procrystal density for complete structure) at $y=0$ of apatites $Sr_5(PO_4)_3Cu_{0.1}OH_{0.9-\delta}$ with different content δ of peroxide and copper ions in higher oxidation state. Contour levels: from 1 to 50 e/Å^3, step 1 e/Å^3. High-resolution synchrotron X-ray powder diffraction data with $\sin\theta/\lambda = 0.93$ Å^{-1}. Arrows show the distortion of the electron density near the copper atom.

a) $Sr_5(PO_4)_3Cu_{0.1}OH_{0.9-\delta}$ (sample SrA(0.1Cu-1), δ = 0.038)

b) $Sr_5(PO_4)_3Cu_{0.1}OH_{0.9-\delta}$ (sample SrA(0.1Cu-2), δ = 0.10)

c) $Sr_5(PO_4)_3Cu_{0.1}OH_{0.9-\delta}$ (sample SrA(0.1Cu-3), δ = 0.26)

d) $Sr_5(PO_4)_3Cu_{0.1}OH_{0.9-\delta}$ (sample SrA(0.1Cu-4), δ > 0.26)

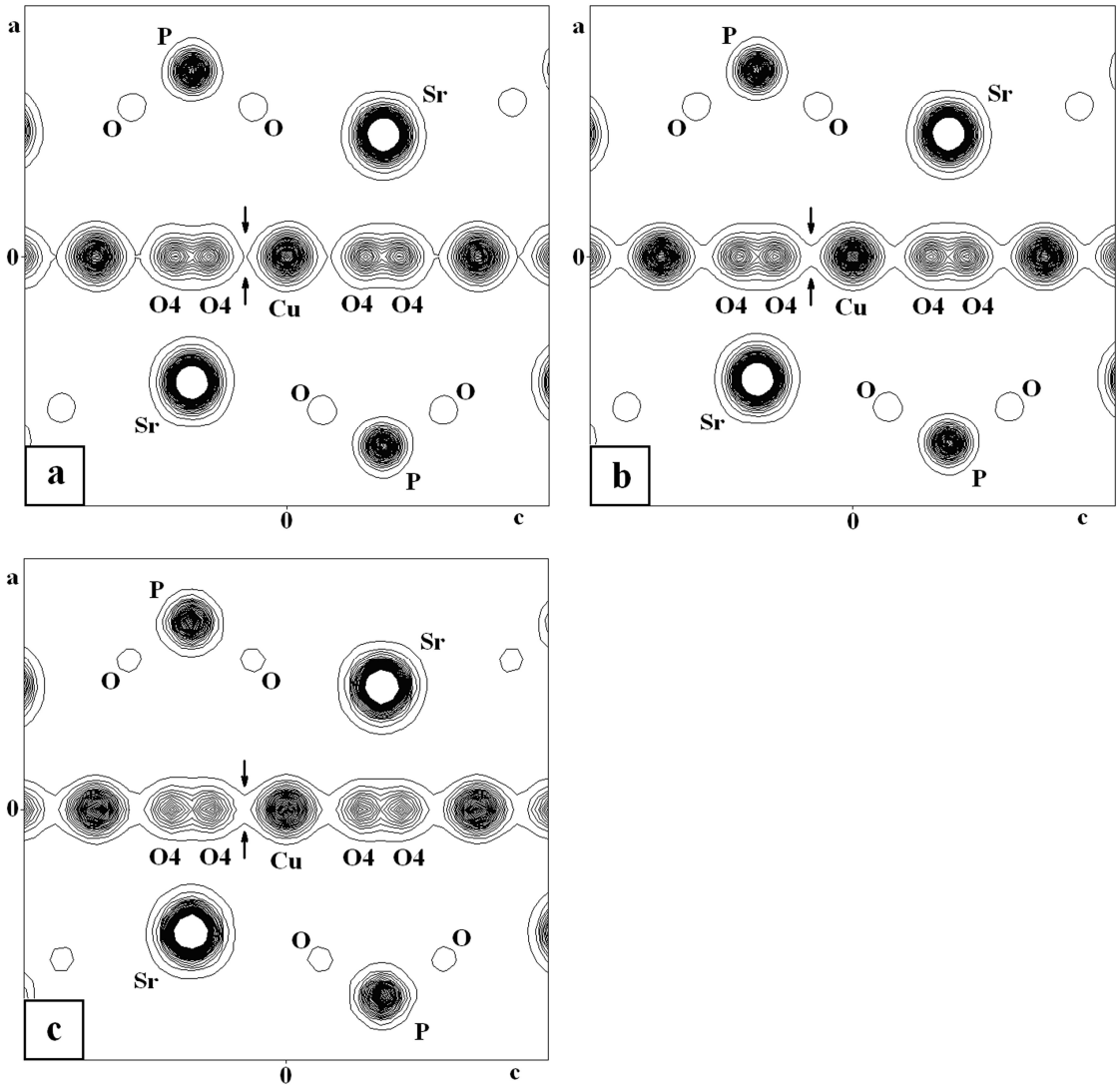

Figure 2.28. Two-dimensional electron-density maps based on F_{obs}+G–constraints (with procrystal density for complete structure) at $y=0$ of apatites $Sr_5(PO_4)_3Cu_{0.3}OH_{0.7-\delta}$ with different content δ of peroxide and copper ions in higher oxidation state. Contour levels: from 1 to 50 e/Å^3, step 1 e/Å^3. High-resolution laboratory X-ray powder diffraction data. Arrows show the distortion of the electron density near the copper atom.

a) $Sr_5(PO_4)_3Cu_{0.3}OH_{0.7-\delta}$ (sample SrA(0.3Cu-1), δ = 0.022)

b) $Sr_5(PO_4)_3Cu_{0.3}OH_{0.7-\delta}$ (sample SrA(0.3Cu-2), δ = 0.104)

c) $Sr_5(PO_4)_3Cu_{0.3}OH_{0.7-\delta}$ (sample SrA(0.3Cu-3), δ = 0.29)

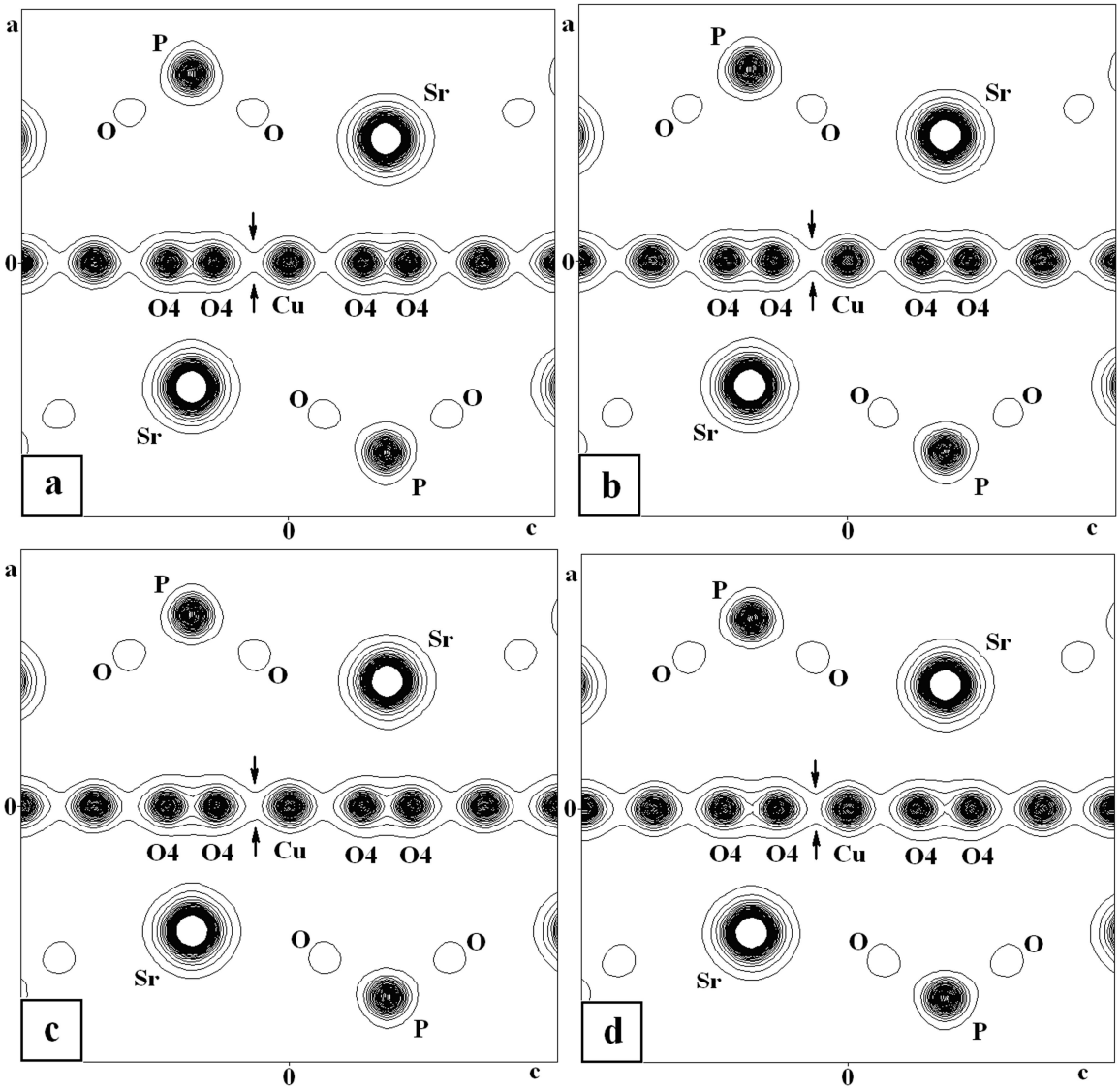

Figure 2.29a. Two-dimensional electron-density maps based on F_{obs}+G–constraints (with procrystal density for complete structure) at $y=0$ of apatites $Sr_5(PO_4)_3Cu_{0.1}OH_{0.9-\delta}$ with different content of peroxide and copper ions in higher oxidation state. Contour levels: from 1 to 50 e/Å^3, step 1 e/Å^3. High-resolution synchrotron X-ray powder diffraction data with sin□/□□= 0.55 Å^{-1}. Arrows show the distortion of the electron density near the copper atom.

a) $Sr_5(PO_4)_3Cu_{0.1}OH_{0.9-\delta}$ (sample SrA(0.1Cu-1), δ = 0.038)

b) $Sr_5(PO_4)_3Cu_{0.1}OH_{0.9-\delta}$ (sample SrA(0.1Cu-2), δ = 0.10)

c) $Sr_5(PO_4)_3Cu_{0.1}OH_{0.9-\delta}$ (sample SrA(0.1Cu-3), δ = 0.26)

d) $Sr_5(PO_4)_3Cu_{0.1}OH_{0.9-\delta}$ (sample SrA(0.1Cu-4), δ > 0.26)

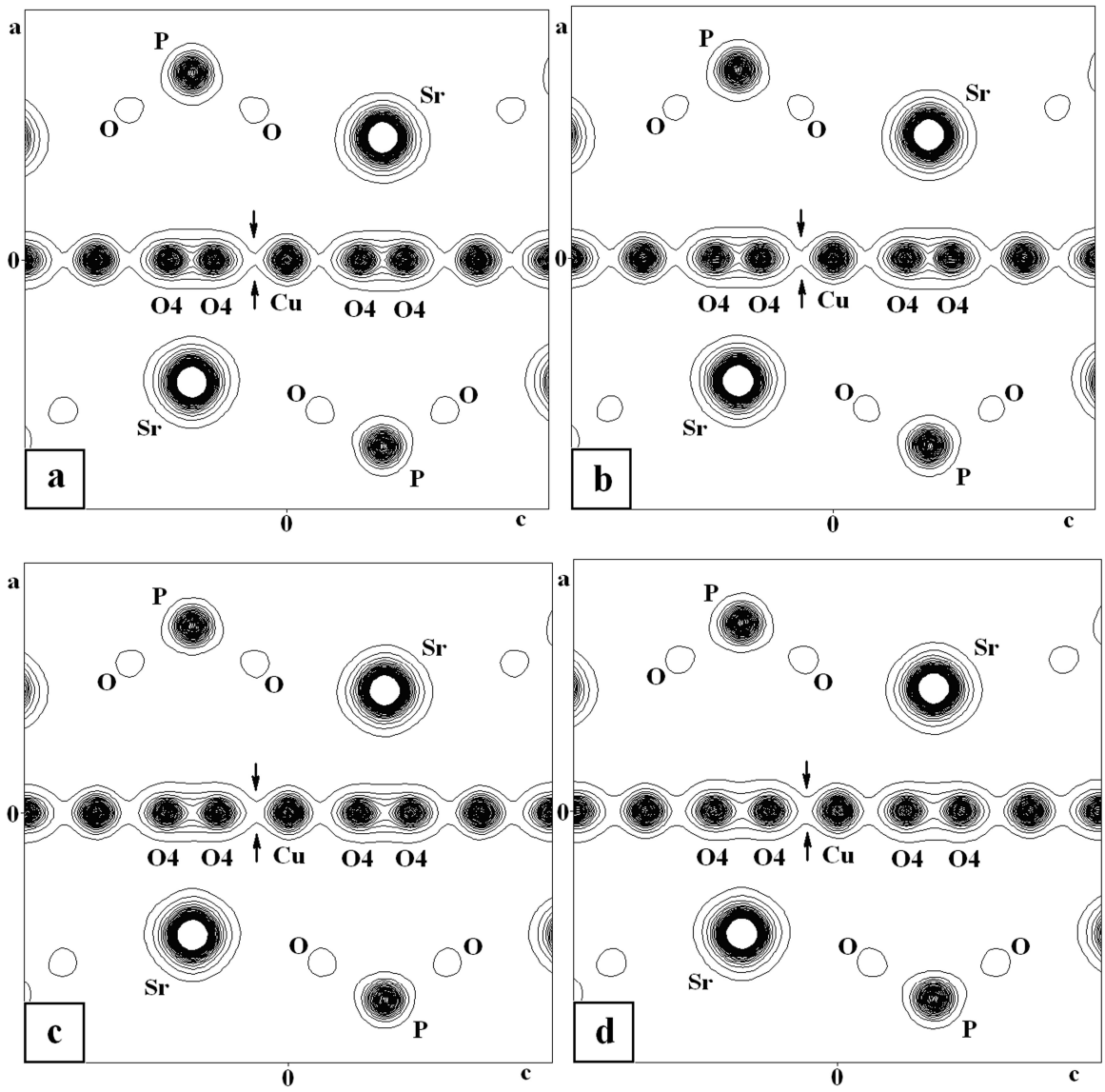

Figure 2.29b. Two-dimensional electron-density maps based on F_{obs}+G–constraints (with procrystal density for complete structure) at $y=0$ of apatites $Sr_5(PO_4)_3Cu_{0.1}OH_{0.9-\delta}$ with different content of peroxide and copper ions in higher oxidation state. Contour levels: from 1 to 50 e/Å^3, step 1 e/Å^3. High-resolution synchrotron X-ray powder diffraction data with $\sin\theta/\lambda = 0.65$ Å^{-1}. Arrows show the distortion of the electron density near the copper atom.

a) $Sr_5(PO_4)_3Cu_{0.1}OH_{0.9-\delta}$ (sample SrA(0.1Cu-1), $\delta = 0.038$)

b) $Sr_5(PO_4)_3Cu_{0.1}OH_{0.9-\delta}$ (sample SrA(0.1Cu-2), $\delta = 0.10$)

c) $Sr_5(PO_4)_3Cu_{0.1}OH_{0.9-\delta}$ (sample SrA(0.1Cu-3), $\delta = 0.26$)

d) $Sr_5(PO_4)_3Cu_{0.1}OH_{0.9-\delta}$ (sample SrA(0.1Cu-4), $\delta > 0.26$)

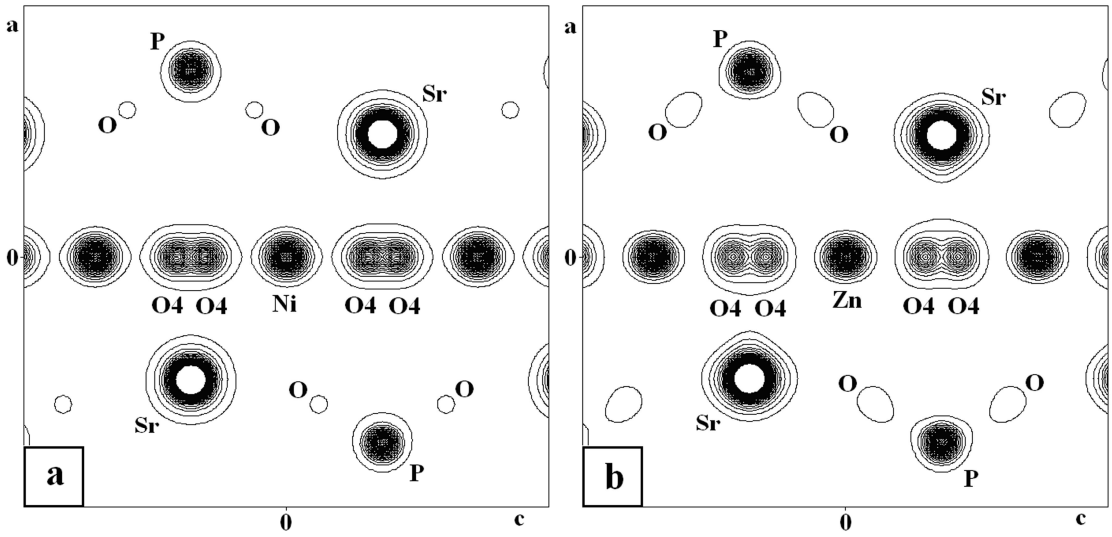

Figure 2.30. Two-dimensional electron-density maps based on F_{obs}+G–constraints (with procrystal density for complete structure) at *y=0* of apatites:

a) $Sr_5(PO_4)_3Ni_{0.2}OH_{0.8-\delta}$ (sample SrA(0.2Ni))

b) $Sr_5(PO_4)_3Zn_{0.15}OH_{0.85-\delta}$ (sample SrA(0.15Zn))

Contour levels: from 1 to 50 e/Å^3, step 1 e/Å^3. High-resolution laboratory X-ray powder diffraction data.

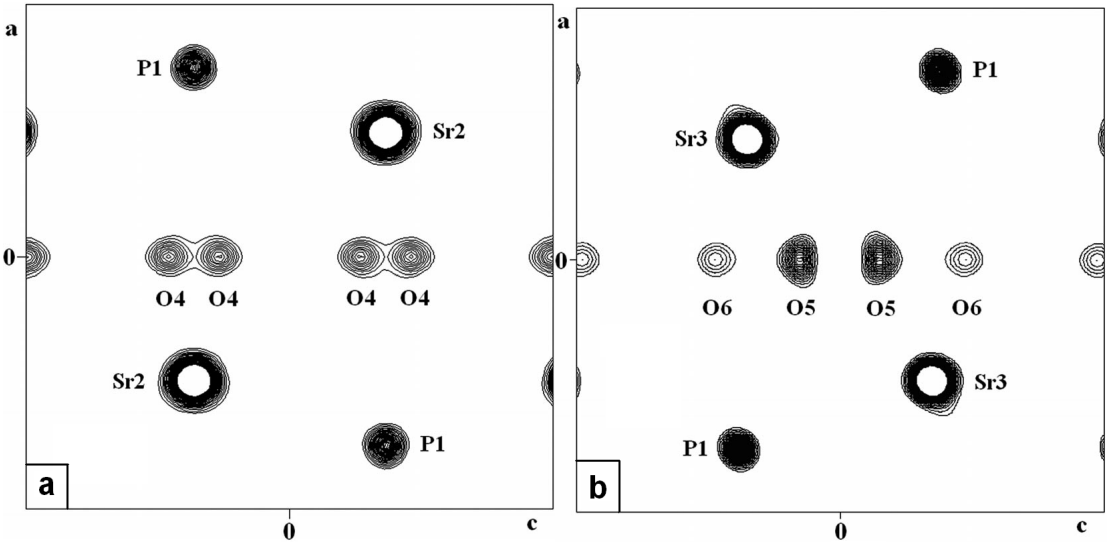

Figure 2.31. Two-dimensional electron-density maps based on F_{obs}+G–constraints (with procrystal density for complete structure) at *y=0* of apatites:

a) $Sr_{10}(PO_4)_6(O_2)_x(OH)_{2-2x}$, x=0 (hydroxy-apatite)

b) $Sr_{10}(PO_4)_6(O_2)_x(OH)_{2-2x}$, x=0.68 (hydroxyperoxy-apatite)

Contour levels: from 3 to 50 e/Å^3, step 1 e/Å^3. High-resolution laboratory X-ray powder diffraction data.

2.3.6. Conclusion

The missing intercalated metal atoms in the crystal structures of Sr– and Ca–apatites have been successfully localized from high-resolution laboratory X-ray powder diffraction data by the Maximum Entropy Method (MEM). The MEM has been applied in a series of calculations using different types of experimental constraints (F_{obs}, F_{obs}+G, and F_{LeBail}+G) and allowed precise location of copper atoms with fractional occupancies >= 0.05 in the apatite structure (corresponding to approximately 1.4 electrons per site) using an initial structural model without the intercalated metal atoms. As a common tendency it could be confirmed that the MEM map based on F_{obs}–constraints is the most biased by the model, and the MEM map based on F_{LeBail}+G–constraints is the least biased by the model. For the MEM maps calculated with procrystal density, the value of the electron density of located metal atoms is increased in the order of maps based on F_{obs}–, F_{obs}+G–, and F_{LeBail}+G–constraints. The MEM map based on F_{LeBail}+G–constraints is the best choice for localization of missing atoms in centrosymmetric structures.

The use of a structural model without intercalated metal atoms leads to many falsely assigned phases of weak reflections. Applying G–constraints for a sum of intensities of groups of overlapping reflections decreases the model bias not only through the absence of the model-biased partitioning of the overlapping intensities but presumably also through the decrease of the number of reflections with incorrect phases in the F–constraints.

The results obtained with high-resolution laboratory X-ray powder diffraction data were compared with high-resolution synchrotron powder diffraction data. It was shown that the MEM can be successfully used for the determination of the accurate electron density distribution from high-resolution laboratory X-ray powder diffraction data. The difference between MEM maps from laboratory and synchrotron diffraction data are caused primarily by different instrumental peak profiles and different resolution $\sin\theta/\lambda$.

2.4. Application of MEM for reconstruction of electron density of $BaZnF_4$ and $BaMgF_4$ from low-temperature X-ray powder diffraction data

2.4.1. Background information

Ternary fluorides $BaZnF_4$ and $BaMgF_4$ crystallize in space group $Cmc2_1$. The Zn/Mg cations are surrounded by six fluoride atoms forming layers perpendicular to *b*-axis (Fig. 2.32). Between these layers the Ba cations are located.

In the present work the experimental determination of the electron charge density of $BaZnF_4$ and $BaMgF_4$ at 10 K using high-resolution synchrotron powder diffraction data and MEM is reported. It was previously shown that at 10 K the thermal motion on the true electronic charge is minimized and can be compared with the DFT-calculated electron density distribution (Butcher *et al.*, 2011). MEM reconstructed electron density distribution for $LiBD_4$ showed that high-resolution powder diffraction data can be successfully used for experimental determination of atomic and ionic charges for compounds comprised of light elements (Buchter *et al.*, 2011). The question about the applicability of MEM for compounds of heavy elements remained open.

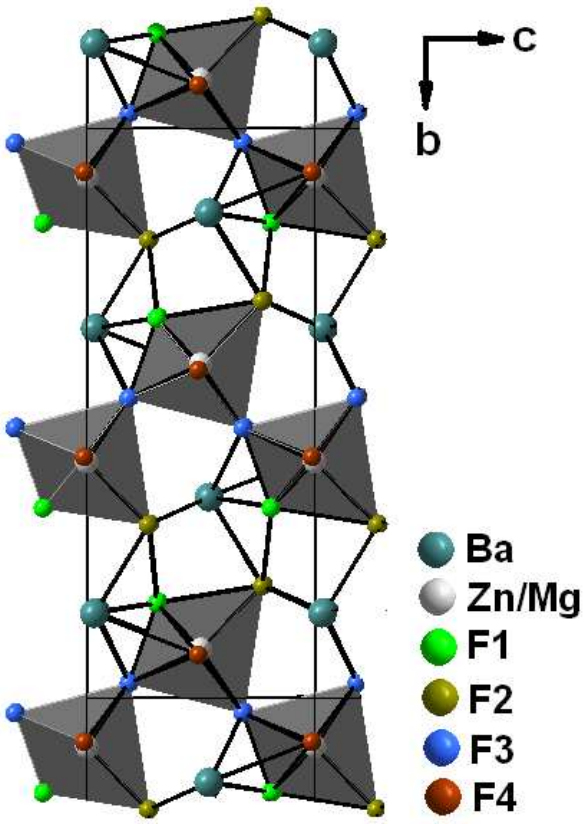

Figure 2.32. Crystal structure of $BaZnF_4$ and $BaMgF_4$ in a projectin along *a*-axis.

2.4.2. X-ray powder diffraction investigation of $BaZnF_4$ and $BaMgF_4$

High-resolution synchrotron powder diffraction data of $BaZnF_4$, $BaMgF_4$, and $BaMnF_4$ were measured by Posse *et al.* (2009) at ID31, ESRF (Grenoble, France).

The program TOPAS 4.1 (Coelho, 2007) was used for extraction of intensities after whole powder pattern fitting (WPPF) according to the Rietveld method. The amplitudes of the structure factors were corrected for anomalous scattering according to the procedure of Bagautdinov *et al.* (1998). Crystallographic and refinement data for all samples at ambient conditions are given in Appendix 2, Tables A1-A2. Experimental and calculated profiles for Rietveld refinements are given in Figs. 2.33 and 2.34.

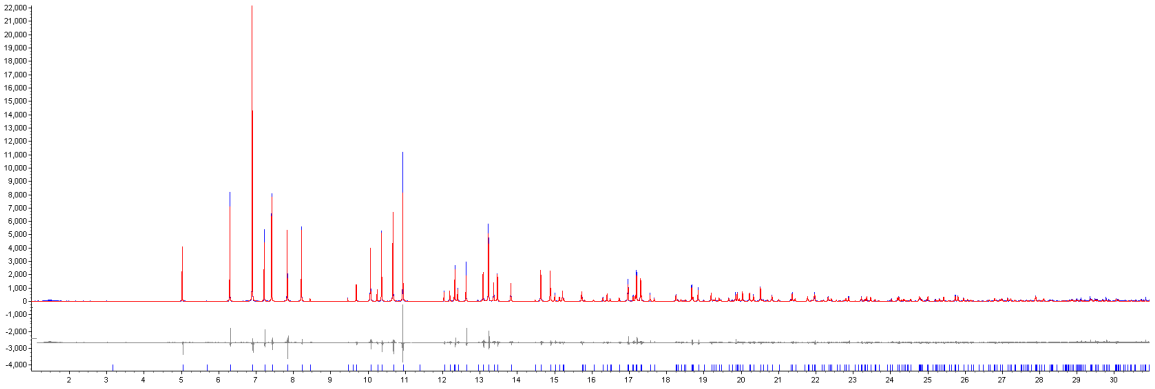

Figure 2.33. Rietveld plot of $BaZnF_4$.

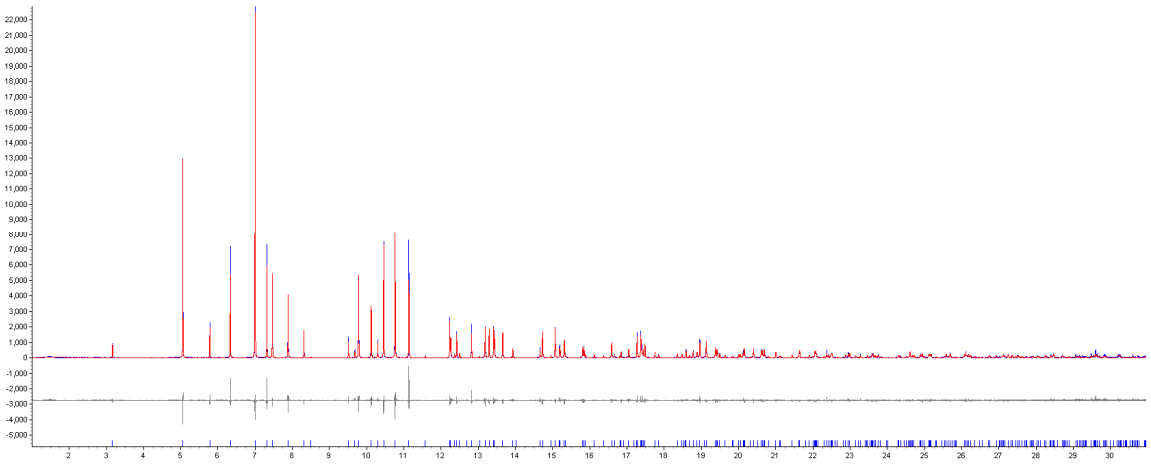

Figure 2.34. Rietveld plot of $BaMgF_4$.

2.4.3. MEM calculations of electron density of $BaZnF_4$ and $BaMgF_4$

All MEM calculations were performed using the computer program BayMEM (van Smaalen *et al.*, 2003), employing the Sakata–Sato algorithm (Sakata & Sato, 1990). A pixel grid of 48×144×128 along the crystallographyc axes *a*, *b*, and *c* was chosen for MEM calculations, corresponding to ~0.1 Å per pixel resolution in each directions. Details about the maximum-entropy calculations are given in Appendix 2, Tables A1-A2. The maximal resolution $\sin\theta/\lambda$ was ~0.65 $Å^{-1}$. Optimal values for the Lagrange multiplier were obtained by trial and error. The stopping criterion according to Hofmann *et al.* (2007) was not precise enough to determine the most "featureless" distribution of residual electron density, so the criterion of Meindl & Henn (2008) was applied. The final model from the Rietveld refinement was used to create the procrystal density in the form of ISAM (independent spherical atom model), (Fig. 2.35). Atomic charges were determined from the MEM and DFT electron density distribution by applying the Bader analysis for atoms in molecules (Bader, 1990), using the program EDMA for MEM reconstructed electron density distribution (Palatinus *et al.*, 2012) with partition mode "near-grid".

2.4.4. DFT calculations of electron density of $BaZnF_4$ and $BaMgF_4$

DFT-calculations for $BaZnF_4$ and $BaMgF_4$ were performed using the program WIEN2K with PBE-functional (Table 2.2).

2.4.5. Analysis of electron density distribution of atoms in $BaZnF_4$ and $BaMgF_4$

Series of MEM calculations with procrystal electron density (Table 2.3) based on experimental constraints of different order n = 2, 4, 6 were performed. MEM calculations based on F_2 – constraints allow precise determination of atomic charges, but the electron density distribution is distorted in the low density region (Fig. 2.36). In order to improve the electron density distribution in the low density region, generalized constraints of order n=4 (χ^4) and n=6 (χ^6) were used, which allow to use high-order central moments of the distribution of the residuals: F_4 – constraints and F_6 – constraints (Palatinus & van Smaalen, 2002). In the presented case the histograms of the structure factors residuals are distorted, when the generalized F_4 – and F_6 – constraints are used. As a result, the electron density distribution in the low density region remains distorted, and the integrated atomic charges are incorrect (Figs.

2.37 and 2.38, Table 2.3). Application of prior-derived F_{PD}–constraints (Palatinus & van Smaalen, 2005) up to 2.0 Å^{-1} with F_2 – constraints (F_2+F_{PD}) and the application of G–constraints with F_2 – constraints (F_2+G) led to an almost undistorted distribution of the electron density and very good agreement between MEM- and DFT-calculated atomic charges (Figs. 2.39 and 2.41, Table 2.3). The results of the corresponding calculations with generalized constraints showed large variations in the atomic charges and in the distribution of the electron density (Figs. 2.40, Table 2.3). The MEM calculations of $LiBD_4$ also revealed that F_2+G – constraints are the most accurate for the experimental characterization of the electron density distribution (Buchter *et al.*, 2011). The MEM calculations based on F_2+G+F_{PD} did not converge. Results of MEM calculations clearly showed that the use of an uniform prior density prevents any reliable determination of the electron density distribution and atomic charges (Fig. 2.42 and Table 2.3).

The results of extended MEM calculations performed in this work confirmed that the use of G-constraints for overlapping reflections is mandatory for accurate MEM reconstruction of the electron density distribution and determination of precise ionic charges. Using of G-constraints decreases the model-bias effect due to extraction of individual structure factors amplitudes and allows the determination of atomic charges from X-ray powder diffraction data with a resolution of $\sin\theta/\lambda \sim 0.65$ Å^{-1}. The successful application of prior-derived F_{PD}-constraints was unexpected, since they were useless for the reconstruction of the electron density of $LiBD_4$ (Butcher *et al.*, 2011). Understanding of applicability of F_{PD}-constraints requires additional investigations.

Table 2.2. Prior (IASM) and DFT electron density distribution and corresponding integrated atomic charges.

Density	Ba (e)	Zn/Mg (e)	F1 (e)	F2 (e)	F3 (e)	F4 (e)	$\sum_{i-1}^{4} F_i$ (e)
$BaZnF_4$ (prior)	53.896	28.315	9.991	9.981	9.917	9.947	39.836
$BaMgF_4$ (prior)	53.884	10.281	10.021	9.924	9.938	9.952	39.835
$BaZnF_4$ (DFT)	54.297	28.553	9.792	9.789	9.776	9.796	39.153
$BaMgF_4$ (DFT)	54.301	10.246	9.853	9.851	9.875	9.882	39.461

Table 2.3. MEM calculations of the electron density distribution and corresponding integrated atomic charges.

Density	Prior	*n* (order)	*G*	F_{PD}	Ba (e)	Zn/Mg (e)	F1 (e)	F2 (e)	F3 (e)	F4 (e)	$\sum_{i-1}^{4} F_i$ (e)
$BaZnF_4$	IASM	2			54.266	28.420	9.827	9.797	9.834	9.903	39.361
	IASM	4			54.368	28.485	9.752	9.759	9.753	9.930	39.194
	IASM	6			54.433	28.493	9.687	9.744	9.729	9.961	39.121
	IASM	2	Y		54.310	28.416	9.791	9.772	9.805	9.953	39.321
	IASM	4	Y		54.387	28.487	9.763	9.729	9.714	9.967	39.173
	IASM	2		Y	54.287	28.379	9.897	9.793	9.789	9.902	39.380
	IASM	4		Y	54.352	28.527	9.804	9.760	9.731	9.874	39.169
	IASM	2	Y	Y	54.319	28.330	9.869	9.819	9.797	9.914	39.398
	uniform	2			51.464	27.727	9.892	9.399	9.607	9.398	38.295
	uniform	4			52.396	28.226	9.672	9.670	9.638	9.485	38.465
	uniform	6			52.425	28.223	9.714	9.581	9.637	9.522	38.455
	uniform	2		Y	51.254	27.829	9.413	9.134	9.367	9.682	37.595
$BaMgF_4$	IASM	2			54.288	10.206	9.886	9.911	9.794	9.916	39.507
	IASM	4			54.393	10.179	9.816	9.872	9.773	9.967	39.428
	IASM	6			54.432	10.176	9.799	9.839	9.746	10.008	39.392
	IASM	2	Y		54.277	10.253	9.859	9.907	9.792	9.912	39.47
	IASM	4	Y		54.453	10.185	9.804	9.865	9.699	9.993	39.361
	IASM	2		Y	54.484	10.173	9.860	9.703	9.803	9.977	39.343
	IASM	4		Y	54.424	10.157	9.793	9.801	9.792	10.032	39.418
	IASM	2	Y	Y	53.884	10.281	10.021	9.924	9.938	9.952	39.835
	uniform	2			52.807	10.271	9.976	9.726	9.517	9.746	38.965

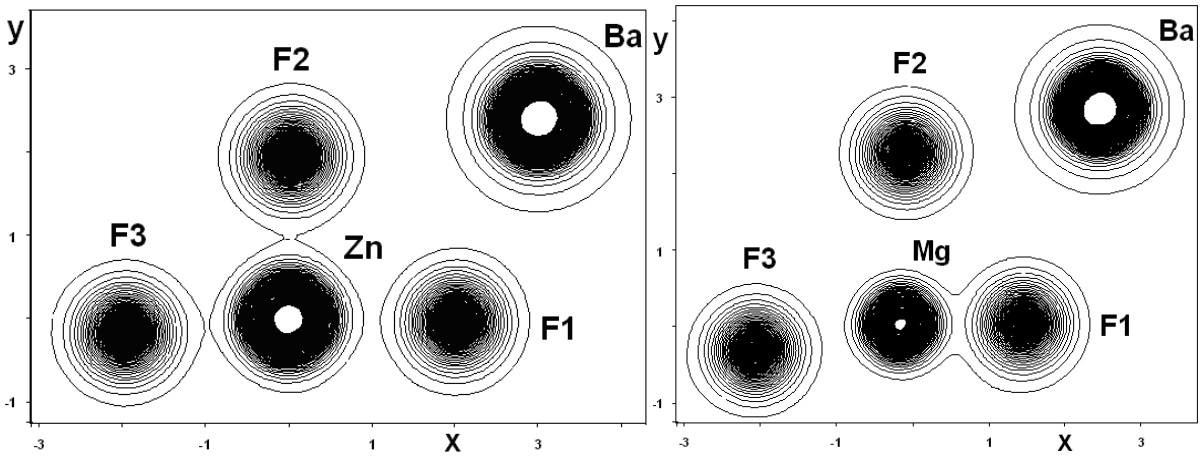

Figure 2.35. Two-dimensional procrystal electron-density maps at *z=0* of $BaZnF_4$ (left) and $BaMgF_4$ (right). Contour levels: from 0.5 to 200 e/Å^3, step 0.5 e/Å^3.

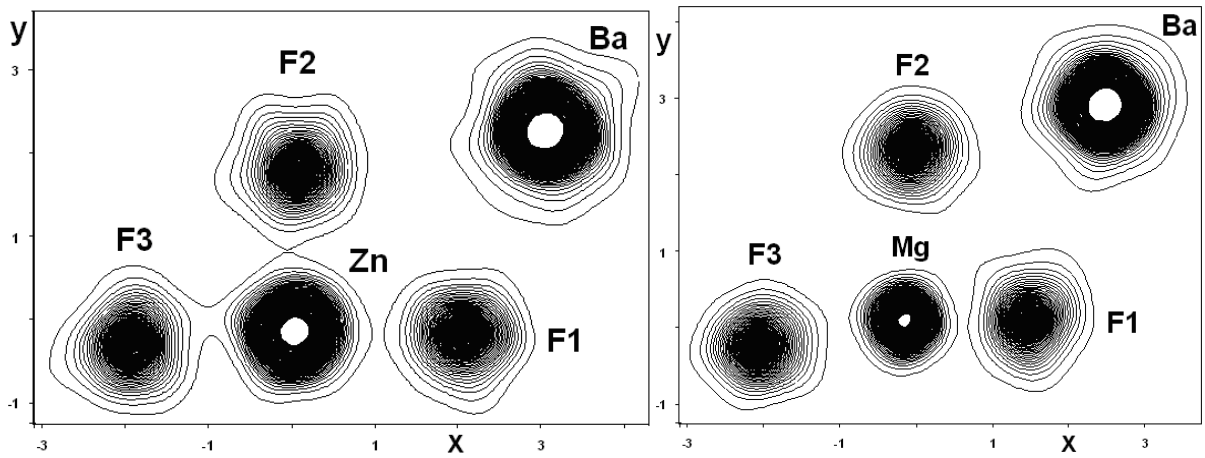

Figure 2.36. Two-dimensional electron-density maps at *z=0* of $BaZnF_4$ (left) and $BaMgF_4$ (right) based on F_2–constraints. Contour levels: from 0.5 to 200 e/Å^3, step 0.5 e/Å^3.

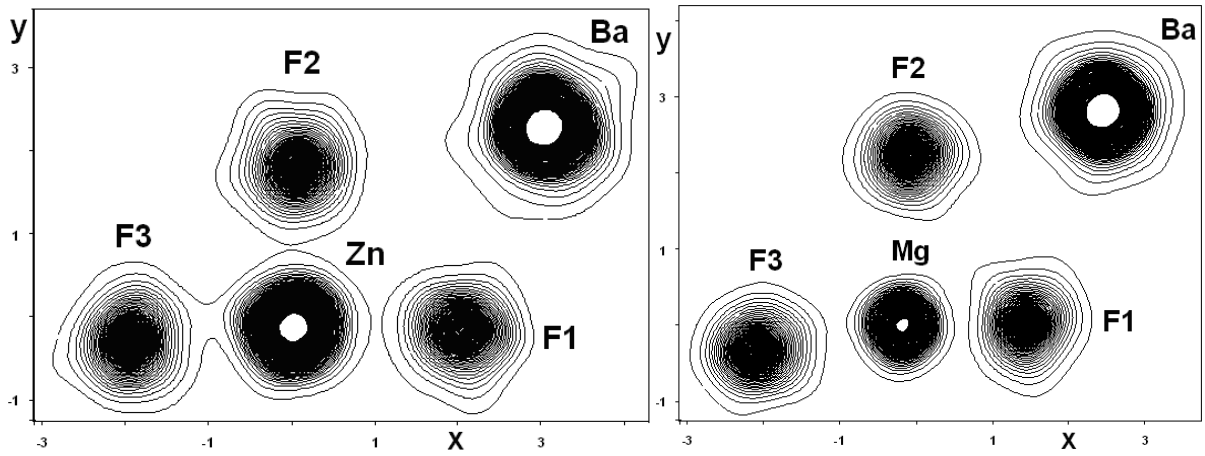

Figure 2.37. Two-dimensional electron-density maps at *z=0* of $BaZnF_4$ (left) and $BaMgF_4$ (right) based on F_4–constraints. Contour levels: from 0.5 to 200 e/Å^3, step 0.5 e/Å^3.

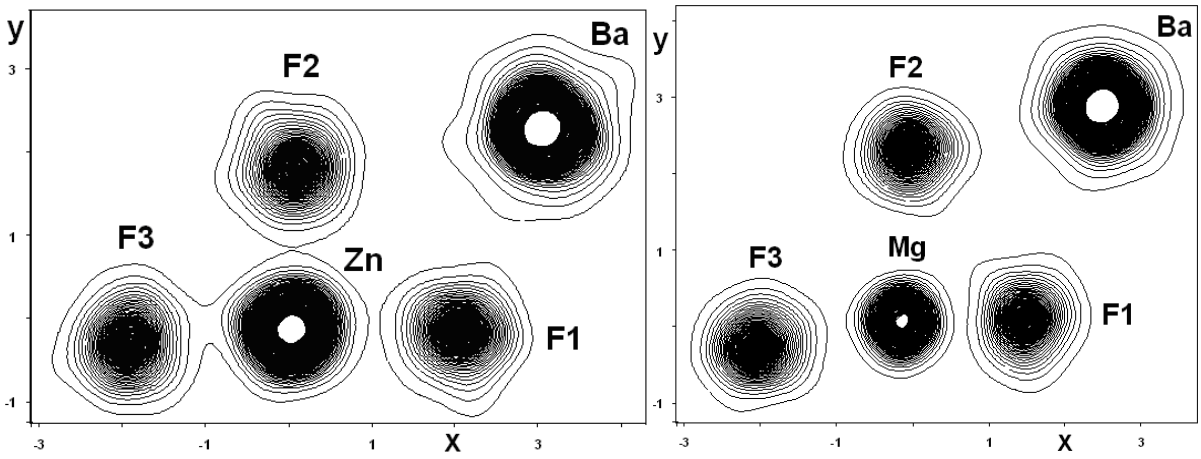

Figure 2.38. Two-dimensional electron-density maps at *z=0* of $BaZnF_4$ (left) and $BaMgF_4$ (right) based on F_6–constraints. Contour levels: from 0.5 to 200 e/Å^3, step 0.5 e/Å^3.

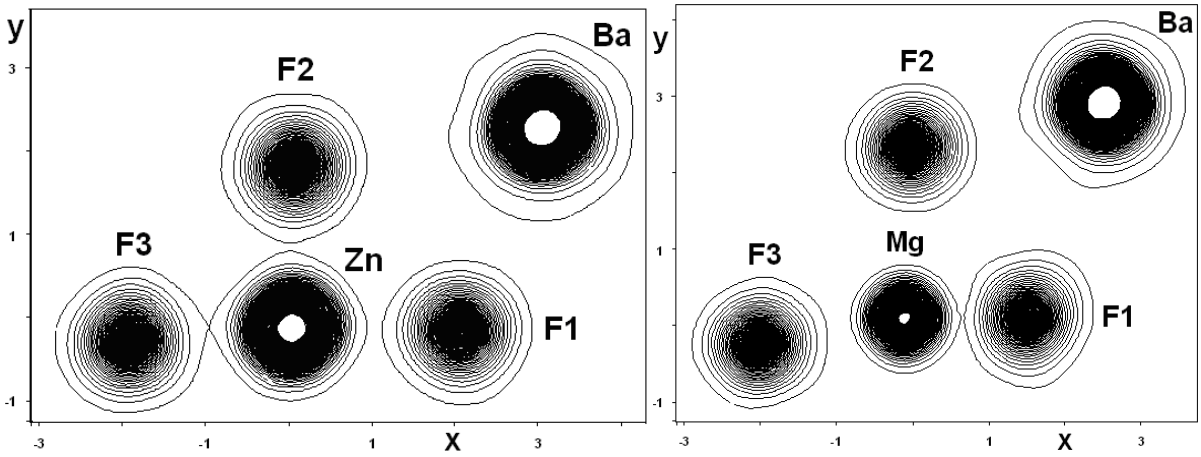

Figure 2.39. Two-dimensional electron-density maps at *z=0* of $BaZnF_4$ (left) and $BaMgF_4$ (right) based on F_2– and F_{PD}–constraints (F_{PD}–constraints up to 2.0 Å^{-1}). Contour levels: from 0.5 to 200 e/Å^3, step 0.5 e/Å^3.

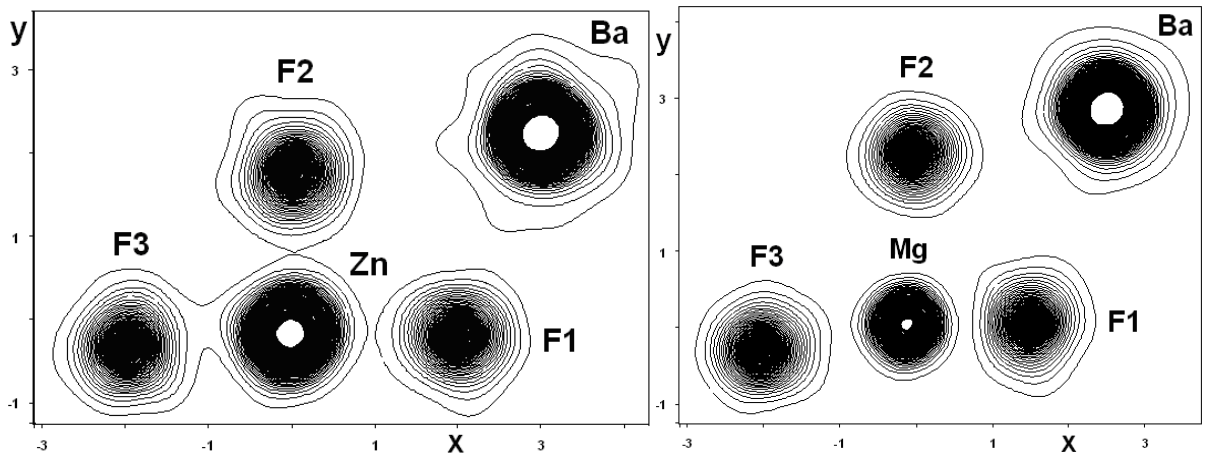

Figure 2.40. Two-dimensional electron-density maps at *z=0* of $BaZnF_4$ (left) and $BaMgF_4$ (right) based on F_4– and F_{PD}–constraints (F_{PD}–constraints up to 2.0 $Å^{-1}$). Contour levels: from 0.5 to 200 e/$Å^3$, step 0.5 e/$Å^3$.

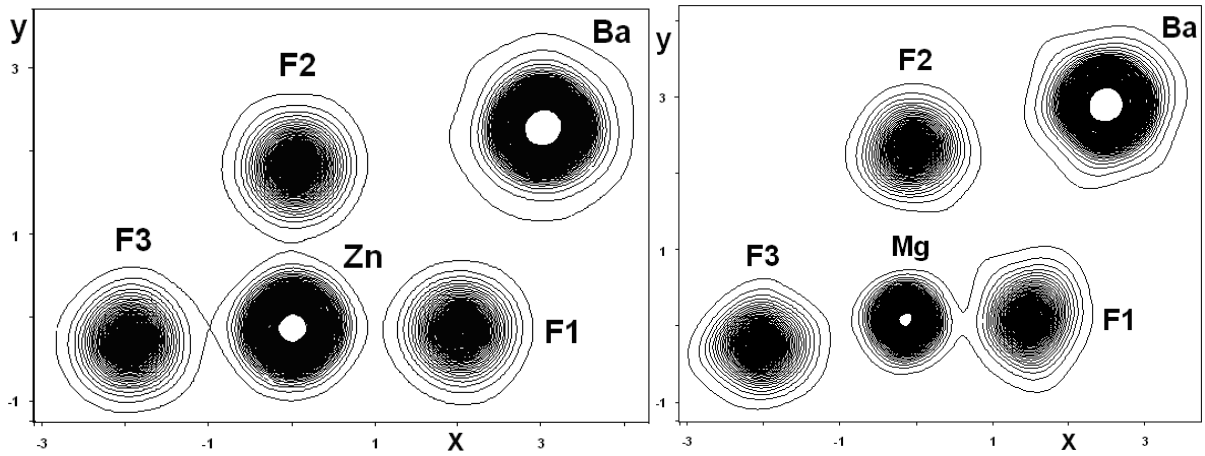

Figure 2.41. Two-dimensional electron-density maps at *z=0* of $BaZnF_4$ (left) and $BaMgF_4$ (right) based on F_2+G–constraints. Contour levels: from 0.5 to 200 e/$Å^3$, step 0.5 e/$Å^3$.

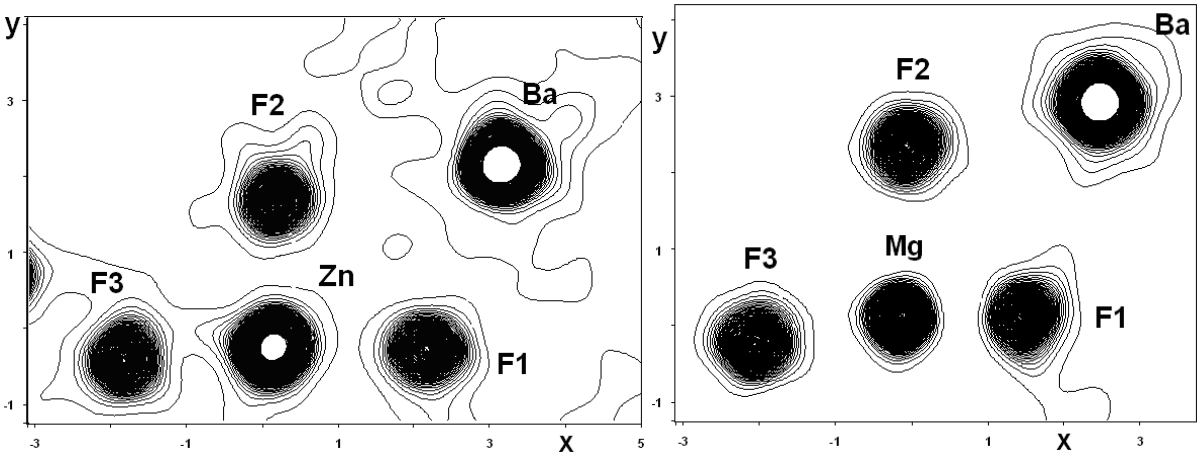

Figure 2.42. Two-dimensional electron-density maps at *z=0* of $BaZnF_4$ (left) and $BaMgF_4$ (right) based on F_2–constraints with uniform prior. Contour levels: from 0.5 to 200 e/Å^3, step 0.5 e/Å^3.

2.4.6. Conclusion

The experimental electron density distribution and the integrated ionic charges of $BaZnF_4$ and $BaMgF_4$ were determined by application of the maximum entropy method from high-resolution synchrotron X-ray powder diffraction data at 10 K. It was confirmed that MEM can be successfully applied for the determination of the accurate electron density distribution of heavy-atom compounds. The best electron density distribution was obtained by using *G*-constraints for strongly overlapping reflections (F_2+*G*-constraints) and by using prior-derived constraints (F_2+F_{PD}-constraints). The use of procrystal electron density in the form of IASM was necessary in both cases. The experimental atomic charges are in good agreement with the charges calculated by DFT.

2.5. Publications and authors contribution

Chapters 2.1, 2.2, and 2.3 were published:

1) Magdysyuk, O.V.; Dinnebier, R.E.; van Smaalen, S.; Zykin, M.A.; Kazin, P.E.; Jansen, M. (2012). Reconstructions of electron density by the Maximum Entropy Method from X-ray powder diffraction data based on incomplete and complete crystal structure models: a case study of apatites with different intercalated metal atoms. *Z. Kristallogr.* **227**, 321-333.

2) Kazin, P.E.; Zykin, M.A.; Dinnebier, R.E.; Magdysyuk, O.V.; Tretyakov, Yu.D.; Jansen, M. (2012). An Unprecedented Process of Peroxide Ion Formation and its Localization in the

Crystal Structure of Strontium Peroxy-Hydroxyapatite $Sr_{10}(PO_4)_6(O_2)_x(OH)_{2-2x}$. *Z. Anorg. Allg. Chem.* **638**(6), 909–919.

Chapter 2.4 will be published:

3) Magdysyuk *et al.* Experimental charge densities of $BaZnF_4$ and $BaMgF_4$ from maximum entropy method (in preparation).

Prof. P.E. Kazin, Mr. M.A. Zykin, Prof. Yu.D. Tretyakov, and Prof. M. Jansen synthesized all investigated apatites. Prof. S. van Smaalen supported the use of program BayMEM. Support with synchrotron measurements at Diamond, I11 to Dr. J.E. Parker and Dr. C.C. Tang (Diamond Light Source, UK), Mr. F. Adams (Max Planck Institute for Solid State Research, Stuttgart, Germany) is gratefully acknowledged.

Synthesis and high-resolution synchrotron powder diffraction measurements of $BaZnF_4$ and $BaMgF_4$ were performed by Posse, J.M.; Grzechnik, A.; Friese, K. (Universidad del Pais Vasco**,** Spain) and published (Posse *et al.*, 2009). DFT calculations were performed by Dr. U. Wedig (Max Planck Institute for Solid State Research, Stuttgart, Germany).

2.6. References

Bader, R.F.W. (1990). *Atoms in Molecules: A Quantum Theory.* Clarendon, Oxford.

Bagautdinov, B.; Luedecke, J.; Schneider, M.; van Smaalen, S. (1998). *Disorder in the Crystal Structure of Cs_2HgCl_4 Studied by the Maximum Entropy Method. Acta Cryst.* **B54**, 626–634.

Buchter, F.; Lodziana, Z.; Remhof, A.; Mauron, Ph.; Friedrichs, O.; Borgschulte, A.; Züttel, A.; Filinchuk, Y.; Palatinus, L. (2011). *Experimental charge density of $LiBD_4$ from maximum entropy method. Phys. Rev.* **B86**, 064107.

Cheary, R. W.; Coelho, A. A. (1992). *A fundamental parameters approach to X-ray line-profile fitting. J. Appl. Cryst.* **25**, 109–121.

Coelho, A.A. (2007). TOPAS. Version 4.1. Coelho Software, Brisbane, Australia.

Dinnebier, R. E.; Schneider, M.; van Smaalen, S.; Olbrich, F.; Behrens, U. (1999). *Disorder determined by high-resolution powder diffraction: structure of pentamethylcyclopentadienyllithium*. *Acta Cryst.* **B55**, 35–44.

Dinnebier, R.E.; Vensky, S.; Jansen, M.; Hanson, J.C. (2005). *Crystal Structures and Topological Aspects of the High-Temperature Phases and Decomposition Products of the Alkali-Metal Oxalates $M_2[C_2O_4]$ (M=K, Rb, Cs). Chem. Eur. J.* **11**, 1119–1129.

Fukuda, K.; Asaka, T.; Oyabu, M.; Urushihara, D.; Berghout, A.; Bechade, E.; Masson, O.; Julien, I.; Thomas, Ph. (2012). *Crystal Structure and Oxide-Ion Conductivity along c-Axis of Apatite-Type Lanthanum Silicate with Excess Oxide Ions. Chem. Mater.* **24**, 4623−4631.

Hofmann, A.; Netzel, J.; van Smaalen, S. (2007). *Accurate charge density of trialanine: a comparison of the multipole formalism and the maximum entropy method (MEM). Acta Cryst.* **B63**, 285–295.

Ikeda, T.; Izumi, F.; Kodaira, T.; Kamiyama, T. (1998). *Structural study of sodium-type zeolite LTA by combination of Rietveld and maximum-entropy methods. Chem. Mater.* **10**, 3996–4004.

Karpov, A.S.; Nuss, J.; Jansen, M.; Kazin, P.E.; Tretyakov, Yu.D. (2003). *Synthesis, crystal structure and properties of calcium and barium hydroxyapatites containing copper ions in hexagonal channels. Solid State Science.* **5**, 1277–1283.

Kazin, P.E.; Karpov, A.S.; Jansen, M. Pat.: EP020144515 from 28.06.2002, EP020195426 from 30.08.2002, WO 2004/002892 A1 from 08.01.2004.

Kazin, P.E.; Karpov, A.S.; Jansen, M.; Nuss, J.; Tretyakov, Yu.D. (2003). *Crystal structure and properties of strontium phosphate apatite with oxocuprate ions in hexagonal channels. Z. Anorg. Allg. Chem.* **629**, 344–352.

Kazin, P.E.; Gazizova, O.R.; Karpov, A.S.; Jansen, M.; Tretyakov, Yu.D. (2007). *Incorporation of 3d-metal ions in the hexagonal channels of the $Sr_5(PO_4)_3OH$ apatite. Solid State Science.* **9**, 82–87.

Kazin, P.E.; Zykin, M.A.; Tretyakov, Yu.D.; Jansen, M. (2008). *Synthesis and properties of colored copper-containing apatites of composition $Ca_5(PO_4)_3Cu_yO_{y+\delta}(OH)_{0.5-y-\delta}X_{0.5}$ (X = OH, F, Cl). Russ. J. Inorg. Chem.* **53**, 409–414.

Kazin, P.E.; Zykin, M.A.; Dinnebier, R.E.; Magdysyuk, O.V.; Tretyakov, Yu.D.; Jansen, M. (2012). *An Unprecedented Process of Peroxide Ion Formation and its Localization in the Crystal Structure of Strontium Peroxy-Hydroxyapatite $Sr_{10}(PO_4)_6(O2)_x(OH)_{2-2x}$. Z. Anorg. Allg. Chem.* **638**(6), 909–919.

Kazin, P.E.; Zykin, M.A.; Zubavichus, Y.V.; Magdysyuk, O.V.; Dinnebier, R.E.; Jansen, M. (2014). *Identification of the Chromophore in the Apatite Pigment $[Sr_{10}(PO_4)_6(Cu_xOH_{1-x-y})_2]$: Linear $OCuO^-$ Featuring a Resonance Raman Effect, an Extreme Magnetic Anisotropy, and Slow Spin Relaxation. Chem. Eur. J.* **20**, 165 – 178

Kitaura, R.; Kitagawa, S.; Kubota, Y.; Kobayashi, T. C.; Kindo, K.; Mita, Y.; Matsuo, A.; Kobayashi, M.; Chang, H.; Ozawa, T. C.; Suzuki, M.; Sakata, M.; Takata, M. (2002). *Formation of a one-dimensional array of oxygen in a microporous metal-organic solid. Science.* **298**, 2358–2361.

Le Bail, A.; Duroy, H.; Fourquet, J.L. (1988). *Ab-initio structure determination of $LiSbWO_6$ by x-ray powder diffraction. Mat. Res. Bull*. **23**, 447–452.

Matsuda, R.; Kitaura, R.; Kitagawa, S.; Kubota, Y.; Belosludov, R. V.; Kobayashi, T. C.; Sakamoto, H.; Chiba, T.; Takata, M.; Kawazoe, Y.; Mita, Y. (2005). *Highly controlled acetylene accommodation in a metal–organic microporous material*. *Nature.* **436**, 238–241.

Meindl, K.; Henn, J. (2008). *Foundations of residual-density analysis. Acta Cryst.* A**64**, 404–418.

Mondal, S.; Prathapa, S.J.; van Smaalen, S. (2012). *Experimental dynamic electron densities of multipole models at different temperatures. Acta Cryst.* A**68**, 568–581.

Palatinus, L.; van Smaalen, S. (2002), *The Generalized F-constraint in the Maximum Entropy Method: a study on simulated data, Acta Crystallogr.* A**58**, 559–567.

Palatinus, L.; van Smaalen, S. (2005). *The prior-derived F constraints in the maximum entropy method. Acta Cryst.* A**61**, 363–372.

Palatinus, L.; Prathapa, S.J.; van Smaalen, S. (2012). *EDMA: a computer program for topological analysis of discrete electron densities. J. Appl. Cryst.* **45**, 575–580.

Papoular, R. J.; Cox, D. E. (1995). *Model-free search for extra-framework cations in zeolites using powder diffraction. Europhys. Lett.* **32**, 337 – 342.

Parker, J.E.; Thompson, S.P.; Cobb, T.M.; Yuan, F.; Potter, J.; Lennie, A.R.; Alexander, S.; Tighe, C.J.; Darr, J.A.; Cockcroft, J.C.; Tang, C.C. (2011). *High-throughput powder diffraction on beamline I11 at Diamond. J. Appl. Cryst.* **44**, 102 – 110.

Posse, J.M.; Grzechnik, A.; Friese, K. (2009). *Ternary fluorides $BaMF_4$ (M = Zn, Mg and Mn) at low-temperatures. Acta Cryst.* **B65**, 576–586

Rietveld, H. M. (1967). *Line profiles of neutron powder-diffraction peaks for structure refinement. Acta Cryst.* **22**, 151–152.

Rietveld, H. M. (1969). A Profile Refinement Method for Nuclear and Magnetic Structures. J. Appl. Cryst. **2**, 65–71.

Rodriguez-Lorenzo, L.M.; Hart, J.N.; Gross, K.A. (2003). *Structural and chemical analysis of well-crystallized hydroxyfluorapatites. J. Phys. Chem.* **B107**, 8316 – 8320.

Roversi, P.; Irwin, J.J.; Bricogne, G. (1998). *Accurate Charge-Density Studies as an Extension of Bayesian Crystal Structure Determination. Acta Cryst.* A**54**, 971–996.

Sakata, M.; Sato, M. (1990). Accurate structure analysis by the maximum-entropy method. *Acta Cryst.* **A46**, 263 – 270.

Sakata, M.; Mori, R.; Kumazawa, S.; Takata, M.; Toraya, H. (1990). *Electron-Density Distribution from X-ray Powder Data by Use of Profile Fits and the Maximum-Entropy Method. J. Appl. Cryst.* **23**, 526–534.

Samy, A.; Dinnebier, R. E.; van Smaalen, S.; Jansen, M. (2010). *Maximum entropy method and charge flipping, a powerful combination to visualize the true nature of structural disorder from in situ X-ray powder diffraction data. Acta Cryst.* **B66**, 184 – 195.

Shannon, C.E. (1948a). *A Mathematical Theory of Communication. Bell System Technical Journal.* **27**, 379–423.

Shannon, C.E. (1948b). *A Mathematical Theory of Communication. Bell System Technical Journal.* **27**, 623–656.

van Smaalen, S.; Palatinus, L.; Schneider, M. (2003). *The maximum entropy method in superspace. Acta Cryst.* **A59**, 459 – 469.

Sudarsanan, K.; Young, R.A. (1972). Structure of strontium hydroxide phosphate, $Sr_5(PO_4)_3OH$. *Acta Cryst.* **B28**, 3668 – 3670.

Takata, M. (2008). *The MEM/Rietveld method with nano-applications – accurate charge-density studies of nano-structured materials by synchrotron-radiation powder diffraction. Acta Cryst.* A**64**, 232–245.

Thompson, S.P.; Parker, J.E.; Marchal, J.; Potter, J.; Birt, A.; Yuan, F.; Fearn, R.D.; Lennie, A.R.; Street, S.R.; Tang, C.C. (2011). *Fast X-ray powder diffraction on I11 at Diamond. J. Synchrotron Rad.* **18**, 637–648.

Thompson, S.P.; Parker, J.E.; Potter, J.; Hill, T.P.; Birt, A.; Cobb, T.M.; Yuan, F.; Tang, C.C. (2009). *Beamline I11 at Diamond: A new instrument for high resolution powder Diffraction. Rev. Sci. Instrum.* **80**, 075107.

de Vries, R. Y.; Briels, W. J.; Feil, D. (1994). *Novel treatment of the experimental data in the application of the maximum-entropy method to the determination of the electron-density distribution from X-ray experiments. Acta Cryst.* **A50**, 383–391.

White, T.J.; ZhiLi, D. (2003). *Structural derivation and crystal chemistry of apatites. Acta Cryst.* **B59**, 1–16.

Wopenka, B.; Pasteris, J.D. (2005). *A mineralogical perspective on the apatite in bone. Materials Science and Engineering.* **C25**, 131–143.

Zheludev, A.; Papoular, R.J.; Ressouche, E.; Schweizer, J. (1995). *A Non-Uniform Reference Model for Maximum-Entropy Density Reconstruction from Diffraction Data. Acta Cryst.* A**51**, 450**–**455.

Chapter 3

Application of parametric refinement and group-theoretical analysis to structural phase transitions

3.1. Introduction

Landau theory for structural phase transitions (Landau & Lifshitz, 1959) was widely and very successfully used for the description of ferroelastic ("translationengleich") and co-elastic ("klassengleich") phase transition in crystalline solids (reviewed by Cowley, 1980; Bruce & Cowley, 1981; Wadhawan, 1982; Salje, 1990, 1991a, 1991b, 1992, 1993; Dove, 1997; Carpenter *et al*., 1998a; Carpenter & Salje, 1998b). A formal basis for the analysis of structural distortions in crystals associated with a phase transition is provided by Landau theory through introduction of the order parameter. The order parameter is created by breaking the symmetry and quantifies how far the low-symmetry structure deviates from the high-symmetry form. The structural order parameter originates from some structural features (*i.e.* polyhedral tilting). The order parameter is set to *0* for the high-symmetry phase and typically normalized to a maximum of *1* for the low-symmetry phase. The order parameter breaks a particular symmetry which exists in the high-symmetry form but does not exist in the low-symmetry form. Thus the transformation behavior of the order parameter is given by the symmetry-breaking irreducible representation (irrep) of the high-symmetry space group.

The distortion mode analysis can be easy combined with Landau theory for structural phase transitions, because both distortion mode analysis and Landau theory consider the low-symmetry structure as a distorted version of the high-symmetry structure (real or pseudo-symmetrical). For distortion modes analysis, the group-subgroup relation must exist between low- and high-symmetry structures, and the structural distortion of the low-symmetry structure is analyzed in terms of the distortion of parent high-symmetry structure. Structural distortion can be displacive distortion, order-disorder distortion, or their combination. Distortion modes are associated with different irreducible representation (irrep) of the high-symmetry space group, have different origin and amplitude. Analysis of the origin and contribution of different distortion modes is a subject of the symmetry-mode analysis (Perez-Mato *et al.*, 1981, 1986; Manes *et al.*, 1982; Hatch *et al.*, 1990; Stokes *et al.*, 1991b; Aroyo & Perez-Mato, 1998).

In this work, the free internet-based computer programs ISODISTORT (Campbell *et al.*, 2006) and AMPLIMODES (Orobengoa *et al.*, 2009) were used for the symmetry-mode analysis. Program AMPLIMODES allows analyzing of the structural distortion without consideration of the strain and without implementation of the distortion modes into refinement process of experimental data. Program ISODISTORT provide the possibility for analyzing structural distortion and strain, and also the implementation of all distortion modes into refinement process of experimental data. Atomic distortion modes are given in terms of atomic displacement relatively to the high-symmetry structure.

Usually at least one irrep is a symmetry-breaking irrep and is responsible for the lowering of the symmetry; the corresponding distortion modes are symmetry-breaking or primary distortion modes. Distortion modes corresponding to other irreps are non-symmetry-breaking or secondary distortion modes.

Any real structural phase transition in crystals is accompanied by lattice relaxations, which are usually analyzed in terms of symmetry-adapted strains. Such strains can provide detailed insights into the nature and mechanisms of the structural phase transition. The strain interacts with the order parameter, and the coupling of the strain with order parameter determines the structural transformation in the system with a single order parameter (reviewed in Salje, 1991a, 1993; Carpenter *et al*., 1998a, Carpenter & Salje, 1998b; Carpenter, 2000). Also strain is a dominant mechanism in coupling between different orders parameters in systems with more than one order parameter resulting from consecutive phase transitions. Such coupling might occur between cation ordering, electronic ordering, magnetic ordering, octahedral tilting, etc., (reviewed in Salje, 1991a, 1992, 1993; Salje *et al*., 2005; Salje & Devarajan, 1986; Carpenter & Salje, 1998b; Carpenter *et al*., 1998a; Carpenter & Howard, 2009a, 2009b; Stokes & Hatch, 1991a).

The correlation between the changes in the crystal structure during the phase transition and lattice strain leads to symmetry constraints on possible coupling mechanisms. The group-theoretical approach to phase transitions allows the prediction of possible coupling mechanisms between strain and order parameter (Salje, 1991a, 1993; Carpenter & Salje, 1998b; Carpenter *et al*., 1998a; Carpenter, 2000) or between different order parameters via common strain (Salje & Devarajan, 1986; Salje, 1985a, 1991a, 1993; Salje *et al*., 1985b; Stokes & Hatch, 1991a; Carpenter & Howard, 2009a, 2009b). Thus, possible problems in the analysis of structural phase

transitions connected with poor or insufficient experimental data can be avoided and a correct description of the phase transition mechanism can be derived.

Parametric refinement is a relatively new refinement technique suggested by Stinton & Evans (2007). The basic idea of parametric refinement is a simultaneous refinement of the whole set of multiple experimental data. In contrast, the traditional sequential refinement is based on independent refinements of each powder pattern. The analysis of results of sequential refinements is done by application of mathematical models to the set of parameters received from all individual sequential refinements. The parametric refinement allows the application of a realistic physical model during refinement. Thus, testing of different models describing the investigated physical process can be performed with increased accuracy. The parametric refinement was successfully used for improving the precession of cell parameter determination (Stinton & Evans 2007, Halasz *et al.*, 2010; Müller *et al.*, 2010, 2011), refining non-crystallographic parameters (Stinton & Evans 2007), and analysis of the kinetics of reactions (Stinton & Evans 2007, Müller *et al.*, 2009).

3.2. Basics of application of parametric refinement and group-theoretical analysis to structural phase transitions

3.2.1. Landau theory for structural phase transitions

Landau assumed that the Gibbs free energy G can be described in a Taylor power series for small values of Q (Landau potential), (Landau & Lifshitz, 1959). Nevertheless, the polynomial form of G was found to be a good approximation over an extended temperature interval and for large values of Q:

$$G = G_0 + A_0Q + AQ^2 + CQ^3 + BQ^4 + \ldots \quad (1)$$

where G_0 is a non-singular part of the Gibbs free energy and A_0, A, B, and C are being smooth functions of temperature and pressure. The temperature dependence of the coefficients A_0 and B is usually neglected.

The Gibbs free energy is by definition zero in the high-symmetry phase (ignoring short-range ordering and fluctuations) and varies as a direct function of Q only in the low-symmetry phase. The equilibrium condition $\partial G/\partial Q = 0$ has a trivial solution $G(T) = 0$ for the high-temperature phase. Different assumptions on the parameters of the polynomial form of G can be

made. In case of the so-called 2-4 potential, corresponding to a classical second-order phase transition:

$$G = G_0 + atQ^2 + BQ^4, \tag{2}$$

with $t = \frac{T - Tc}{Tc}$, Tc – critical temperature of phase transition; T – given temperature of the low-symmetry phase; a and B – constants, $a > 0$ and $B > 0$. For the equilibrium condition $\partial G/\partial Q = 0$ it follows immediately that

$$Q = \sqrt{\frac{a}{2B}} \left|\frac{T - Tc}{Tc}\right|^{1/2} = \sqrt{\frac{a}{2B}}\,|t|^{1/2} \quad \text{for } T < Tc \tag{3}$$

and $Q = 0$ for $T > Tc$.

Including the Q^6-term into the 2-4 potential leads to

$$G = G_0 + AQ^2 + BQ^4 + DQ^6, (D > 0) \tag{4}$$

and does not introduce any new effects in case of $B > 0$. But for $B \leq 0$ the character of the phase transition is changed to tricritical ($B = 0$) or weak first-order ($B < 0$). In case of the so-called 2-6 potential ($B = 0$):

$$G = G_0 + atQ^2 + DQ^6 \tag{5}$$

For the equilibrium condition $\partial G/\partial Q = 0$ it follows immediately that

$$Q = \sqrt[4]{\frac{a|t|}{2D}} = \sqrt[4]{\frac{a}{2D}}\,|t|^{1/4} = \sqrt[4]{\frac{a}{2D}} \left|\frac{T - Tc}{Tc}\right|^{1/4} \quad \text{for } T < Tc \tag{6}$$

and $Q = 0$ for $T > Tc$.

A so-called weak first-order phase transition for non-ferroelastic materials can also be achieved by including a cubic Q^3-term into the 2-4 potential (Cowley, 1980):

$$G = G_0 + atQ^2 + btQ^3 + BQ^4 \tag{7}$$

In this case:

$$Q = -\frac{3b}{8B}t \pm \frac{1}{8B}\sqrt{9b^2t^2 - 32aB|t|} \tag{8}$$

In general, the phase transition can be characterized by the so-called critical exponent β, where $\beta = 1/2$ for a classical second-order phase transition, $\beta = 1/4$ for a tricritical phase transition and $1/4 < \beta < 1/2$ for a phase transition which can be described as intermediate between pure classical second-order phase transition and tricritical phase transition:

$$Q = \left(\frac{a}{2R}\right)^{\beta} |t|^{\beta} = \left(\frac{a}{2R}\right)^{\beta} \left|\frac{T - Tc}{Tc}\right|^{\beta} = E\, t^{\beta} \quad \text{for } T < Tc \tag{9}$$

To take into account the saturation of the order parameter at low-temperatures (usually less than 150 K), the Landau free-energy expansion in the following form can be used (Salje *et al*., 1991c; Perez-Mato & Salje, 2000, 2001):

$$G = G_0 + \frac{ATs}{2}\left(\coth\left(\frac{Ts}{T}\right) - \coth\left(\frac{Ts}{Tc}\right)\right)Q^2 + BQ^4 + DQ^6 \tag{10}$$

with the saturation temperature *Ts* and the critical temperature *Tc*.

3.2.2. Coupling mechanisms between symmetry-adapted strain and order parameter

The Landau model can be extended to include strain and to analyze it from a macroscopic (thermodynamic) point of view (Salje, 1991a, 1993; Carpenter *et al*., 1998b; Carpenter & Salje, 1998a; Carpenter, 2000).

For a structural phase transition, in which the strain e arises by coupling with a structural order parameter Q, the Gibbs free energy of the low-symmetry phase with respect to the high-symmetry phase (at the same conditions of temperature, pressure, etc.) can be expressed as:

$$G = G_Q + G_{e,Q} + G_e, \tag{11}$$

where G_Q describes the change in free energy due to the effect of Q alone, $G_{e,Q}$ describes the coupling energy due to the interaction between spontaneous strain e and order parameter Q, and G_e describes the elastic energy from the relaxation of the unit cell (Salje, 1993).

A substantial part of the driving force for the phase transition can be associated with the spontaneous strain due to the coupling between Q and e (eq. 11). Coupling between Q and e is characterized by a long correlation length in the material and the order of the phase transition depends on the strength of coupling between order parameter and strain (Salje, 1993).

The group-theoretical approach allows the prediction of possible relations between strain and order parameter and was described in detail by (Carpenter *et al*., 1998a; Carpenter & Salje, 1998b; Carpenter, 2000). Each combination of strain and order parameter for the Gibbs free energy in eq. 11 must obey the symmetry rules and cannot be added arbitrarily. The formal requirement is that each term must be invariant with respect to all symmetry operations of the space group of the high-symmetry space group, or, in other words, the product of the related irreducible representations must contain the identity representation. Thus, every term should

transform as the identity representation of the space group of the high-symmetry phase. The product of any two components which individually transform as the same representation is allowed, since the square of an irreducible representation is always equal to the identity representation.

In the following, we will consider on a common basis the different coupling mechanisms between strain and order parameter. The determination of the correct coupling mechanisms is important for the correct description of a phase transition.

1) Bilinear coupling between symmetry-adapted strain *e* and order parameter *Q*.

Bilinear coupling between symmetry-adapted strain *e* and order parameter *Q* suggests that spontaneous strain and order parameter are simply proportional to each other. It is allowed only for a strain which transforms according to a symmetry-breaking representation (=symmetry-breaking strain), because the order parameter transforms according to a symmetry-breaking representation.

In case of bilinear coupling *eQ* between strain and order parameter a Landau free-energy expansion for a second-order phase transition will be:

$$G = G_0 + atQ^2 + BQ^4 - deQ + \frac{f}{2}e^2 \qquad (12a)$$

where *d* and *f* are constants with $d > 0$ and $f > 0$.

We also can write a Landau free-energy expansion for a tricritical phase transition ($B = 0$):

$$G = G_0 + atQ^2 + DQ^6 - deQ + \frac{f}{2}e^2 \qquad (12b)$$

Or for the general case:

$$G = G_0 + atQ^2 + BQ^4 + DQ^6 - deQ + \frac{f}{2}e^2 \qquad (13)$$

The term *eQ* in eq. 13 is only allowed if the term Q^2 is also present and the strain *e* transforms as a symmetry-breaking representation (Carpenter *et al.*, 1998a; Salje, 1991a). In this case, the term *eQ* transforms as the identity representation. A bilinear coupling is allowed only for some (but not all) transitions associated with the center of the Brillouin zone $\vec{k}$ = (0, 0, 0), and the transition should be equitranslational for which the active representation has an associated basis function with second-rank tensor properties (proper ferroelastic transition),

(Carpenter *et al*., 1998a). It is not allowed for all zone-boundary transitions (Carpenter *et al*., 1998a).

Application of the equilibrium condition for the strain to eq. 13 and $0.25 \leq \beta \leq 0.5$ results in:

$$\frac{\partial G}{\partial e} = -dQ + fe = 0$$

$$e = \frac{d}{f}Q = \frac{d}{f}\left(\frac{a}{2R}\right)^{\beta}\left|\frac{T-Tc}{Tc}\right|^{\beta} = E\left|\frac{T-Tc}{Tc}\right|^{\beta} = E\,|t|^{\beta} \qquad \text{for } T < Tc \qquad (14)$$

where R is a coefficient depending on both coefficients B and D in the Landau free-energy expansion (eq. 13).

Bilinear coupling between strain e and order parameter Q suggests that $e \sim Q \sim |t|^{\beta}$. For a second-order phase transition $\beta = ½$ and $e^2 \sim |t|$, for a tricritical phase transition $\beta = ¼$ and $e^4 \sim |t|$. The graphical imaging of the strain as a function of $t = \frac{T-Tc}{Tc}$, $e(t)$, or as a function of T, $e(T)$, is widely used for the determination of the character of the phase transition, although this method can be ambiguous. To receive precise results it is necessary to fit the experimental data by an analytical function $e(t)$.

2) Linear-quadratic coupling between symmetry-adapted strain e and order parameter Q.

Linear-quadratic coupling between symmetry-adapted strain e and order parameter Q is different for symmetry-adapted strains transformed as a symmetry-breaking representation or as a non-symmetry-breaking representation.

If the strain transforms according to a non-symmetry-breaking representation (= non-symmetry-breaking strain), a term eQ^2 is always allowed because Q^2 transforms according to a non-symmetry-breaking representation. The term eQ^2 is allowed to be present in a Landau free-energy expansion only if the term Q^2 is also present (Carpenter *et al.*, 1998a; Salje, 1991a).

In general for $0.25 \leq \beta \leq 0.5$:

$$e = \frac{d}{f}Q^2 = \frac{d}{f}\left(\frac{a}{2R}\right)^{2\beta}\left|\frac{T-Tc}{Tc}\right|^{2\beta} = E\left|\frac{T-Tc}{Tc}\right|^{2\beta} = E\,|t|^{2\beta} \qquad \text{for } T < Tc \qquad (15)$$

where d, f, R, E – constants.

Linear-quadratic coupling between strain e and order parameter Q suggests $e \sim Q^2 \sim |t|^{2\beta}$. For the second-order phase transition $\beta = 1/2$ and $e \sim |t|$; for the tricritical phase transitions $\beta = 1/4$ and $e^2 \sim |t|$.

If strain transforms as an active representation (=symmetry-breaking strain), a term eQ^2 is allowed only for transitions, for which a term Q^3 is present in the free energy (corresponding to a first-order phase transition), (Carpenter *et al.*, 1998a; Salje, 1991a).

3) Linear-cubic coupling between symmetry-adapted strain *e* and order parameter *Q*.

Linear-cubic coupling between symmetry-adapted strain *e* and order parameter *Q* is different for symmetry-adapted strains transformed according to a symmetry-breaking representation or according to a non-symmetry-breaking representation.

If the strain transforms as a symmetry-breaking representation (=symmetry-breaking strain), a term eQ^3 is allowed to be present in the Landau expansion for free energy only when a term Q^4 is also present in the equation for free energy (Carpenter *et al.*, 1998a; Salje, 1991a).

In general for ¼ < $\beta \leq$ ½:

$$e = \frac{d}{f}Q^3 = \frac{d}{f}\left(\frac{a}{2R}\right)^{3\beta}\left|\frac{T-Tc}{Tc}\right|^{3\beta} = E\left|\frac{T-Tc}{Tc}\right|^{3\beta} = E\,|t|^{3\beta} \quad \text{for } T < Tc \qquad (16)$$

If the strain transforms according to a non-symmetry-breaking representation (=non-symmetry-breaking strain), a term eQ^3 is allowed only when the term Q^3 is also present in the equation for free energy. Therefore, the corresponding phase transition should be a first-order phase transition (Carpenter *et al.*, 1998a; Salje, 1991a).

4) Biquadratic coupling between symmetry-adapted strain *e* and order parameter *Q*.

Biquadratic coupling e^2Q^2 between symmetry-adapted strain *e* and order parameter *Q* is always allowed by symmetry and suitable for strains transformed according to a symmetry-breaking representation (=symmetry-breaking strain) and according to a non-symmetry-breaking representation (=non-symmetry-breaking strain), since e^2 and Q^2 are always transformed according to a non-symmetry-breaking representation.

The general solution for ¼ < $\beta \leq$ ½:

$$e = \sqrt{\frac{d}{f}}Q = \sqrt{\frac{d}{f}}\left(\frac{a}{2R}\right)^{\beta}\left|\frac{T-Tc}{Tc}\right|^{\beta} = E\left|\frac{T-Tc}{Tc}\right|^{\beta} = E\,|t|^{\beta} \quad \text{for } T < Tc \text{ and } E > 0 \qquad (17)$$

Formally eq. 17 for biquadratic coupling between symmetry-adapted strain *e* and order parameter *Q* coincides with eq. 14 for bilinear coupling, so, without explicit temperature dependence of strain, the biquadratic coupling is similar to bilinear coupling. The bilinear coupling is valid only for symmetry-adapted strain transformed according to a symmetry-

breaking representation and should be given preference if there are no other reasons to consider biquadratic coupling.

5) Biquadratic coupling between symmetry-adapted strain *e* and order parameter *Q* with explicit temperature dependence of strain.

It is possible to introduce a physically meaningful explicit temperature dependence of symmetry-adapted strain in the case of biquadratic coupling between strain and displacive order parameter. For the biquadratic coupling a Landau expansion for free energy can be written as:

$$G = G_0 + atQ^2 + BQ^4 - \frac{d}{2}e^2Q^2 + \frac{f}{4}e^4 \tag{18}$$

Or in alternate form:

$$G = G_0 + atQ^2 + B'Q^4 + \left(\frac{M}{4}Q^4 - \frac{M}{2}e^2Q^2 + \frac{M}{4}e^4\right) \tag{19}$$

where the constant *M* was chosen for simplification, allowing eq. 18 to be of the form

$$G = \widetilde{G}_0 + \frac{M}{4}\left(Q^2 - e^2\right)^2 \tag{20}$$

where $\widetilde{G}_0 = G_0 + atQ^2 + B'Q^4$

Under the assumption that strain is an explicit function of temperature and changes its value slowly with changing temperature, the term $\left(\frac{\partial e}{\partial t}\right)^2$ needs to be added to eq. 20 for free energy.

$$\widetilde{G} = \widetilde{G}_0 + \frac{M}{4}\left(Q^2 - e^2\right)^2 - \frac{K}{4}\left(\frac{\partial e}{\partial t}\right)^2 \tag{21}$$

where *K* is a constant.

Eq. 21 is valid for strain transforming as a symmetry-breaking representation as well as for strain transforming as an identity representation, because $\left(\frac{\partial e}{\partial t}\right)^2$ necessarily transforms as an identity representation.

Therefore, the Gibbs free energy in the range of the explicit temperature dependence of strain is

$$\Delta G = \frac{M}{4}\left(Q^2 - e^2\right)^2 - \frac{K}{4}\left(\frac{\partial e}{\partial t}\right)^2 \tag{22}$$

Eq. 22 has a minimum when

$$\frac{M}{4}\left(Q^2 - e^2\right)^2 = \frac{K}{4}\left(\frac{\partial e}{\partial t}\right)^2 \quad (23)$$

or

$$\frac{\partial e}{\partial t} = \sqrt{\frac{M}{K}}\left(Q^2 - e^2\right) \quad (24)$$

And after integration (using the integral $\int \frac{1}{1+x^2} = \tanh(x)$):

$$e = |Q| \tanh\left(|tQ|\sqrt{\frac{M}{K}}\right) = |Q| \tanh\left(A|tQ|\right) \quad (25)$$

When the displacive order parameter is saturated (at temperatures far from the phase transition), the strain is not explicitly temperature dependent and is close to its equilibrium value.

In eq. 25 one assumes explicit temperature dependence of the strain, not of the coupling coefficient. The same functional behaviour is expected for the temperature dependence of the coupling coefficient if the coefficient is large near the phase transition but then becomes smaller. As a result, a strong coupling near the phase transition reducing to much weaker coupling at low-temperatures could have exactly this effect.

To the best of our knowledge, only coupling mechanisms without explicit temperature-dependence of strain were applied to experimental X-ray and neutron diffraction data of structural phase transitions. Although some notes on a possible temperature dependence of strain (or coupling coefficient between strain and order parameter) can be found in several papers (Carpenter & Salje, 1998b; Becerro *et al*., 2002; Glazer *et al.*, 2010), theoretical calculations were not performed.

6) Higher-order coupling between symmetry-adapted strain *e* and order parameter *Q* is also possible but rare and therefore will not be considered here.

3.3. Parameterization of the coupling between strain and order parameter for LuF[SeO3]

3.3.1. Background information

The synthesis of $LuF[SeO_3]$ was described previously (Lipp & Schleid, 2007, 2009; Lipp *et al.*, 2013).

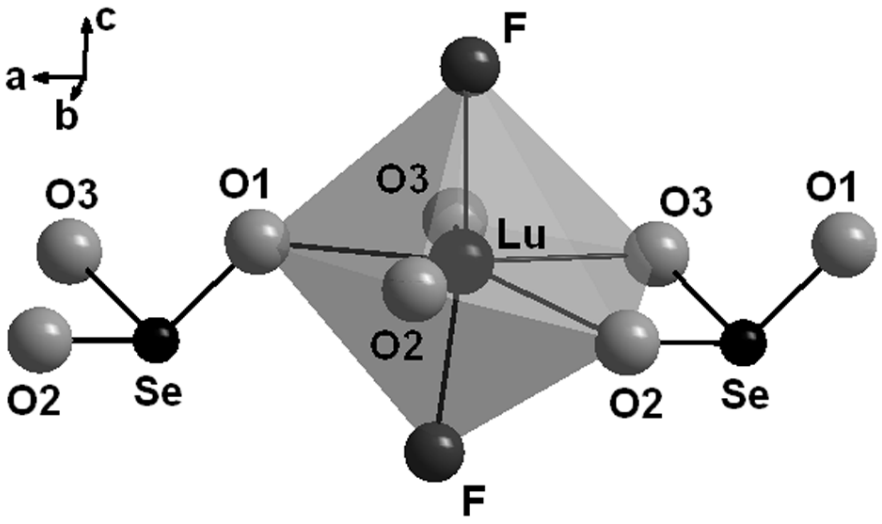

Figure 3.1. Structural fragment of $LuF[SeO_3]$, showing a LuF_2O_5 polyhedron at ambient conditions (Lipp *et al.*, 2013).

$LuF[SeO_3]$ (Fig. 3.1) exhibits two confirmed phase transitions: a low-temperature phase transition ($P\bar{1}$ - $P2_1/c$) was found by single crystal diffraction with a transition temperature on cooling below -41°C by DSC, below -75°C by powder diffraction (Lipp *et al.*, 2013), and below -60°C on cooling and at 10°C on heating by Raman spectroscopy. It is of first-order and accompanied by a change of the coordination number of the Se atom and a huge drop in volume (~16 %). Complementary investigations using laboratory powder diffraction showed that the phase transition either occurs only for part of the sample or not at all, which is attributed to kinetic hindrance (Lipp *et al.*, 2013). A high-temperature phase transition ($P\bar{1}$ - $P2_1/m$) was detected by DSC measurements at a transition temperature of 109°C and the high-temperature crystal structure was solved from single crystal data (Lipp *et al.*, 2013). Using synchrotron X-ray powder diffraction, a strong dependence of the transition temperature on the thermal history of the sample was found, leading to an increase of the phase transition temperature when the sample was previously cooled down to -173°C in absence of the low-temperature phase. This behavior is attributed to strain-order parameter coupling. To investigate this effect further, the high-temperature phase transition of $LuF[SeO_3]$ was analyzed in detail by comparing different models for the strain-order parameter coupling using parametric refinement techniques (Stinton & Evans, 2007).

3.3.2. X-ray powder diffraction investigation of the high-temperature phase transition of $LuF[SeO_3]$

Powder diffraction data of $LuF[SeO_3]$ were collected at the high-resolution powder diffractometer I11 at Diamond, Great Britain (Parker *et al.*, 2011; Thompson *et al.*, 2009, 2011). The wavelength was determined to be 0.8264(3) Å from a silicon standard. The sample was contained in a sealed 0.1-mm quartz capillary and was rotated around θ in order to improve randomization of the crystallites. The diffracted beam was detected with a series of PSD(Mythen2)-detectors with 90° aperture (Schmitt *et al.*, 2003; Bergamaschi *et al.*, 2010). The sample was first cooled from room-temperature (RT) down to -173°C and then was heated up to RT with 2 °/min. Powder patterns were continuously collected for 12 seconds/frame. The sample was then kept at RT around 12 hours to reach equilibrium conditions (which explains the small offset of the lattice parameters between runs 2 and 3 of Figs. 3.3 and 3.4) before it was heated up to 300°C and consecutively cooled down to RT with 3 °/min. Powder patterns were collected continuously for 14 seconds/frame.

The program TOPAS 4.1 (Coelho, 2007) was used for refinement according to the Rietveld (Rietveld, 1967, 1969) and Le Bail (Le Bail *et al.*, 1988) methods. Cut-outs of two-dimensional projections (so called simulated heating/cooling-Guinier patterns) of the observed scattered X-ray intensity of $LuF[SeO_3]$ as a function of diffraction angle (*x*-axis) and temperature (*y*-axis) are shown in Fig. 3.2.

In the present work, precise values of the strain components for the high-temperature phase transition of $LuF[SeO_3]$ were determined directly from the measured lattice parameters by Le Bail fits of the experimental X-ray powder diffraction data. The program ISODISTORT (Campbell *et al.*, 2006) was used for the distortion mode decomposition of the high-symmetry phase in $P2_1/m$ into the low-symmetry phase $P\bar{1}$. The strain components *e(t)* received in this way were corrected for thermal expansion. Typical input files for the sequential and parametric (Stinton & Evans, 2007; Campbell *et al.*, 2007; Halasz *et al.*, 2010) Le Bail fits and Rietveld refinements have been deposited as Appendix 3.

The essential feature of the X-ray diffraction experiment under investigation is the initial cooling of the $LuF[SeO_3]$ sample down to -173°C, which considerably changed the thermal behavior (Fig. 3.2). The structural changes are primarily determined by deformation and rotation of the LuF_2O_5-polyhedra around the *c*-axis (Fig. 3.1). The expected first-order phase transition

$P\bar{1}$ –> $P2_1/c$ on cooling was kinetically hindered (Lipp *et al.*, 2013), thus cooling down to -173°C created extensive volume strain in the triclinic structure of $LuF[SeO_3]$. During subsequent heating of this sample from RT up to 300°C, a second-order phase transition is observed at 120°C, while during the consecutive cooling down to RT a tricritical phase transition is observed at 98°C (Fig. 3.2). Detailed analysis of both phase transitions revealed that they are determined by different coupling mechanisms between strain and displacive order parameter depending on the previous thermal treatment of the material.

In the course of the investigation of the phase transitions in $LuF[SeO_3]$ using high-resolution *in situ* synchrotron X-ray diffraction measurements in dependence on temperature, an extreme effect of such a coupling was detected being the motivation for the present work.

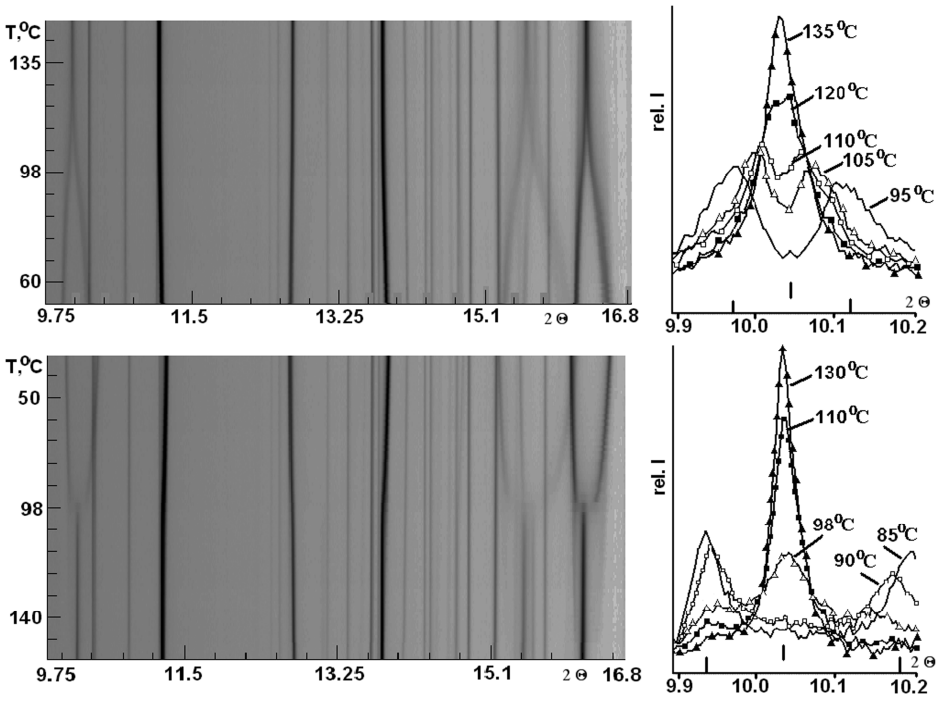

Figure 3.2. Left: two-dimensional projection (simulated heating/cooling-Guinier pattern, prepared using Powder3D (Hinrichsen *et al.*, 2006)) of the observed scattered X-ray intensity for $LuF[SeO_3]$ as a function of diffraction angle (x-axis) and temperature (*y*-axis), top – on heating, bottom – on cooling. Right: splitting of the (210) peak during the phase transition in $LuF[SeO_3]$ from monoclinic to triclinic symmetry.

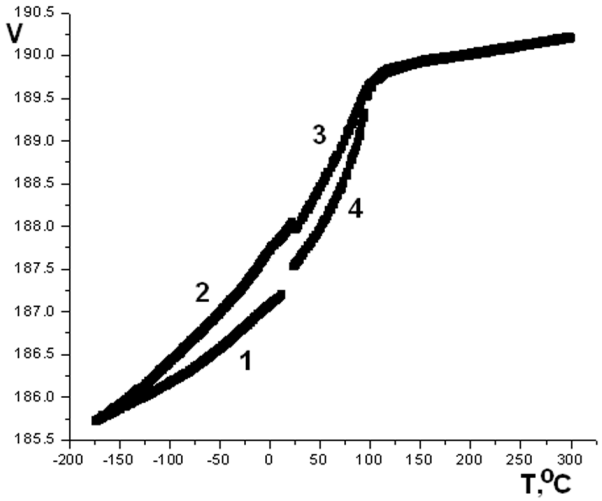

Figure 3.3. Temperature dependence of the unit cell volume of $LuF[SeO_3]$. Numbers show the sequence of cooling and heating: 1 – cooling from RT to -173°C, 2 – heating from -173°C to RT, 3 – heating from RT to 300°C, 4 – cooling from 300°C to RT. (The offset of the lattice parameters between runs 2 and 3 is explained in the text).

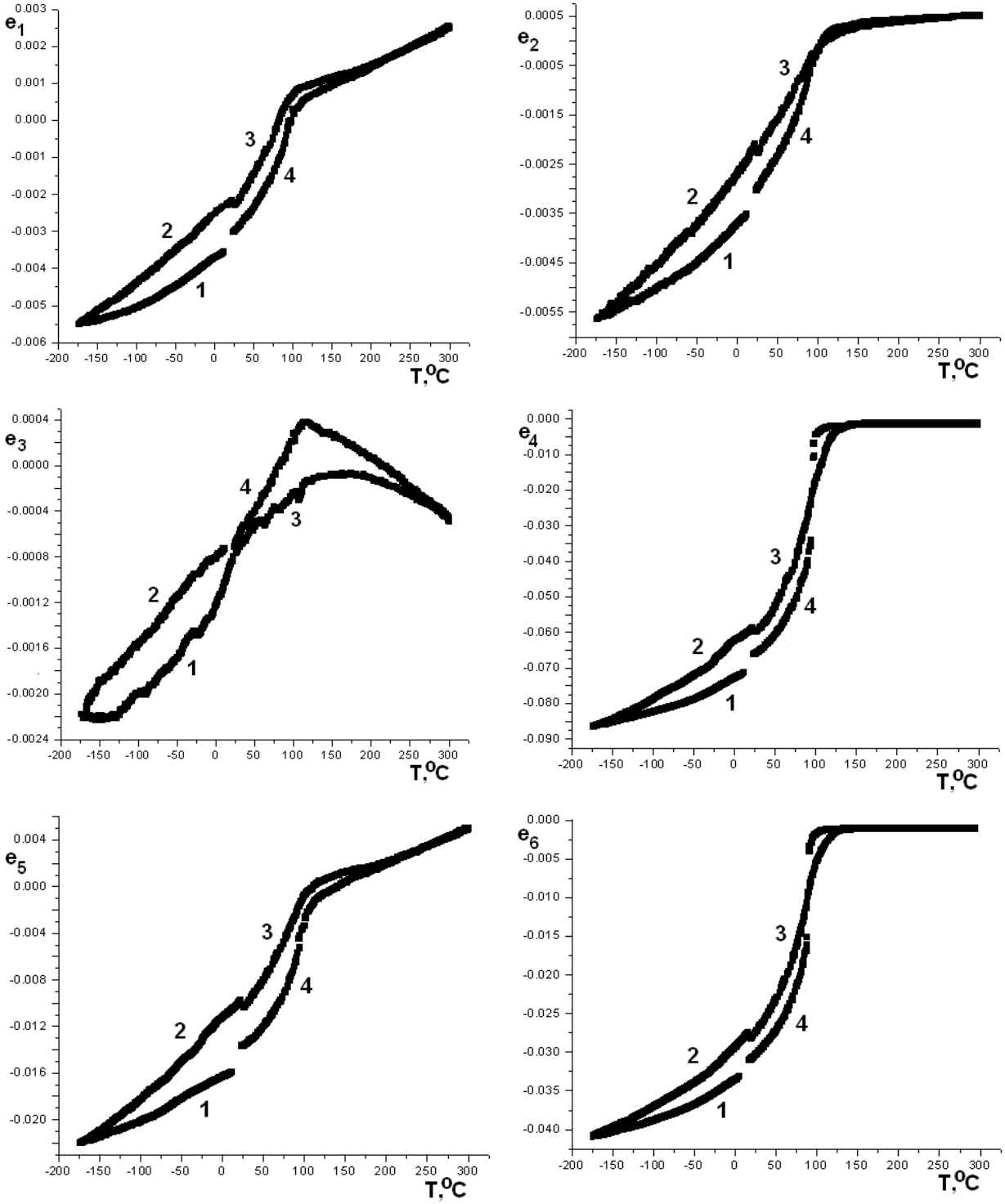

Figure 3.4. Temperature dependence of symmetry-adapted strains for $LuF[SeO_3]$. Numbers show the sequence of cooling and heating: 1 – cooling from RT to -173°C, 2 – heating from -173°C to RT, 3 – heating from RT to 300°C, 4 – cooling from 300°C to RT.

3.3.3. Distortion modes analysis of the coupling mechanism between strain and displacive order parameter for the phase transition $P2_1/m$–>$P\bar{1}$ of LuF[SeO_3]

Determination of possible coupling mechanisms between symmetry-adapted strain and displacive order parameter requires the determination of strains which have properties of the symmetry-breaking irreducible representation and of the non-symmetry-breaking representation. According to Stokes & Hatch, (1988) the phase transition $P2_1/m$ –> $P\bar{1}$ is associated with $\vec{k}$ = (0, 0, 0), and the displacive order parameter is one-dimensional. Two irreducible representations correspond to this phase transition: GM1+, (non-symmetry-breaking) and GM2+, (symmetry-breaking). The phase transition is allowed to be continuous by both, Landau theory and renormalization-group theory.

The distortion mode decomposition of the high-symmetry structure in $P2_1/m$ space group into the low-symmetry structure in $P\bar{1}$ space group revealed two sets of structural distortion modes: one set transforming according to non-symmetry-breaking GM1+ irrep and related to the thermal expansion (a_1, a_2, a_4, a_5, a_7, a_8, a_{10}, a_{11}, a_{13}, a_{14}, a_{15}), and another set transforming according to symmetry-breaking GM2+ irrep (a_3, a_6, a_9, a_{12}, a_{16}, a_{17}, a_{18}) and related to the lowering of the symmetry from monoclinic to triclinic primarily due to the deformation and rotation of the Lu-polyhedron around the *c*-axis. All distortion modes exhibit very small amplitudes. Since distortion modes a_3, a_6, a_9, a_{12}, a_{16}, a_{17}, and a_{18} belong to the same symmetry-breaking GM2+ irrep, they are linearly dependent and thus reduced to one normalized displacive structural order parameter Q, reflecting the cooperative structural changes due to symmetry-breaking distortion modes. Therefore, the displacive order parameter Q is a measure of the structural distortion of the triclinic phase in comparison to the parent monoclinic phase and is determined by eq. 9.

In the present case the symmetry-adapted strains are simply strain components e_1, e_2, e_3, e_4, e_5, and e_6 (Voigt notation). Formulas used for calculation of the strains are given in Appendix 4. The following relations between strains and lattice parameters were used in the analysis of the phase transition $P2_1/m$ –> $P\bar{1}$: e_1, e_2, e_3, e_5 – non-symmetry-breaking strain (corresponding to lattice parameters *a*, *b*, *c*, β, respectively), and e_4, e_5 – symmetry-breaking strain (corresponding to angles α, γ, respectively)

The symmetry-breaking strains e_4 and e_6 transform according to the symmetry-breaking representation GM2+. Accordingly, the temperature dependence of the symmetry-breaking strains during the phase transition should be identical to that of the displacive order parameter (if strain is

not explicitly temperature dependent) (Salje, 1991a; Carpenter *et al.*, 1998a). Therefore, the symmetry-breaking strains are often considered as an one-dimensional displacive order parameter for ferroelastic phase transitions, and precise measurements of the lattice parameters are used for the determination of the displacive order parameter behaviour without the need of additional structural information, although only the real displacive order parameter should reflect the structural changes. The non-symmetry-breaking strains e_1, e_2, e_3, e_5 transform according to the identity representation GM1+.

Possible low-order coupling mechanisms between symmetry-breaking strains and displacive order parameters for the continuous phase transition $P2_1/m$ <–> $P\bar{1}$ are:

1) bilinear coupling (allowed only for symmetry-breaking strains e_4 and e_6)

2) linear-quadratic coupling (allowed only for non-symmetry-breaking strains e_1, e_2, e_3, e_5)

3) biquadratic coupling (allowed for all strains: e_1, e_2, e_3, e_4, e_5, e_6)

4) linear-cubic coupling (allowed only for symmetry-breaking strains e_4 and e_6)

3.3.4. Experimental analysis of the coupling mechanism between strain and displacive order parameter for the phase transition $P\bar{1}$ –>$P2_1/m$ on heating of LuF[SeO_3] from RT to 300°C

The precise values of the strain components during heating of LuF[SeO_3] from RT to 300°C were determined directly by Le Bail fits and coincided with those determined by Rietveld refinements. They are presented by filled squares in Fig. 3.5. The strain components (and lattice parameters) in dependence on temperature show an unusual S-shape. Detailed analysis of the peak profile (Fig. 3.2) clearly shows the splitting of the peaks of the triclinic structure below 120°C and a small anisotropic broadening of the peaks of the monoclinic structure above 120°C. Application of the phenomenological microstrain-model of Stephens (1999) to model the anisotropic peak broadening near the phase transition improved the fitting slightly. The result of the sequential refinement for strain e_3 (corresponding to *c*-axes) is characterized by unphysical oscillations due to the relatively small value of this strain. The uncertainties of the lattice parameters are probably underestimated (Kaduk & Partenheimer, 1997).

Attempts to fit analytically the temperature dependence of the strain for an uncoupled displacive order parameter using eq. 9 are visualized as blue and green lines in Fig. 3.5 (blue line: β = 0.40 and Tc = 120°C; green line: β = 0.40 (for e_4 and e_6) and β = 0.50 (for e_1, e_2, e_3, and e_5), Tc = 100°C). Both

fits do not describe the measured data satisfactorily, making it necessary to take the coupling between strain and displacive order parameter into account.

As was pointed out above, three coupling mechanisms between symmetry-adapted strain and displacive order parameter are allowed for symmetry-breaking strains e_4 and e_6: bilinear, biquadratic, and linear-cubic coupling. Higher-order coupling mechanisms are not considered for the current study. Since bilinear coupling suggests that the strain and displacive order parameter are simply proportional to each other, eq. 14 for bilinear coupling coincides with eq. 9 for the uncoupled displacive order parameter. Therefore the blue and green lines in Fig. 3.5 also represent the best analytical fit for bilinear coupling, which can thus be ruled out. The same holds for linear-cubic coupling (Fig. 3.5, orange and purple lines).

An excellent analytical description of the experimental dependence of the symmetry-breaking strains e_4 and e_6 from temperature can only be achieved assuming biquadratic coupling between strain and displacive order parameter with explicit temperature dependence of the strain near the phase transition, *i.e.* by using eq. 25 with a critical exponent $\beta = 0.4$ and $Tc = 120^{o}$C (red line on Fig. 3.5).

For non-symmetry-breaking strains e_1, e_2, e_3, and e_5 there are two possible coupling mechanisms: linear-quadratic and biquadratic. Theoretically, it is possible to describe all non-symmetry-breaking strains by linear-quadratic coupling with a critical exponent $0.40 \leq \beta \leq 0.50$ (almost straight line) and by the assumption of a lower temperature of the phase transition for non-symmetry-breaking strains – around either 109^{o}C (Fig. 3.7) or 98^{o}C and (Fig. 3.8). Nevertheless, such a description requires an additional phase transition at a temperature lower than 120^{o}C from a triclinic to another triclinic structure (the splitting of the peaks of the confirmed triclinic structure is present up to 120^{o}C). In contrast, biquadratic coupling between strain and displacive order parameter with explicit temperature dependence of the strain near the phase transition (*i.e.* by using eq. 25) allows to use the same transition temperature (120^{o}C) and the same critical exponent $\beta = 0.40$ for non-symmetry-breaking strains as for symmetry-breaking strains (red line on Fig. 3.5).

Although the classical mean-field Landau theory operates only with $\beta = ½$ (2^{nd} order phase transition) and $\beta = ¼$ (trictitical phase transition), the found critical exponent $\beta = 0.4$ can be considered as pseudo-critical exponent and is close to the corresponding critical exponent for a 2^{nd} order phase transition.

To verify the preferred model for biquadratic coupling between strain and displacive order parameter with explicit temperature dependence of the strain, parametric refinement was applied. The analytical equation for *e(t)* allows the variation of all parameters for each powder pattern independently (sequential refinement) and for all powder patterns simultaneously (parametric refinement) making the latter an ideal tool to determine the type of phase transition and the type of coupling between strain and displacive order parameter. Here, parametric refinement of symmetry-adapted strains based on Le Bail fits (Fig. 3.6) was performed. The parameterization stabilized the refinement considerably and all symmetry-adapted strains were calculated as a direct function of the temperature according to eq. 25. The reliability factors *Rwp* of the parametric refinement were nearly the same as for the corresponding sequential refinements with individually refined strains (Fig. 3.9).

For comparison reason, parametric refinements were also performed for linear-quadratic coupling between non-symmetry-breaking strains e_1, e_2, e_3, and e_5 (eq. 15) and displacive order parameter and biquadratic coupling between symmetry-breaking strains e_4 and e_6 and displacive order parameter with explicit temperature dependence of the strain (eq. 25). The parameterization by eq. 25 was chosen for symmetry-breaking strains e_4 and e_6 since it gave the best possible fit. Therefore the *R*-factors of the parametric refinement reflect the quality of fit only for non-symmetry-breaking strains. Two different critical temperatures were used for non-symmetry-breaking strains (98^{o}C and 109^{o}C); the critical temperature for symmetry-breaking strains was fixed to 120^{o}C, since this value provided the best fit of the corresponding data from sequential refinement. The resulting *Rwp*-factors were quite different from the corresponding *Rwp*-factors of the sequential refinements (Figs. 3.7, 3.8, 3.9) and clearly confirm that all non-symmetry breaking strains are biquadratically coupled with the displacive order parameter according to eq. 25. The linear-quadratic coupling for non-symmetry-breaking strains with a critical temperature of 120^{o}C led to much worse agreement factors for parametric refinement, since the fitting of the strain values near the phase transition is quite poor.

Biquadratic coupling between strain and displacive order parameter with explicit temperature dependence of the strain for $LuF[SeO_3]$ is not the first example of such a mechanism. Similar behaviour of the displacive order parameter was found earlier from temperature-dependent powder diffraction measurements (for example, Carpenter *et al.*, 2003, 2009c, 2012; Tan *et al.*, 2012) and from temperature-dependent birefringence measurements (Bismayer *et al*., 1986; Glazer *et al*., 2010). The explicit temperature dependence of the strain must be caused by structural changes

during the preceding cooling of the material. These changes are expected to be very small and therefore below the detection limit in a structural refinement from powder diffraction data.

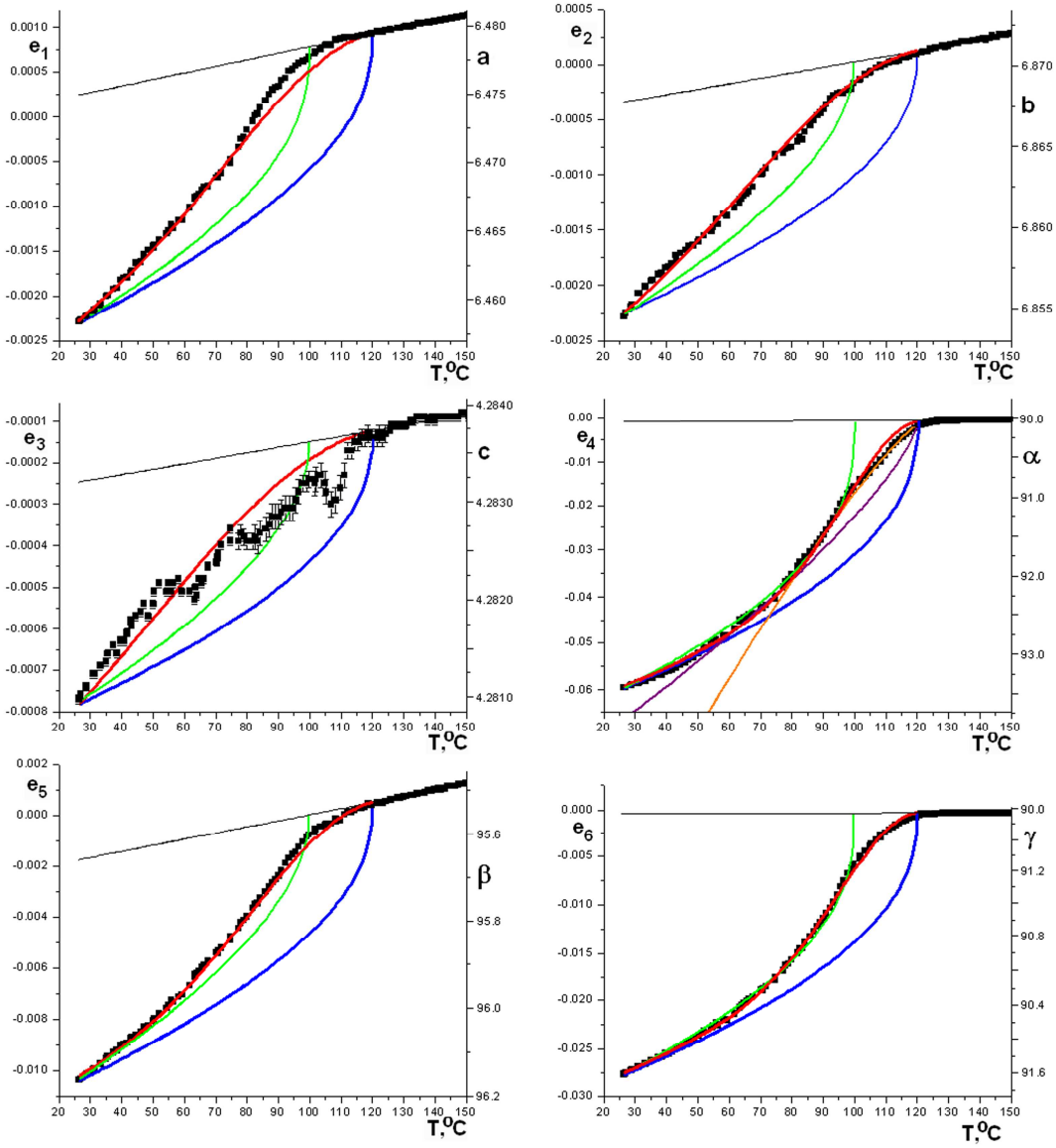

Figure 3.5. Dependence of the strain components for $LuF[SeO_3]$ upon heating from room-temperature to 300°C. Dark squares – sequential Le Bail fit, blue line – theoretical fitting by eq. 9 for uncoupled displacive order parameter (and by eq. 14 for bilinear coupling) with $\beta = 0.40(1)$ and $Tc = 120^{o}C$, green line – theoretical fitting by eq. 9 for uncoupled displacive order parameter (and by eq. 14 for bilinear coupling) with $\beta = 0.40(1)$ (for e_4 and e_6) and $\beta = 0.50(1)$ (for e_1, e_2, e_3, and e_5) and $Tc = 100^{o}C$, red line – theoretical fitting by eq. 25 with $\beta = 0.40(1)$ and $Tc = 120^{o}C$. Orange and purple lines for e_4 represent linear-cubic coupling according to eq. 16 for $\beta = 0.40$ and $\beta = 0.25$, respectively. Error bars are not shown when they are less or equal to the size of symbols. The thin dark line represents the extrapolation of the thermal expansion of the high-symmetry phase into the low-temperature regime.

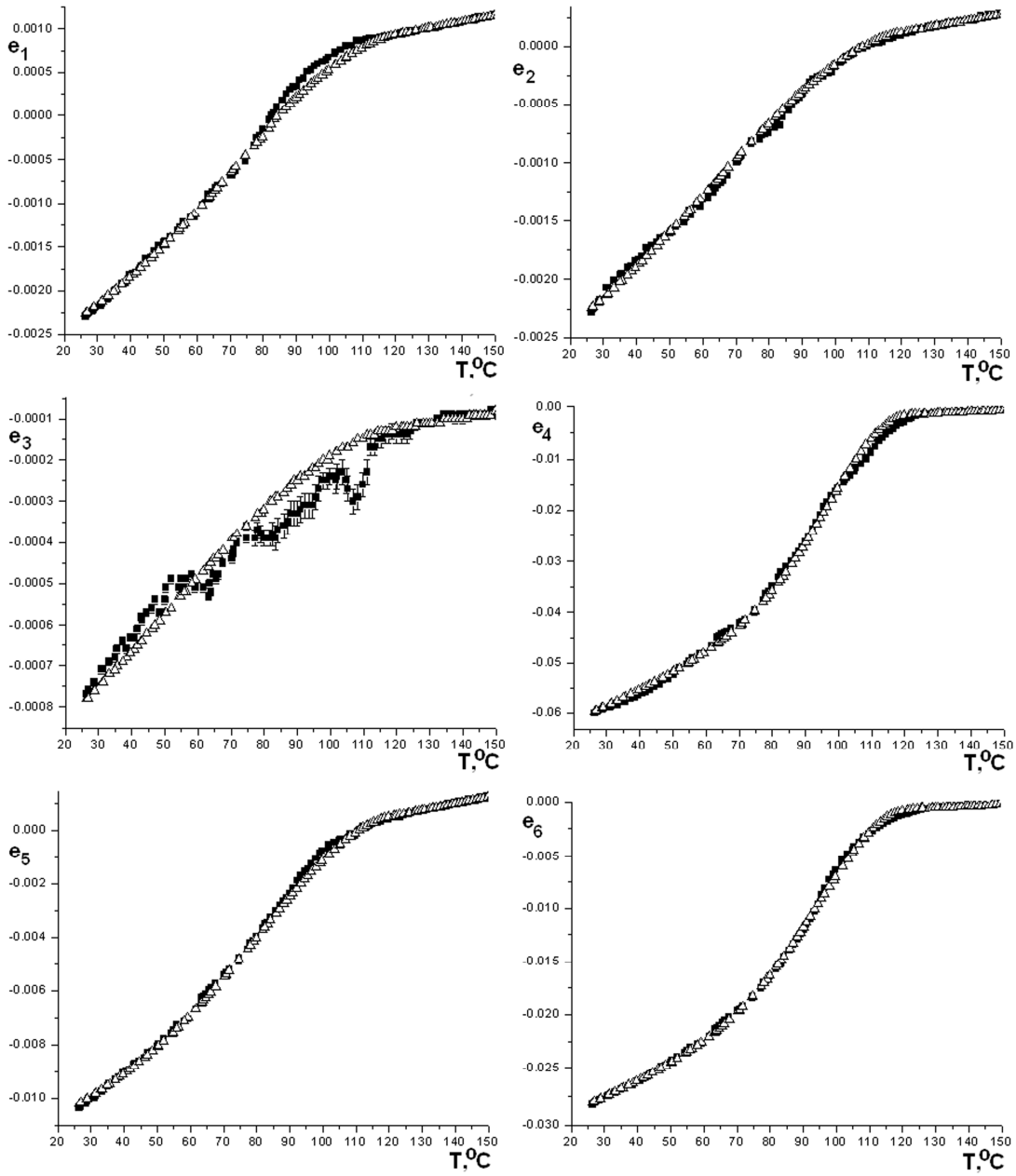

Figure 3.6. Dependence of the strain components for $LuF[SeO_3]$ upon heating from room-temperature to 300°C from Le Bail fits. Filled squares – sequential refinement, open triangles – parametric refinements. The parametric refinement is based on eq. 25 (biquadratic coupling between strain and displacive order parameter with explicit temperature dependence of strain) with Tc = 120°C and β = 0.4. Error bars are not shown when they are less or equal to the size of symbols.

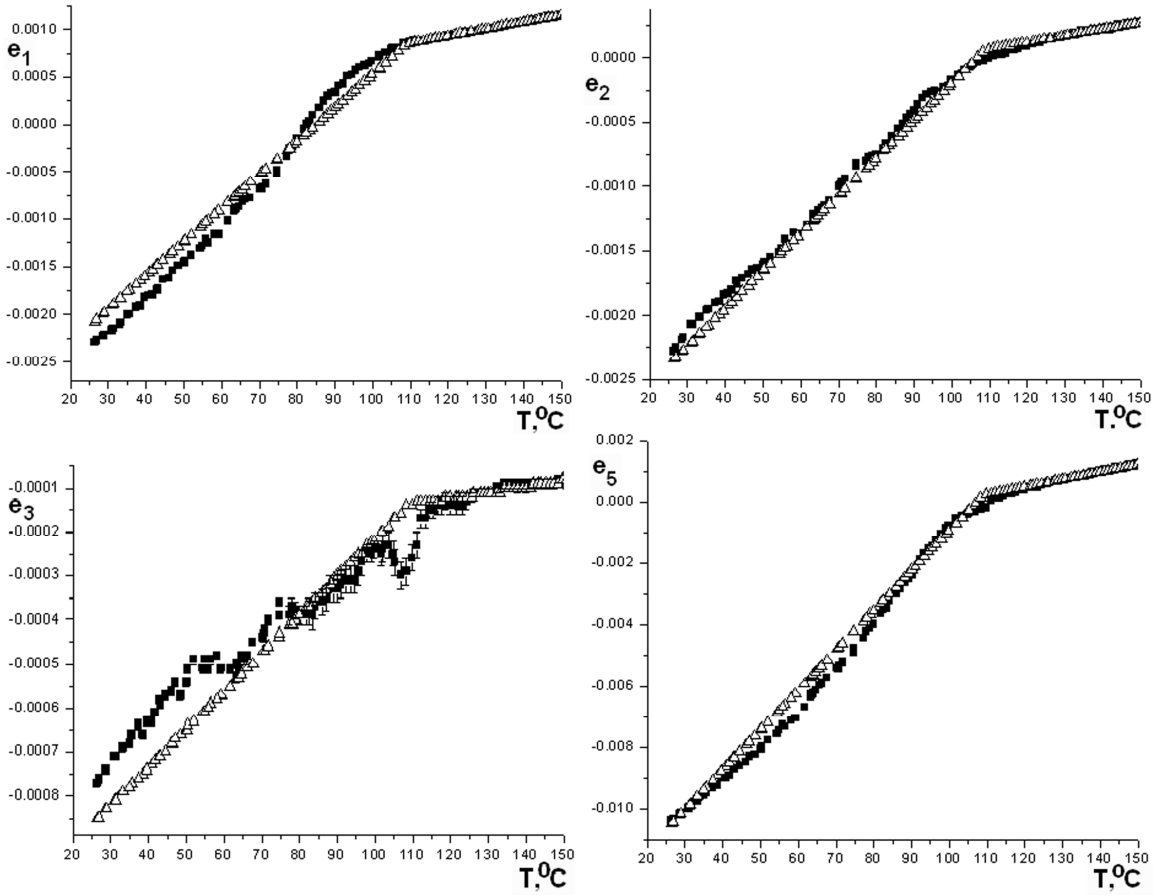

Figure 3.7. Sequential (filled squares) and parametric (open triangles) refinements based on Le Bail fits of $LuF[SeO_3]$ upon heating from RT to 300°C. Parameterization is based on eq. 15 for linear-quadratic coupling between non-symmetry-breaking strains e_1, e_2, e_3, e_5 and displacive order parameter with Tc = 109°C and β = 0.50(1), and based on eq. 25 for biquadratic coupling between symmetry-breaking strains e_4, e_6 and displacive order parameter with explicit temperature dependence of strain near phase transition (Tc = 120°C, β = 0.40(1)). Error bars are not shown when they are less or equal to the size of symbols. The results of the parameterization for symmetry-breaking strains e_4, e_6 are the same as in Fig. 3.6.

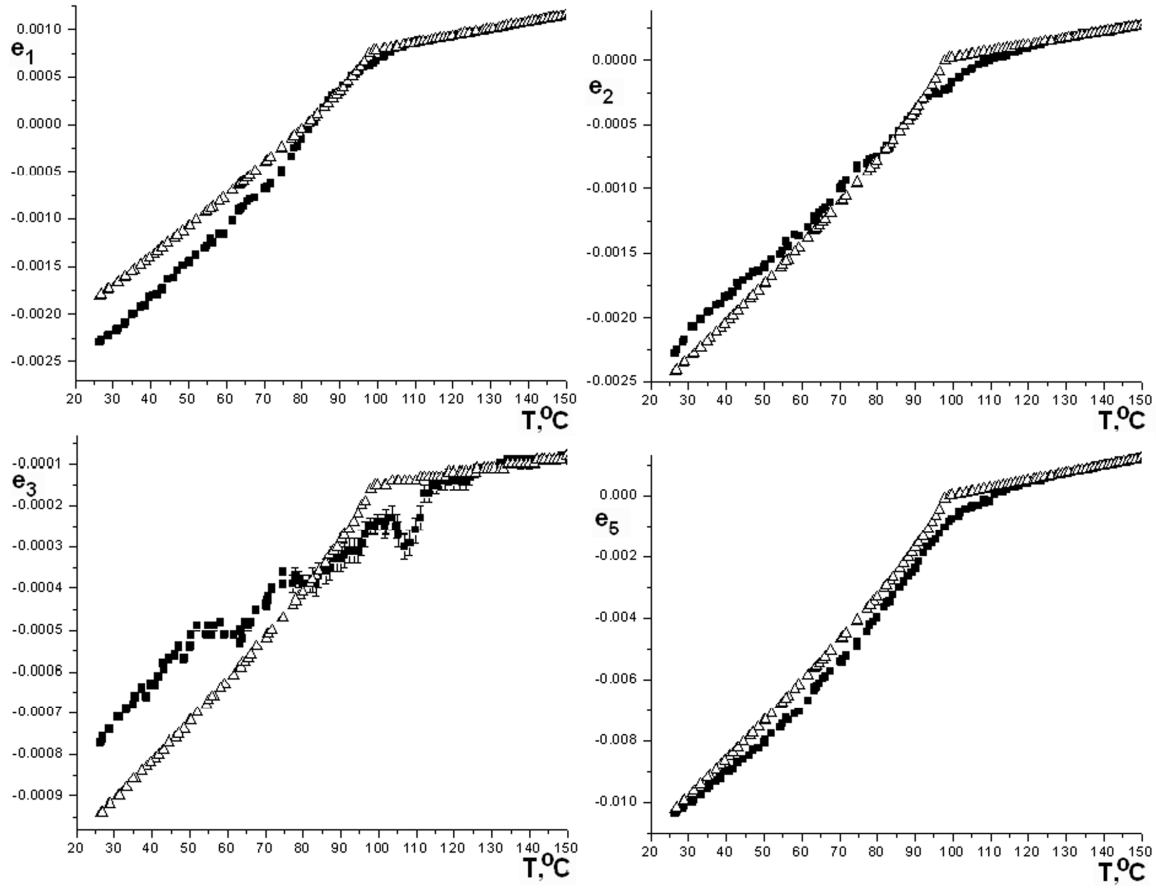

Figure 3.8. Sequential (filled squares) and parametric (open triangles) refinements based on Le Bail fits of $LuF[SeO_3]$ upon heating from RT to 300°C. Parameterization is based on eq. 15 for linear-quadratic coupling between non-symmetry-breaking strains e_1, e_2, e_3, e_5 and displacive order parameter with $Tc = 98^oC$ and $\beta = 0.40(1)$, and on eq. 25 for biquadratic coupling between symmetry-breaking strains e_4, e_6 and displacive order parameter with explicit temperature dependence of strain near phase transition ($Tc = 120^oC$, $\beta = 0.40(1)$). Error bars are not shown when they are less or equal to the size of symbols. The results of the parameterization for symmetry-breaking strains e_4, e_6 are the same as in Fig. 3.6.

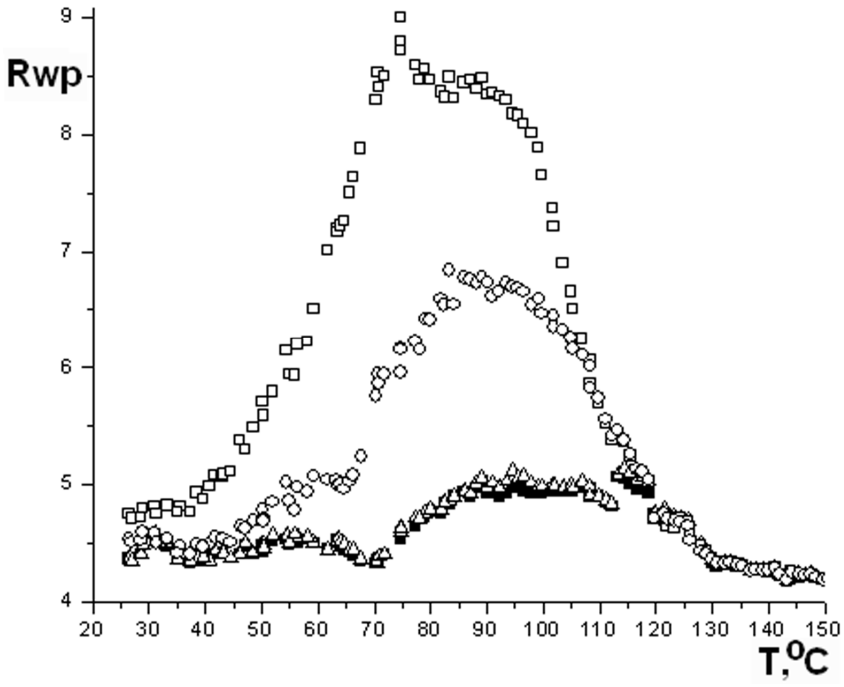

Figure 3.9. Comparison of *Rwp* agreement factors of sequential (filled squares) and different parametric (open symbols) refinements based on Le Bail fits for $LuF[SeO_3]$ upon heating from room-temperature to 300°C. Open triangles – parametric refinement based on eq. 25 (biquadratic coupling between strain and displacive order parameter with explicit temperature dependence of strain), Tc = 120°C and β = 0.40(1); open circles – parametric refinement based on eq. 15 (linear-quadratic coupling between strain and displacive order parameter) with Tc = 109°C and β = 0.50(1) for non-symmetry breaking strains e_1, e_2, e_3, e_5, and based on eq. 25 with Tc = 120°C and β = 0.40(1) for symmetry-breaking strains e_4, e_6; open squares – parametric refinement based on eq. 15 with Tc = 98°C and β = 0.40(1) for non-symmetry breaking strains e_1, e_2, e_3, e_5, and based on eq. 25 with Tc = 120°C and β = 0.40(1) for symmetry-breaking strains e_4, e_6.

3.3.5. Experimental analysis of the coupling mechanism between strain and displacive order parameter for the phase transition $P2_1/m \rightarrow P\bar{1}$ on cooling of $LuF[SeO_3]$ from 300°C down to RT

Compared to the phase transition on heating, the phase transition of $LuF[SeO_3]$ on cooling from 300°C to RT is characterized by a different critical temperature Tc and a different critical exponent β. The peaks of the triclinic structure are split below 98°C (Fig. 3.2), while for the

monoclinic structure above 98°C strong anisotropic peak broadening is observed. The latter was successfully modeled by the phenomenological microstrain model of Stephens (1999).

The temperature dependence of the symmetry-breaking strains e_4 and e_6 can be well described by the assumption of bilinear coupling between strain and displacive order parameter (eq. 14) with a critical temperature of 98°C and a critical exponent β *of* ¼, which corresponds to a tricritical phase transition (open triangles on Fig. 3.10, which simultaneously represents eq. 9 for the uncoupled displacive order parameter).

The non-symmetry-breaking strains e_1, e_2, and e_3 can be described by eq. 15 for linear-quadratic coupling between strain and displacive order parameter with a critical temperature of 98°C and a critical exponent β of ¼, but the strain e_5 cannot be described in this way (dotted line on Fig. 3.10). The description of the strain e_5 by eq. 15 for linear-quadratic coupling with a critical exponent of β = 1/8 (open triangles on Fig. 3.10) gave the best fit but without physical meaning, and was therefore discarded.

The open triangles in Fig. 3.10 for strain e_5 describe simultaneously the bilinear (according to eq. 14) and the biquadratic coupling between strain and displacive order parameter (according to eq. 17) with a critical temperature of 98°C and a critical exponent β of ¼. Additionally, e_3 can be described by eq. 15 for linear-quadratic coupling with a critical temperature of 98°C and a critical exponent β of ½ (resulting into a straight line), but the values of the strain e_3 are the smallest among all strains and thus less accurate (the real uncertainties for e_3 are clearly larger as those obtained from the Le Bail fit).

As a result, the non-symmetry-breaking strains e_1, e_2, e_3 are linear-quadratically coupled with the displacive order parameter and the non-symmetry-breaking strains e_5 is biqudratically coupled with the displacive order parameter. To verify this model, parametric refinement based on Le Bail fits was performed (Fig. 3.10), leading to identical *R*-factors as those obtained from sequential refinement.

Since the symmetry-breaking strains e_4 and e_6 are linearly coupled with the displacive order parameter (and, therefore, proportional), they are often considered as displacive order parameter instead of the real displacive order parameter which quantifies the structural changes.

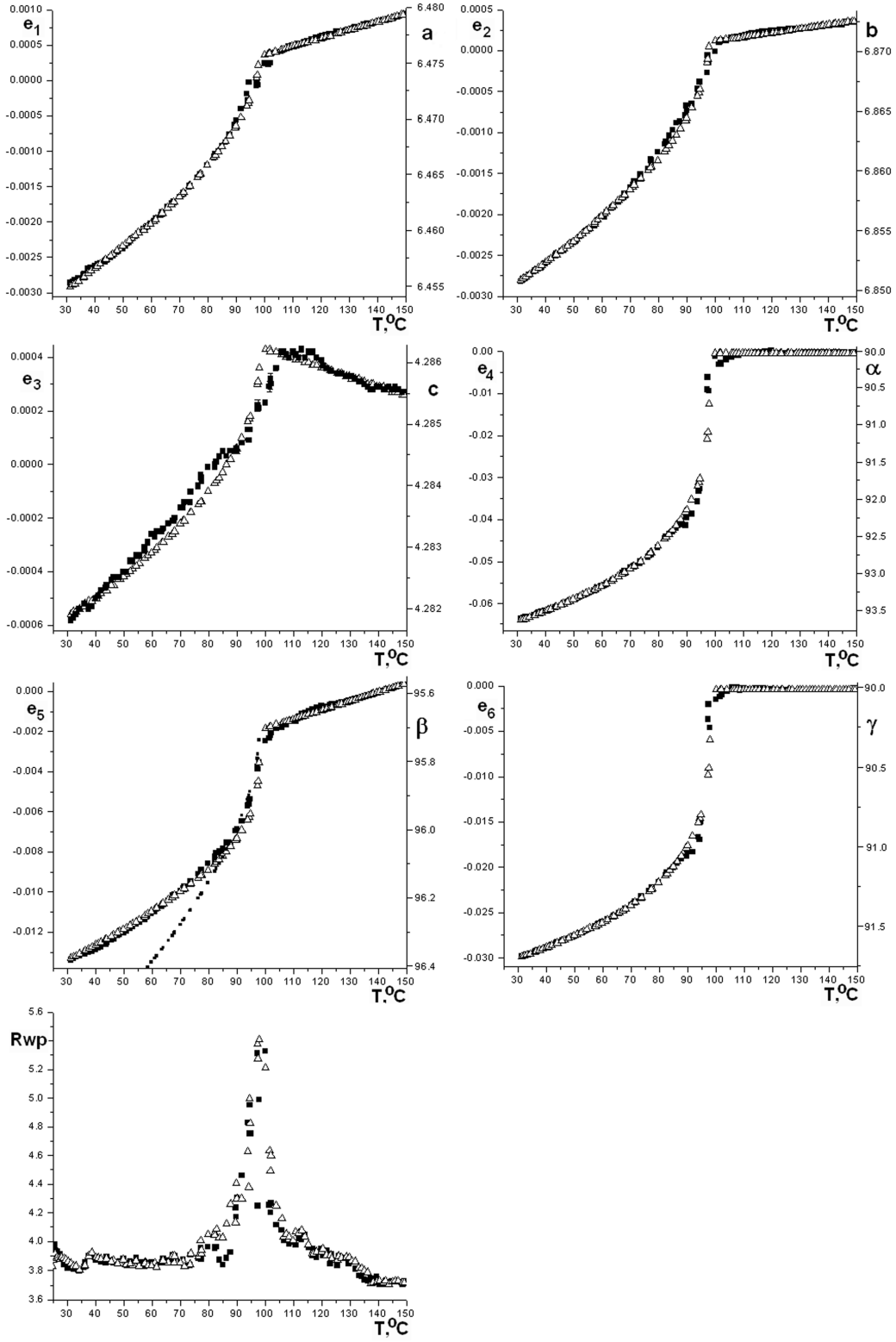

Figure 3.10. Dependence of the strain components for $LuF[SeO_3]$ upon cooling from 300°C to room-temperature as derived from Le Bail fits: filled squares – sequential refinement, open triangles – parametric refinements. The parametric refinement is based on eq. 15 (linear-quadratic coupling between

strain and displacive order parameter) for non-symmetry-breaking strains e_1, e_2, e_3, on eq. 17 (biquadratic coupling between strain and displacive order parameter) for non-symmetry-breaking strain e_5, and on eq. 14 (bilinear coupling between strain and displacive order parameter) for symmetry-breaking strains e_4, e_6 with Tc = 98°C and β = 0.25(1). Dotted line – theoretical fitting by eq. 9 for uncoupled displacive order parameter (and by eq. 14 for bilinear coupling) with β = 0.50 and Tc = 98°C. Error bars are not shown when they are less or equal to the size of symbols.

3.3.6. Conclusion

Parametric whole powder pattern refinement was established as a powerful tool to test different models of coupling between strain and displacive order parameter during a structural phase transition. In the current case study, the high-temperature ferroelastic phase transition $P\bar{1}$ <-> $P2_1/m$ in $LuF[SeO_3]$ was analyzed in detail. Strong strain created during preliminary cooling of the sample possesses explicit temperature dependence and its variation on heating can be described by biquadratic coupling between symmetry-adapted strain and displacive order parameter with explicit temperature dependence of the strain. The excess of strain is removed by the high-temperature phase transition and during the subsequent cooling of the sample down to room-temperature the symmetry-adapted strains are coupled with the displacive order parameter without explicit temperature dependence of the strain. It could thus be proven that different coupling mechanisms are responsible for the large hysteresis of the lattice parameters (and symmetry-adapted strains) during this phase transitions.

3.4. Analysis and parameterization of the high-temperature phase transition for Sr_2CoOsO_6

3.4.1. Background information

The double perovskite Sr_2CoOsO_6 has a typical rock salt arrangement of Co- and Os-cations in distinct crystallographic positions (Fig. 3.11). The fully ordered undistorted high-temperature structure of Sr_2CoOsO_6 in space group $Fm\bar{3}m$ exists at temperatures above ~350°C. On decreasing temperature, the cubic structure transforms into a tetragonal structure with space group *I*4/*m*. The corresponding phase transition $Fm\bar{3}m$ –> *I*4/*m* is caused be the octahedral tilting around *c*-axis and can be described by Glazer notation as a^0a^0c- (Glazer, 1972). On cooling below 108 K another structural phase transition occurs. The corresponding low-temperature phase has a monoclinic structure *I*2/*m* (maximal subgroup of *I*4/*m*), and is characterized by the same octahedral tilting around the *c*-axis $a^0a^0c^-$.

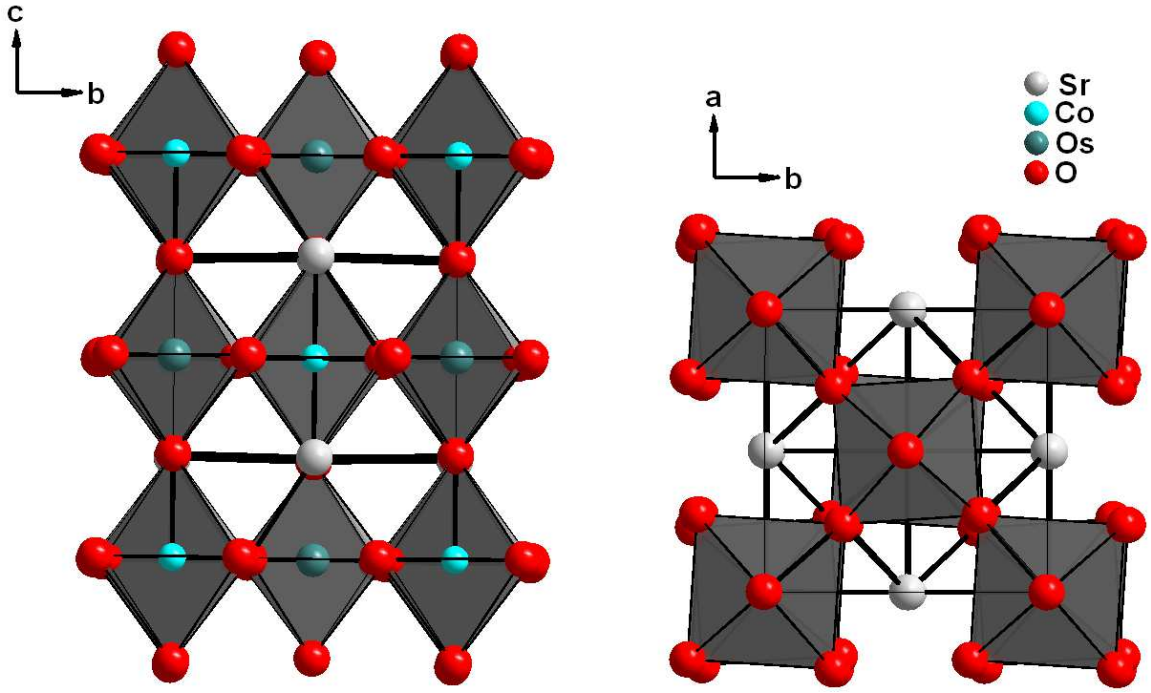

Figure 3.11. Crystal structure of Sr_2CoOsO_6 at room-temperature.

3.4.2. X-ray powder diffraction investigation of high-temperature phase transition of Sr_2CoOsO_6

The synthesis of Sr_2CoOsO_6 was described previously (Avijit *et al.*, 2013).

Powder diffraction data of Sr_2CoOsO_6 were collected at the high-resolution powder diffractometer MS-powder at the Swiss Light Source (SLS), Switzerland (Willmott *et al.*, 2013). The wavelength was determined to be 0.7749(3) Å from a silicon standard. The sample was contained in a sealed 0.3-mm quartz capillary and was rotated around θ in order to improve randomization of the crystallites. The diffracted beam was detected with a series of PSD(Mythen2)-detectors with 90° aperture (Schmitt *et al.*, 2003; Bergamaschi *et al.*, 2010). A hot air blower was used to heat sample in steps of 10 K with a holding time of minimum 1 min before measurements were started. Powder patterns were collected for 5 min/frame.

The program TOPAS 4.1 (Coelho, 2007) was used for refinement according to the Rietveld (Rietveld, 1967, 1969) and Le Bail (Le Bail *et al.*, 1988) methods.

In the present work, precise values of the strain components for the high-temperature phase transition of Sr_2CoOsO_6 were determined directly from the measured lattice parameters by Le Bail fits of the experimental X-ray powder diffraction data. The program ISODISTORT (Campbell *et al.*, 2006) was used for the distortion mode decomposition of the high-symmetry phase ($Fm\bar{3}m$) into the low-symmetry phase ($I4/m$).

3.4.3. Symmetry modes analysis and analysis of the coupling mechanism between strain and displacive order parameter for the phase transition $Fm\bar{3}m$–>$I4/m$ of Sr_2CoOsO_6

According to Stokes & Hatch (1988), the proper ferroelastic phase transition $Fm\bar{3}m$ –> $I4/m$ is associated with $\vec{k}$ = (0, 0, 0), and the displacive order parameter is one-dimensional. Three irreducible representations correspond to this phase transition: GM1+, (non-symmetry-breaking), GM3+ (non-symmetry-breaking), and GM4+, (symmetry-breaking). The phase transition is allowed to be continuous by both, Landau theory and renormalization-group theory.

The relation between the high-symmetry cell in $Fm\bar{3}m$ and the low-symmetry cell in $I4/m$ is presented in Fig. 3.12.

The only possible group-subgroup relation for the investigated phase transition is $Fm\bar{3}m$ –> *I*4*/mmm* –> *I*4*/m*, where

$Fm\bar{3}m$ (N. 225) –> *I*4*/mmm* (N. 139): index =3

Transformation matrix:

$$\left(\begin{array}{ccc|c} 1/2 & -1/2 & 0 & 0 \\ 1/2 & 1/2 & 0 & 0 \\ 0 & 0 & 1 & 0 \end{array}\right)$$

*I*4*/mmm* (N. 139) –> *I*4*/m* (N. 87): index =2

Transformation matrix:

$$\left(\begin{array}{ccc|c} 1 & 0 & 0 & 0 \\ 0 & 1 & 0 & 0 \\ 0 & 0 & 1 & 0 \end{array}\right)$$

The geometrical representation of the distortion modes for the phase transition $Fm\bar{3}m$ –> *I*4*/m* is given in Fig. 3.13.

Distortion mode a_1 corresponds to irrep GM1+ and describes the isotropic expansion/contraction of octahedra during heating/cooling.

Distortion mode a_2 corresponds to irrep GM3+ and expands the octahedra in the equatorial plane *ab* of the tetragonal structure (*i.e.* oxygen atoms in position O2), while the two apical oxygen atoms (*i.e.* in position O1) are shifted towards the center of the octahedra.

Distortion mode a_3 corresponds to irrep GM4+ and is sufficient to break the symmetry from cubic $Fm\bar{3}m$ to tetragonal *I*4*/m*. This distortion mode describes a rotation of the octahedra around *c*-axes. Only this distortion mode exhibits a large value of amplitude in sequential Rietveld refinement. Since distortion mode a_3 belongs to the symmetry-breaking GM4+ irrep, it can be considered as a single order parameter *Q*. Thus, the degree of rotation of the octahedra quantifies the distortion of the low-symmetry phase in comparison to the undistorted high-symmetry cubic phase.

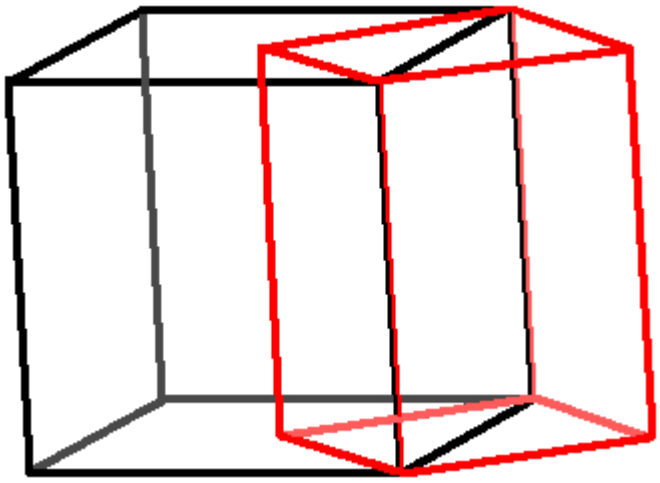

Fugure 3.12. Relative orientation of the unit cells of high-temperature cubic ordered double perovskite (black line) and low-temperature tetragonal ordered double perovskite (red line).

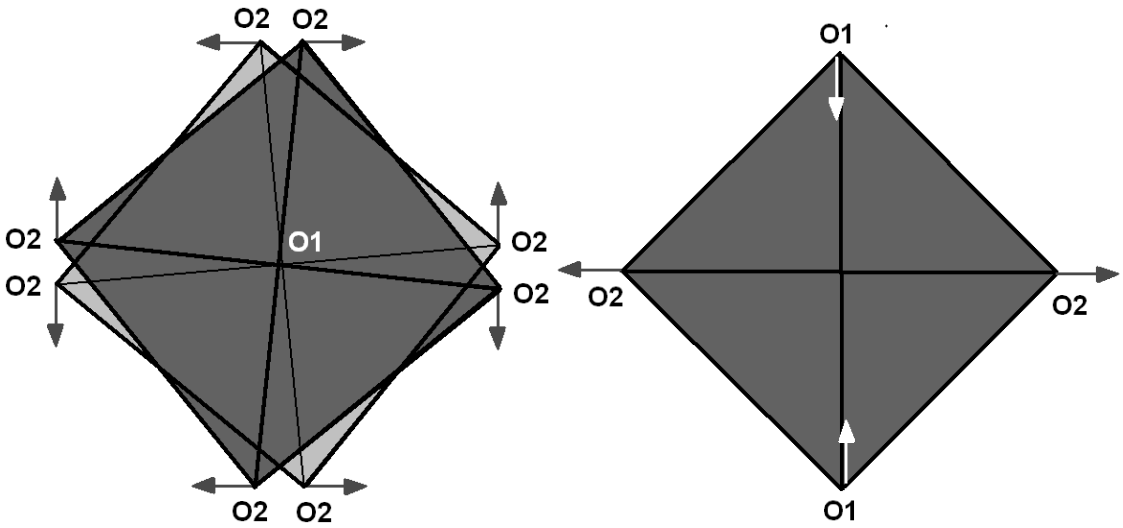

Fugure 3.13. Geometrical representation of the distortion modes. Left: GM4+, rotation of octahedra in the *aa*-plane of the tetragonal unit cell; right: GM3+, distortion of octahedra in the *ac*-plane of the tetragonal unit cell.

3.4.4. Experimental analysis of the coupling mechanism between strain and displacive order parameter for the phase transition $Fm\bar{3}m$ –> *I4/m* on heating of Sr_2CoOsO_6 from 170°C to 370°C

Temperature dependencies of the lattice parameters and symmetry-adapted strains are shown in Fig. 3.14, and suggest that the thermally induced $Fm\bar{3}m$ –> *I4/m* phase transition is

continuous. Two symmetry-adapted strains are associated with the phase transition: s_1 and s_2. They belong to non-symmetry-breaking irreps GM1+ and GM3+, respectively. The strain s_1 is often called a volume strain, and s_2 is a tetragonal strain, since it describes the *c*/*a* ratio of the lattice parameters for the tetragonal unit cell. For octahedral tilting transitions in perovskites, the order parameter is represented by the tilt angle, which can be estimated from the atomic coordinates of the oxygen atoms (Zhang *et al.*, 2012).

Bilinear and linear-cubic coupling is not allowed for both symmetry-adapted strains s_1 and s_2, because they belong to non-symmetry-breaking irreps. Both strains s_1 and s_2 must be linear-quadratically coupled with the order parameter. Linear-quadratic coupling of the tetragonal strain with order parameter for the phase transition in perovskites, induced by the octahedral tilting, was reported earlier (Carpenter *et al.*, 1998a; Zhang *et al.*, 2012).

Coupling of the strain with an order parameter is then given by

$$G = G_0 + atQ^2 + BQ^4 + DQ^6 - d_1 s_1 a_3^2 - d_2 s_2 a_3^2 - d_3 a_1 a_3^2 - d_4 a_2 a_3^2 + \frac{f_1}{2} s_1^2 + \frac{f_2}{2} s_2^2 \qquad (26)$$

where a_3 is an order parameter, s_1 and s_2 are symmetry-adapted strains; G_0, a, B, D, d_1, d_2, d_3, d_4, f_1, f_2 – constants, $t = \frac{T - Tc}{Tc}$, Tc – critical temperature of phase transition; T – given temperature of the low-symmetry phase.

Sequential and parametric Le Bail fits (Fig. 3.14) allowed the precise determination of the critical exponent β: both s_1 and s_2 are described by application of eq. 15 with $\beta = 0.50(1)$, thus the phase transition $Fm\bar{3}m$ –> $I4/m$ for Sr_2CoOsO_6 is of second-order.

Structural analysis of the high-temperature structural phase transition in Sr_2CoOsO_6 was performed using symmetry-modes description (Campbell *et al.*, 2007) and rigid body symmetry-modes description (rotational modes), (Mueller *et al.*, 2014). Additionally, rigid body refinement was also performed.

It was found from sequential Rietveld refinements that amplitudes of distortion modes a_1 and a_2 were too small to be analyzed with sufficient accuracy. Therefore, their values were fixed to zero, and all refinements were repeated. The value of 0.50(1) for the distortion mode a_3 was found from sequential Rietveld refinement and confirmed by parametric Rietveld refinement (Fig. 3.15). Distortion mode a_3 describes the octahedral rotation around *c*-axis and is considered to be an order parameter for the low-symmetry $I4/m$ phase of Sr_2CoOsO_6. Because distortion

modes a_1 and a_2 were fixed to zero, a simple relation between x- and y-coordinates of the O2 oxygen atom follows: x(O2) = 0.25 - a_3, y(O2) = 0.25 + a_3. As a result, the atomic coordinates of O2 can be directly parameterized with the same critical exponent β = 0.50(1).

The amplitudes and the temperature dependence of a_1 could not be determined from sequential Rietveld refinements. Parametric Rietveld refinement provides the possibility of accurate refinement of a_1. Distortion mode a_1 belongs to non-symmetry-breaking irrep, and thus must be linear-quadratically coupled with the order parameter a_3. The results of the corresponding parametric Rietveld refinement are presented in Fig. 3.16. In this case, the coordinates x and y of O2 cannot be directly parameterized with the same critical exponent β = ½. The coordinate x(O2) is determined by the differences between a_1 and a_3 distortion modes, and y(O2) is determined by the sum of a_1 and a_3 distortion modes (both x- and y-coordinates are expressed in the tetragonal unit cell). The temperature dependence of the O2 atomic coordinates can only be fitted by unphysical critical exponents of 0.55 for y(O2) and 0.44 for x(O2). For the $Fm\bar{3}m$ –> $I4/m$ phase transition in Sr_2CoOsO_6, the absolute value of a_1 is relatively small, and can be fixed to zero. But care must be taken during analysis of the phase transitions, for which the value of the "isotropic" distortion mode a_1 is comparable to the values of symmetry-breaking distortion modes (i.e. pressure-induces phase transitions).

Distortion mode a_2 describes the possible Jahn-Teller distortion (Balachandran & Rondinelli, 2013). Since Sr_2CoOsO_6 shows only a weak Jahn-Teller effect (Avijit *et al.*, 2013), its value was fixed to zero.

Sequential and parametric Rietveld refinements were also performed using the rigid body symmetry-mode description (Mueller *et al.*, 2014).

Application of rigid bodies to model relatively "rigid" fragments of the structure are widely used because they allow to decrease the amount of refined parameters considerably (Dinnebier, 1999). In the present case, application of rigid bodies leads to only one refined parameter – the tilt angle of the octahedron, which is equivalent to the distortion mode refinement with the only refined mode a_3. Sequential and parametric Rietveld refinements of rigid body symmetry-modes (Fig. 3.17) lead to the same results as the distortion modes refinement (Fig. 3.15) and can be considered as a validation of the recently introduced rigid body symmetry-modes method. The results of the classical rigid body refinement (Fig. 3.18) fully coincide with those from distortion modes refinement and rigid body symmetry-modes refinement.

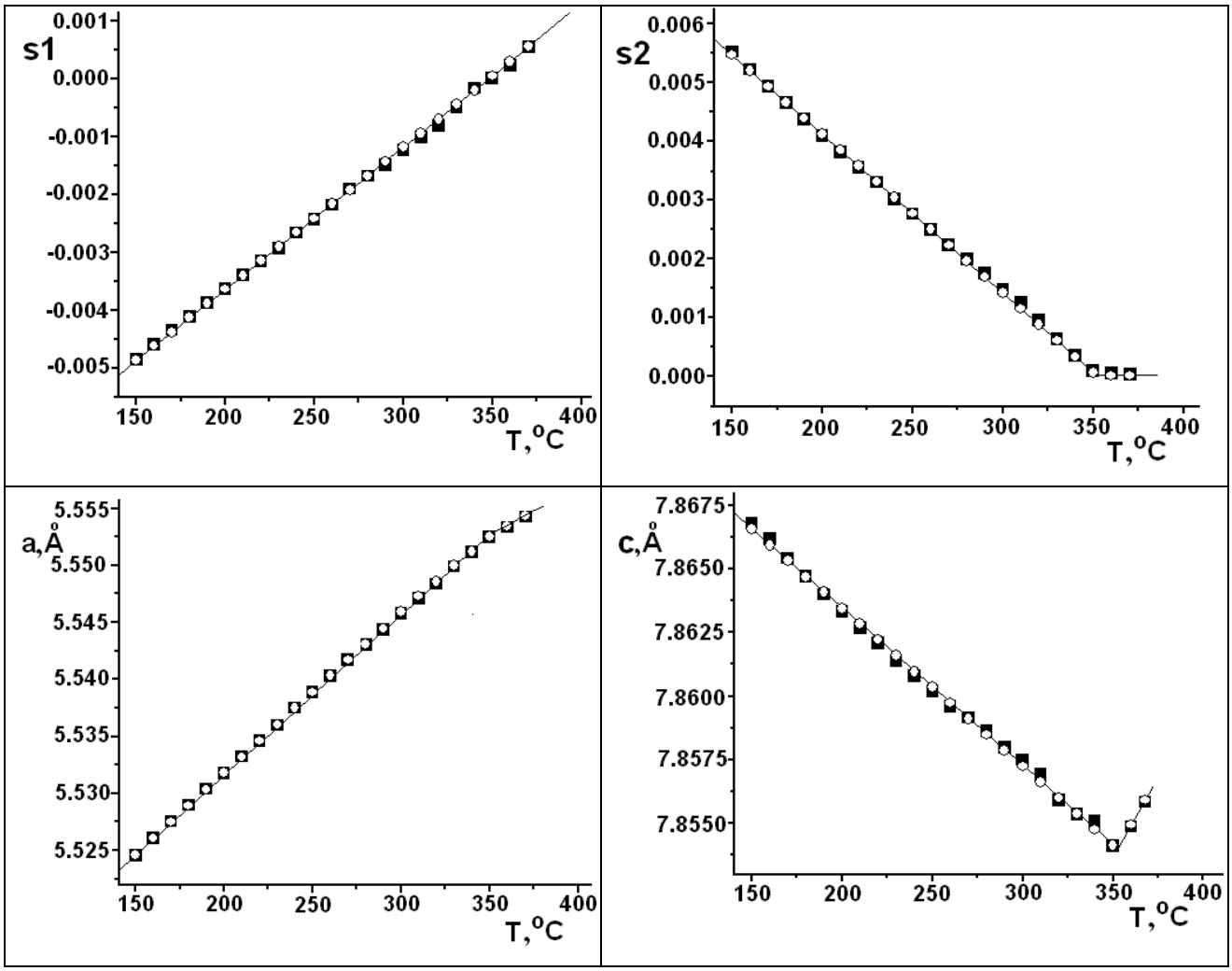

Figure 3.14. Temperature dependence of the strain components (top) and lattice parameters (bottom) for Sr_2CoOsO_6 upon heating from 150°C to 370°C derived from Le Bail fits. Filled squares – sequential refinement, open triangles – parametric refinement. The parametric refinement is based on eq. 15 (linear-quadratic coupling between strain and displacive order parameter) with Tc = 352°C and β = 0.50(1). Error bars are not shown when they are less or equal to the size of symbols.

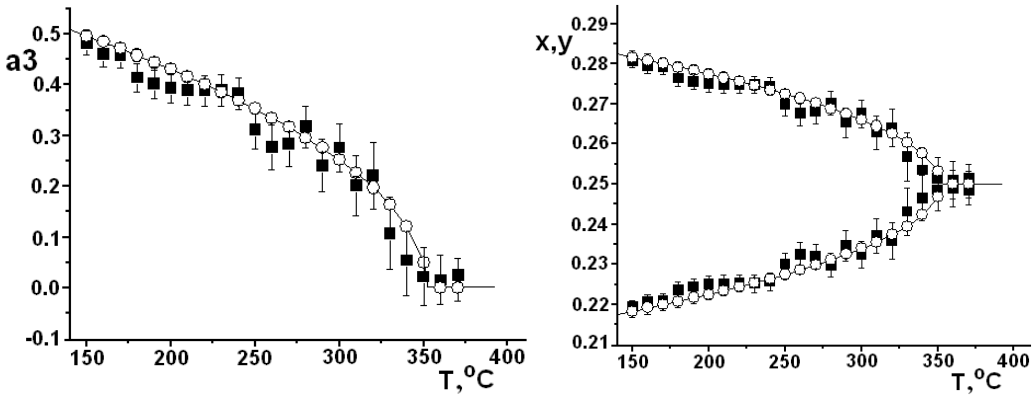

Figure 3.15. Temperature dependence of the distortion mode a_3 and the atomic *x*- and *y*-coordinates of the oxygen atom O2 for Sr_2CoOsO_6 upon heating from 150°C to 370°C from symmetry-modes refinement. Filled symbols – sequential refinement, open symbols – parametric refinement with Tc = 352°C and β = 0.50(1). Error bars are not shown when they are less or equal to the size of symbols.

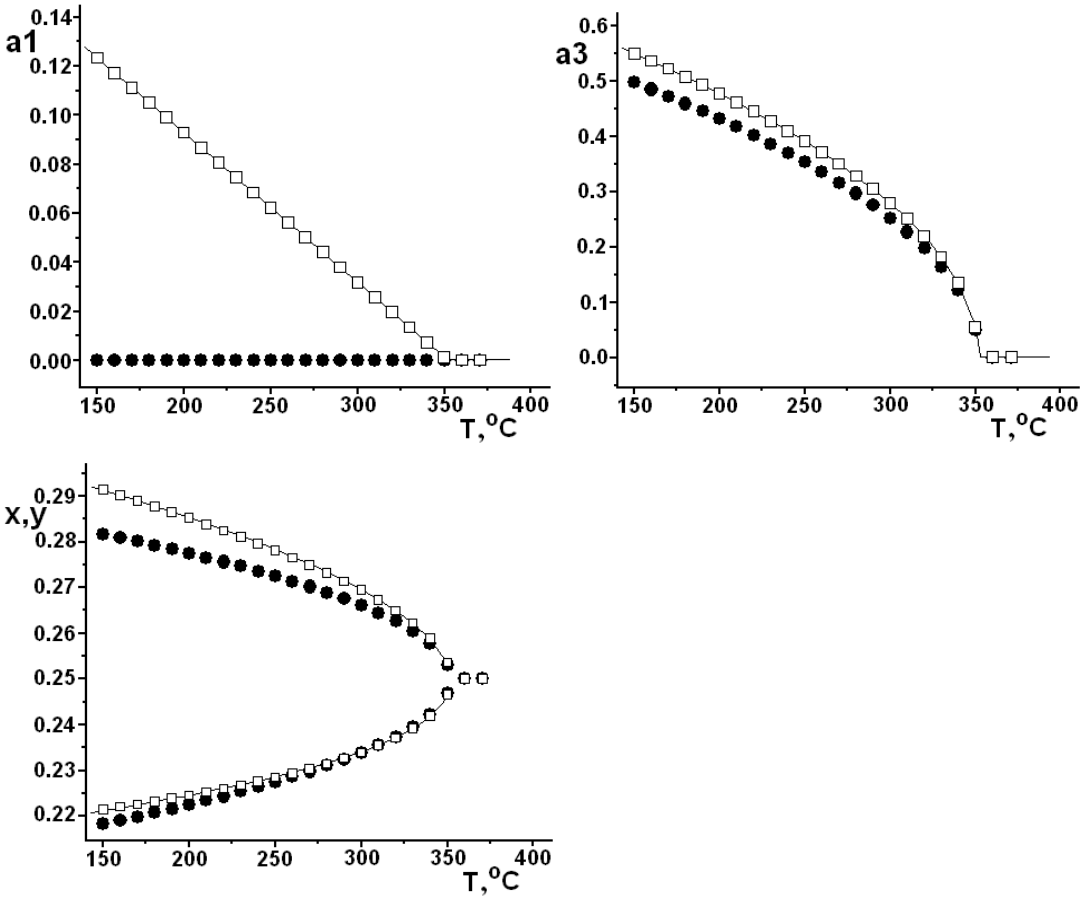

Figure 3.16. Temperature dependence of the distortion modes a_1 and a_3 and the atomic *x*- and *y*-coordinates of the oxygen atom O2 for Sr_2CoOsO_6 upon heating from 150°C to 370°C from symmetry-modes refinement. Filled symbols – parametric refinement with a_1=*0*, a_3 – refined; open symbols – parametric refinement with refined a_1 and a_3.

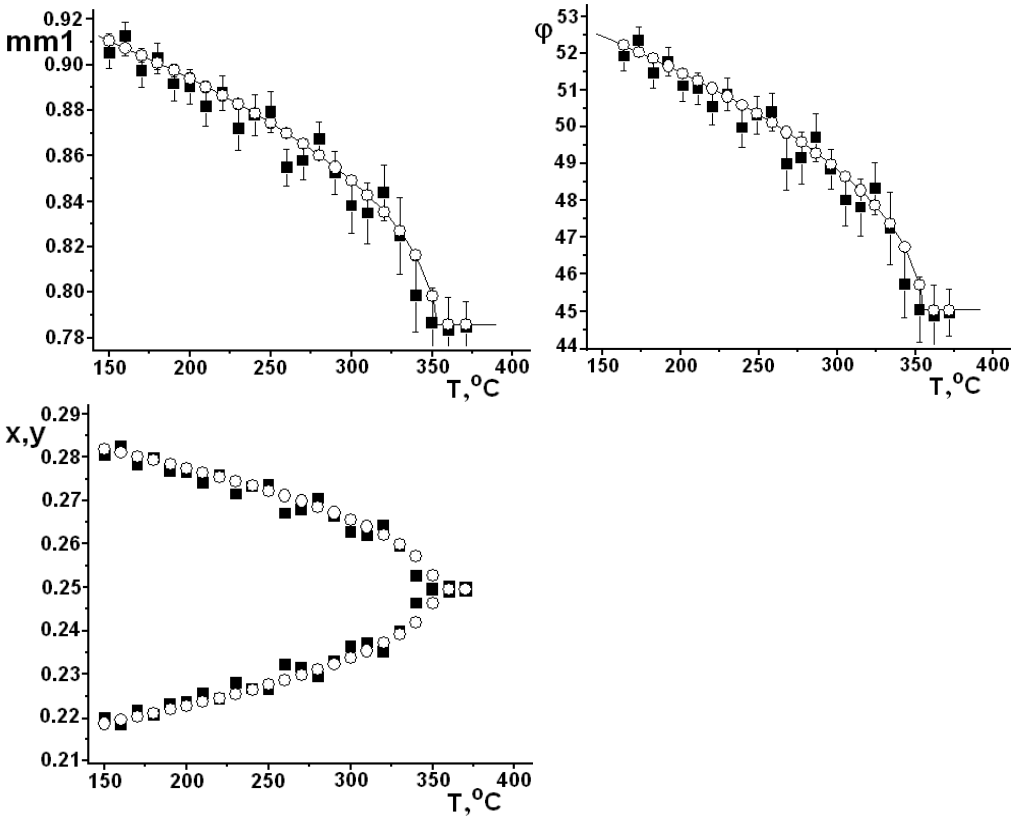

Figure 3.17. Temperature dependence of the rotational vector mm_1, corresponding tilt angle φ, and the atomic *x*- and *y*-coordinates of the oxygen atom O2 for Sr_2CoOsO_6 upon heating from 150°C to 370°C from rigid body symmetry-modes refinement. Filled symbols – sequential refinement, open symbols – parametric refinement with Tc = 352°C and β = 0.50(1). Error bars are not shown when they are less or equal to the size of symbols.

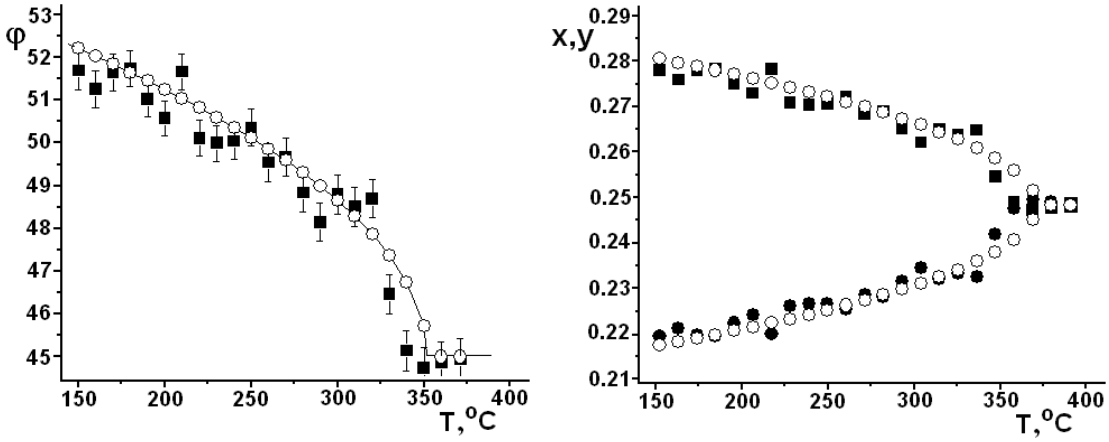

Figure 3.18. Temperature dependence of the tilt angle φ, and the atomic *x*- and *y*-coordinates of the oxygen atom O2 for Sr_2CoOsO_6 upon heating from 150°C to 370°C from rigid body refinement. Filled symbols – sequential refinement, open symbols – parametric refinement with Tc = 352°C and β = 0.50(1). Error bars are not shown when they are less or equal to the size of symbols.

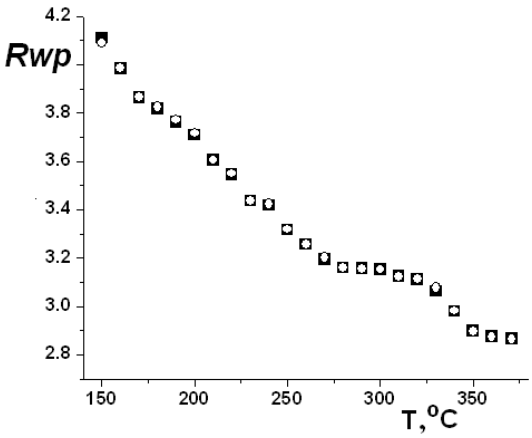

Figure 3.19. *Rwp*-factors for parametric (open symbols) and sequential (filled symbols) refinement for the rotational modes approach.

3.4.5. Conclusion

Temperature-dependent X-ray powder diffraction data reveal that Sr_2CoOsO_6 undergoes a high-temperature structural phase transition of second order. This phase transition is equally described using distortion modes and parametric refinement, based on classical distortion modes, rigid body refinement, and rotational modes refinement.

3.5. Publications and authors contribution

Chapters 3.2 and 3.3 were published:

1) Magdysyuk, O.V.; Müller, M.; Dinnebier, R.E.; Lipp, C.; Schleid, Th. (2014) Parameterization of the coupling between strain and order parameter for $LuF[SeO_3]$. *J. Appl. Cryst*. **47**, 701–711.

Chapter 3.4 will be published:

2) O.V. Magdysyuk *et al.* Parametric Rietveld refinement of the high-temperature structural phase transition in double perovskites (in preparation).

Dr. C. Lipp and Prof. Th. Schleid synthesized $LuF[SeO_3]$. M. Müller performed sequential Rietveld refinements, which were not included into the presented work. Dr. Avijit K. Paul, Prof. C. Felser, and Prof. M. Jansen synthesized Sr_2CoOsO_6. Support with synchrotron measurements at Diamond, I11 to Dr. J.E. Parker and Dr. C.C. Tang (Diamond Light Source, UK), and with synchrotron measurements at SLS (PSI), MS (proposal 20130236) to Dr. A. Cervellino (Swiss Light Source, Paul Scherrer Institut, Villigen, Switzerland), Mr. F. Adams (Max Planck Institute for Solid State Research, Stuttgart, Germany) is gratefully acknowledged.

3.6. References

Aroyo, M.I.; Perez-Mato, J.M. (1998). *Symmetry-Mode Analysis of Displacive Phase Transitions using International Tables for Crystallography. Acta Cryst.* A**54**, 19–30.

Avijit Paul, K.; Reehuis, M.; Felser, C.; Abdala, P.M.; Jansen, M. (2013). *Synthesis, Crystal Structure, and Properties of the Ordered Double Perovskite Sr_2CoOsO_6. Z. Anorg. Allg. Chem.* **639**(14), 2421–2425.

Balachandran, P.V.; Rondinelli, J.M. (2013). *Interplay of octahedral rotations and breathing distortions in charge-ordering perovskite oxides. Phys. Rev. B.* **88**, 054101.

Becerro, A.I.; Redfern, S.A.T.; Carpenter, M.A.; Knight, K.S.; Seifert, F. (2002). *Displacive phase transition in and strain analysis of Fe-doped $CaTiO_3$ perovskites at high-temperatures by neutron diffraction. J. Solid State Chem.* **167**, 459–471.

Bergamaschi, A.; Cervellino, A.; Dinapoli, R.; Gozzo, F.; Henrich, B.; Johnson I.; Kraft, P.; Mozzanica, A.; Schmitt, B.; Shi, X. (2010). *The MYTHEN detector for X-ray powder diffraction experiments at the Swiss Light Source. J. Synchrotron Rad.* **17**, 653–668.

Bismayer, U.; Salje, E.; Glazer, A.M.; Cosier, J. (1986). *Effect of Strain-Induced Order-Parameter Coupling on the Ferroelastic Behaviour of Lead Phosphate-Arsenate Phase Transitions.* **6**, 129–151.

Bruce, A.D.; Cowley, R.A. (1981). *Structural phase transitions.* Taylor and Francis, London, 326 p.

Campbell, B.J.; Stokes, H.T.; Tanner, D.E.; Hatch, D.M. (2006). *ISODISPLACE: a web-based tool for exploring structural distortions. J. Appl. Cryst.* **39**, 607–614.

Campbell, B.J.; Evans, J.S.O.; Perselli, F.; Stokes, H.T. (2007). *Rietveld refinement of structural distortion-mode amplitudes. IUCr Computing Commission Newsletter.* **8**, 81–95.

Carpenter, M.A.; Salje, E.K.H.; Graeme-Barber, A. (1998a). *Spontaneous strain as a determinant of thermodynamic properties for phase transitions in minerals. Eur. J. Mineral.* **10**, 621–691.

Carpenter, M.A.; Salje, E.K.H. (1998b). *Elastic anomalies in minerals due to structural phase transition. Eur. J. Mineral.* **10**, 693–812.

Carpenter, M.A. (2000). *Strain and elasticity at structural phase transitions in minerals. Reviews in Mineralogy and Geochemistry.* **39**, 35–64.

Carpenter, M.A.; Meyer, H.-W.; Sondergeld, P.; Marion, S.; Knight, K.S. (2003). *Spontaneous strain variations through the low-temperature phase transitions of deuterated lawsonite. Am. Mineral.* **88**, 534–546.

Carpenter, M.A.; Howard, C.J. (2009a). *Symmetry rules and strain/order-parameter relationships for coupling between octahedral tilting and cooperative Jahn–Teller transitions in ABX_3 perovskites. I. Theory. Acta Cryst.* **B65**, 134–146.

Carpenter, M.A.; Howard, C.J. (2009b). *Symmetry rules and strain/order-parameter relationships for coupling between octahedral tilting and cooperative Jahn–Teller transitions in ABX_3 perovskites. II. Application. Acta Cryst.* **B65**, 147–159.

Carpenter, M.A.; McKnight, R.E.A.; Howard, C.J.; Zhou, Q.; Kennedy, B.J.; Knight, K.S. (2009c). *Characteristic length scale for strain fields around impurity cations in perovskites. Phys. Rev. B.* **80**, 214101.

Carpenter, M.A.; Bryson, J.F.J.; Catalan, G.; Howard, C.J. (2012). *J. Phys.: Condens. Matter.* **24**, 045901.

Coelho, A.A. (2007). TOPAS. Version 4.1. Coelho Software, Brisbane, Australia.

Cowley, R.A. (1980). *Structural phase transitions. 1. Landau theory. Advances in Physics.* **29**, 1–110.

Dinnebier, R.E. (1999). *Rigid bodies in powder diffraction. A practical guide. Powder Diffraction.* **14**(2), 84–92.

Dove, M.T. (1997). *Theory of displacive phase transitions in minerals. Am. Mineral.* **82**, 213–244.

Glazer, A.M. (1972). *The Classification of Tilted Octahedra in Perovskites. Acta Cryst.* B**28**, 3384–3392.

Glazer, A.M.; Zhang, N.; Bartasyte, A.; Keeble, D.S.; Huband, S.; Thomas, P.A. (2010). *Observation of unusual temperature-dependent stripes in $LiTaO_3$ and $LiTa_xNb_{1-x}O_3$ crystals with near-zero birefringence. J. Appl. Cryst.* **43**, 1305–1313.

Halasz, I.; Dinnebier, R.E.; Angel, R. (2010). *Parametric Rietveld refinement fort he evaluation of powder diffraction patterns collected as a function of pressure. J. Appl. Cryst.* **43**, 504–510.

Hatch, D.M.; Artman, J.I.; Boerio-Goates, J. (1990). *Phase transition in potassium cadmium sulfate (K2Cd2(SO4)3): order parameter and microscopic distortions. Phys. Chem. Miner.* **17**, 334–343.

Hinrichsen, B.; Dinnebier, R.E.; Jansen, M. (2006). *Powder3D: An easy to use program for data reduction and graphical presentation of large numbers of powder diffraction patterns. Z. Krist.* S**23**, 231–236.

Kaduk, J.A.; Partenheimer, W. (1997). *Chemical accuracy and precision in Rietveid analysis: The crystal structure of cobalt(ll) acetate tetrahydrate. Powder Diffraction.* **12**(1). 27–39.

Landau, L.D.; Lifshitz, E.M. (1959). *Statistical Physics.* Pergamon, 484 p.

Le Bail, A.; Duroy, H.; Fourquet, J.L. (1988). *Ab-initio structure determination of $LiSbWO_6$ by X-ray powder diffraction. Mat. Res. Bull*. **23**, 447–452.

Lipp, C.; Schleid, Th. (2007). *$LuF[SeO_3]$ and $LuCl[SeO_3]$: Two Non-Isotypic Halide Oxoselenates(IV) of Lutetium. Z. Anorg. Allg. Chem.* **633**, 1429–1434.

Lipp, C.; Schleid, Th. (2009). *Die Selten-Erd-Metall(III)-Fluorid-Oxoselenate(IV) $MF[SeO_3]$ (M = Y, Ho–Lu) imYF[SeO_3]-Typ. Z. Naturforsch.* **64b***,* 375–382.

Lipp, C.; Dinnebier, R.E.; Schleid, Th. (2013). *$LuF[SeO_3]$: The Structural Chameleon of Lanthanoid Fluoride Oxoselenates(IV). Inorg. Chem.* **52**, 10788–10794.

Manes, J.L.; Tello, M.J.; Perez-Mato, J.M. (1982). *Symmetry modes and description of distorted phases in hexagonal ABX_3 compounds. Application to $KNiCl_3$ room-temperature structure. Phys. Rev. B.* **26**, 250–268.

Müller, M.; Dinnebier R.E.; Jansen, M.; Wiedemann, S.; Plüg, C. (2009). *Kinetic analysis of the phase transformation from α to β-copper phthalocyanine: A case study for sequential and parametric Rietveld refinements. Powder Diffraction.* **24**, 191–199.

Müller, M.; Dinnebier R.E.; Ali, N.Z.; Campbell, B.J.; Jansen, M. (2010). *Direct access to the order parameter: parameterized symmetry modes and rigid body movements as a function of temperature. Materials Science Forum.* **651**, 79–95.

Müller, M.; Dinnebier R.E.;Schorr, S. (2011). *A case study of parametrized Rietveld refinement: the structural phase transition of $CuInSe_2$*. Z. Kristallogr. **226**(12), 956–962.

Müller, M.; Dinnebier R.E.; Dippel, A-C.; Stokes, H.T.; Campbell, B.J. (2014). *A symmetry-mode description of rigid-body rotations in crystalline solids: a case study of $Mg(H_2O)_6RbBr_3$. J. Appl. Cryst.* **47**. (accepted).

Orobengoa, D.; Capillas, C.; Aroyo, M.I.; Perez-Mato, J.M. (2009). *AMPLIMODES: symmetry-mode analysis on the Bilbao Crystallographic Server. J. Appl. Cryst.* **42**, 820–833.

Parker, J.E.; Thompson, S.P.; Cobb, T.M.; Yuan, F.; Potter, J.; Lennie, A.R.; Alexander, S.; Tighe, C.J.; Darr, J.A.; Cockcroft, J.C.; Tang, C.C. (2011). *High-throughput powder diffraction on beamline I11 at Diamond. J. Appl. Cryst.* **44**, 102–110.

Perez-Mato, J.M.; Manes, J.L.; Tello, M.J.; Zuniga, F.J. (1981). *Structural phase transitions in crystals with $P6_3/mmc$ symmetry. J. Phys. C: Solid State Phys.* **14**, 1121–1132.

Perez-Mato, J.M.; Gaztelua, F.; Madariaga, G.; Tello, M.J. (1986). *Symmetry-mode analysis of the ferroelectric phase in K_2SeO_4. J. Phys. C: Solid State Phys.* **19**, 1923–1935.

Perez-Mato, J.M.; Salje, E.K.H. (2000). *Quantum fluctuations of order parameters in structural phase transitions and the pressure dependence of transition temperatures. J. Phys.: Condens. Matter.* **12**, L29–L34.

Perez-Mato, J.M.; Salje, E.K.H. (2001). *Order-parameter saturation at low-temperatures: displacive phase transitions with coupled Einstein oscillators. Philosophical Magazine Letters.* **81**(12), 885–891.

Rietveld, H.M. (1967). *Line profiles of neutron powder-diffraction peaks for structure refinement. Acta Cryst.* **22**, 151–152.

Rietveld, H.M. (1969). *A profile refinement method for nuclear and magnetic structures. J. Appl. Cryst.* **2**, 65–71.

Salje, E.K.H. (1985a). *Thermodynamics of Sodium Feldspar I: Order Parameter Treatment and Strain Induced Coupling Effects. Phys. Chem. Mineral.* **12**, 93–98.

Salje, E.K.H.; Kuscholke, B., Wruck, B.; Kroll, H. (1985b). *Thermodynamics of Sodium Feldspar II: Experimental Results and Numerical Calculations. Phys. Chem. Mineral.* **12**, 99–107.

Salje, E.; Devarajan, V. (1986). *Phase transitions in systems with strain-induced coupling between two order parameters. Phase Transitions.* **6**, 235–247.

Salje, E.K.H. (1990). *Phase transitions in ferroelastic and co-elastic crystals. Ferroelectrics.* **104**, 111–120.

Salje, E.K.H. (1991a). *Crystallography and Structural Phase Transitions, an Introduction. Acta Cryst.* **A47**, 453–469.

Salje, E.K.H. (1991b). *Some aspects of the thermodynamic behaviour of ferroelastic and co-elastic phase transitions. Phase Transition.* **34**, 25–52.

Salje, E.K.H.; Wruck, B.; Thomas, H. (1991c). *Order-parameter saturation and low-temperature extension of Landau theory. Z. Phys. B - Condensed Matter.* **82**, 399–404.

Salje, E. (1992). *Applications of Landau theory for the analysis of phase transitions in minerals. Phys. Rep.* **215**, 49–99.

Salje, E. (1993). *Phase transitions in ferroelastic and co-elastic crystals.* Cambridge University Press, Cambridge, 229 p.

Salje, E.K.H.; Hayward, S.A.; Lee, W.T. (2005). *Ferroelastic phase transitions: structure and micro-structure. Acta Cryst.* A**61**, 3–18.

Schmitt, B.; Brönnimann, Ch.; Eikenberry, E.F.; Gozzo, F.; Hörmann, C.; Horisberger, R.; Patterson, B. (2003). *Mythen detector system. Nuclear Instruments and Methods in Physics Research.* **A501**, 267–272.

Stephens, P.W. (1999). *Phenomenological model of anisotropic peak broadening in powder diffraction. J. Appl. Cryst.* **32**, 281–289.

Stinton, G.W.; Evans, J.S.O. (2007). *Parametric Rietveld refinement. J. Appl. Cryst.* **40**, 87–95.

Stokes, H.T.; Hatch, D.M. (1988). *Isotropy subgroups of the 230 crystallographic space groups.* World Scientific, Singapore.

Stokes, H.T.; Hatch, D.M. (1991a). *Coupled order parameters in the Landau theory of phase transitions in solids. Phase Transitions.* **34**, 53–67.

Stokes, H.T.; Hatch, D.M.; Wells, J.D. (1991b). *Group-theoretical methods for obtaining distortions in crystals: Applications to vibrational modes and phase transitions. Phys. Rev. B.* **43**, 11010–11018..

Tan, T.-Y.; Kennedy, B.J.; Zhou, Q.; Ling, C.D.; Miiller, W.; Howard, C.J.; Carpenter, M.A.; Knight, K.S. (2012). *Impact of Jahn-Teller active* Mn^{3+} *on strain effects and phase transitions in* $Sr_{0.65}Pr_{0.35}MnO_3$. *Phys. Rev. B.* **85**, 104107.

Thompson, S. P.; Parker, J. E.; Potter, J.; Hill, T. P.; Birt, A.; Cobb, T. M.; Yuan, F.; Tang, C. C. (2009). *Beamline I11 at Diamond: A new instrument for high resolution powder Diffraction. Rev. Sci. Instrum.* **80**, 075107.

Thompson, S. P.; Parker, J. E.; Marchal, J.; Potter, J.; Birt, A.; Yuan, F.; Fearn, R. D.; Lennie, A. R.; Street, S. R.; Tang, C. C. (2011). *Fast X-ray powder diffraction on I11 at Diamond. J. Synchrotron Rad.* **18**, 637–648.

Wadhawan, V.K. (1982). *Ferroelacticity and related properties of Crystals. Phase Transitions.* **3**, 3–103.

Willmott, P.R.; Meister, D.; Leake, S.J.; Lange, M.; Bergamaschi, A.; Böge, M.; Calvi, M.; Cancellieri, C.; Casati, N.; Cervellino, A.; Chen, Q.; David, C.; Flechsig, U.; Gozzo, F.; Henrich, B.; Jäggi-Spielmann, S.; Jakob, B.; Kalichava, I.; Karvinen, P.; Krempasky, J.; Lüdeke, A.; Lüscher, R.; Maag, S.; Quitmann, C.; Reinle-Schmitt, M.L.; Schmidt, T.; Schmitt, B.; Streun, A.; Vartiainen, I.; Vitins, M.; Wang, X.; Wullschleger, R. (2013). *The Materials Science beamline upgrade at the Swiss Light Source. J. Synchrotron Rad.* **20**, 667–682.

Zhang, Z.; Kennedy, B.J.; Howard, C.J.; Carpenter, M.A.; Miiller, W.; Knight, K.S.; Matsuda, M.; Miyake, M. (2012). *Crystal structures, strain analysis, and physical properties of* $Sr_{0.7}Ce_{0.3}MnO_3$. *Phys. Rev. B.* **85**, 174110.

Chapter 4

X-ray powder diffraction investigation of noble gas adsorption in metal-organic frameworks (MOFs)

4.1. Introduction

Noble gases play a significant role in many industrial and medical applications, but their practical using is restricted by high cost of noble gas separation due to the lack of chemical reactivity and very low boiling/melting points. A mixture of Xe and Kr noble gases is received by energetically intensive cryogenic distillation of air. This mixture can be further separated either by cryogenic distillation or, less expensive, by molecular sieves of nanoporous materials such as zeolites, MOFs, and activated carbon. Thus the development of new porous materials (zeolites and MOFs) for adsorption-based separation of noble gases is critically important for their industrial applications. MOFs have several advantages as compared to zeolites: cheaper and simpler synthesis, high diversity of pore structures, and numerous possibilities for postsynthetic modifications.

Despite the importance of MOFs for noble gas storage and separations, only few studies of krypton and xenon adsorption were reported to date (Mueller *et al.*, 2006; Farrusseng *et al.*, 2009; Thallapally *et al.*, 2012; Liu *et al.*, 2012, 2014; Meek *et al.*, 2012; Fernandez *et al.*, 2012; Soleimani Dorcheh *et al.*, 2012a; Bae *et al.*, 2013; Wang *et al.*, 2014), and only three studies of adsorption sites of noble gases in MOFs by means of X-ray or neutron diffraction (Rowsell *et al.*, 2005; Soleimani Dorcheh *et al.*, 2012b; Hulvey *et al.*, 2013), despite the fact that the major adsorption sites and their binding energies are the key features of a system that determines its adsorption properties at a given temperature and pressure, and their identification is a basis for further modifications of the crystal structure of the MOF in order to achieve maximal storage capacity and selectivity. The study of noble gas adsorption in HKUST-1 (Hulvey *et al.*, 2013) revealed that the interaction of noble gases with MOFs can be completely different from the adsorption of other atoms and molecules like D_2, C_2H_2, CO_2, or CH_4 (methane is a nonpolar gas whose diameter and polarizability are similar to those of Kr). They bind the open metal sites (Peterson *et al.*, 2006; Xiang *et al.*, 2009; Wu *et al.*, 2010a, 2010b), while structural investigations did not show any evidence of binding of noble gases Ne, Ar, Kr, and Xe with open metal sites (Hulvey *et al.*, 2013).

In this work, adsorption of Kr and Xe was investigated by means of X-ray powder diffraction in several MOFs with different topology: ZIF-8 (MOF with large pores and inaccessible metal sites), CPO-27-Ni and CPO-27-Mg (MOFs with channel structure and abundant open metal sites), Zn-MFU-4*l* and Cu-MFU-4*l* (MOFs with large pores and relatively low number of open metal sites). The importance of structural investigation is underlined by the fact, that molecular dynamic calculations not always lead to correct results for adsorption sites, *i.e.* for hydrogen adsorption on ZIF-8 only the first two adsorption sites out of six could be identified this way (Assfour *et al.*, 2010).

4.2. X-ray powder diffraction investigation of noble gas adsorption in MOFs

4.2.1. Laboratory X-ray powder diffraction investigation of noble gas adsorption in MOFs

An in-house developed gas loading system (Soleimani Dorcheh *et al.*, 2012b) was used for investigation of the Xe adsorption in Zn-MFU-4*l* and ZIF-8. Measurements were performed on a laboratory powder diffractometer (D8, Bruker, CuKα_1 radiation from a primary Ge(111)-Johannson-type monochromator; a Vånteg-1 position sensitive detector (PSD) with an opening angle of 6^o) in Debye–Scherrer geometry with the sample in an open quartz glass capillary of 0.5 mm diameter (Hildenberg). For gas loading, a modified version of an *in situ* capillary cell (Brunelli & Fitch, 2003) was used, which allows 180^o rocking of the capillary (Fig. 4.1). In order to be able to switch between vacuum pumping and gas loading, a T-connector to a turbo pump and a Xe gas bottle equipped with a needle valve were attached (Fig. 4.2). For heating of the capillary, a closed furnace was used (Fig. 4.3), while for cooling a Cryostream 600 cold nitrogen blower (Oxford Cryosystems) was attached horizontally (Fig. 4.4).

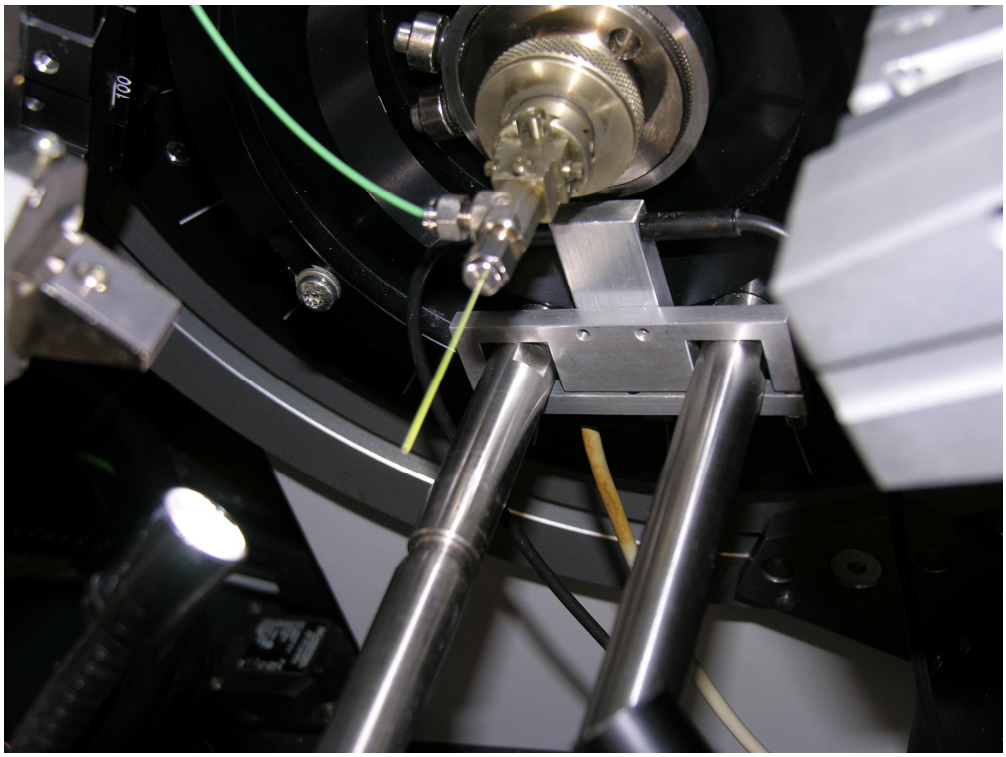

Figure 4.1. Capillary gas cell for *in situ* X-ray powder diffraction, installed with capillary on laboratory powder diffractometer Bruker-D8.

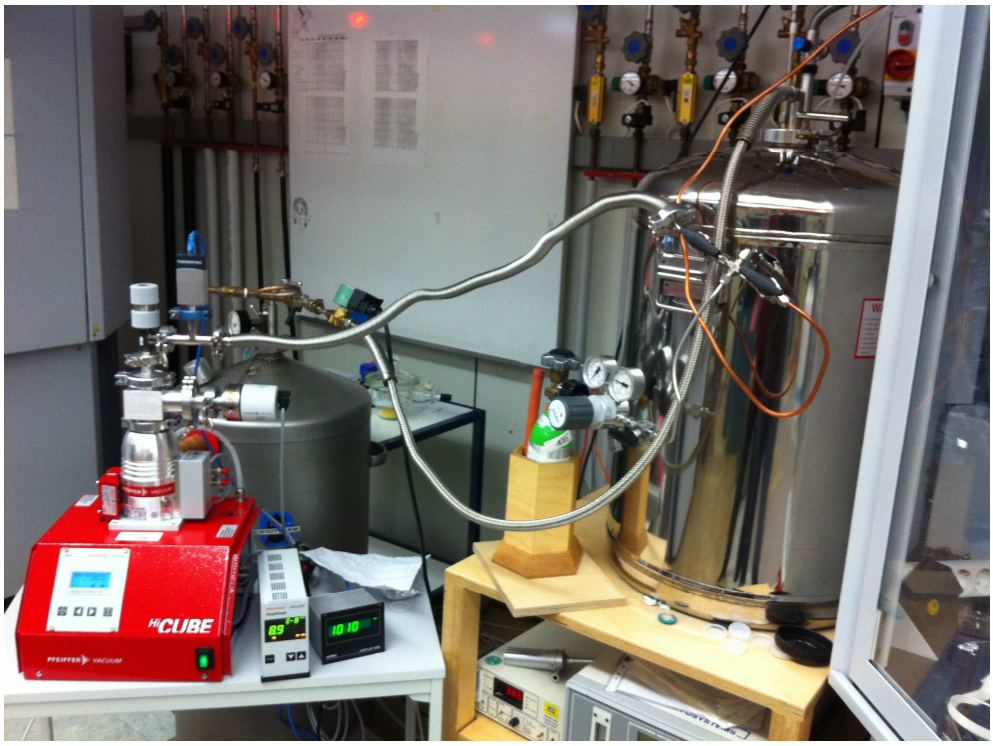

Figure 4.2. T-connector to a turbo pump and gas bottle equipped with a needle valve for switching between vacuum pumping and gas loading.

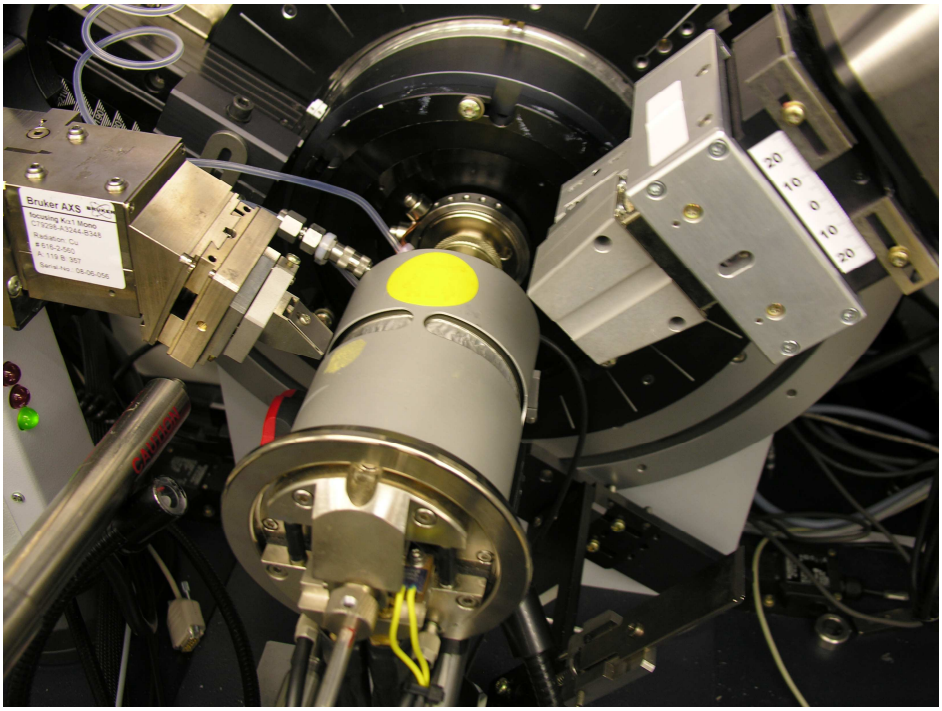

Figure 4.3. Installed closed furnace for heating capillary in gas cell (heating is possible under vacuum). Windows of the furnace are covered by aluminum foil and allow measurements during heating and evacuation of capillary.

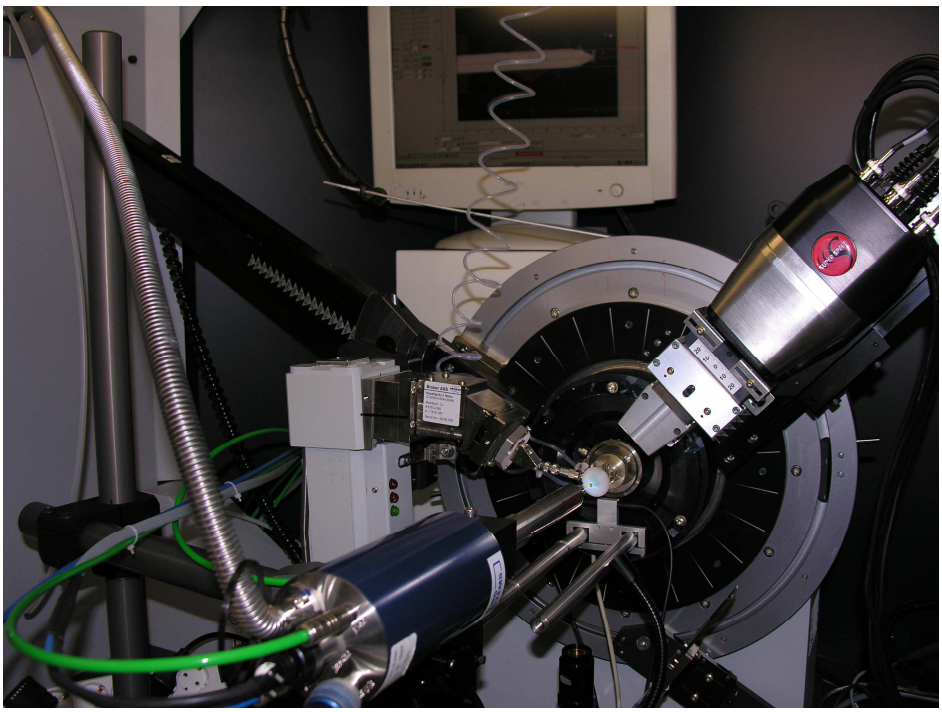

Figure 4.4. Installed cold nitrogen blower for capillary cooling in gas cell by liquid N_2 (cooling is possible under vacuum).

4.2.2. Synchrotron X-ray powder diffraction investigation of noble gas adsorption in MOFs

Synchrotron X-ray powder diffraction measurements of CPO-27-Ni (Kr and Xe adsorption), CPO-27-Mg (Kr adsorption), Zn-MFU-4*l* (Kr adsorption), Cu-MFU-4*l* (Kr and Xe adsorption), and ZIF-8 (Kr and Xe adsorption) were performed at beamline ID31 (λ = 0.4 Å) of the ESRF synchrotron facility (Grenoble, France). Synchrotron X-ray powder diffraction measurements of CPO-27-Ni (Kr and Xe adsorption), CPO-27-Mg (Xe adsorption), and Zn-MFU-4*l* (Xe adsorption) were performed at beamline P02.1 (λ = 0.20727 Ǻ) of the PETRA III synchrotron facility (Hamburg, Germany). All samples were loaded in quartz capillaries, activated *in situ*, and the evacuated MOFs were checked by Rietveld refinement for the absence of any solvent molecules before they were cooled and loaded with Kr or Xe of different pressures. The ESRF developed gas loading system was used for gas loading and measurements at ESRF (Figs. 4.5 and 4.6), while an in-house developed gas loading system (Soleimani Dorcheh *et al.*, 2012b) was used for gas loading at PETRA III (Fig. 4.7). All diffraction data were analyzed by the Rietveld method, simulated annealing and difference Fourier synthesis as implemented in the program TOPAS 4.1 (Coelho, 2007). The global optimization method of simulated annealing was used to determine the positions of the missing atoms, which were subsequently refined by Rietveld refinement. The final crystal structure was validated by difference Fourier maps.

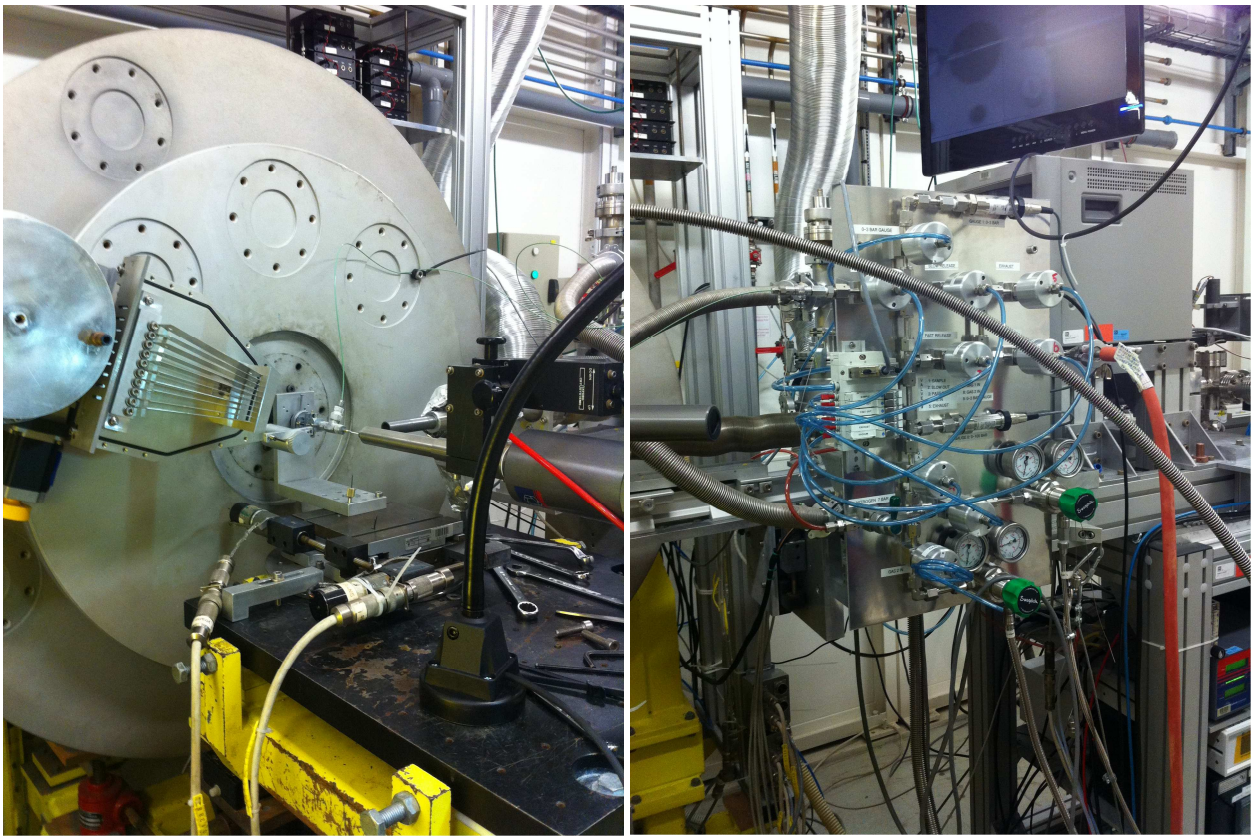

Figure 4.5. High-resolution X-ray powder diffractometer ID31 (ESRF) with installed gas cell (left) and gas loading system (right).

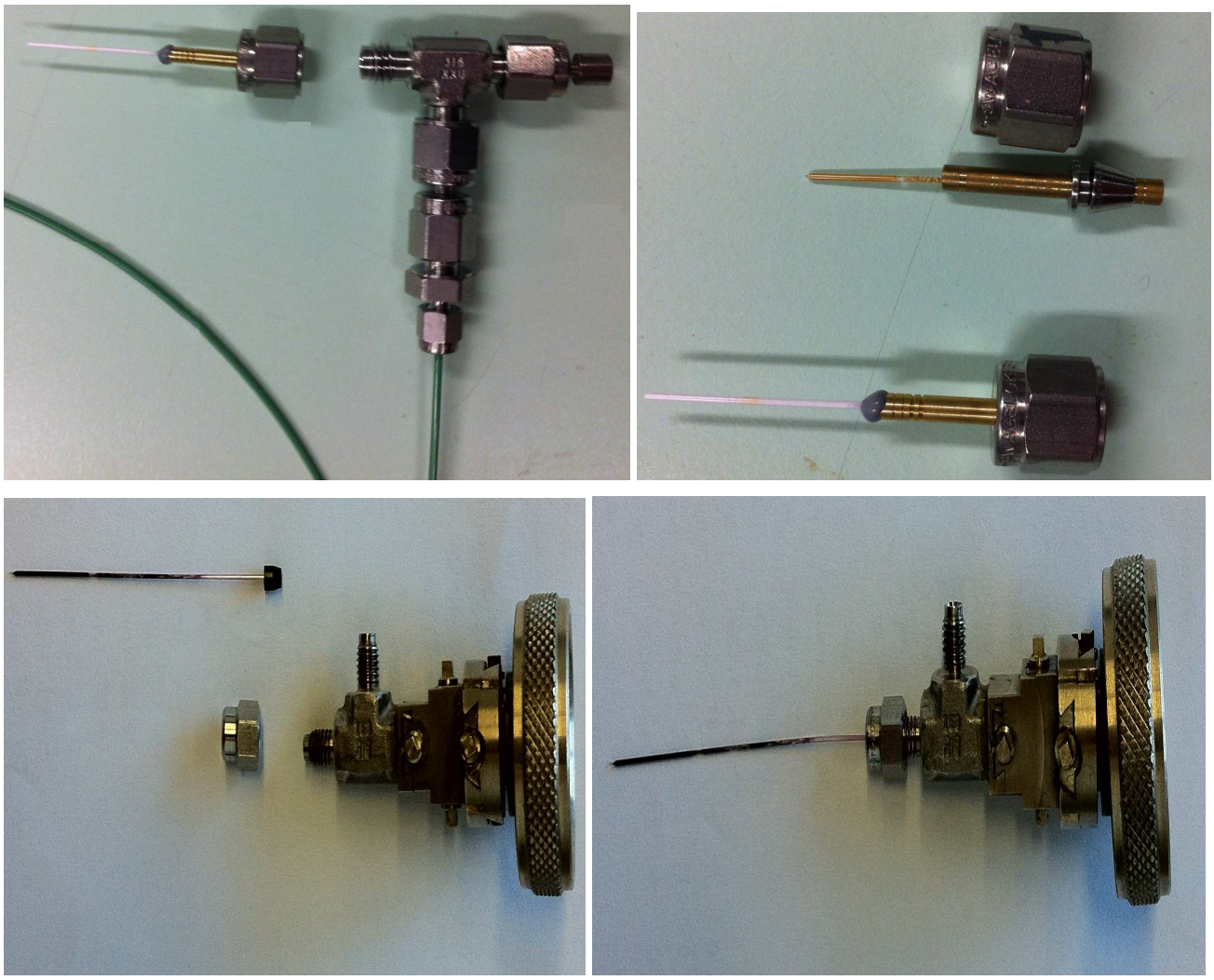

Figure 4.6. Top: gas cell with capillary at ID31 (ESRF); bottom: in-house gas cell with capillary (was used also for experiments at PETRA III (Hamburg)).

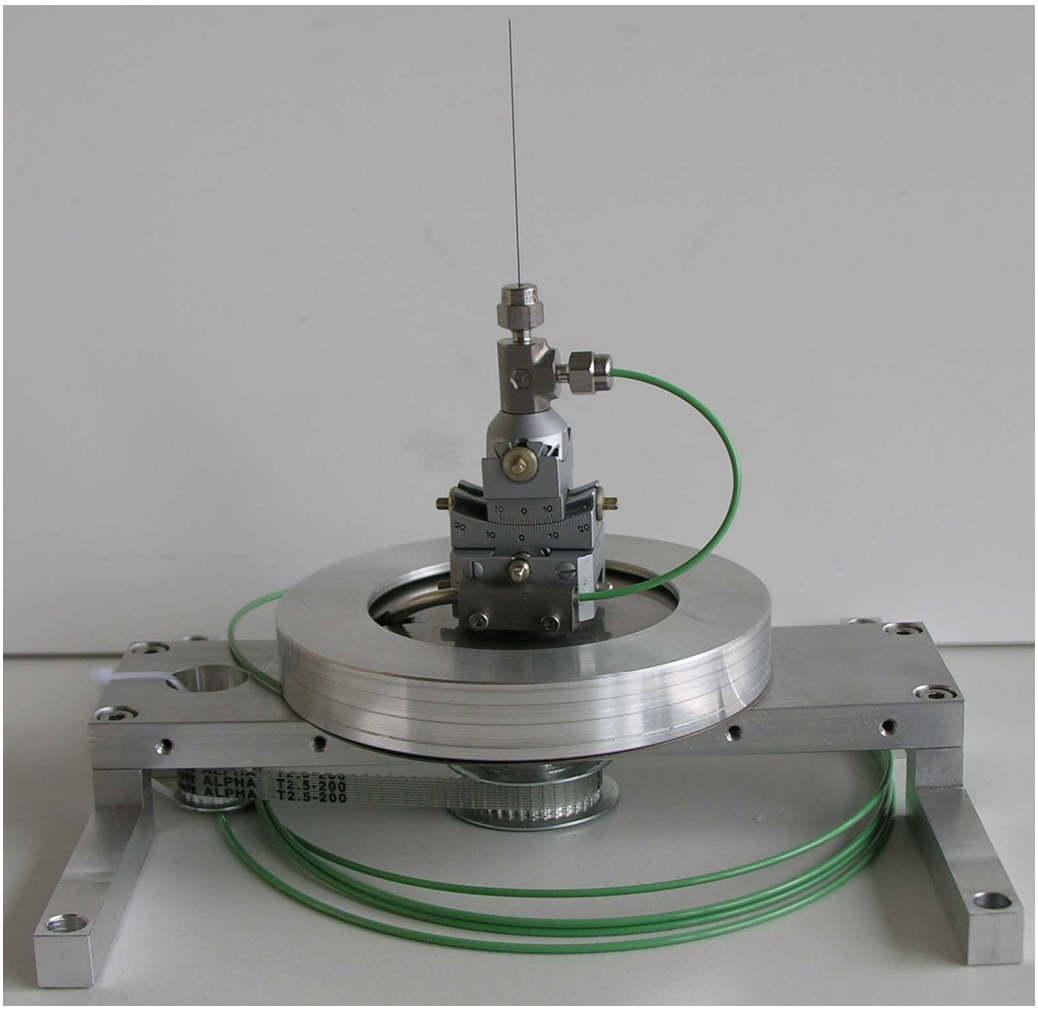

Figure 4.7. Capillary gas cell with capillary and rocking mechanism at P02 (PETRA III).

4.3. Structural investigation of noble gas adsorption in CPO-27-Ni and CPO-27-Mg

4.3.1. Background information

A recent detailed theoretical study revealed that CPO-27 is one of few promising MOFs for noble gas storage and separation due to relatively high selectivity, gas permeability, and working capacity (Sikora *et al.*, 2012; Gurdal & Keskin, 2012, 2013). Nevertheless, the origin of gas selectivity and the effect of different metal ions on the noble gas adsorption ability of CPO-27 are still unclear.

The metal-organic framework CPO-27 (MOF-74) was synthesized in 2005 by (Rosi *et al.*, 2005) and is still one of the most interesting MOFs due to several unique characteristics: highest concentration of open metal sites reported to date for MOFs (Märcz *et al.*, 2012), very high surface area, uniform 1D channels. Isosteric heats of adsorption up to 13 kJ mol^{-1} for hydrogen,

59 kJ mol^{-1} for carbon monoxide and 43 kJ mol^{-1} for carbon dioxide disclose very strong interactions between the porous host CPO-27 and accommodated gas molecules (Märcz *et al.*, 2012). Another attractive property of CPO-27 is the existence of a series of isostructural MOFs obtained by replacement of the metal atom, thus providing the unique possibility to investigate the influence of different metal ions (Zn, Co, Ni, Mg, Mn, Fe, Cu, Zn/Co, Mg/Ni, Cd) for adsorption properties (Rosi *et al.*, 2005; Dietzel *et al.*, 2005, 2006; Caskey *et al.*, 2008; Zhou *et al.*, 2008; Bloch *et al.*, 2011; Botas *et al.*, 2011; Märcz *et al.*, 2012; Sanz *et al.*, 2013; Kahr *et al.*, 2013, Diaz-Garcia & Sanchez- Sanchez, 2014), as well as the possibility to expand the pore apertures of CPO-27 to the isoreticular series with pore apertures ranging from 14 to 98 Å (Deng *et al.*, 2012), diverse possibilities for postsynthetic fictionalization (Liu *et al.*, 2014; Bae *et al.*, 2014; Cozzolino *et al*., 2014), and preserving of the 1D tube-like topology even when an organic linker different from 2,5-dioxido-1,4-benzenedicarboxylate is used (Liu *et al.*, 2013).

CPO-27 is composed of M^{II} cations generating linear, infinite-rod secondary building units (SBUs) bound by 2,5-dioxido-1,4-benzenedicarboxylate (DOBDC) organic linker, resulting in a hexagonal, 1D pore structure (Fig. 4.8). The pores are filled with H_2O molecules, which complete the coordination sphere of the M^{II} cations (5 oxygens from organic linker and one oxygen from water molecule). The water molecules are removed upon heating and/or evacuation in order to generate coordinately unsaturated metal sites (Dietzel *et al.*, 2006, Dietzel *et al.*, 2008a). The activated material has a characteristic honeycomb structure composed of 1D channels with abundant open metal sites. Since CPO-27 with different metal atoms constitutes an isostructural series of compounds, they are an excellent subject for studying the influence of the specific metal on the properties of the material.

Adsorption of different gases in CPO-27 has been intensively studied including several X-ray and neutron powder diffraction investigations in order to resolve preferable adsorption sites for guest atoms and molecules and the sequence of their filling. For different molecules: O_2 and N_2 in CPO-27-Fe (Bloch *et al.*, 2011), CO_2 in CPO-27-Ni (Dietzel *et al.*, 2008b) and CPO-27-Mg (Wu *et al.*, 2010b), CH_4 in CPO-27-Mg (Wu *et al.*, 2009a), H_2S in CPO-27-Ni (Chavan *et al.*, 2013), and C_2H_2 in CPO-27-Co (Xiang *et al.*, 2010), C_2H_2, C_2H_4, C_2H_6, C_3H_6, and C_3H_8 in CPO-27-Fe (Bloch *et al.*, 2012) the open metal sites were found to be preferable and thus immediately occupied.

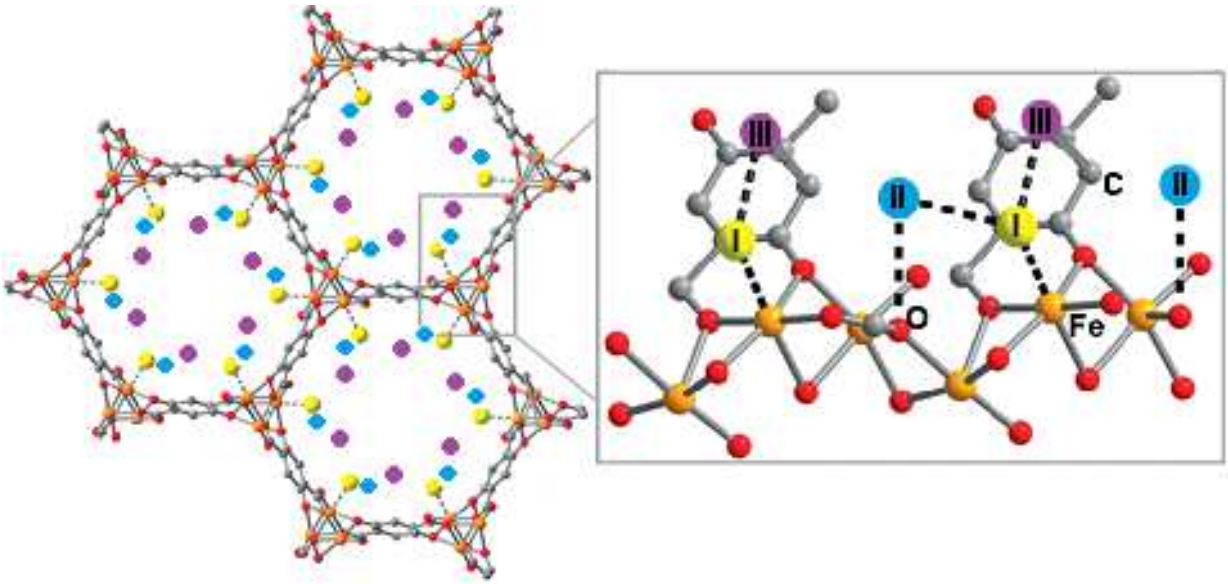

Figure 4.8. Projection of the crystal structure of CPO-27 along *c*-axis with intercalated D_2 molecules.

Neutron powder diffraction measurements of D_2 adsorption on CPO-27-Zn, CPO-27-Mg, and CPO-27-Fe revealed four adsorption sites for the D_2 molecule (Liu *et al.*, 2008; Sumida *et al.*, 2011; Queen *et al.*, 2012). In all MOFs the strongest adsorption site was indentified near the metal atom. The second strongest adsorption site appears almost simultaneously with the first and was located near the carboxylate oxygen of the organic linker in CPO-27-Mg and near the triangle of oxygen atoms from the organic linker in CPO-27-Zn and CPO-27-Fe. The third adsorption site for CPO-27-Zn and CPO-27-Fe was indentified near the benzene ring with a nearest distance to the framework atoms of ≈3.3 Å and the fourth adsorption site for CPO-27-Zn was found to be disordered inside the channels.

4.3.2. X-ray powder diffraction investigation of noble gas adsorption in CPO-27-Ni and CPO-27-Mg

Synchrotron X-ray powder diffraction measurements were performed at different temperatures (170 K and 250 K for Xe; 130 K, 170 K, 250 K for Kr) and gas pressures (50 mbar, 100 mbar, 250 mbar, 500 mbar, 1000 mbar). Samples were evacuated at 180°C for 2-3

hours before gas loading, and checked by Rietveld refinement (Fig. 4.9). Then they were cooled down to room-temperature and exposed to Kr or Xe gas. Before changing the gas pressure, samples were heated 30 K above the measurement's temperature.

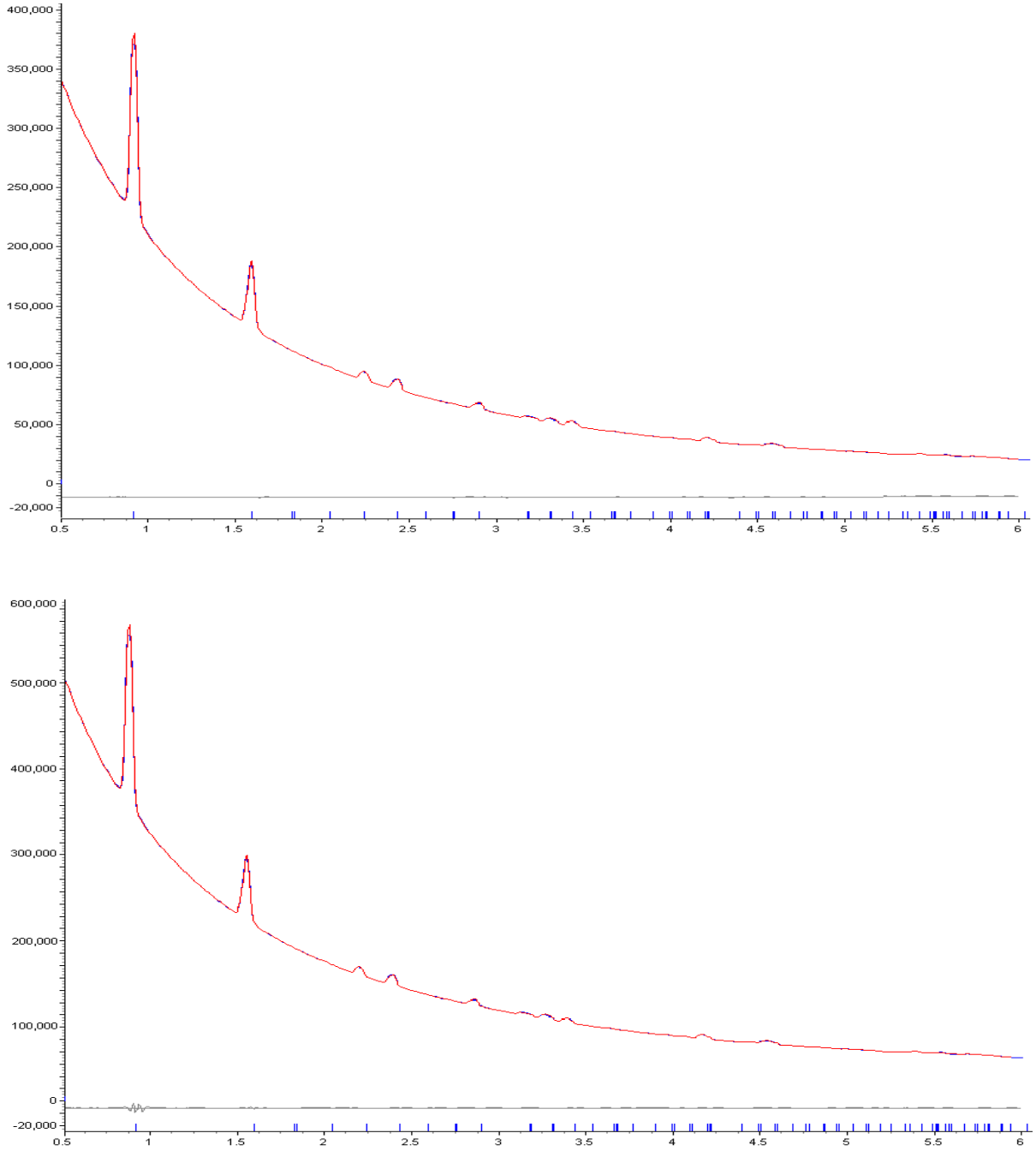

Figure 4.9. Rietveld plots of evacuated CPO-27-Ni (top) and CPO-27-Mg (bottom).

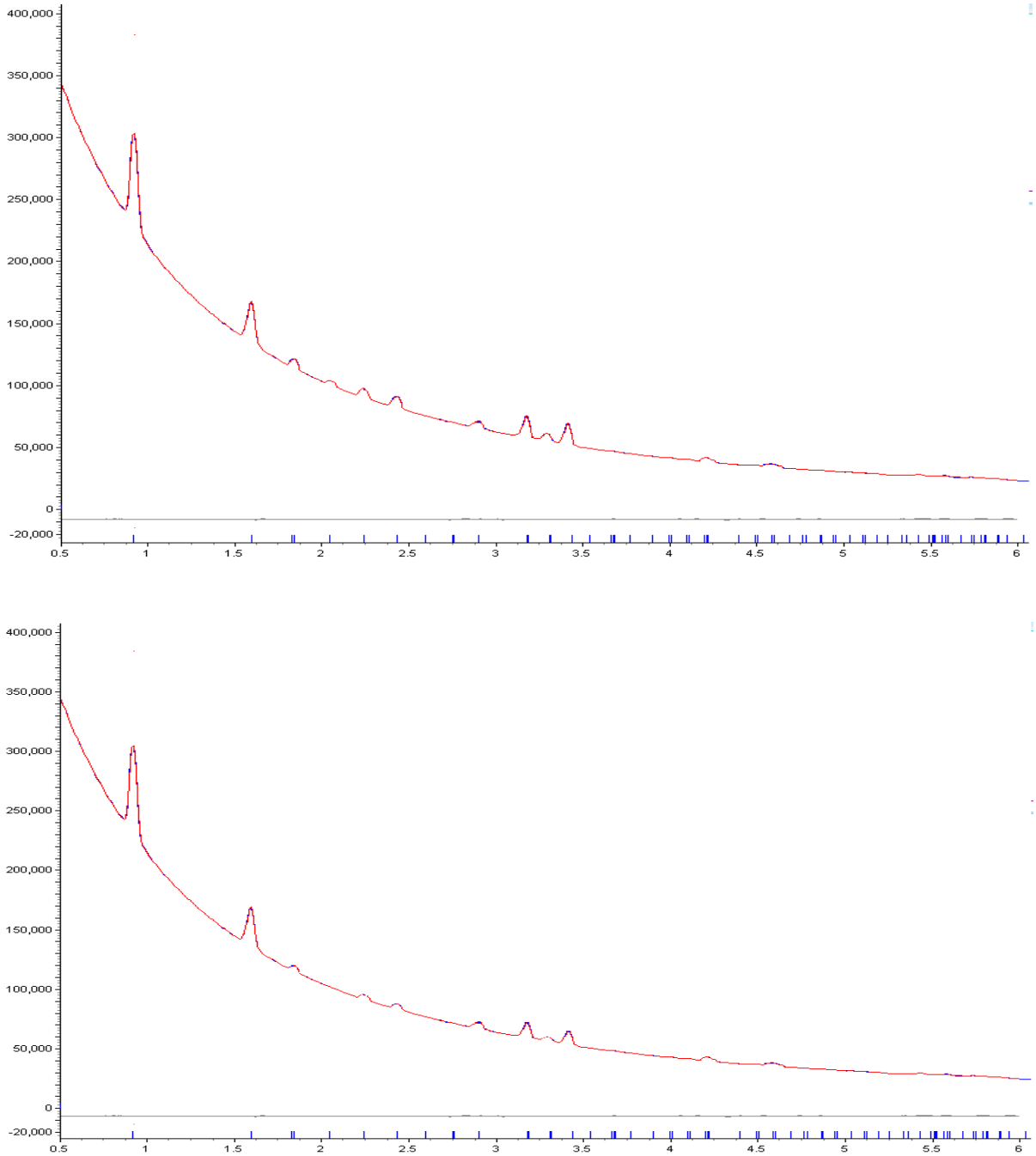

Figure 4.10. Rietveld plots of CPO-27-Ni with 1000 mbar of Xe (top) and Kr (bottom) at 170K.

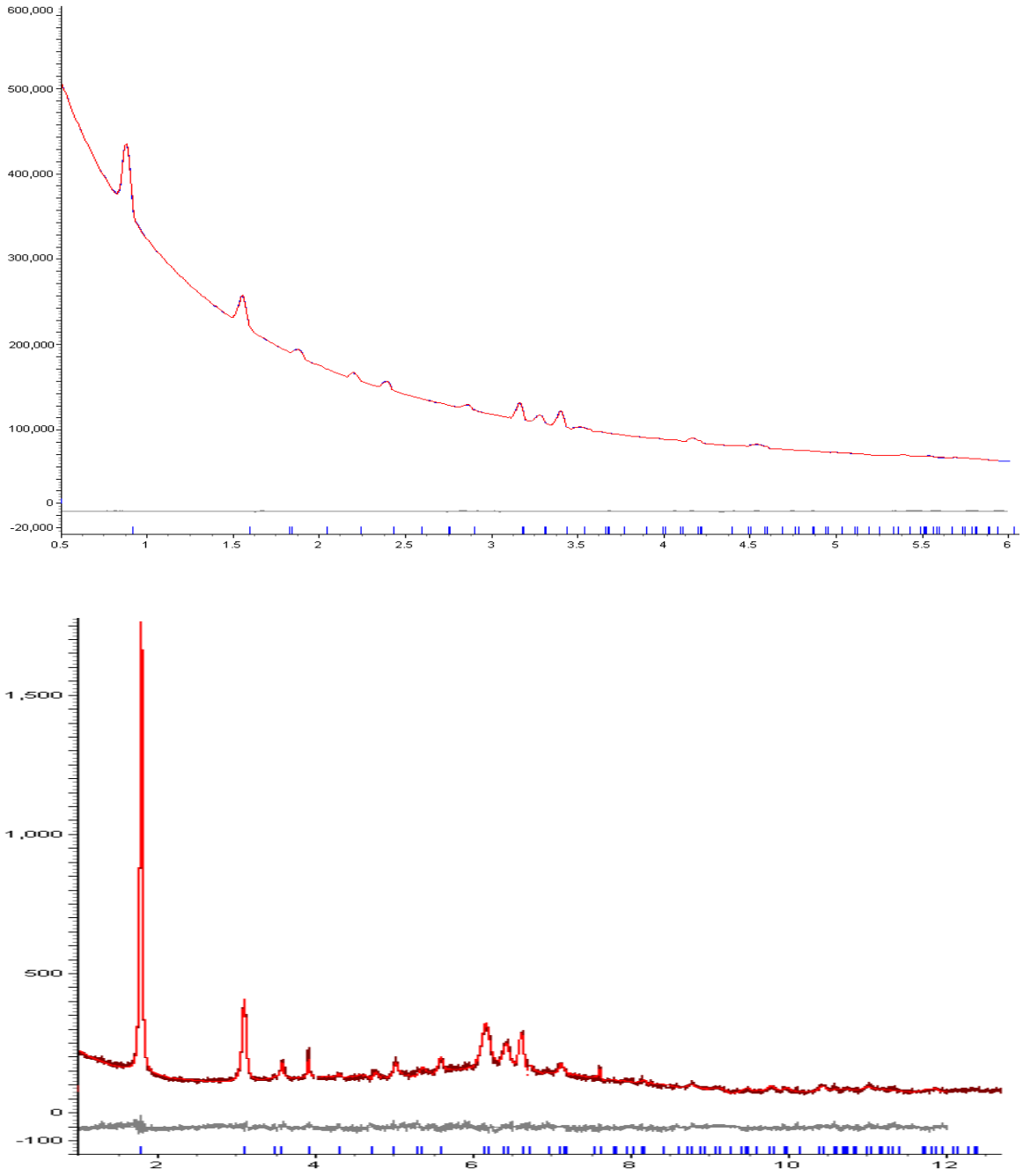

Figure 4.11. Rietveld plots of CPO-27-Mg with 500 mbar of Xe (top) and Kr (bottom) at 170K.

Structural investigations of the adsorption process of noble gases in CPO-27 were supported by gas adsorption measurements and determination of isosteric heat of adsorption. Experimental heats of adsorption curves were determined from measured gas adsorption isotherms at temperatures 180^{o}C, 200^{o}C, and 220^{o}C by applying the Clausius-Clayperon equation (Figs. 4.12 and 4.13).

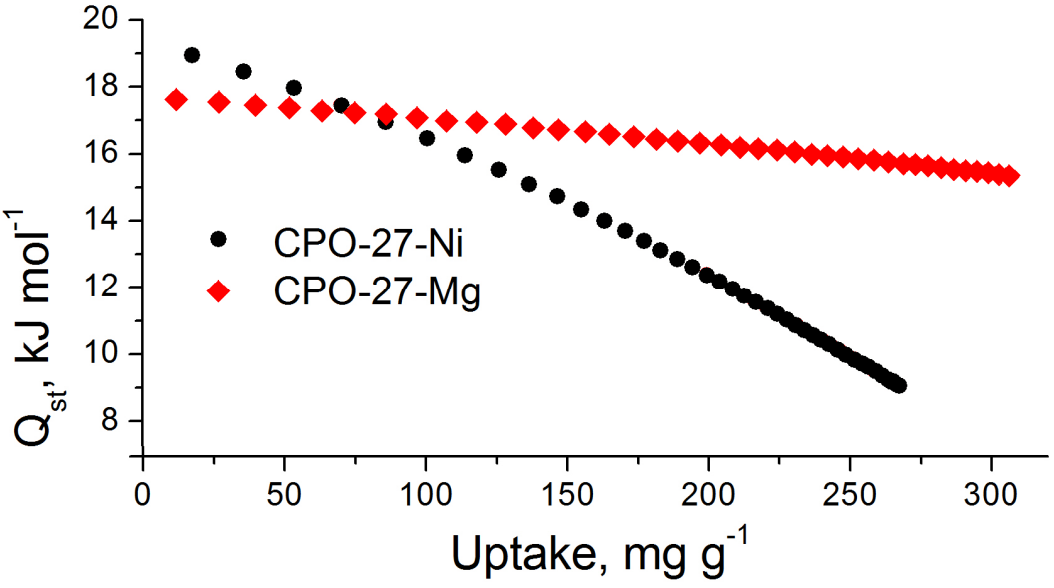

Figure 4.12. Isosteric heat of Kr adsorption for CPO-27-Ni and CPO-27-Mg.

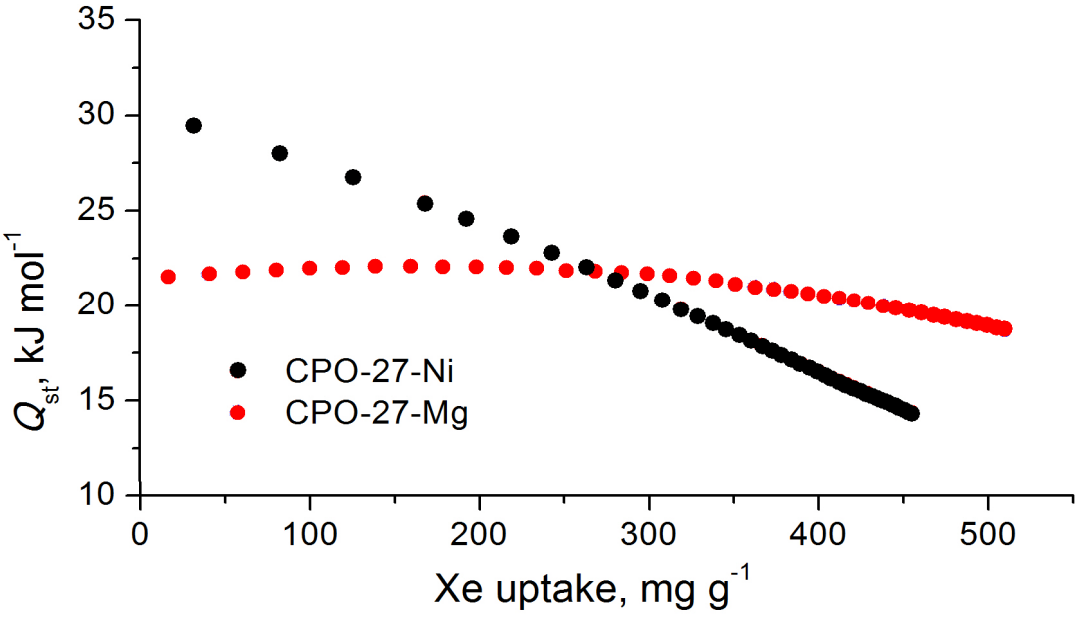

Figure 4.13. Isosteric heat of Xe adsorption for CPO-27-Ni and CPO-27-Mg.

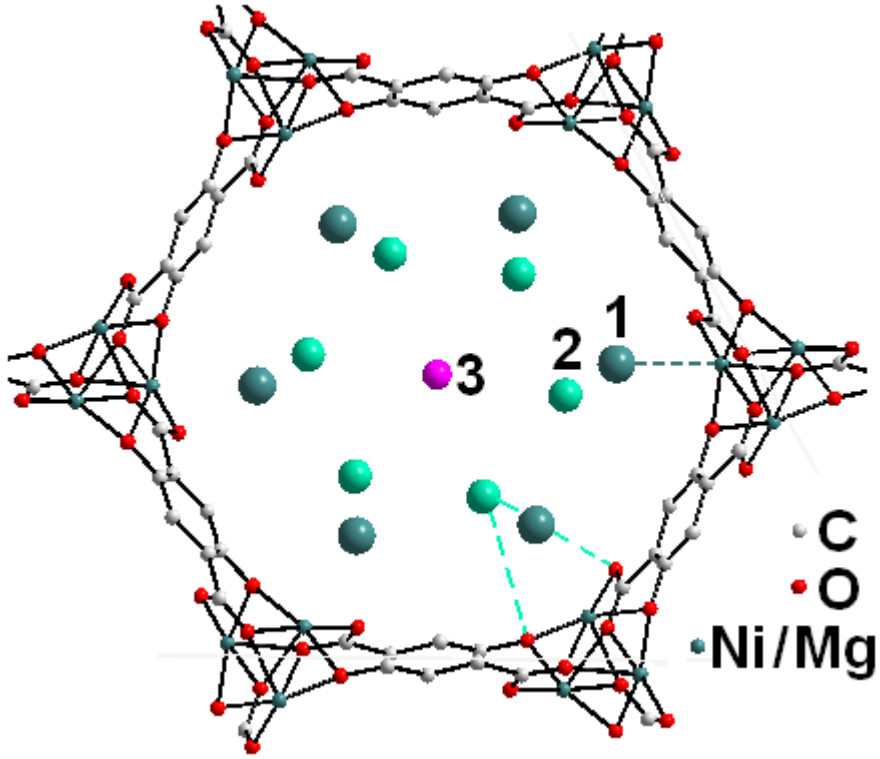

Figure 4.14. Crystallographically different positions of Kr and Xe atoms (numbers 1, 2, and 3) in 1D channel of CPO-27-Ni and CPO-27-Mg (projection along c-axis).

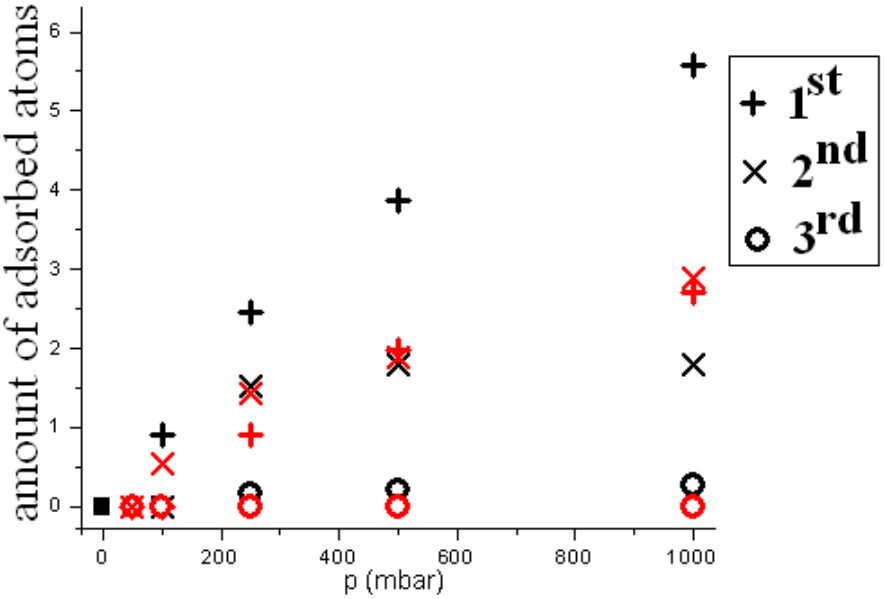

Figure 4.15. Amount of adsorbed Kr atoms by CPO-27-Ni (black symbols) and CPO-27-Mg (red symbols) at 250K at different gas pressures in each of the three identified positions.

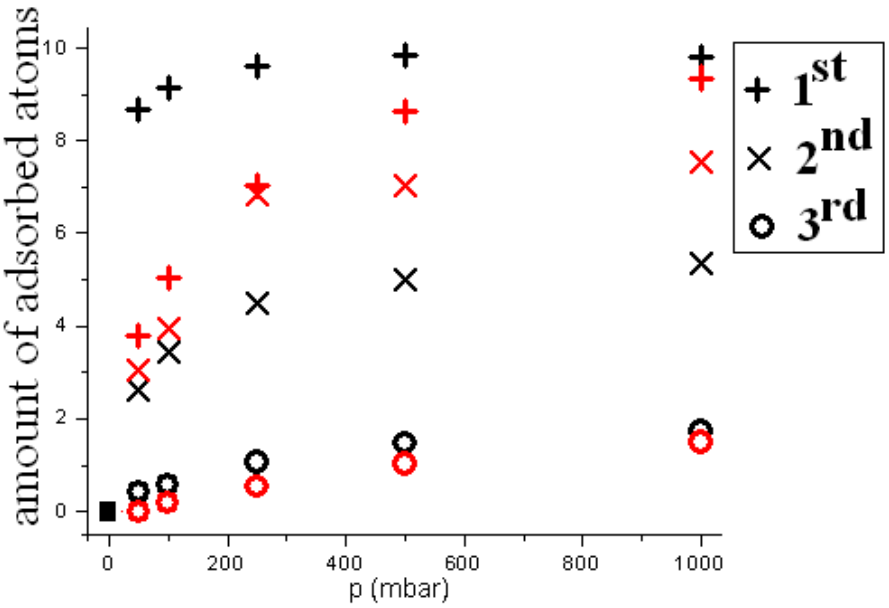

Figure 4.16. Amount of adsorbed Kr atoms by CPO-27-Ni (black symbols) and CPO-27-Mg (red symbols) at 170K at different gas pressures in each of the three identified positions.

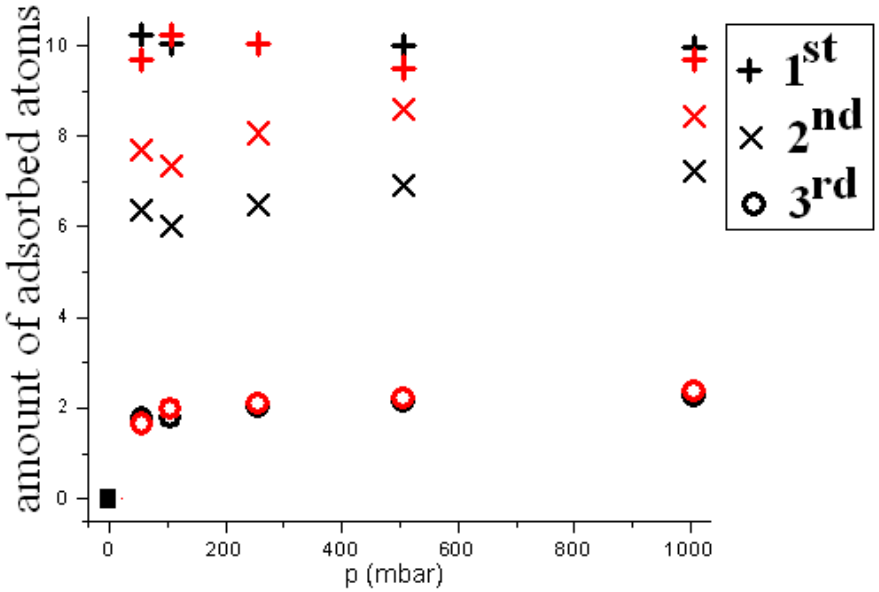

Figure 4.17. Amount of adsorbed Kr atoms by CPO-27-Ni (black symbols) and CPO-27-Mg (red symbols) at 130K at different gas pressures in each of three identified positions.

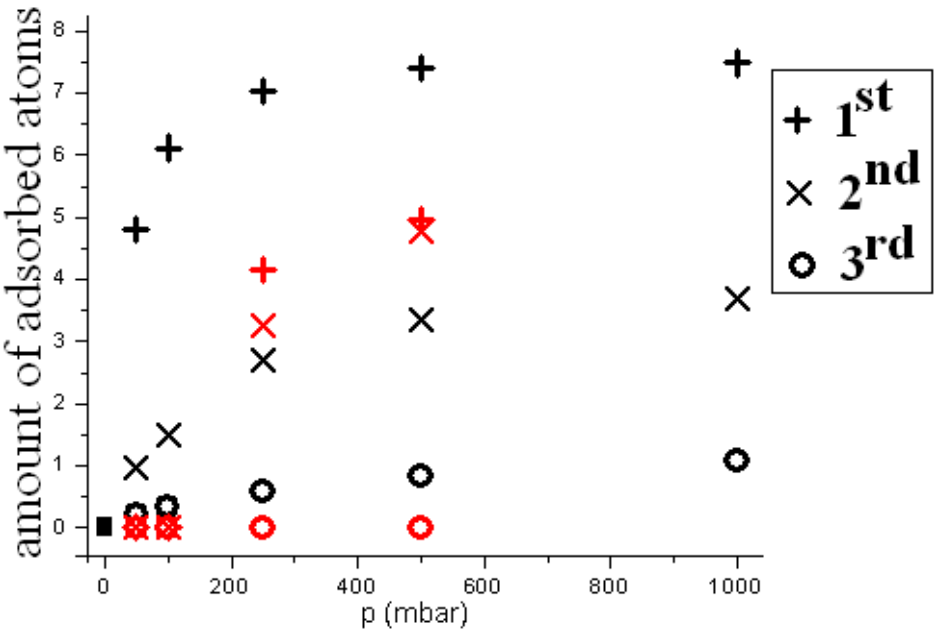

Figure 4.18. Amount of adsorbed Xe atoms by CPO-27-Ni (black symbols) and CPO-27-Mg (red symbols) at 250K at different gas pressures in each of the three identified positions.

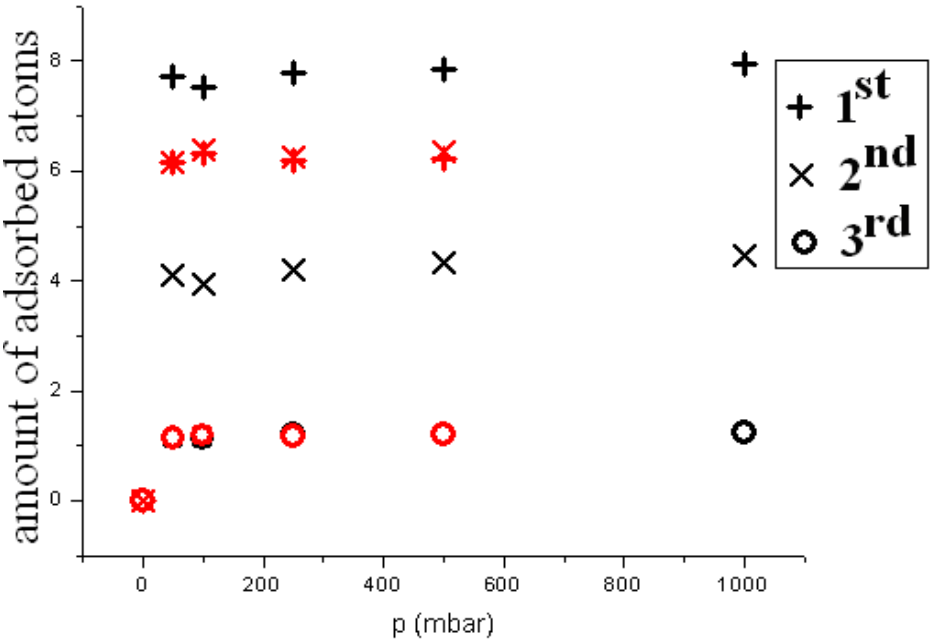

Figure 4.19. Amount of adsorbed Xe atoms by CPO-27-Ni (black symbols) and CPO-27-Mg (red symbols) at 170K at different gas pressures in each of the three identified positions.

Rietveld refinements of CPO-27-Ni and CPO-27-Mg loaded with Kr and Xe (Figs. 4.10 and 4.11) revealed that the preferable adsorption positions for Kr are similar to those of Xe in the corresponding MOF with only slight differences in the refined positions (Fig. 4.14).

The crystal structure of CPO-27-Ni determined for low loading of Xe and Kr confirms that the open 5-coordinated metal ion sites are the strongest adsorption sites with a Ni-Xe distance of 3.01(2) Å and a Ni-Kr distance of 3.03(3) Å at 1000 mbar. The second adsorption site for Xe is located at a distance of 4.10(3) Å from the carboxylate oxygen and at 4.23(3) Å from the oxygen atoms of the benzene ring (170K, 1000 mbar). The second adsorption site for Kr is located at a distance of 4.02(3) Å from the carboxylate oxygen and 4.10(3) Å from the oxygen atoms of the organic linker (130K, 1000 mbar), having approximately half the occupancy of the first adsorption site at all measured temperatures. The second adsorption site appears almost simultaneously with the first adsorption site. The third adsorption site for both, Xe and Kr, is located in the center of the channels and represents unbounded noble gas atoms. With increasing pressure, the amount of unbounded adsorbed Xe approaches 1 atom per unit cell at 170K. The amount of adsorbed unbounded Kr is close to 2 atoms per unit cell at 130K, and drops to ca. 0.3 atoms per unit cell at 250K. The maximal amount of adsorbed Xe corresponds to 0.75 Xe atoms per Ni atom at 170K (1000 mbar), and ca. 0.65 Xe atoms per Ni atom at 250K (1000 mbar), (ca. 0.6 Xe atoms per Ni atom at 250K, 500 mbar), but saturation of Xe adsorption is not reached at 250K, 1000 mbar and the amount of adsorbed Xe can be increased by further increasing gas pressure. The maximal amount of adsorbed Kr corresponds to ca. 1.0 Kr atom per Ni atom at 130K, 0.95 Kr atom per Ni atom at 170K, and 0.45 Kr atom per Ni atom at 250K.

Unexpected Xe and Kr adsorption behavior was found for CPO-27-Mg. In this case the second binding site near the oxygen atoms is almost simultaneously occupied with the first binding site near the open metal ion and has a similar value of the occupancy factor. The Mg-Xe distance is 3.14(2) Å at 170K (500 mbar), and the Mg-Kr distance is 3.23(3) Å at 130K (1000 mbar). The second adsorption site for Xe is at a distance of 4.10(3) Å from the carboxylate oxygen group and at a distance of 4.23(3) Å from the oxygen atoms of the benzene ring (170K, 500 mbar). The second adsorption site for Kr is at 3.92(3) Å from the carboxylate oxygen group and 3.96(3) Å from the oxygen atoms of the benzene ring (130K, 1000 mbar). The third adsorption site for both, Xe and Kr, is located in the center of the channel, and its occupancy is highest at lowest temperatures and is decreasing with increasing temperature. At 250K the third

adsorption site is unoccupied since the first and the second strong adsorption sites are not fully occupied at this temperature. The maximal amount of adsorbed Xe corresponds to 0.75 Xe atom per Mg atom at 170K, and ca. 0.55 Xe atoms per Mg atom at 250K (500 mbar), but saturation of Xe adsorption is not reached at 250K, 500 mbar and can be increased by further increasing gas pressure. The maximal amount of adsorbed Kr corresponds to ca. 1.1 Kr atoms per Mg atom at 130K, 1.0 Kr atoms per Mg atom at 170K, and 0.3 Kr atoms per Mg atom at 250K (1000 mbar). Thus, CPO-27-Mg shows weaker binding to both Xe and Ke atoms than CPO-27-Ni, presumably due to the larger polarizability of the Ni atom in comparison to the Mg atom. In contrast to noble gas adsorption, the adsorption of methane in CPO-27-Mg revealed much stronger binding of the CD_4 molecule to open metal sites than to the second adsorption site near oxygen atoms (Wu *et al.*, 2009a)

The experimental results for CPO-27 revealed that the open metal sites are the major (in the case of Ni^{2+}) or one of two major (in the case of Mg^{2+}) binding sites for Xe and Kr gases. On the other site, a recent report of noble gas adsorption in HKUST-1 (Hulvey *et al.*, 2013) did not show any interaction of noble gas atoms with open Cu^{2+} metal sites. Thus, noble gas adsorption behavior depends not only on the presence of the open metal sites, but also on the pore's topology. The small pockets in HKUST-1 provide strong geometrical confinement of noble gas atoms, while the uniform channels of CPO-27 do not imply geometrical restrictions on noble gas adsorption, and more easily polarizable sites along the channels are the main adsorption sites.

For the noble gas atoms, the only mechanism to interact with the framework is based on its polarizability and the polarizability of adsorption sites. The polarizability of Xe atoms exceeds the polarizability of Kr atoms, and polarizable metal ions enhance the interaction with noble gas atoms. This effect is responsible for noble gas adsorption in CPO-27-Ni. On the other hand, CPO-27-Mg possesses a less polarizable metal ion, but highly polarizable oxygen atoms from carboxylate groups, providing more homogeneous distribution of adsorption sites along the channels.

The measured heat of adsorption of CPO-27-Mg is 18(1) kJ/mol for Kr and 22(1) kJ/mol for Xe at low loadings, remaining almost unchanged over the measured pressure range (Figs. 4.12 and 4.12). The measured heat of adsorption of CPO-27-Ni is 19(1) kJ/mol for Kr and 30(1) kJ/mol for Xe at low loadings, dropping nearly by a factor of 2 with increasing loading (Figs.

4.12 and 4.12), indicating strong interaction between open metal sites and adsorbed atoms. The small variation of isosteric heats of adsorption for CPO-27-Mg during Kr and Xe adsorption indicates homogeneity of distribution of adsorption sites along the channels and is fully consistent with the presence of two major adsorption sites with a very similar binding strength: open metal sites Mg^{2+} and carboxylate oxygen atoms. A similar effect was observed for isosteric heat of adsorption of Ar, Kr, and Xe in porous $Co_3(HCOO)_6$ (Wang *et al.*, 2014): accessible but not abundant metal sites and oxygen atoms from C=O bonds are homogeneously distributed along the channels, and the isosteric heat of adsorption of noble gases remains almost constant. CPO-27-Ni shows a more heterogeneous distribution of adsorption sites along the channels – the open metal sites provide stronger binding of noble gas atoms than the oxygen groups, and this is reflected in a strong variation of isosteric heat of adsorption as a function of loading, when filling of available open metal sites leads to a decrease of isosteric heat of adsorption. The experimental results indicates that CPO-27-Ni possesses better selectivity in Xe/Kr separation than CPO-27-Mg.

The reported isosteric heat of adsorption of CH_4 is 18(1) kJ/mol for CPO-27-Mg and 19(1) kJ/mol for CPO-27-Ni and remains almost unchanged with increasing loading (Yu *et al.*, 2013). This allows some speculations, that both CPO-27-Mg and CPO-27-Ni can have two main adsorption sites of similar strength for methane molecules – open metal sites and oxygen groups. There is also a possibility of strong attractive interaction between adsorbed CH_4 molecules, which can compensate the decrease of the isosteric heat of adsorption due to heterogeneous distribution of the adsorption sites. The structural investigations of CH_4 adsorption in CPO-27 would allow comparison of similarities and differences of adsorption process of noble gases and methane in these MOFs. The isosteric heat of adsorption of hydrogen is slightly higher for CPO-27-Ni then for CPO-27-Mg, and remains constant until ca. one hydrogen atom per metal atom is adsorbed (Dietzel *et al.*, 2010), and the corresponding metal-H_2 distances are shorter for CPO-27-Ni (Zhou *et al.*, 2008), thus, the binding energy of H_2 at the nickel open metal site is stronger in comparison to the magnesium open metal site.

4.4. Structural investigation of noble gas adsorption in ZIF-8.

4.4.1. Background information.

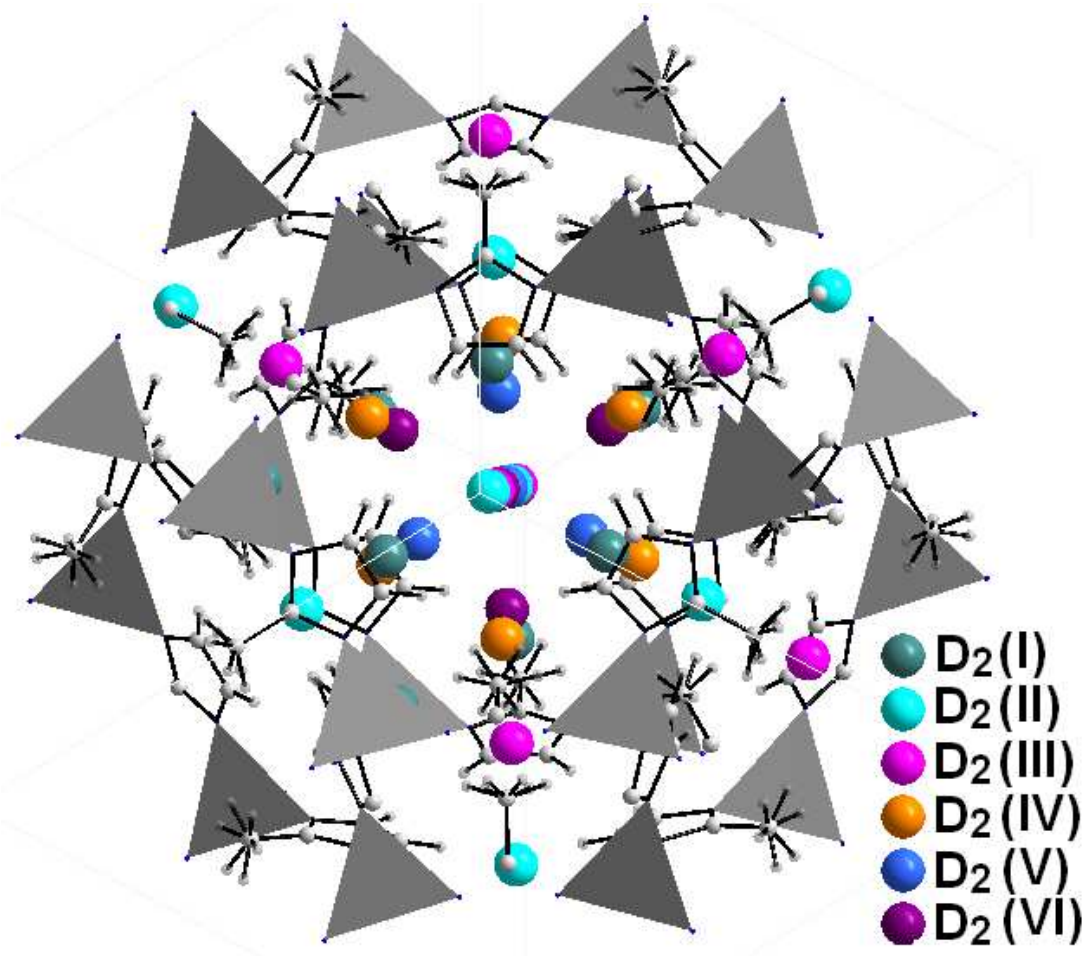

Figure 4.20. Crystal structure of ZIF-8 with intercalated D_2 molecules, (Wu *et al.*, 2007). Grey polyhedra – ZnN_4, gray spheres – carbon (large) and hydrogen (small).

Recently, large selectivity of ZIF-8 for Xe/Kr separation was predicted from single adsorption isotherm measurements, with ratio of ~ 8 at low pressure, decreasing to ~ 5.5 at a pressure above 1000 mbar (Ryan *et al*., 2011, 2014). Isosteric heat of adsorption of 20 kJ/mol for Xe and of 14 kJ/mol for Kr was reported, remaining almost constant upon gas loading up to 1000 mbar (Ryan *et al*., 2014).

ZIF-8 belongs to the class of zeolitic imidazolate frameworks (ZIFs). It consists of tetrahedral clusters of ZnN_4 linked by 2-methylimidazolate ligands, forming a sodalite-type structure (Huang *et al.*, 2006; Park *et al.*, 2006). Nanopores are accessible only through narrow channels, and even adsorption of small H_2 molecules was not expected (Wu *et al.*, 2007). Recent

investigations showed that ZIF-8 can adsorb even C_4 hydrocarbon molecules with an effective diameter size of 5.0 Å, although their diffusitivity is 14 orders of magnitude lower than for He (2.6 Å) (Zhang *et al.*, 2012). The effective aperture size of ZIF-8 for molecular sieving was estimated to be in the range of 4.0 to 4.2 Å, which is significantly larger than the XRD-derived value of 3.4 Å, and can be applied for separation of C_3 and C_4 hydrocarbon mixtures, including mixtures of the corresponding isomers (Zhang *et al.*, 2012). The explanation of this effect was suggested by Fairen-Jimenez *et al.*, (2011), and associated with the gate-opening effect, which is initiated by linker distortion: methyl imidazolate linkers of ZIF-8 show a swing effect upon gas adsorption; thus the pores open and give access to the cavity. Other attractive properties of ZIF-8 include exceptional chemical and thermal stability.

The adsorption sites for adsorption of D_2 molecules in ZIF-8 were identified from powder neutron diffraction measurements (Wu *et al.*, 2007). The strongest adsorption site for the D_2 molecule was found near the organic linker, in contrast to other MOFs, where the metal sites are typically the primary adsorption sites (Fig. 4.20). This feature was explained by steric hinderance of the metal site surrounded by closely located nitrogen atoms from the imidazolate organic linker (Zhou *et al.*, 2009). Second and third adsorption sites are located at the center of 6-membered ZnN_4 windows on different sites. The fourth adsorption position coordinates the center of 4-membered ZnN_4 windows, fifth and sixth adsorption sites are close to the center of the cavities of ZIF-8, and form the second adsorption layer. Structural analysis of adsorption sites of methane CD_4 molecules (which polarizability and atomic radius are similar to those of Kr) showed two adsorption sites: a major adsorption site near the imidazolate organic linker (corresponds to major adsorption site for D_2 molecule) and secondary adsorption site in the center of 6-membered ZnN_4 windows (corresponds to second adsorption site for D_2 molecule), (Wu *et al.*, 2009b).

4.4.2. X-ray powder diffraction investigation of noble gas adsorption in ZIF-8

4.4.2.1. Synchrotron X-ray powder diffraction investigation of Xe and Kr adsorption in ZIF-8

X-ray powder diffraction measurements of Xe adsorption in ZIF-8 were performed at 180 K at different pressures (9 mbar, 17 mbar, 36 mbar, 53 mbar, 93 mbar, 395 mbar, 500 mbar, 1000 mbar). Samples were evacuated at 160^{o}C for 5 hours before gas loading, and checked by

Rietveld refinement (Fig. 4.21). Then they were cooled to room-temperature and exposed to Kr or Xe gas. Before changing gas pressure, samples were always heated to room-temperature.

X-ray powder diffraction measurements of Kr adsorption in ZIF-8 were performed at 250 K, 180 K, and 130 K at different pressures (50 mbar, 100 mbar, 250 mbar, 500 mbar, 750 mbar, 1000 mbar). Samples were evacuated at 170^{o}C for 3 hours before gas loading, and checked by Rietveld refinement. Then they were cooled to room-temperature and exposed to Kr or Xe gas. Before changing gas pressure, samples were heated 30 K above the temperature of measurement.

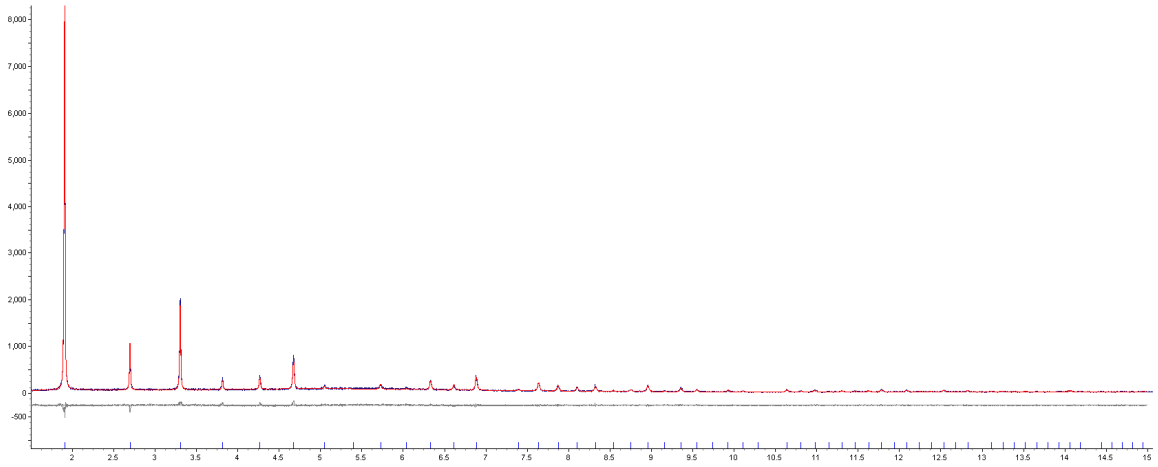

Figure 4.21. Rietveld plot of evacuated ZIF-8.

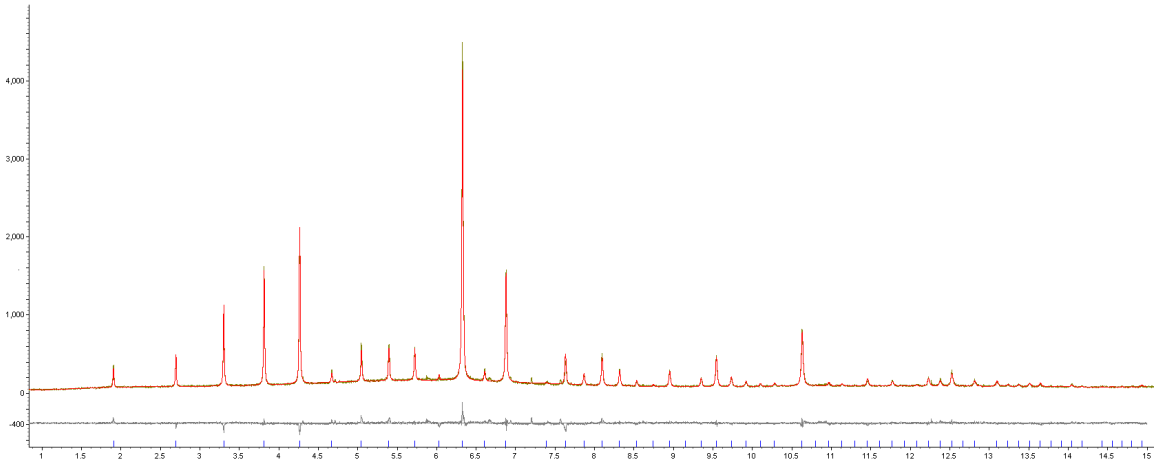

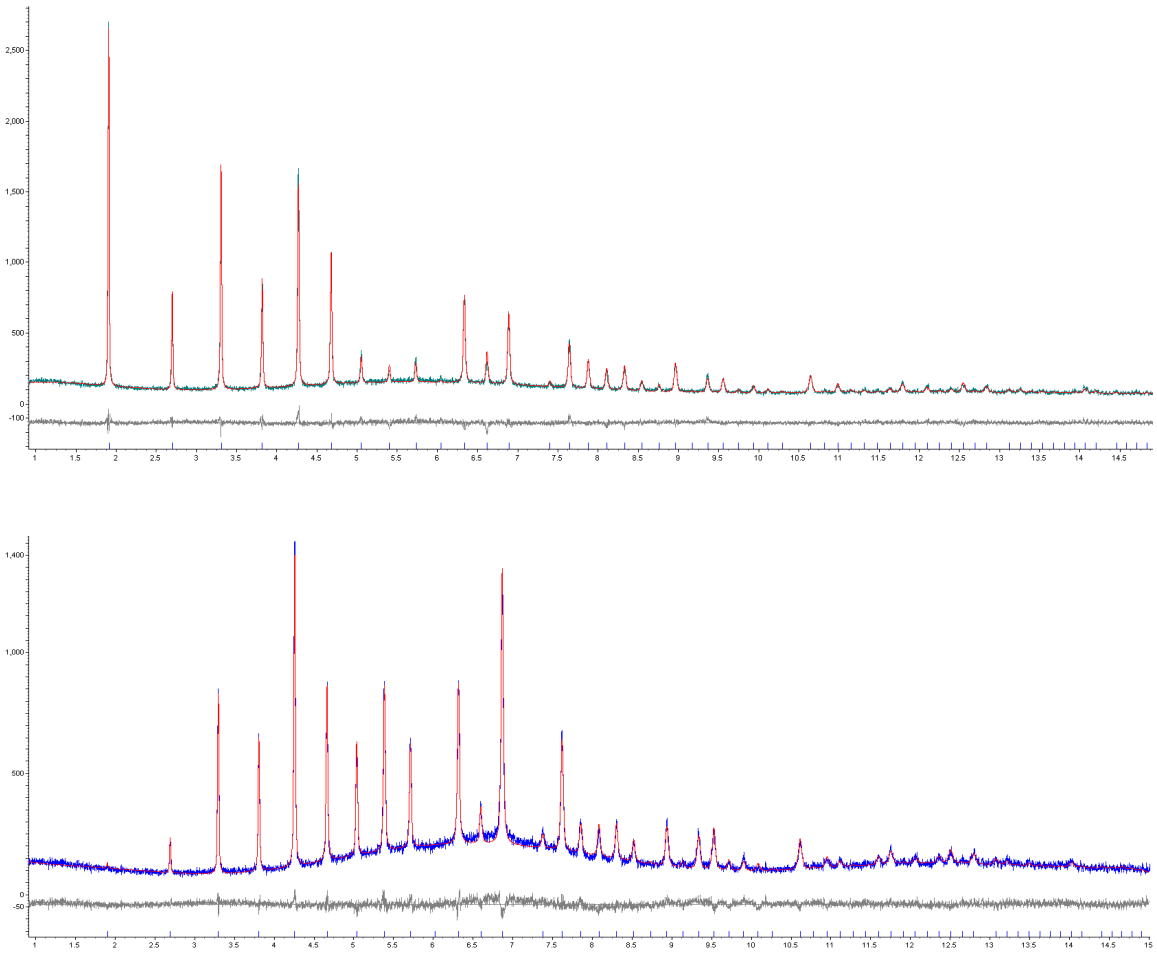

Figure 4.22. Rietveld plots of ZIF-8 with 1000 mbar of Xe at 180K (top), 1000 mbar of Kr at 180 K (middle), and 1000 mbar of Kr at 130 K (bottom).

Structural investigation of Xe and Kr adsorption revealed the important role of the gate-opening effect, which is responsible for the strong increase of noble gas adsorption by ZIF-8.

The main adsorption site for both Kr and Xe atoms was found near the imidazolate organic linker, similar to D_2(I) adsorption (Wu *et al.*, 2007), in contradiction to CPO-27, where the main adsorption sites were identified as the open metal atoms and/or the highly polarizable C=O bond. Metal sites in ZIF-8 are not accessible even for the small D_2 molecules due to steric hinderance by surrounding organic linkers (Zhou *et al.*, 2009), and there are no highly polarizable carbon-oxygen bonds in the ZIF-8 structure. The most polarizable bond remaining accessible for intercalated noble gas atoms in ZIF-8 is the C=C double bond of the organic imidazolate linker. Thus, this adsorption site with multiplicity 24 is the first filling site during noble gas adsorption and has the highest occupancy. The second adsorption site with

multiplicity 8 is located at the center of 6-membered ZnN_4 windows and corresponds to the position of D_2(III). The sequence of filling of the adsorption sites and their localization are different for Xe and for Kr atoms due to large differences in their atomic radii and polarizability, as well as due to the geometrical factor of the relatively small pore volume of ZIF-8 (geometrical factor can play a critical role in noble gas adsorption, see Hulvey *et al.*, (2013)).

At very low pressure of 9 mbar Xe atoms occupy three crystallographically different positions (Figs. 4.23 and 4.24): near the C=C bond of the imidazolate (at a distance of ~ 4 Å from the carbon atom in C=C bond), the center of 6-membered ZnN_4 windows (at a distance of ~ 4 Å from the carbon atom in C=C bond), and within the 4-membered ZnN_4 windows. The third position of the Xe atom in the 4-membered ZnN_4 windows has multiplicity 12, and is quite dynamic – the distances from the Xe atom to the nearest carbon atom in the C=C bond vary from ~ 5.4 Å at 9 mbar to ~ 4.8 Å at 93 mbar, and the distances from the Xe atom to the nearest carbon atom in methyl group vary from ~ 4.6 Å at 9 mbar to ~ 3.9 Å at 93 mbar. The occupancies of different Xe positions at 93 mbar reach 0.45(2) for the first position, 0.25(2) for the second position, and 0.12 for the third position (Fig. 4.27). Between 93 mbar and 394 mbar the gate-opening effect was observed, and the forth position in the center of the pore was occupied (this position was not observed for D_2 adsorption). Simultaneously, the occupancy of the third position in the 4-membered ZnN_4 windows dropped to zero, and the occupancy of the second position decreased (Figs. 4.25 and 4.26). Further increasing of pressure to 1000 mbar results only in slight increasing of occupancies of all three Xe positions (Fig. 4.27). The maximal amount of adsorbed Xe atoms at 180K by ZIF-8 corresponds to 2 Xe atoms per Zn atom. The gate-opening was also observed for CO and N_2 loading in ZIF-8 (Ania *et al.*, 2012). In general, the gate-opening effect appears when the gas pressure becomes high enough to promote the expansion of the crystal structure through its deformation, resulting in a reorganization of the adsorbed atoms. The deformation of the structure allows a considerable increase of the amount of adsorbed gas.

The gate-opening effect was not directly observed during the Kr adsorption in ZIF-8 at 180K, but its presence can be postulated based on the filling of some adsorption sites inside the cavities exclusively on increasing pressure. The sequence of filling of the adsorption sites by Kr is different from Xe adsorption. Three positions were occupied by Kr at 50 mbar and 100 mbar at 180K: near C=C bond of imidazolate (at a distance of ~ 4.1 Å from the carbon atom in C=C

bond), the center of 6-membered ZnN_4 windows (at a distance of ~ 3.8 Å from the carbon atom in C=C bond), and the center of the cavity (Figs. 4.28 and 4.29). Increasing pressure to 250 mbar results in the formation of fourth position in the 4-membered ZnN_4 windows, which is split and located at a distance of ~ 4.1 Å to the nearest carbon atom of the C=C bond and at a distance of ~ 4.0 Å to the nearest carbon atom of the methyl group (Figs. 4.30 and 4.31). The maximal amount of adsorbed Kr atoms at 180K by ZIF-8 corresponds to 1.7 Kr atoms per Zn atom (Fig. 4.32)

The sequence of filling of the adsorption sites by Kr at 130K is similar to that at 180 K: three positions were occupied by Kr at 50 mbar and 130K: near C=C bond of imidazolate, the center of 6-membered ZnN_4 windows and the center of cavity. Increasing pressure to 100 mbar results in the formation of a fourth position in the 4-membered ZnN_4 windows, which is split. Maximal amount of adsorbed Kr atoms at 130K by ZIF-8 corresponds to 3 Kr atoms per Zn atom (Fig. 4.33) and the occupancies of all positions are above 50%. For comparison, the maximal uptake of methane CD_4 molecules was found to be 3 CD_4 molecules per Zn atom (Wu *et al.*, 2009b). Also the experimentally determined positions for both Kr and Xe atoms correlate well with theoretically simulated positions for Ar atoms (Pantatosaki *et al.*, 2010)

The adsorption of noble gases by MOFs is based on the polarizability of both possible adsorption sites of the MOF and the intercalated noble gases. All adsorption sites in ZIF-8 have a relatively low polarizability, although some of them are slightly more polarizable (*i.e.* C=C bond of imidazolate linker). This fact is also confirmed by isosteric heat of adsorption measurements, which showed no decreasing of the isosteric heat upon Kr and Xe loading (Ryan *et al*., 2014). Thermal desorption measurements showed one broad peak at low loading, which is splitted into a few peaks with increasing gas loading (Soleimani Dorcheh *et al.*, 2012a). Splitting of the desorption peak can be explained only by the gate-opening effect due to the absence of strong adsorption sites (*i.e.* sites with strength similar to open metal sites). Thus, the geometrical factor of pore size and shape is the main driving force of noble gas storage and separation in ZIF-8.

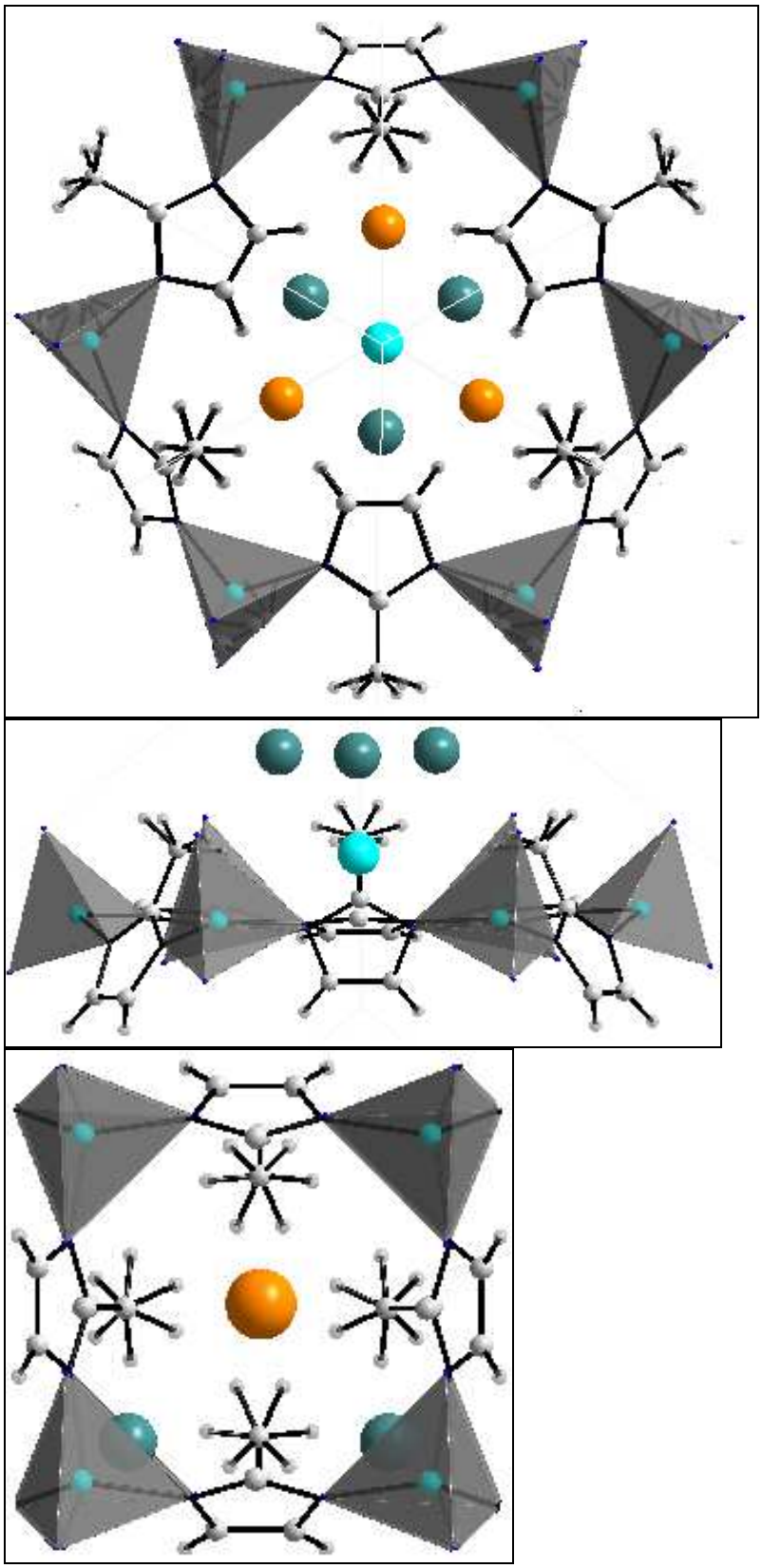

Figure 4.23. Positions of Xe atoms in cavity of ZIF-8 before gate-opening effect.

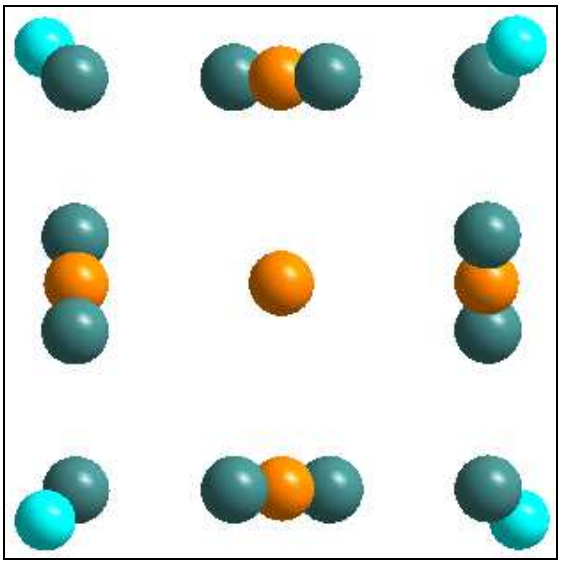

Figure 4.24. Positions of Xe atoms in pore ZIF-8 before gate-opening effect, view along *c*-axis.

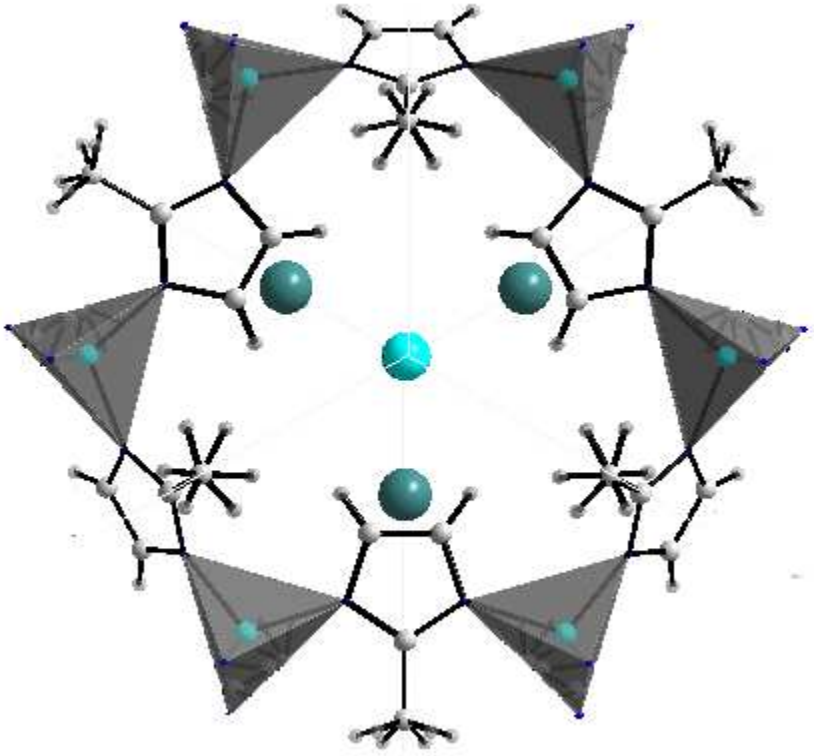

Figure 4.25. Positions of Xe atoms in pore ZIF-8 after gate-opening effect.

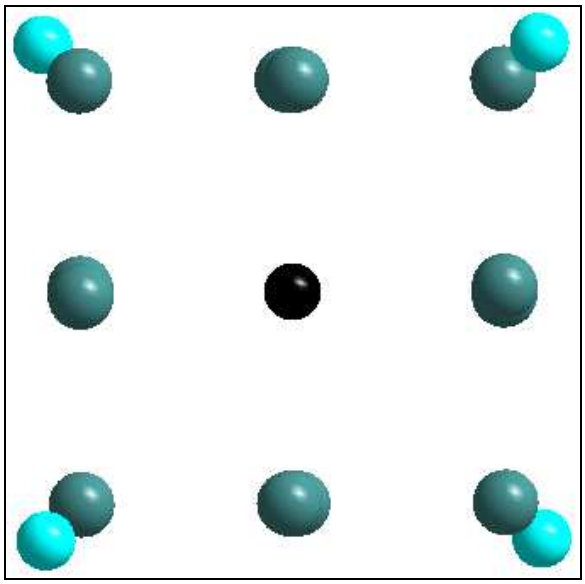

Figure 4.26. Positions of Xe atoms in pore ZIF-8 after gate-opening effect, view along *c*-axis.

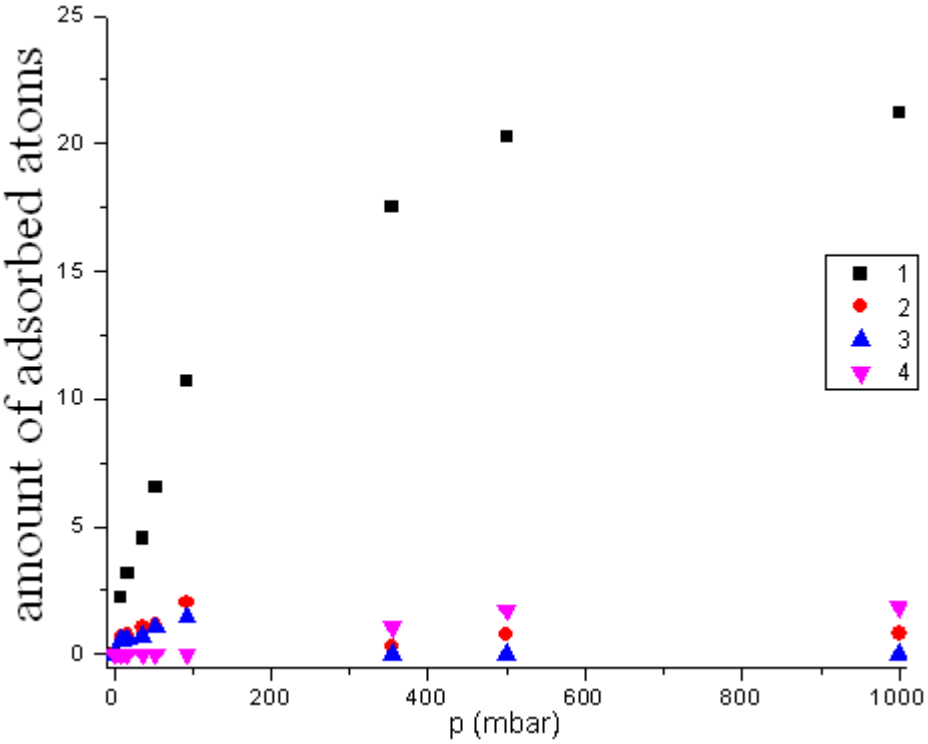

Figure 4.27. Amount of adsorbed Xe atoms in different crystallographic positions of ZIF-8 at different pressures at 180 K.

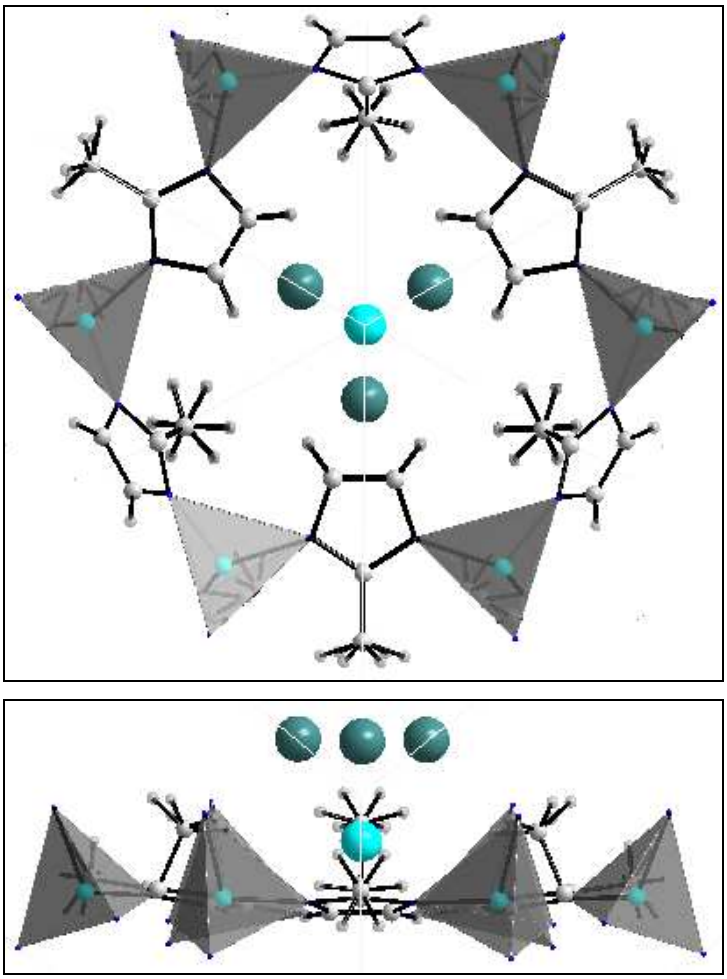

Figure 4.28. Positions of Kr atoms in pore ZIF-8 before gate-opening effect.

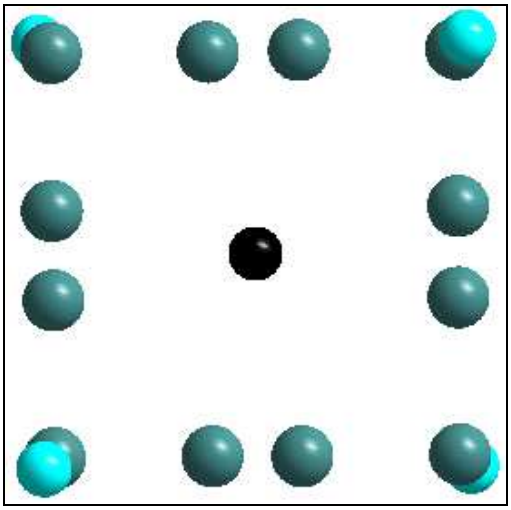

Figure 4.29. Positions of Kr atoms in pore ZIF-8 before gate-opening effect, view along *c*-axis.

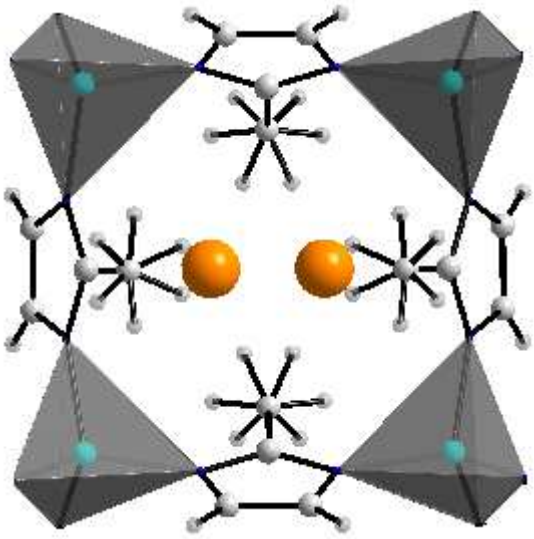

Figure 4.30. Additional position of Kr atoms in pore ZIF-8 after gate-opening effect.

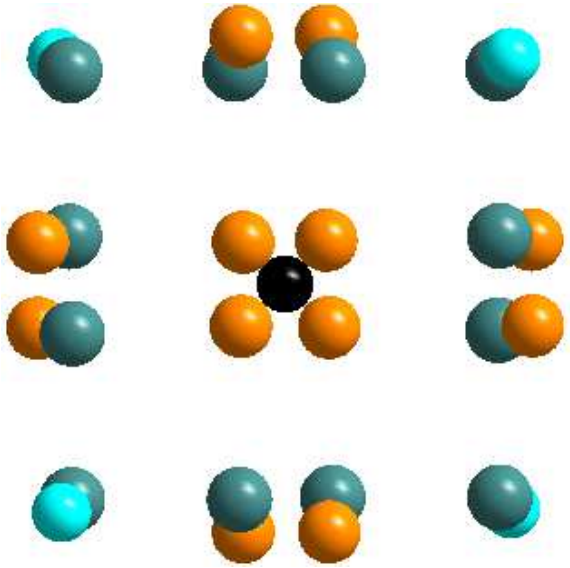

Figure 4.31. Positions of Kr atoms in pore ZIF-8 after gate-opening effect, view along *c*-axis.

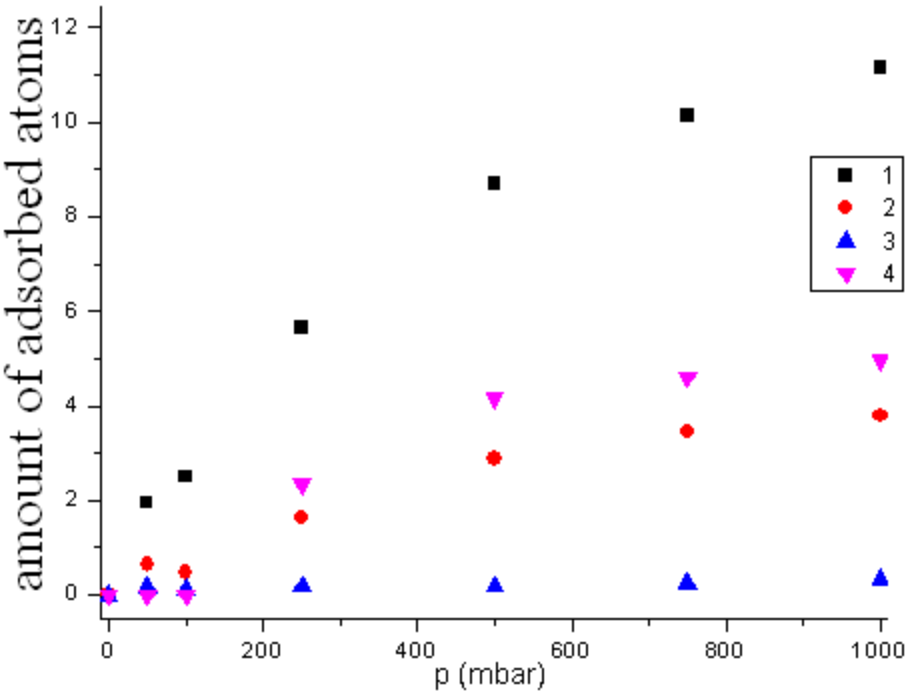

Figure 4.32. Amount of adsorbed Kr atoms in different crystallographic positions of ZIF-8 at different pressures at 180 K.

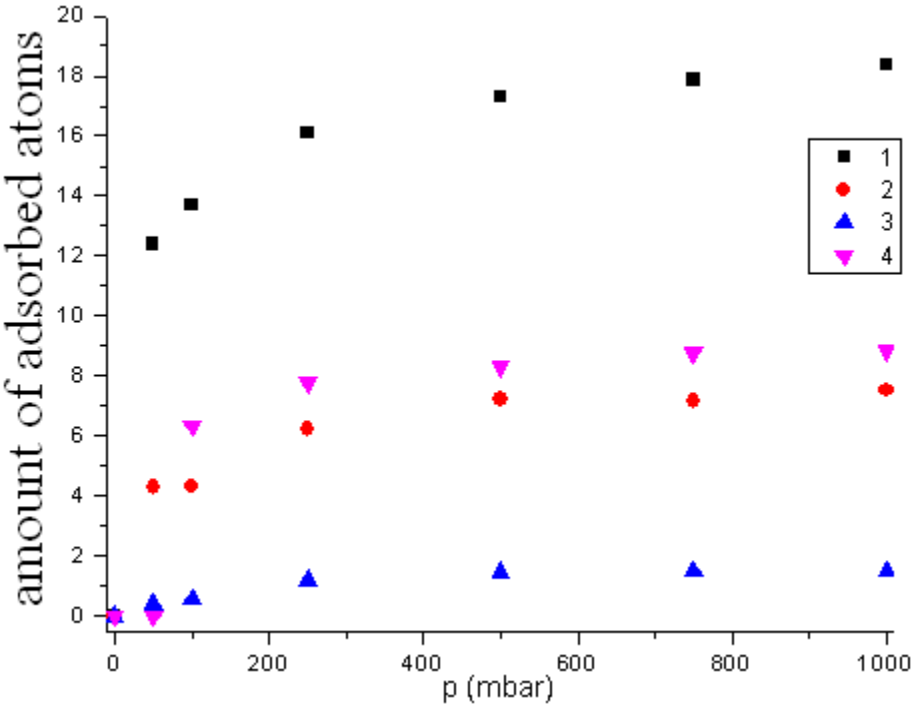

Figure 4.33. Amount of adsorbed Kr atoms in different crystallographic positions of ZIF-8 at different pressures at 130 K.

4.4.2.2. Laboratory X-ray powder diffraction investigation of Xe adsorption in ZIF-8

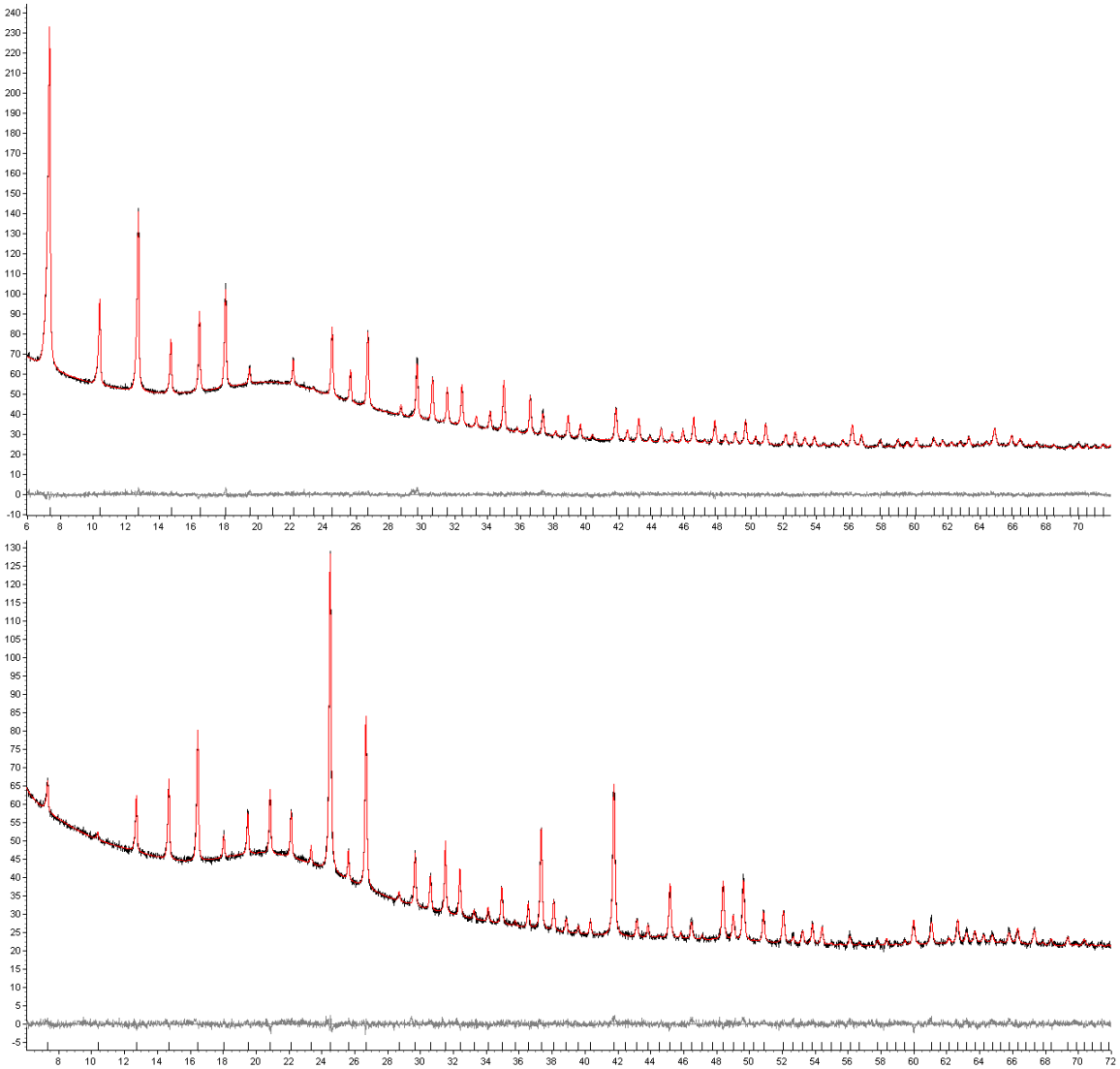

Figure 4.34. Rietveld plots of ZIF-8 with 20 mbars of Xe, 110K (top) and with 50 mbar of Xe, 110K (bottom). Laboratory X-ray powder diffraction data, Y-axis scale – square root of X-ray counts for better visibility of low-intensity reflections.

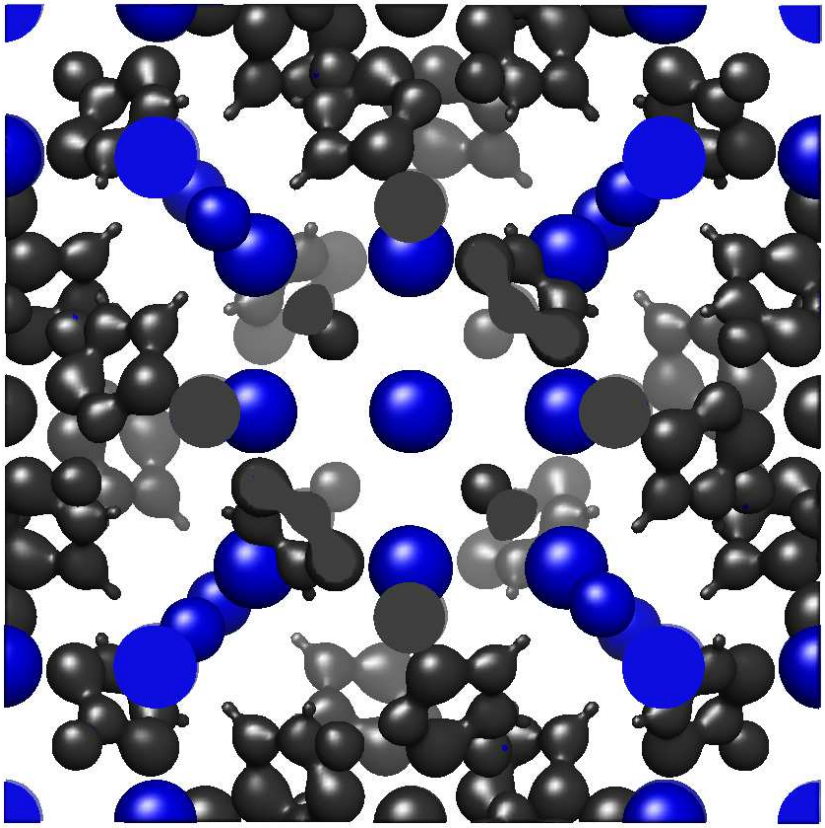

Figure 4.35. Electron density distribution of Xe atoms (blue) in ZIF-8 (grey) from MEM calculations at 50 mbar, 110K.

ZIF-8 was evacuated at 180^{o}C for 6 hours, cooled to room-temperature, loaded with 20 mbar and 50 mbar of Xe gas, and cold down to 110K for measurements. The positions of intercalated Xe atoms were determined by the global optimization method of simulated annealing and Rietveld refinement using the program TOPAS 4.1 (Coelho, 2007). Crystallographic and refinement data are given in Table 4.1.

The Maximum Entropy Method (MEM) is in particular well suited to locate missing atoms with low occupancy in incomplete crystal structures (Soleimani Dorcheh *et al.*, 2012a; Matsuda *et al.*, 2005; Kitaura *et al.*, 2002) and to determine the accurate electron density distribution (Samy *et al.*, 2010, Buchter *et al.*, 2011). Therefore, in the present case, MEM was used for localization of Xe atoms and for reconstruction of the electron density distribution of all Xe atoms in the unit cell.

All MEM calculations were performed using the program BayMEM (van Smaalen *et al.*, 2003), employing the Sakata-Sato algorithm (Sakata & Sato, 1990). The procrystal electron

density was created from the Rietveld refinement of the incomplete crystal structure (empty MOF), not containing any information about intercalated Xe atoms. The obtained MEM map did not contain noise and allowed to locate the intercalated Xe atoms unambiguously. Details about the maximum-entropy calculations are given in Table 4.2. Optimal values for the Lagrange multiplier λ were obtained by trial and error; an automated adjustment of λ during iterations was not possible due to an increase of the constraints value for several cycles of the iteration.

At 20 mbar (110K) only two positions of Xe atoms were localized: near C=C bond of imidazolate (corresponds to the position Xe(I) from synchrotron diffraction data) and in the center of 6-membered ZnN_4 windows (corresponds to the position Xe(II) from synchrotron data), (Fig. 4.23). The position in the 4-membered ZnN_4 windows remains empty, probably due to different temperatures, used for laboratory and synchrotron measurements, and, as a result, different interactions between intercalated atoms and MOF occur. It is also necessary to take into account the low occupancy of the position in the 4-membered ZnN_4 windows determined from synchrotron powder diffraction data. At 50 mbar (110K) three positions of Xe atoms were localized, which correspond to three positions localized from synchrotron diffraction data: Xe(I) near C=C bond of imidazolate, Xe(II) in the center of 6-membered ZnN_4 windows, and Xe(III) in the center of cavity (Figs. 4.25, 4.26). Thus, the gate-opening effect in ZIF-8 could still be observed through the sharp decrease of the occupancy of the second position and the increase of the occupancy of the third position upon Xe loading.

Table 4.1. Crystallographic and refinement data for ZIF-8 with various Xe loadings (R_{Br}, *Rp*, *Rwp* and *GooF* as defined in Topas).

Sample	ZIF-8 (110K, 20mbar)	ZIF-8 (110K, 50mbar)
Molecular formula	$ZnN_4C_8H_{10}Xe_{0.23}$	$ZnN_4C_8H_{10}Xe_{2.2}$
Space group	I4-3m (217)	I4-3m (217)
Z	12	12
a / Å	16.99688	17.01844
Xe1, 24g (*x, x, z*)	0.186(5), 0.008(5)	0.190(5), 0.0004(5)
Uiso	20.0	4.7
Frac. occ.	0.09	0.90
Xe2, 8c (x, x, x)	0.167(5)	0.236(5)
Uiso	20.0	17.0
Frac. occ.	0.7	0.23
Xe3, 2a (0, 0, 0)	-	0
Uiso	-	5.6
Frac. occ.	-	0.91
R_{Br}, %	1.30	1.26
*R*p, %	2.20	2.76
*R*wp, %	2.89	3.50
GooF	1.23	1.26
Temperature (K)	110	110
Wavelength (Å)	1.540596	1.540596
Starting angle (° 2θ)	6	6
Final angle (° 2θ)	72	72
Step width (° 2θ)	0.0079	0.0079

Table 4.2. Details about maximum-entropy calculations (based on F_{obs}+*G*) for investigated MOFs from laboratory X-ray diffraction data with all atoms included.

Sample	ZIF-8 (110K, 20mbar)	ZIF-8 (110K, 50mbar)
The grid / pixels	192×192×192	
Resolution / $Å^3$	0.09×0.09×0.09	
χ^2_{aim}	0.05	0.05
R_F / R_{wF}, %	0.84/0.74	0.62/0.34
R_G / R_{wG}, %	0.60/0.44	0.36/0.21
No. of unique reflections	34	34
No. of overlapping reflections	93	93
No. of groups of the overlapping reflections	38	38

4.5. Structural investigation of noble gas adsorption in Zn-MFU-4*l* and Cu-MFU-4*l*

4.5.1. Background information

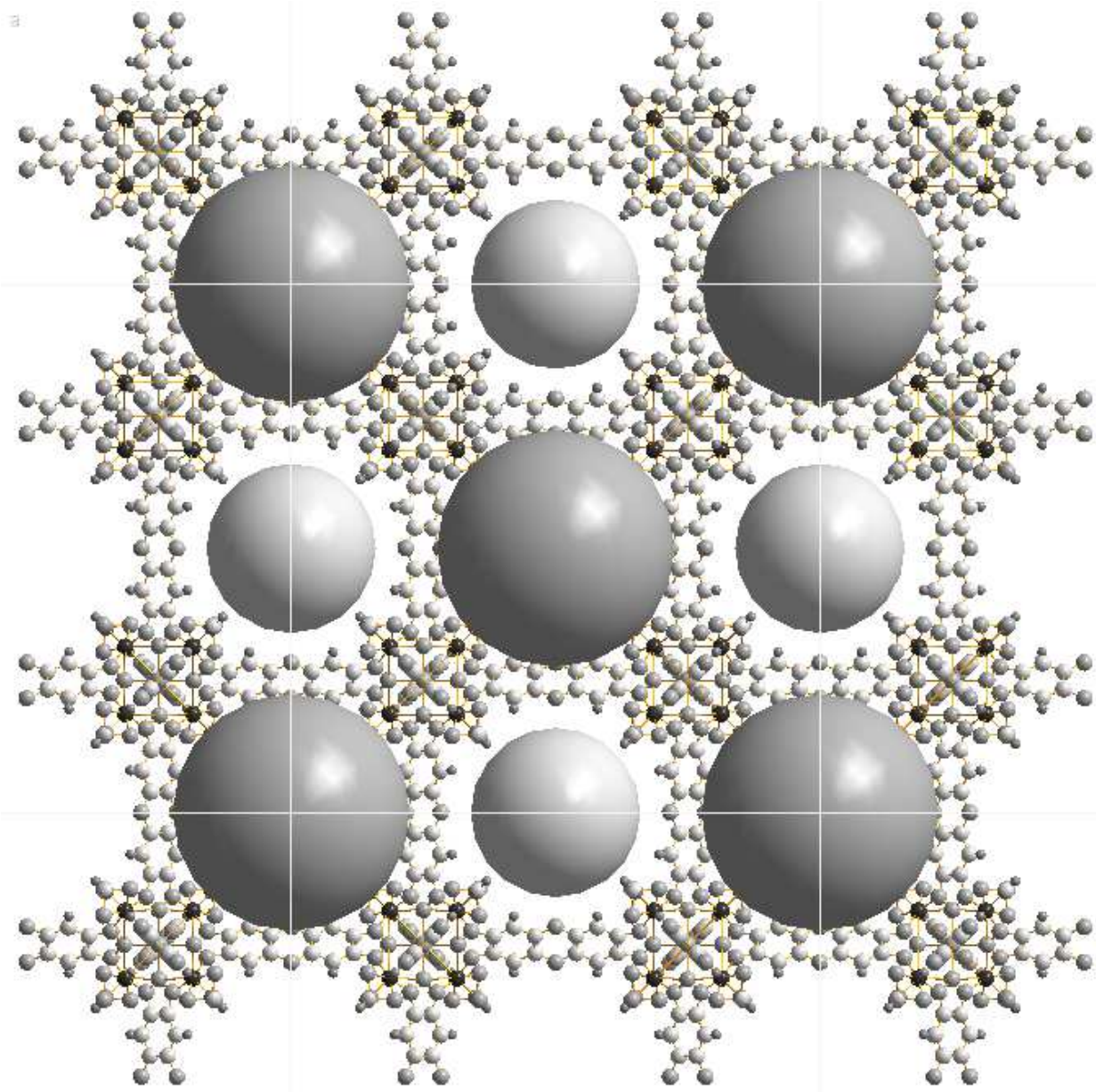

Figure 4.36. MFU-4*l* framework with two types of cavities alternating in three dimensions.

Zn-MFU-4*l* is a new recently synthesized MOF (Denysenko *et al.*, 2011). It is constructed from $[Zn_5Cl_4]^{6+}$ secondary building units and bis(1H-1,2,3-triazolo[4,5-b], [4',5'-i])dibenzo[1,4]dioxin organic linkers. Zn-MFU-4*l* contains two types of cavities alternating in

three dimensions, which differ by the orientation of chlorine atoms pointing towards or away from each other, the orientation of the organic linker, and their sizes.

The crystal structure of Cu-MFU-4*l* is identical to that of Zn-MFU-4*l*, and Cu atoms randomly occupy ~ 50% of the outer Zn atoms of the $[Zn_5Cl_4]^{6+}$ secondary building units (Denysenko *et al.*, 2014). Chlorine atoms coordinate only part of the Zn atoms (the rest of the Zn atoms are coordinated by HCOO groups), and Cu atoms present open metal sites after evacuation of Cu-MFU-4*l*.

The crystal structure of MFU-4*l* has the topology of the well investigated MOF-5 (Spencer *et al.*, 2006), which also consists of small and large pores alternating in three dimensions. Structural investigations of Kr and Xe adsorption in Zn-MFU-4*l* and Cu-MFU-4*l* were inspired by the unique adsorption of argon in MOF-5 (Rowsell *et al.*, 2005).

4.5.2. Laboratory and synchrotron X-ray powder diffraction investigation of noble gas adsorption in Zn-MFU-4*l*

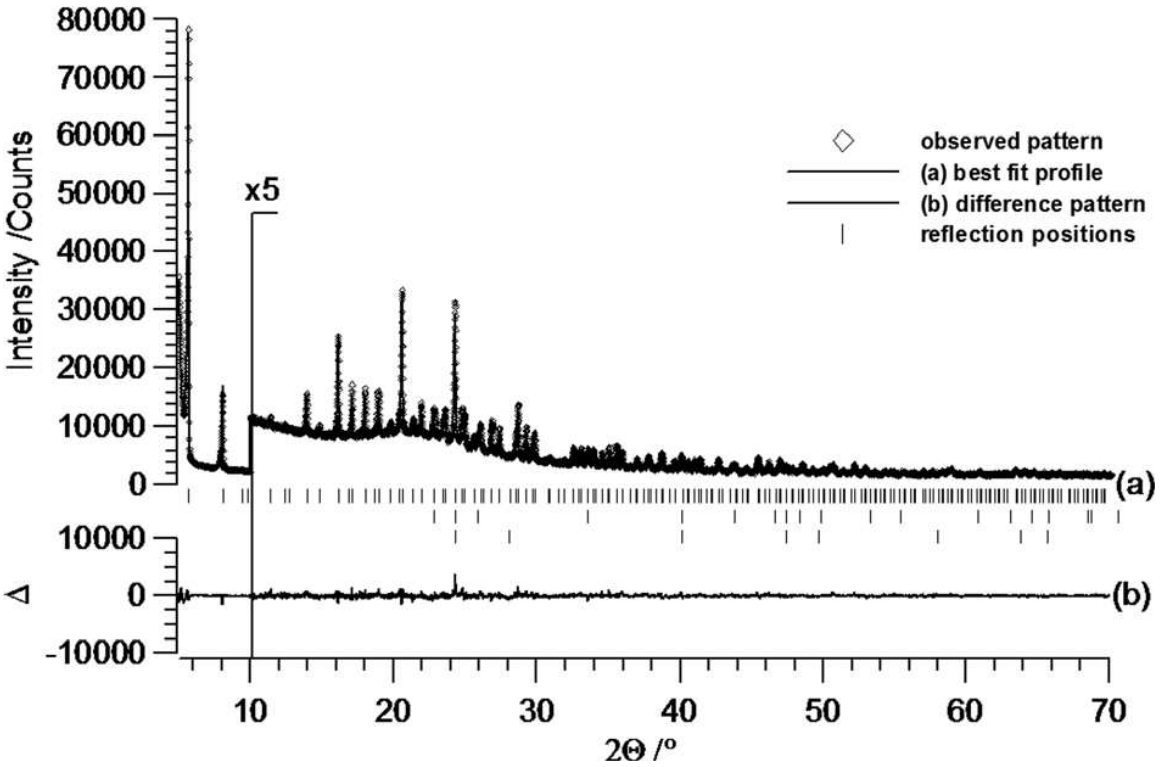

Figure 4.37. Rietveld plot of evacuated Zn-MFU-4*l* at 50 mbar, 110K, using laboratory X-ray powder diffraction data.

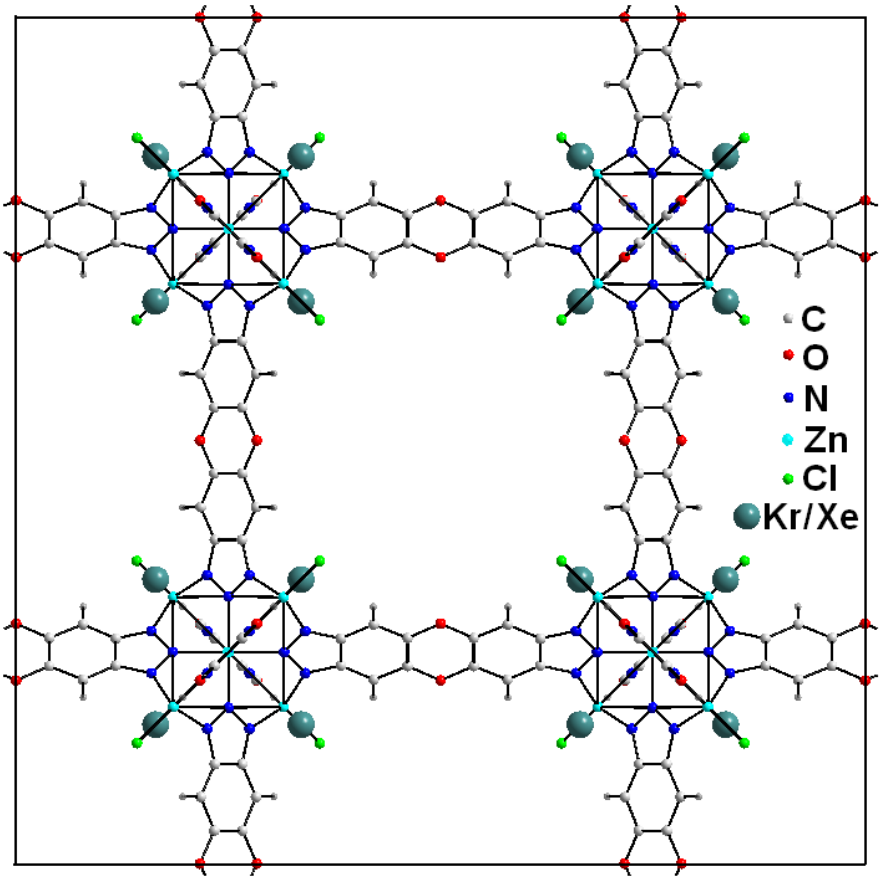

Figure 4.38. Positions of Xe and Kr atoms in pores of Zn-MFU-4*l* from laboratory X-ray powder diffraction data.

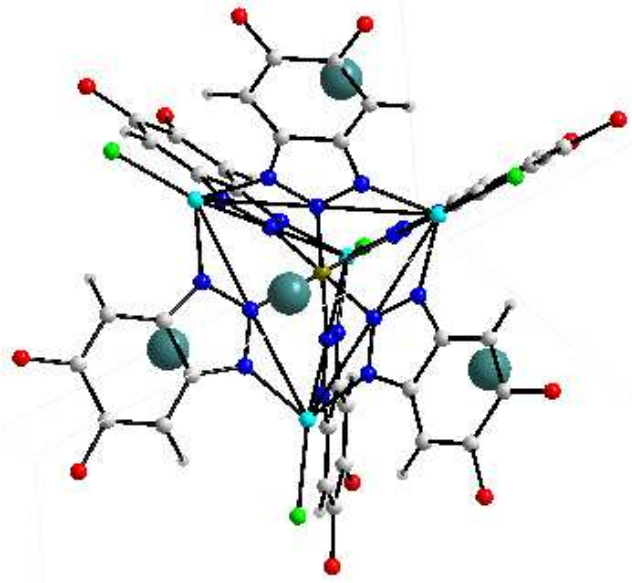

Figure 4.39. Positions of Xe and Kr atoms near metal atom in pore of Zn-MFU-4*l* from laboratory X-ray powder diffraction data.

Simulated annealing and Rietveld refinement applied to laboratory X-ray powder diffraction data revealed only one position of intercalated Xe atom in the large cavity near triangular faces of ZnN_3Cl tetrahedra at the metal site (Figs. 4.38, 4.39). This position coincides with the main adsorption position of argon in MOF-5 (Rowsell *et al.*, 2005). No more positions were found on increasing gas pressure and decreasing temperature. At T = 110 K these position is fully occupied, while at T = 150 K the fractional site occupancy lowers to 25%, which is calculated to be 2 instead of 8 Xe atoms per pore. Synchrotron X-ray powder diffraction data confirmed, that both Xe and Kr have only one adsorption site in the large cavity near triangular faces of ZnN_3Cl tetrahedra at the metal site.

To analyze the electron density distribution of adsorbed Xe atoms, the Maximum Entropy Method (MEM) was used. All MEM calculations were performed using the program BayMEM (van Smaalen *et al.*, 2003), employing the Sakata-Sato algorithm (Sakata & Sato, 1990). The prior information was provided by the electron density distribution corresponding to a refined independent spherical atom model (ISAM) using the same experimental data (procrystal density). In this model, the electron density is modeled as a superposition of electron densities of free, non-interacting atoms placed at their refined positions and convoluted with refined thermal motion (van Smaalen *et al.*, 2003).

The localization of the missing Xe atoms in Zn-MFU-4*l* was performed using experimental data sets – based on F_{obs}+G–constraints (observed structure factors extracted after Rietveld refinements of empty/filled MOF with G–constraints for overlapping reflections). Observed structure factors extracted after Rietveld refinements of the empty MOF were used to find highly occupied positions of Xe atoms, while the data from the filled MOF allowed the detection of possible additional low occupied positions and to reveal finer details on the distribution of electron density of the loaded gas. TOPAS 4.1 (Coelho, 2007) was used for Rietveld refinement.

Initial data used for the MEM calculations did not contain any information about intercalated Xe atoms. The procrystal electron density was created from the Rietveld refinement of the incomplete structure (empty Zn-MFU-4*l*). The analysis of the MEM reconstructed electron density was performed using the program EDMA according to the method “on-grid”

(Palatinus *et al.*, 2012). This program allows to determine not only the value of the electron density but also the integrated charge of atoms based on the Bader theory.

The reconstructed electron density of both data sets taken at 110 K and 150 K unambiguously confirmed the position of the Xe atoms from Rietveld refinement and did not reveal any other distinct atomic positions for the loaded gas. The distribution of the electron density of the Xe atoms was found to be fully isotropic ruling out certain types of positional disorder (Fig. 4.40).

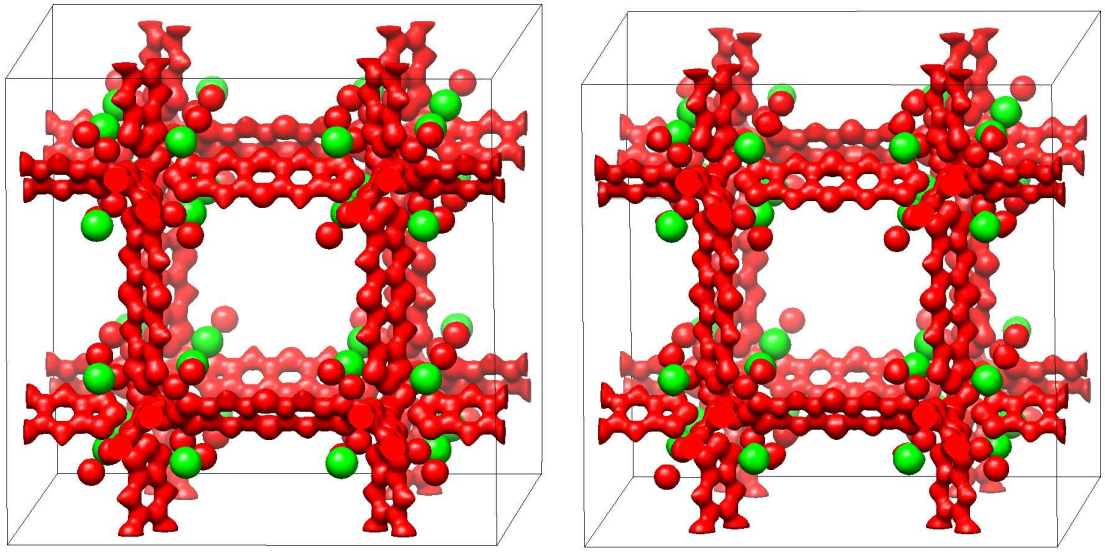

Figure 4.40. Three-dimensional MEM reconstructed electron-density maps of Zn-MFU-4*l* with Xe (created using the program UCSF Chimera) based on F_{obs}+G–constraints at 150 K (left) and 110 K (right). Contour levels: from 1 e/Å^3. Laboratory X-ray powder data.

4.5.3. X-ray powder diffraction investigation of noble gas adsorption in Cu-MFU-4*l*

X-ray powder diffraction measurements of Xe adsorption in Cu-MFU-4*l* were performed at 250K and 170K at different pressures (50 mbar, 100 mbar, 250 mbar, 500 mbar, and 1000 mbar). X-ray powder diffraction measurements of Kr adsorption in ZIF-8 were performed at 250 K, 170 K, and 130 K at different pressures (50 mbar, 100 mbar, 250 mbar, 500 mbar, 750 mbar, and 1000 mbar). Samples were evacuated at 180°C during 3 hours before gas loading, and checked by Rietveld refinement (Fig. 4.41). Then they were cooled to room-temperature and exposed to Kr or Xe gas. Before changing the gas pressure, samples were heated 40 K above measurement's temperature.

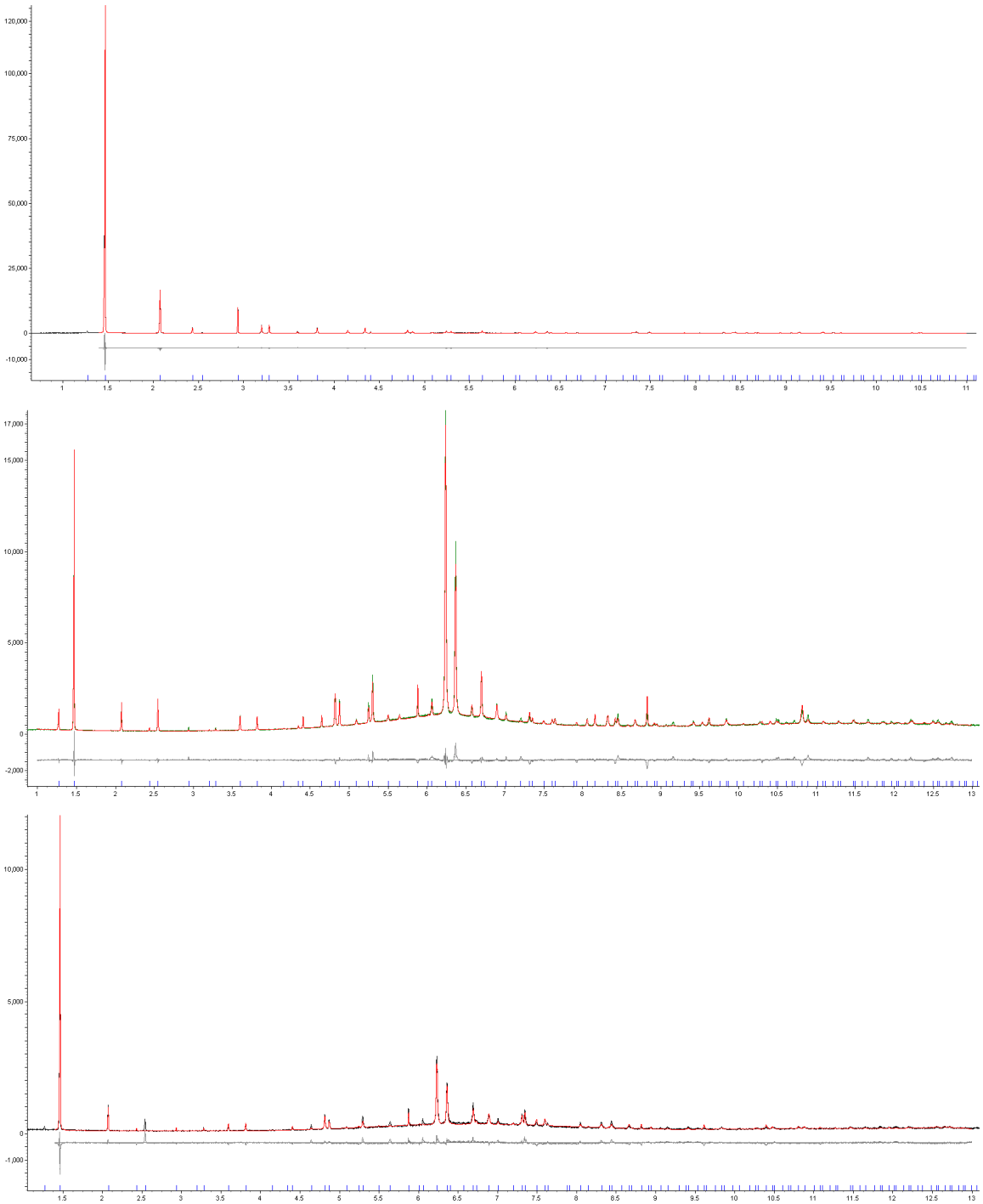

Figure 4.41. Rietveld plots of evacuated Cu-MFU-4*l* (top), with 250 mbar of Xe at 170K (middle), and 1000 mbar of Kr at 130 K (bottom).

The structural investigations showed extremely high adsorption of Kr and Xe atoms by Cu-MFU-4*l* and allowed precise localization of intercalated atoms.

The main adsorption site I for both Kr and Xe was located in the center of the triangular faces of the ZnN_3Cl tetrahedra (metal site), (Figs. 4.42, 4.50). The same position is the unique position for noble gas adsorption in Zn-MFU-4*l*. The second main adsorption site II is located between the first adsorption site and the metal atom (Cu or Zn) from the outer part of the secondary building unit (Figs. 4.43, 4.51). The sum of occupancies of first and second adsorption sites never exceeds one, and the noble gas atoms are statistically disordered between these two positions.

The adsorption site III for both Kr and Xe coordinates the statistically disordered outer Cu atom (Figs. 4.44, 4.45, 4.52), the adsorption site IV is located above the center of the 6-membered C_4O_2 ring of the organic linker (Figs. 4.43, 4.53, 4.55), and Xe and Kr atom in the adsorption site V coordinates oxygen atoms from the organic linker (Figs. 4.44, 4.46, 4.54). Three more adsorption sites for Kr: VI, VII, and VIII, can be seen at 130K at pressure above 250 mbar and they are all located in the center of the large cavity (Figs. 4.47, 4.48, 4.49), forming a second adsorption layer in the pores. Despite the fact that the large cavity is completely filled, the small cavity remains almost empty – only Kr(V) is located near the window inside of the small pore, as well as inside of the large pore. Thus, small and large pores are not equivalent for noble gas adsorption.

Further increase of pressure of Xe gas results in the filling of three positions (VI, VII, andVIII) in the center of the large cavity, which are similar to the positions VI, VII, andVIII, occupied by Kr at high gas loading (Figs. 4.56, 4.57). Only at 170K and pressure 250 mbar and 500 mbar two more Xe positions: IX and X, are located in the small cavity (Fig. 4.57).

For both Xe and Kr atoms, the coordinatively unsaturated Cu sites from the outer part of the metal cluster are not a major adsorption site, and their filing started only when the major adsorption site in the center of triangular faces of the ZnN_3Cl tetrahedral was filled. In contrast, the coordinatively unsaturated Ni and Mg sites in CPO-27-Ni and CPO-27-Mg are (one of) the primary adsorption sites. The coordinatevely unsaturated Cu sites in HKUST-1 also are not coordinated by noble gas atoms even at highest pressure (Hulvey *et al.*, 2013). Thus, the adsorption of noble gases critically depends on the type of metal atom in the secondary building blocks of the MOFs. This interesting phenomenon requires further structural investigation.

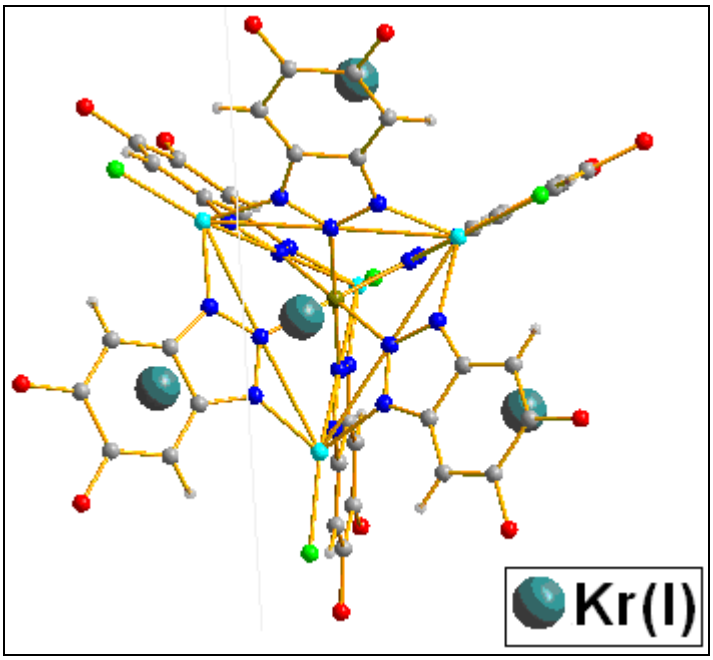

Figure 4.42. Positions of Kr atoms in pores of Cu-MFU-4*l* at 250K (500 mbar and 1000 mbar) and 170K (50 mbar and 100 mbar).

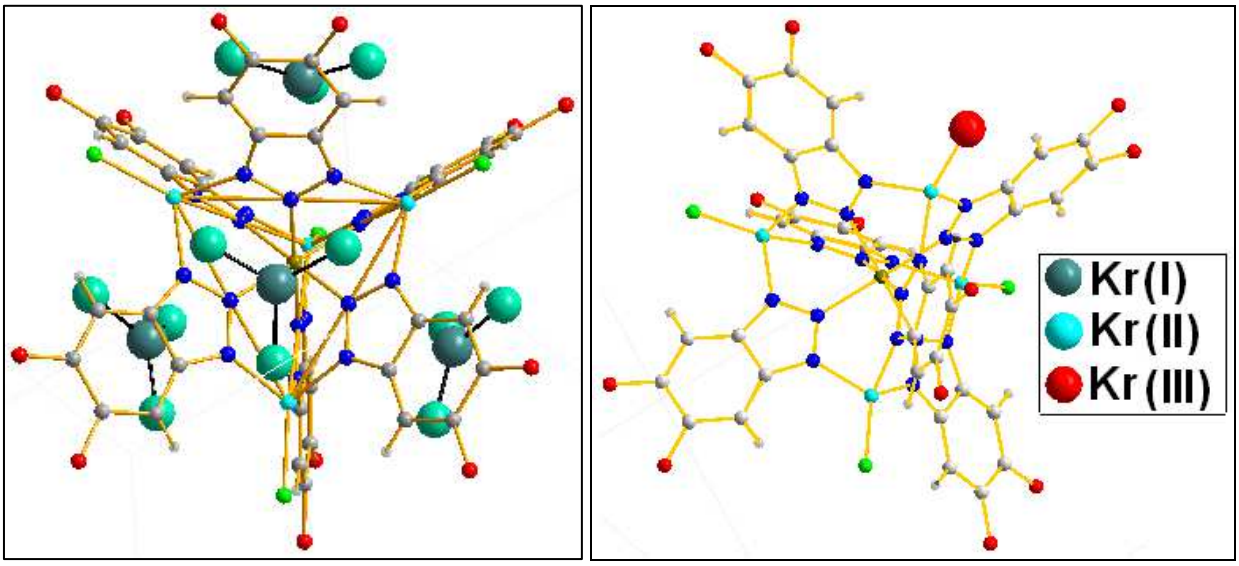

Figure 4.43. Positions of Kr atoms in pores of Cu-MFU-4*l* at 170K, (250 mbar and 500 mbar).

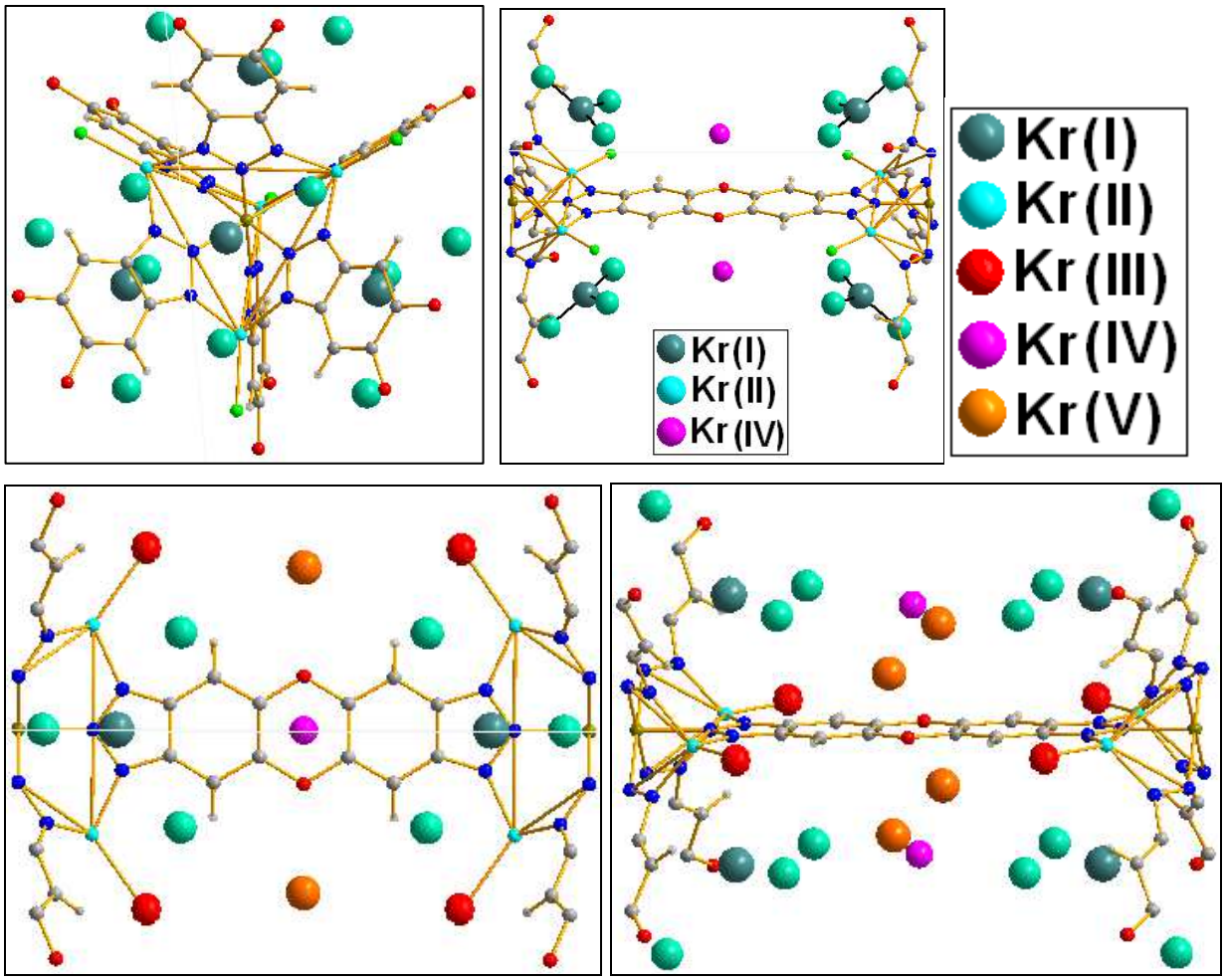

Figure 4.44. Positions of Kr atoms in pores of Cu-MFU-4*l* at 170K (1000 mbar).

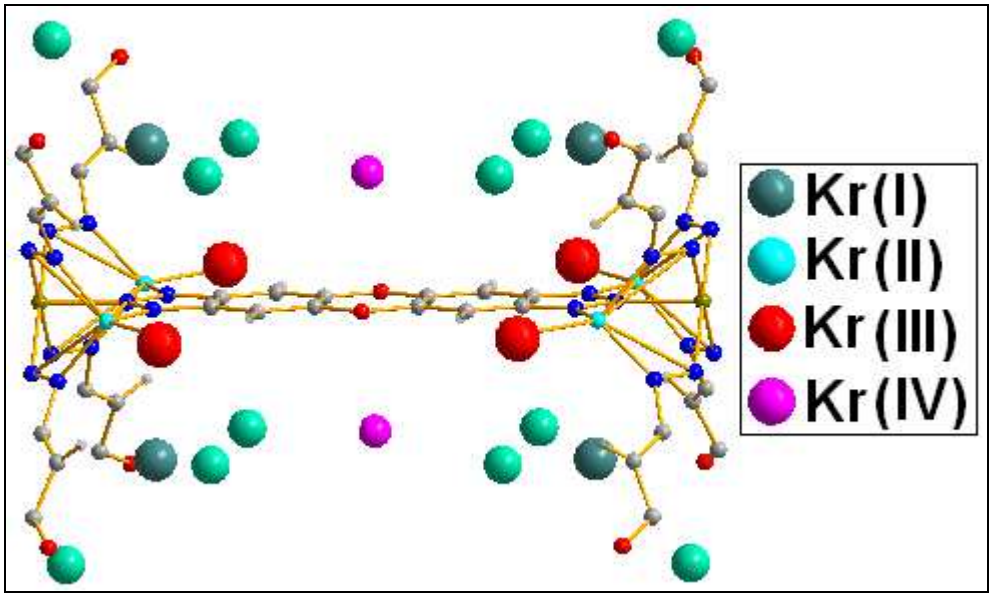

Figure 4.45. Positions of Kr atoms in pores of Cu-MFU-4*l* at 130K (50 mbar).

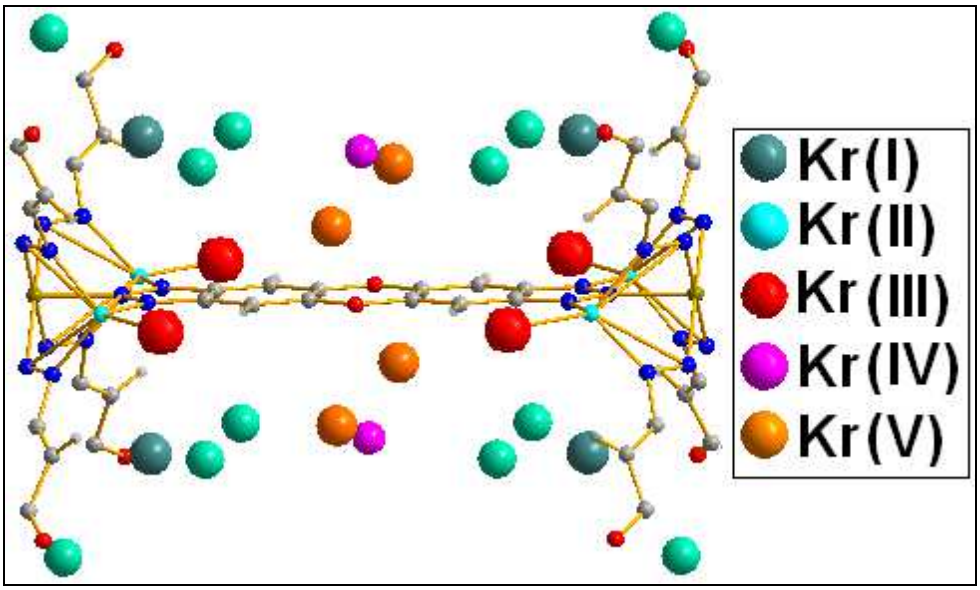

Figure 4.46. Positions of Kr atoms in pores of Cu-MFU-4*l* at 130K (100 mbar).

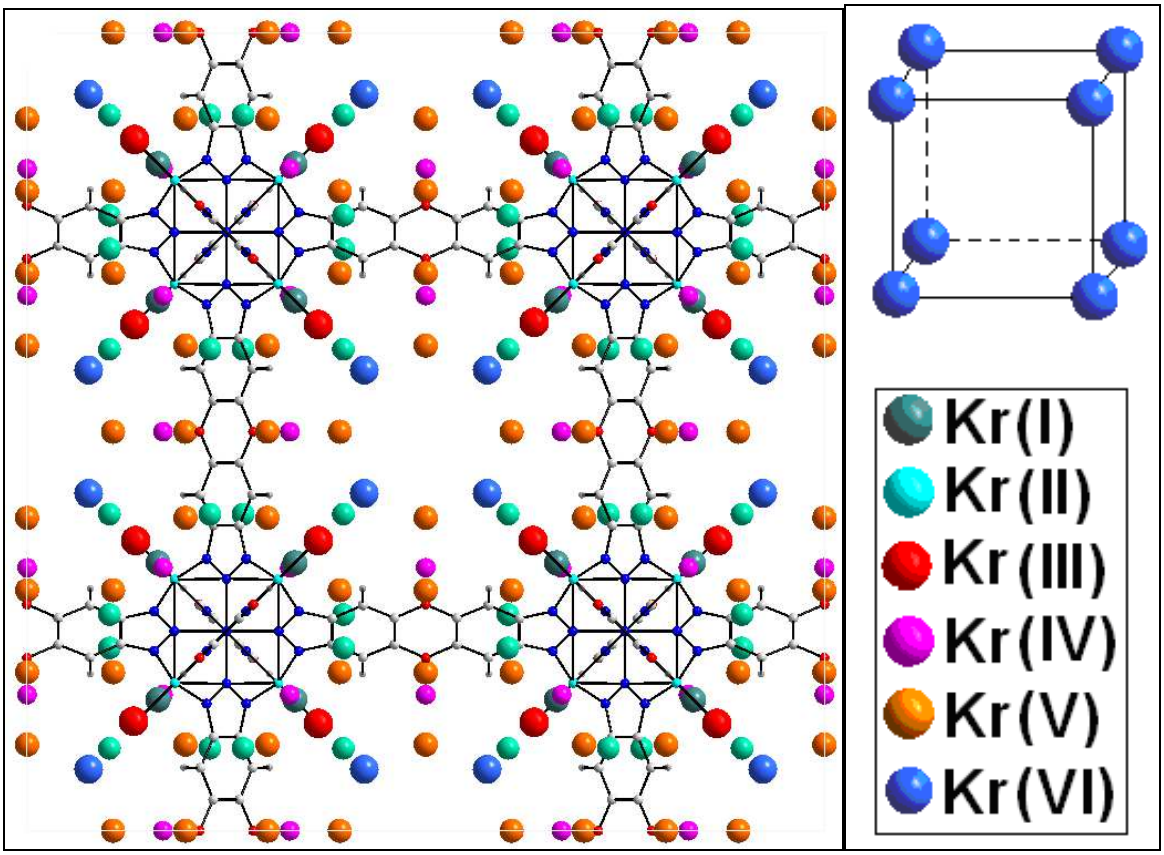

Figure 4.47. Positions of Kr atoms in pores of Cu-MFU-4*l* at 130K (250 mbar); insert – second adsorption layer in the large cavity formed by Kr(VI).

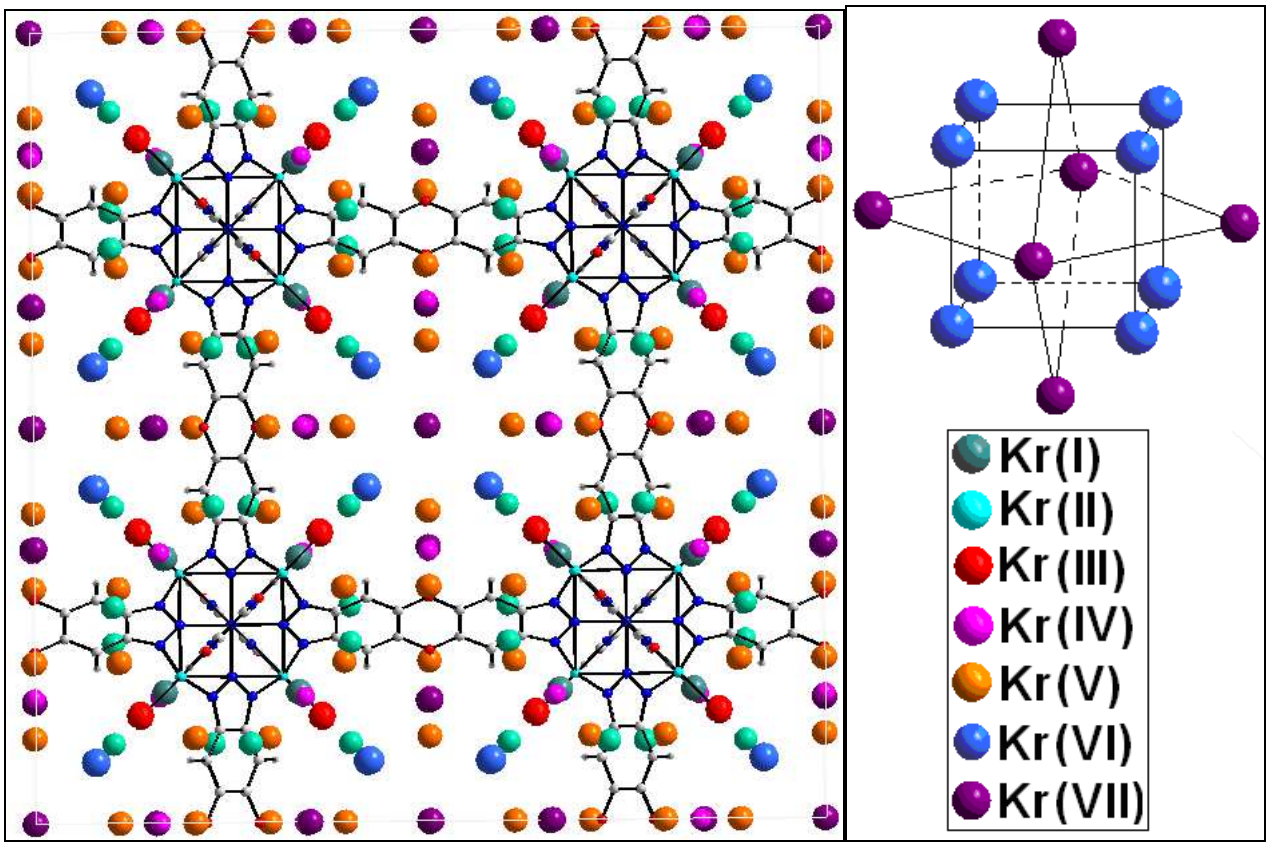

Figure 4.48. Positions of Kr atoms in pores of Cu-MFU-4*l* at 130K (500 mbar); insert – second adsorption layer in the large cavity formed by Kr(VI) and Kr(VII).

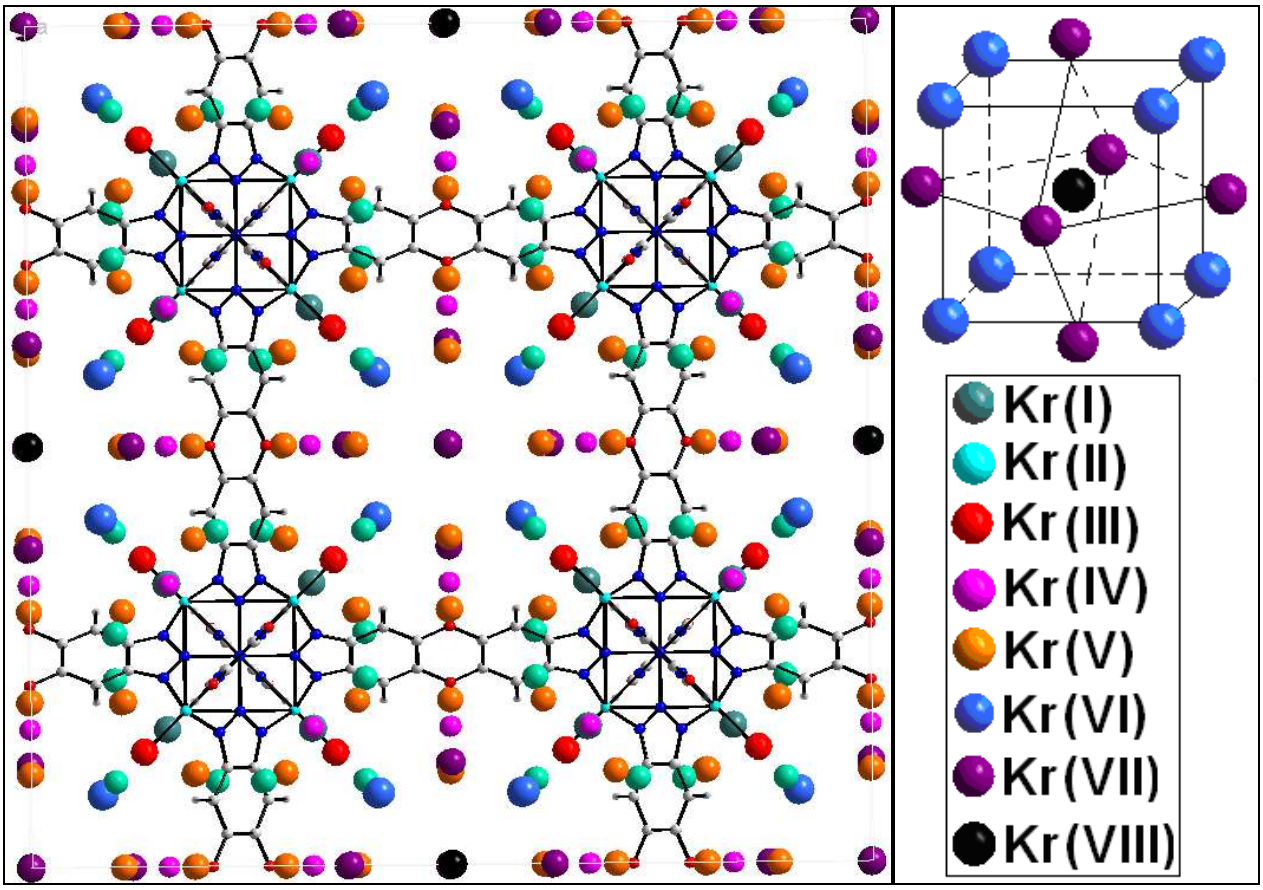

Figure 4.49. Positions of Kr atoms in pores of Cu-MFU-4*l* at 130K (1000 mbar); insert – second adsorption layer in the large cavity formed by Kr(VI), Kr(VII), and Kr(VIII).

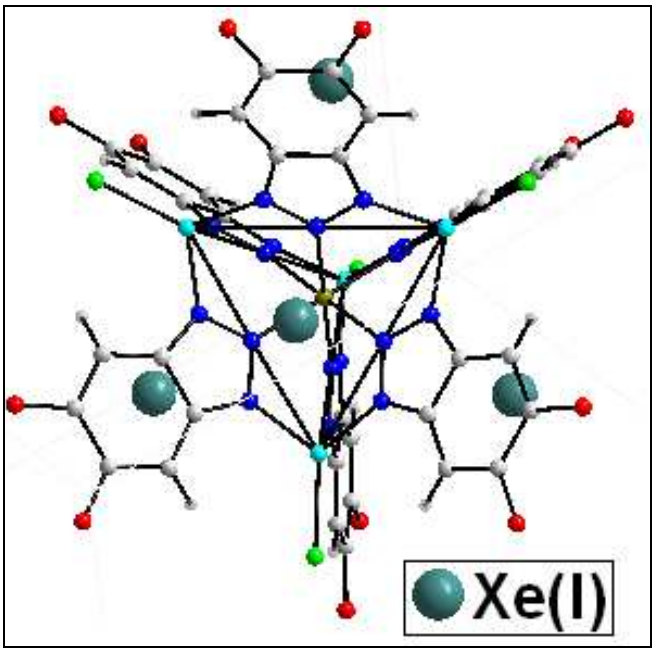

Figure 4.50. Positions of Xe atoms in pores of Cu-MFU-4*l* at 250K (50 mbar and 100 mbar).

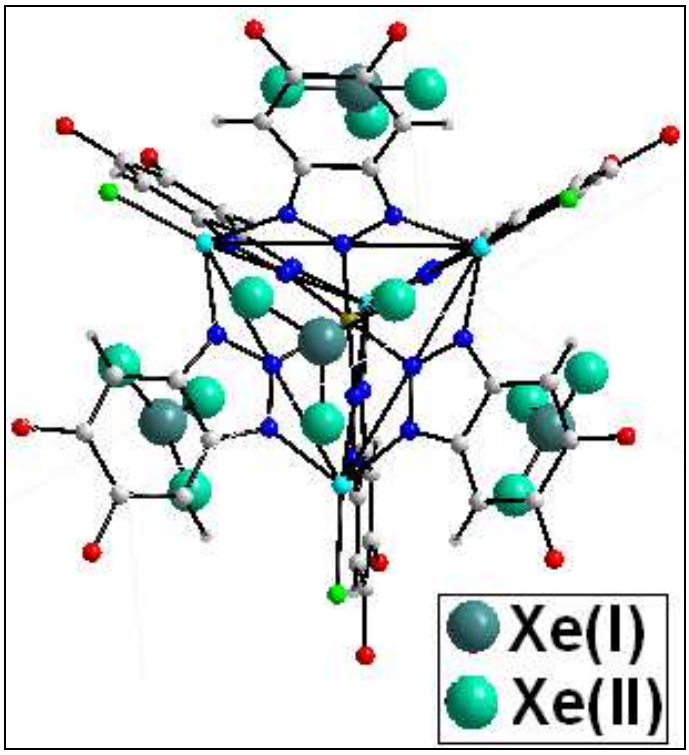

Figure 4.51. Positions of Xe atoms in pores of Cu-MFU-4*l* at 250K (50 mbar and 100 mbar).

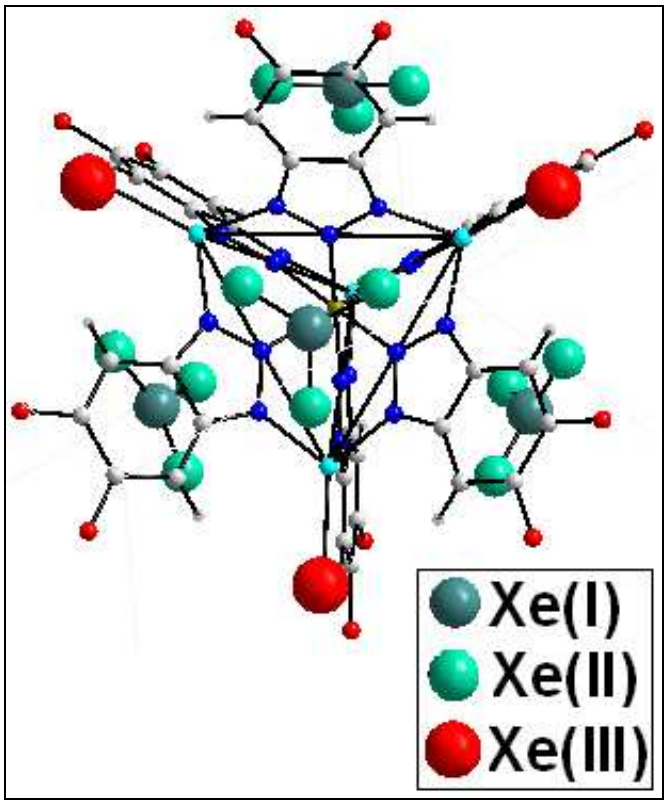

Figure 4.52. Positions of Xe atoms in pores of Cu-MFU-4*l* at 250K (250 mbar).

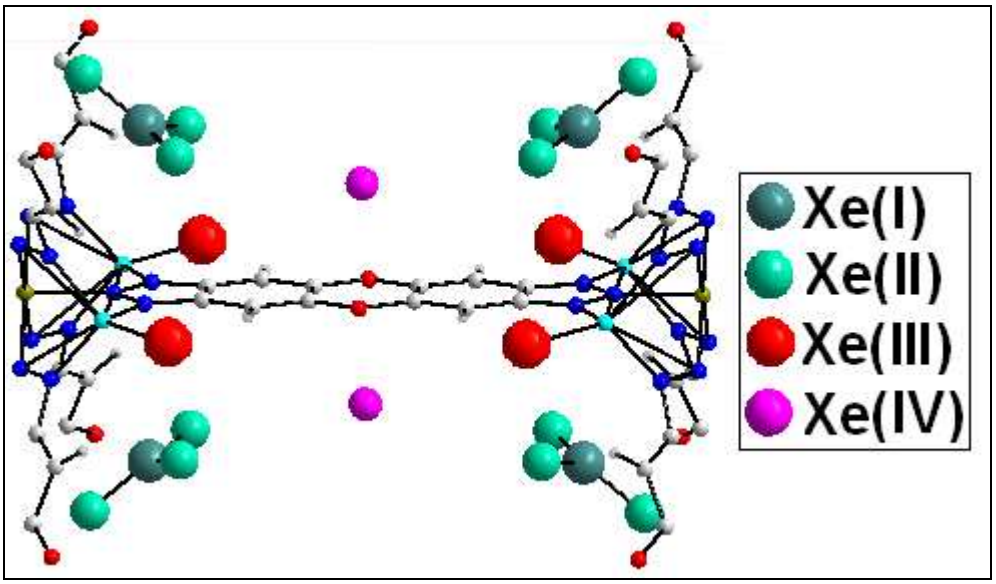

Figure 4.53. Positions of Xe atoms in pores of Cu-MFU-4*l* at 250K (500 mbar).

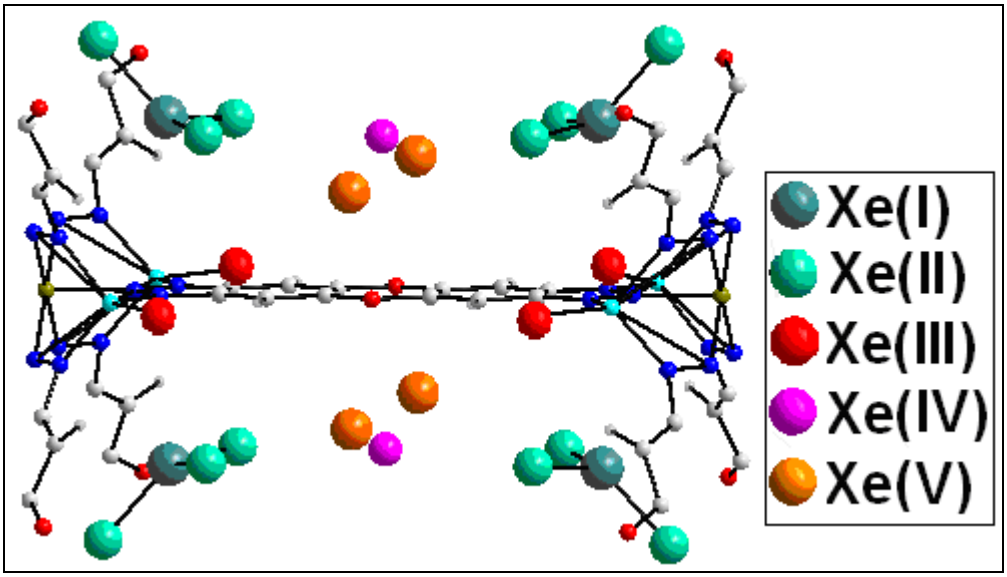

Figure 4.54. Positions of Xe atoms in pores of Cu-MFU-4*l* at 250K (1000 mbar).

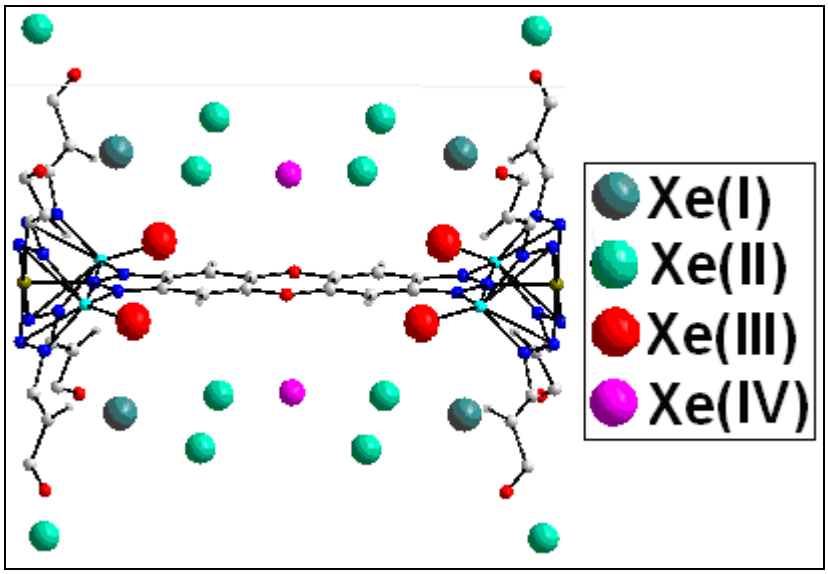

Figure 4.55. Positions of Xe atoms in pores of Cu-MFU-4*l* at 170K (50 mbar).

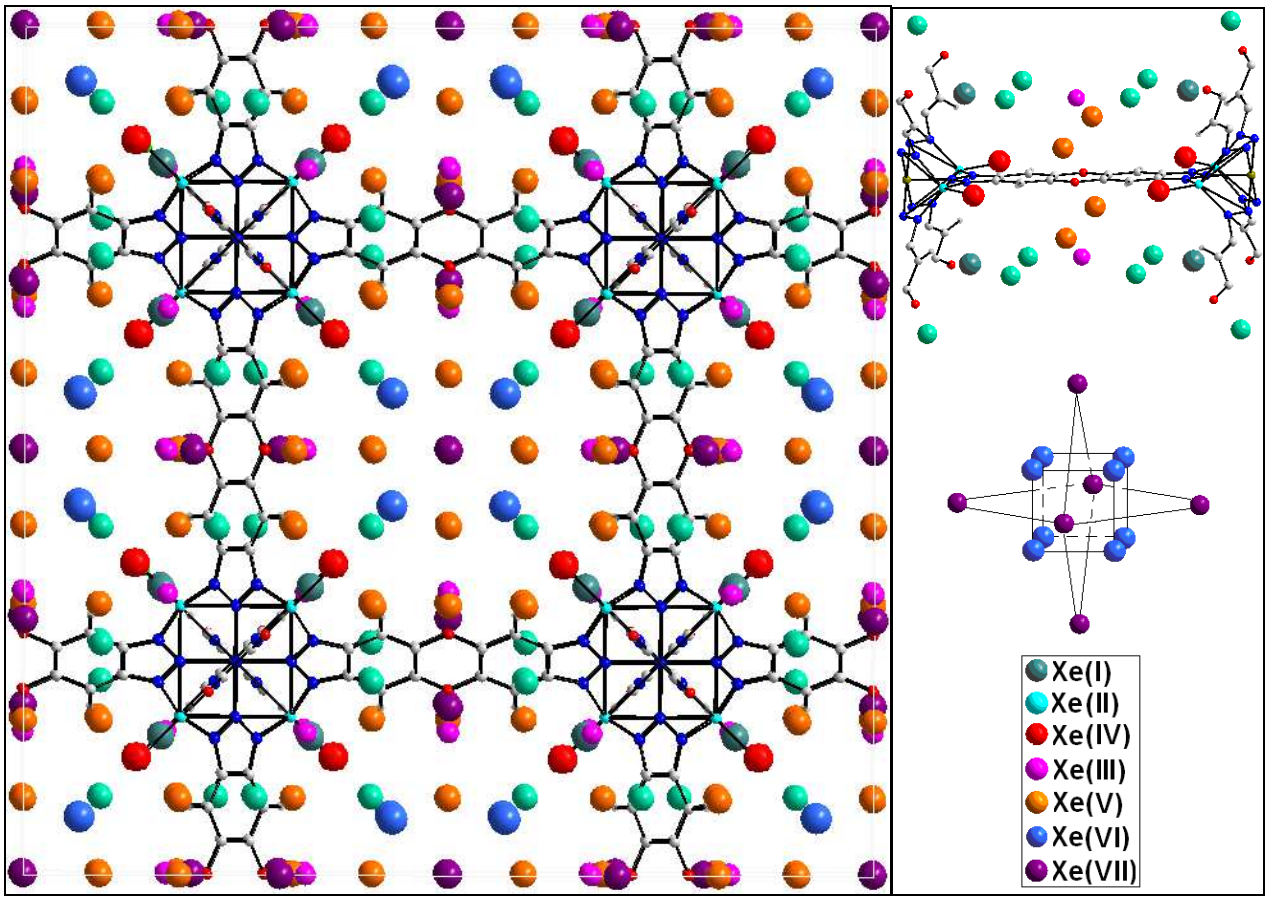

Figure 4.56. Positions of Xe atoms in pores of Cu-MFU-4*l* at 170K (100 mbar).

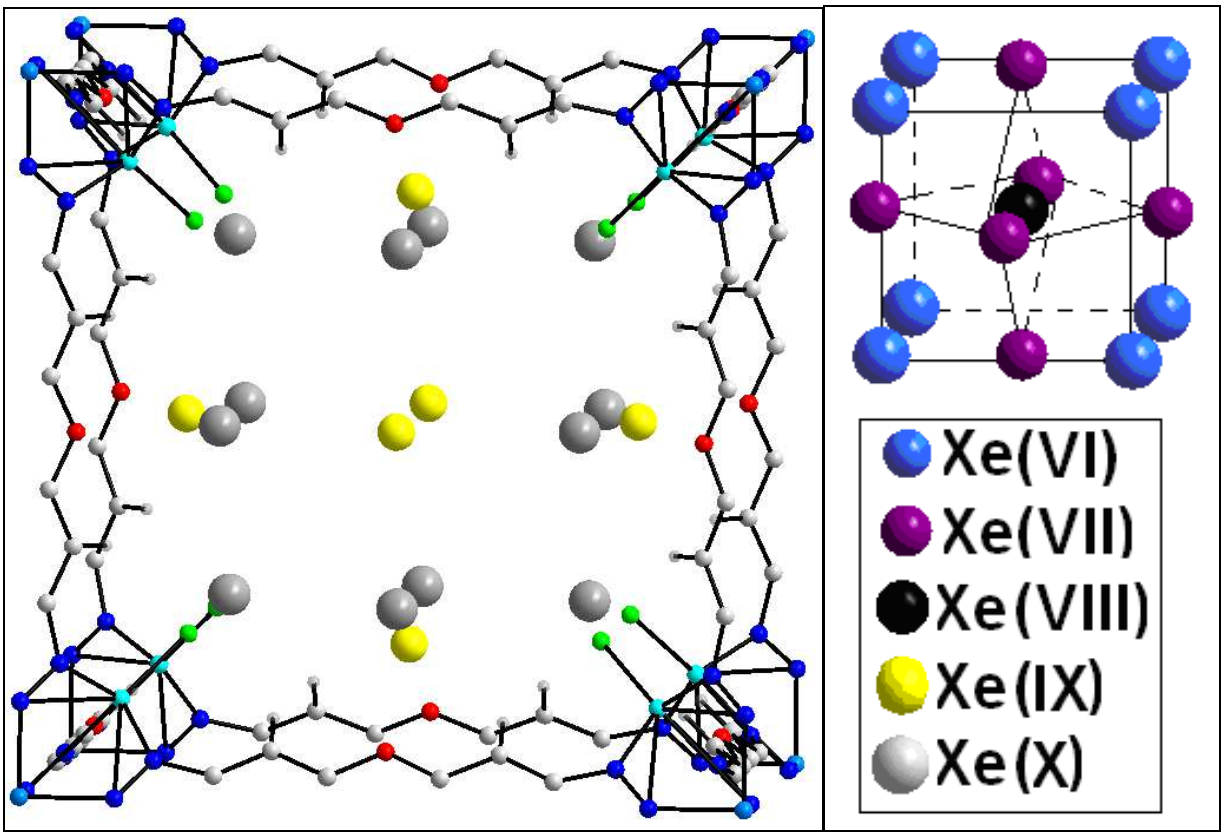

Figure 4.57. Additional positions of Xe atoms in small pores (left) and second adsorption layer in large pores (right) of Cu-MFU-4*l* at 170K (250 mbar and 500 mbar).

Results of Kr and Xe adsorption on Cu-MFU-4*l* are consistent with the adsorption behaviour of the lighter Ar atoms in MOF-5 (Rowsell *et al.*, 2005). In total, 8 different adsorption sites of argon in MOF-5 were found: near metal site in large and small cavities, between three and two oxygen atoms of carboxylate groups from the organic linker, above the center of the benzene ring and in the plane of the benzene ring near hydrogen atoms, and also inside of large and small cavities. Large and small cavities of MOF-5 were also found to be not equivalent for Ar adsorption.

Interesting results were reported for methane adsorption in MOF-5 (Wu *et al.*, 2009b), (methane molecule has polarizability and atomic radius similar to Kr). The strongest adsorption site of CD_4 was determined at the center of the three ZnO_3 triangular faces (metal sites), similar to the single adsorption sites for both Kr and Xe in Zn-MFU-4*l* and the main adsorption site in Cu-MFU-4*l*. The second adsorption site is located above the O-O edge of the ZnO_4 tetrahedra and the third adsorption site is above the center of the benzene ring of the organic linkers. The

forth and fifth adsorption sites are located inside the cavity and the adsorbed methane molecules interact mainly with surrounding methane.

4.6. Conclusion

A systematic structural investigation of Kr and Xe adsorption sites in different types of MOFs, performed as part of the presented PhD thesis, allows the determination of relations between the crystal structure of a MOF and its ability to adsorb, store and separate noble gases. Different types of MOFs were investigated: CPO-27-Ni and CPO-27-Mg with 1D channel topology and abundant open metal sites (created by removing of coordinated water molecules), Zn-MFU-4*l* and Cu-MFU-4*l* with pore structure and accessible metal sites, and ZIF-8 with relatively small pores and inaccessible metal sites. It was found that two main factors influence noble gas adsorption by MOFs: channel morphology and polarizability of adsorption sites. It could be unambiguously confirmed that open metal sites are the primary and strongest adsorption sites for noble gases, if there is no strong geometric confinement of intercalated atoms. This is explained by the nature of noble gas adsorption in MOFs. Since noble gases lack chemical reactivity, the only possible mechanism of adsorption for them is van der Waals interaction based on the polarizability of the atoms. Metal sites are the most polarizable part of the MOF's structure, and thus they are also the main adsorption sites with highest binding energy to intercalated noble gas atoms (CPO-24, MFU-4*l*, MOF-5). The isosteric heat of adsorption of highly polarizable metal sites can be exceeded only by increased interaction between adsorbed atoms and framework, which might be achieved through the geometrical confinement of intercalated atoms in small pores (HKUST-1, ZIF-8). The polarizability of C=O and C-O bonds are usually lower as compared to that of metal sites, and they act as a secondary adsorption site (CPO-27, MOF-5). The less polarizable C=C bond is a major adsorption site for noble gases in ZIF-8 due to the absence of accessible metal sites and carbon-oxygen bonds in the crystal structure. The high isosteric heat of adsorption for noble gases in ZIF-8 is provided by the geometrical confinement of noble gases in small pores.

Thus, MOFs with the small pores and abundant accessible metal sites are promising candidates for noble gas storage and separation.

4.7. Publications and authors contribution

Chapters 4.2.1 and 4.5.2 are partially published:

1) Soleimani Dorcheh, A.; Dinnebier, R.E.; Kuc, A.; Magdysyuk, O.; Adams, F.; Denysenko, D.; Heine, T.; Volkmer, D.; Donner, W.; Hirscher, M. "Novel characterization of the adsorption sites in large pore metal–organic frameworks: combination of X-ray powder diffraction and thermal desorption spectroscopy". *Phys. Chem. Chem. Phys.* (2012b), **14**, 12892–12897.

Chapters 4.1, 4.3, 4.4, 4.5 will be published:

2) Magdysyuk *et al.* Understanding the adsorption mechanism of noble gases Kr and Xe in CPO-27-Ni, CPO-27-Mg, and ZIF-8 (in preparation).

3) Magdysyuk *et al.* Unprecedented formation of a quasi-solid structure by intercalated noble gas atoms in pores of Cu^{I}-MFU-4*l* metal-organic framework (in preparation).

Mr. A. Soleimani Dorcheh, Dr. M Hirscher (Max Planck Institute for Solid State Research), and Prof. W. Donner performed thermal desorption measurements (not presented in this PhD thesis), Mr. D. Denysenko and Prof. D. Volkmer (University of Augsburg, Germany) synthesized Zn-MFU-4*l* and Cu-MFU-4*l*. Dr. A. Kuc and Prof. Th. Heine (University of Bremen, Germany) performed theoretical simulations (not presented in this PhD thesis). CPO-27 was synthesized in the group of Prof. R. Morris (School of Chemistry, University of St Andrews, UK). Dr. P.N. Trikalitis (Department of Chemistry, University of Crete) performed adsorption measurements of CPO-27. Sample ZIF-8 was provided by BASF as Basolite Z-1200.

Capillary gas cells for *in situ* laboratory (Max Planck Institute for Solid State Research, Stuttgart) and synchrotron (PETRA III) X-ray powder diffraction experiments, as well as equipment for *in situ* evacuation and gas loading were developed and constructed by Mr. F. Adams (Max Planck Institute for Solid State Research, Stuttgart).

Support with synchrotron measurements at ESRF, ID31 (proposals ch3737, ch3878) to Dr. Ch. Drathen (ESRF, Grenoble), and with synchrotron measurements at PETRA III, P02.1 (proposal I-20130239) to Dr. H-P. Liermann, Dr. M. Hinterstein, Dr. J. Bednarcik (PETRA III, Hamburg), Mr. F. Adams, Mr. T. Runcevski, Mr. M. Etter (Max Planck Institute for Solid State Research, Stuttgart) is gratefully acknowledged.

4.8. References

Ania, C.O.; Garcia-Perez, E.; Haro, M.; Gutierrez-Sevillano, J.J.; Valdes-Solis, T.; Parra, J.B.; Calero, S. (2012). *Understanding Gas-Induced Structural Deformation of ZIF-8. J. Phys. Chem. Lett.* **3**, 1159−1164.

Assfour, B.; Leoni, S.; Seifert, G. (2010). *Hydrogen Adsorption Sites in Zeolite Imidazolate Frameworks ZIF-8 and ZIF-11. J. Phys. Chem. C.* **114**, 13381–13384.

Bae, Y-S.; Hauser, B.G.; Colón, Y.J.; Hupp, J.T.; Farha, O.K.; Snurr, R.Q. (2013). *High xenon/krypton selectivity in a metal-organic framework with small pores and strong adsorption sites. Microporous and Mesoporous Materials.* **169**, 176–179.

Bae, Y-S.; Liu, J.; Wilmer, C.E.; Sun, H.; Dickey, A.N.; Kim, M.B.; Benin, A.I.; Willis, R.R.; Barpaga, D.; LeVan, M.D.; Snurr, R.Q. (2014). *Effect of pyridine modification of Ni/DOBDC on CO_2 capture under humid conditions. Chem. Commun.* **50**, 3296–3298.

Bloch, E.D.; Murray, L.J.; Queen, W.L.; Chavan, S.; Maximoff, S.N.; Bigi, Ju.P.; Krishna, R.; Peterson, V.K.; Grandjean, F.; Long, G.J.; Smit, B.; Bordiga, S.; Brown, C.M.; Long, J.R. (2011). *Selective Binding of O_2 over N_2 in a Redox-Active Metal-Organic Framework with Open Iron(II) Coordination Sites. J. Am. Chem. Soc.* **133**, 14814–14822.

Bloch, E.D.; Queen, W.L.; Krishna, R.; Zadrozny, J.M.; Brown, C.M.; Long, J.R. (2012). *Hydrocarbon Separations in a Metal-Organic Framework with Open Iron(II) Coordination Sites. Science.* **335**, 1606–1610.

Botas, J.A.; Calleja, G.; Sánchez-Sánchez, M.; Orcajo, M.G. (2011). *Effect of Zn/Co ratio in MOF-74 type materials containing exposed metal sites on their hydrogen adsorption behaviour and on their band gap energy. Int. J. Hydrogen Energy.* **36**, 10834–10844.

Brunelli, M.; Fitch, A.N. (2003). *A glass capillary cell for in situ powder X-ray diffraction of condensed volatile compounds. Solid HCFC-123a and HCFC-124. J. Synchrotron Rad.* **10**, 337–339.

Buchter, F.; Lodziana, Z.; Remhof, A.; Mauron, Ph.; Friedrichs, O.; Borgschulte, A.; Züttel, A.; Filinchuk, Y.; Palatinus, L. (2011). *Experimental charge density of $LiBD_4$ from maximum entropy method. Phys. Rev. B.* **86**, 064107.

Caskey, S.R.; Wong-Foy, A.G.; Matzger, A.J. (2008). *Dramatic Tuning of Carbon Dioxide Uptake via Metal Substitution in a Coordination Polymer with Cylindrical Pores. J. Am. Chem. Soc.* **130**, 10870–10871.

Chavan, S.; Bonino, F.; Valenzano, L.; Civalleri, B.; Lamberti, C.; Acerbi, N.; Cavka, J.H.; Leistner, M.; Bordiga, S. (2013). *Fundamental Aspects of H_2S Adsorption on CPO-27-Ni. J. Phys. Chem. C*. **117**(30), 15615–15622.

Coelho, A.A. (2007). TOPAS. Version 4.1. Coelho Software, Brisbane, Australia.

Cozzolino, A.F.; Brozek, C.K.; Palmer, R.D.; Yano, J.; Li, M.; Dincă, M. (2014). *Ligand Redox Non-innocence in the Stoichiometric Oxidation of Mn_2(2,5-dioxidoterephthalate) (Mn-MOF-74). J. Am. Chem. Soc.* **136**(9), 3334–3337.

Deng, H.; Grunder, S.; Cordova, K.E.; Valente, C.; Furukawa, H.; Hmadeh, M.; Gándara, F.; Whalley, A.C.; Liu, Z.; Asahina, S.; Kazumori, H.; O'Keeffe, M.; Terasaki, O.; Stoddart, J.F.; Yaghi, O.M. (2012). *Large-Pore Apertures in a Series of Metal-Organic Frameworks. Science*. **336**, 1018–1023.

Denysenko, D.; Grzywa, M.; Tonigold, M.; Streppel, B.; Krkljus, I.; Hirscher, M.; Mugnaioli, E.; Kolb, U.; Hanss, J.; Volkmer, D. (2011). *Elucidating Gating Effects for Hydrogen Sorption in MFU-4-Type Triazol. Chem. Eur. J.* **17**, 1837–1848.

Denysenko, D.; Grzywa, M.; Jelic, J.; Reuter, K.; Volkmer, D. (2014). *Scorpionate-type Coordination in MFU-4l Metal-Organic Frameworks: Small Molecule Binding and Activation Upon Thermally Activated Release of Open Metal Sites. Angew. Chem. Int. Ed.* (accepted).

Diaz-Garcia, M; Sanchez- Sanchez, M. (2014). *Synthesis and characterization of a new Cd-based Metal-Organic Framework isostructural with MOF-74 / CPO-27 materials. Microporous and Mesoporous Materials*. **190**, 248–264.

Dietzel, P.D.C.; Morita, Y; Blom, R; Fjellvåg, H. (2005). *An In Situ High-Temperature Single-Crystal Investigation of a Dehydrated Metal–Organic Framework Compound and Field-Induced Magnetization of One-Dimensional Metal–Oxygen Chains. Angew. Chem. Int. Ed.* **44**, 6354–6358.

Dietzel, P.D.C.; Panella, B.; Hirscher, M.; Blom, R.; Fjellvåg, H. (2006). *Hydrogen adsorption in a nickel based coordination polymer with open metal sites in the cylindrical cavities of the desolvated framework. Chem. Commun.* **42**, 959–961.

Dietzel, P.D.C.; Johnsen, R.E.; Blom, R.; Fjellvåg, H. (2008a). *Structural Changes and Coordinatively Unsaturated Metal Atoms on Dehydration of Honeycomb Analogous Microporous Metal–Organic Frameworks. Chem. Eur. J.* **14**, 2389–2397.

Dietzel, P.D.C.; Johnsen, R.E.; Fjellvåg, H.; Bordiga, S.; Groppo, E.; Chavan, S.; Blom, R. (2008b). *Adsorption properties and structure of CO_2 adsorbed on open coordination sites of metal–organic framework Ni_2(dhtp) from gas adsorption, IR spectroscopy and X-ray diffraction. Chem. Commun.* **44**, 5125–5127.

Dietzel, P.D.C.; Georgiev, P.A.; Eckert, Ju.; Blom, R.; Strässle, Th.; Unruh, T. (2010). *Interaction of hydrogen with accessible metal sites in the metal–organic frameworks M_2(dhtp) (CPO-27-M; M = Ni, Co, Mg). Chem. Commun.* **46**, 4962–4964.

Farrusseng, D.; Daniel, C.; Gaudillère, C.; Ravon, U.; Schuurman, Y.; Mirodatos, C.; Dubbeldam, D.; Frost, H.; Snurr, R.Q. (2009). *Heats of Adsorption for Seven Gases in Three Metal-Organic Frameworks: Systematic Comparison of Experiment and Simulation. Langmuir.* **25**(13), 7383−7388.

Fernandez, C.A.; Liu, J.; Thallapally, P.K.; Strachan, D.M. (2012). *Switching Kr/Xe Selectivity with Temperature in a Metal−Organic Framework. J. Am. Chem. Soc.* **134**, 9046−9049.

Fairen-Jimenez, D.; Moggach, S. A.; Wharmby, M. T.; Wright, P.A.; Parsons, S.; Düren, T. (2011). *Opening the gate: framework flexibility in ZIF-8 explored by experiments and simulations. J. Am. Chem. Soc.* **133**, 8900−8902.

Huang, X.C.; Lin, Y.Y.; Zhang, J.-P.; Chen, X.M. (2006). *Ligand-Directed Strategy for Zeolite-Type Metal–Organic Frameworks: Zinc(II) Imidazolates with Unusual Zeolitic Topologies. Angew. Chem., Int.Ed.* **45**, 1557−1559.

Hulvey, Z.; Lawler, K.V.; Qiao, Z.; Zhou, J.; Fairen-Jimenez, D.; Snurr, R.Q.; Ushakov, S.V.; Navrotsky, A.; Brown, C.M.; Forster, P.M. (2013). *Noble Gas Adsorption in Copper Trimesate, HKUST-1: An Experimental and Computational Study. J. Phys. Chem. C.* **117**, 20116−20126.

Gurdal, Y.; Keskin, S. (2012). *Atomically Detailed Modeling of Metal Organic Frameworks for Adsorption, Diffusion, and Separation of Noble Gas Mixtures. Ind. Eng. Chem. Res.* **51**, 7373−7382.

Gurdal, Y.; Keskin, S. (2013). *Predicting Noble Gas Separation Performance of Metal Organic Frameworks Using Theoretical Correlations. J. Phys. Chem. C.* **117**, 5229−5241.

Kahr, J.; Morris, R.E.; Wright, P.A. (2013). *Post-synthetic incorporation of nickel into CPO-27(Mg) to give materials with enhanced permanent porosity. CrystEngComm*. **15**, 9779−9786.

Kitaura, R.; Kitagawa, S.; Kubota, Y.; Kobayashi, T. C.; Kindo, K.; Mita, Y.; Matsuo, A.; Kobayashi, M.; Chang, H.; Ozawa, T. C.; Suzuki, M.; Sakata, M.; Takata, M. (2002). *Formation of a One-Dimensional Array of Oxygen in a Microporous Metal-Organic Solid. Science.* **298**, 2358–2361.

Liu, Y.; Kabbour, H.; Brown, C.M.; Neumann, D.A.; Ahn, C.C. (2008). *Increasing the Density of Adsorbed Hydrogen with Coordinatively Unsaturated Metal Centers in Metal-Organic Frameworks. Langmuir.* **24**, 4772−4777.

Liu, J.; Thallapally, P.K.; Strachan, D. (2012). *Metal−Organic Frameworks for Removal of Xe and Kr from Nuclear Fuel Reprocessing Plants. Langmuir.* **28**, 11584−11589.

Liu, G.; Qin, Y.; Jing, L.; Wei, G.; Li, H. (2013). *Two novel MOF-74 analogs exhibiting unique luminescent selectivity. Chem. Commun.* **49**, 1699−1701.

Liu, J.; Strachan, D.M.; Thallapally, P.K. (2014). *Enhanced Noble Gas Adsorption in Ag@MOF-74Ni. Chem. Commun.* **50**, 466−468.

Märcz, M.; Johnsen, R.E.; Dietzel, P.D.C.; Fjellvåg, H. (2012). *The iron member of the CPO-27 coordination polymer series: Synthesis, characterization, and intriguing redox properties. Microporous and Mesoporous Materials.* **157**, 62–74.

Matsuda, R.; Kitaura, R.; Kitagawa, S.; Kubota, Y.; Belosludov, R. V.; Kobayashi, T. C.; Sakamoto, H.; Chiba, T.; Takata, M.; Kawazoe, Y.; Mita, Y**.** (2005). *Highly controlled acetylene accommodation in a metal−organic microporous material. Nature.* **436**, 238–241.

Meek, S.T.; Teich-McGoldrick, S.L.; Perry IV, J.J.; Greathouse, J.A.; Allendorf, M.D. (2012). *Effects of Polarizability on the Adsorption of Noble Gases at Low Pressures in Monohalogenated Isoreticular Metal−Organic Frameworks. J. Phys. Chem. C.* **116**, 19765−19772.

Mueller, U.; Schubert, M.; Teich, F.; Puetter, H.; Schierle-Arndt, K.; Pastre, J. (2006). *Metal–organic frameworks—prospective industrial applications. J. Mater. Chem.* **16**, 626–636.

Palatinus, L.; Prathapa, S.J.; van Smaalen, S. (2012). *EDMA: a computer program for topological analysis of discrete electron densities. J. Appl. Cryst.* **45**, 575–580.

Pantatosaki, E.; Pazzona, F.G.; Megariotis, G.; Papadopoulos, G.K. (2010). *Atomistic Simulation Studies on the Dynamics and Thermodynamics of Nonpolar Molecules within the Zeolite Imidazolate Framework-8. J. Phys. Chem. B.* **114**, 2493–2503.

Park, K.S.; Ni, Z.; Cote, A.P.; Choi, J.Y.; Huang, R.; Uribe-Romo, F.J.; Chae, H.K.; O'Keefe, M.; Yaghi, O.M. (2006). *Exceptional chemical and thermal stability of zeolitic imidazolate frameworks. Proc. Natl. Acad. Sci. U.S.A.* **103**, 10186–10191.

Peterson, V.K.; Liu, Y.; Brown, C.M.; Kepert, C.J. (2006). *Neutron Powder Diffraction Study of D_2 Sorption in Cu_3(1,3,5-benzenetricarboxylate)$_2$. J. Am. Chem. Soc.* **128**, 15578–15579.

Queen, W.L.; Bloch, E.D.; Brown, C.M.; Hudson, M.R.; Mason, J.A.; Murray, L.J.; Ramirez-Cuesta, A.J.; Peterson, V.K.; Long, J.R. (2012). *Hydrogen adsorption in the metal–organic frameworks Fe_2(dobdc) and $Fe_2(O_2)$(dobdc). Dalton Trans.* **41**, 4180–4187.

Rosi, N.L.; Kim, J.; Eddaoudi, M.; Chen, B. L.; O'Keeffe, M.; Yaghi, O.M. (2005). *Rod Packings and Metal-Organic Frameworks Constructed from Rod-Shaped Secondary Building Units. J. Am. Chem. Soc.* **127**, 1504−1518.

Rowsell, J.L.C.; Spencer, E.C.; Eckert, J.; Howard, J.A.K.; Yaghi, O.M. (2005). *Gas Adsorption Sites in a Large-Pore Metal-Organic Framework. Science,* **309**, 1350–1354.

Ryan, P.; Farha, O.K.; Broadbelt, L.J.; Snurr, R.Q. (2011). *Computational Screening of Metal-Organic Frameworks for Xenon/Krypton Separation. AIChE J.* **57**, 1759.

Ryan, P.J; Farha, O.K.; Broadbelt, L.J.; Snurr, R.Q.; Bae, Y-S. (2014). Patent US 2014/0013943 A1.

Sakata, M.; Sato, M. (1990). *Accurate structure analysis by the maximum-entropy method. Acta Crystallogr.* **A46**, 263–270.

Samy, A.; Dinnebier, R.E.; van Smaalen, S.; Jansen, M. (2010). *Maximum entropy method and charge flipping, a powerful combination to visualize the true nature of structural disorder from in situ X-ray powder diffraction data. Acta Cryst.* **B66**, 184–195.

Sanz, R.; Martínez, F.; Orcajo, G.; Wojtas, L.; Briones, D. (2013). *Synthesis of a honeycomb-like Cu-based metal–organic framework and its carbon dioxide adsorption behaviour. Dalton Trans.* **42**, 2392–2398.

Sikora, B.J.; Wilmer, C.E.; Greenfield, M.L.; Snurr, R.Q. (2012). *Thermodynamic analysis of Xe/Kr selectivity in over 137 000 hypothetical metal–organic frameworks. Chem. Sci.* **3**, 2217.

van Smaalen, S.; Palatinus, L.; Schneider, M. (2003). *The Maximum Entropy Method in Superspace. Acta Crystallogr.* **A59,** 459–469.

Soleimani Dorcheh, A.; Denysenko, D.; Volkmer, D.; Donner, W.; Hirscher, M. (2012a). *Noble gases and microporous frameworks; from interaction to application. Microporous and Mesoporous Materials.* **162**, 64–68.

Soleimani Dorcheh, A.; Dinnebier, R.E.; Kuc, A.; Magdysyuk, O.; Adams, F.; Denysenko, D.; Heine, T.; Volkmer, D.; Donner, W.; Hirscher, M. (2012b). *Novel characterization of the adsorption sites in large pore metal–organic frameworks: combination of X-ray powder diffraction and thermal desorption spectroscopy. Phys. Chem. Chem. Phys.* **14**, 12892–12897.

Spencer, E.C.; Howard, J.A.K.; McIntyre, G.J.; Rowsell, J.L.C.; Yaghi, O.M. (2006). *Determination of the hydrogen absorption sites in Zn_4O(1,4-benzenedicarboxylate) by single crystal neutron diffraction. Chem. Commun.* **42**, 278–280

Sumida, K.; Brown, C.M.; Herm, Z.R.; Chavan, S.; Bordigad, S.; Long, J.R. (2011). *Hydrogen storage properties and neutron scattering studies of Mg_2(dobdc)—a metal–organic framework with open Mg^{2+} adsorption sites. Chem. Commun.* **47**, 1157–1159.

Thallapally, P.K.; Grate, J.W.; Motkuri, R.K. (2012). *Facile Xenon Capture and Release at Room-temperature Using a Metal-Organic Framework: A Comparison with Activated Charcoal. Chem. Commun.* **48**, 347−349.

Wang, H.; Yao, K.; Zhang, Z.; Jagiello, J.; Gong, Q.; Han, Y.; Li, J. (2014). *The first example of commensurate adsorption of atomic gas in a MOF and effective separation of xenon from other noble gases. Chem. Sci.* **5**, 620–624.

Wu, H.; Zhou, W.; Yildirim, T. (2007). *Hydrogen Storage in a Prototypical Zeolitic Imidazolate Framework-8. J. Am. Chem. Soc.* **129**, 5314–5315.

Wu, H.; Zhou, W.; Yildirim, T. (2009a). *High-Capacity Methane Storage in Metal-Organic Frameworks M_2(dhtp): The Important Role of Open Metal Sites. J. Am. Chem. Soc.* **131**, 4995–5000.

Wu, H.; Zhou, W.; Yildirim, T. (2009b). *Methane Sorption in Nanoporous Metal-Organic Frameworks and First-Order Phase Transition of Confined Methane. J. Phys. Chem. C*, **113**, 3029–3035.

Wu, H.; Simmons, J.M.; Liu, Y.; Brown, C.M.; Wang, X.-S.; Ma, S.; Peterson, V.K.; Southon, P.D.; Kepert, C.J.; Zhou, H.-C; Yildirim, T.; Zhou, W. (2010a). *Metal-Organic Frameworks with Exceptionally High Methane Uptake: Where and How is Methane Stored? Chem.—Eur. J.* **16**, 5205–5214.

Wu, H.; Simmons, J.M.; Srinivas, G.; Zhou, W.; Yildirim, T. (2010b). *Adsorption Sites and Binding Nature of CO_2 in Prototypical Metal-Organic Frameworks: A Combined Neutron Diffraction and First-Principles Study. J. Phys. Chem. Lett.* **1**, 1946–1951.

Xiang, S.; Zhou, W.; Gallegos, J. M.; Liu, Y.; Chen, B. (2009). *Exceptionally High Acetylene Uptake in a Microporous Metal-Organic Framework with Open Metal Sites. J. Am. Chem. Soc.* **131**, 12415–12419.

Xiang, S.; Zhou, W.; Zhang, Z.; Green, M. A.; Liu, Y.; Chen, B. (2010). *Open Metal Sites within Isostructural Metal−Organic Frameworks for Differential Recognition of Acetylene and Extraordinarily High Acetylene Storage Capacity at Room-temperature. Angew. Chem., Int. Ed.* **49**, 4615−4618.

Yu, D.; Yazaydin, A.O.; Lane, J.R.; Dietzel, P.D.C.; Snurr, R.Q. (2013). *A combined experimental and quantum chemical study of CO_2 adsorption in the metal–organic framework CPO-27 with different metals. Chem. Sci.* **4**, 3544−3556.

Zhang, C.; Lively, R.P.; Zhang, K.; Johnson, J.R.; Karvan, O.; Koros, W.J. (2012). *Unexpected Molecular Sieving Properties of Zeolitic Imidazolate Framework-8. J. Phys. Chem. Lett.* **3**, 2130−2134.

Zhou, W.; Wu, H.; Yildirim, T. (2008). *Enhanced H_2 Adsorption in Isostructural Metal-Organic Frameworks with Open Metal Sites: Strong Dependence of the Binding Strength on Metal Ions. J. Am. Chem. Soc.* **130**, 15268–15269.

Zhou, W.; Wang, Q.; Zhang, L.; Liu, Y-C., Kang, Y. (2009). *Adsorption Sites of Hydrogen in Zeolitic Imidazolate Frameworks. J. Phys. Chem. B,* **113**(32), 11049−11053.

5. Summary

Due to the reduced informational content of powder diffraction data in comparison with single crystal diffraction, the challenge of increasing the accuracy in powder diffraction is of utmost importance. Several different ways of increasing accuracy in powder diffraction were investigated in the presented PhD thesis: possibilities and limitations of the maximum entropy method (MEM) for increasing accuracy of the electron density determination from high-resolution laboratory and synchrotron powder X-ray diffraction data, application of parametric refinement for the analysis of different models of coupling between strain and order parameter during structural phase transitions, and investigation of noble gas adsorption in MOFs by state of art laboratory and synchrotron powder diffraction.

A series of 24 apatites with intercalated atoms was investigated by the MEM. It was found that conventional Fourier maps based on F_{obs}–constraints (observed structure factors are calculated from the best incomplete model) contain a lot of spurious peaks with high electron density, making it impossible to locate the intercalated metal atoms unambiguously. MEM maps based on F_{obs}–, F_{obs}+G–, and F_{LeBail}+G–constraints allowed unambiguous localization of copper atoms with occupancies down to 0.05 from laboratory X-ray powder diffraction, which corresponds to approximately 1.4 electrons per site. For confirmation of the reliability of the results received from high-resolution laboratory X-ray powder diffraction data, high-resolution synchrotron X-ray powder diffraction data were used for the MEM calculations of Sr-apatite with intercalated copper atoms. These results basically confirmed that the MEM can be successfully used for the determination of accurate electron density distributions from high-resolution laboratory X-ray powder diffraction data. The difference between MEM maps from laboratory and synchrotron sources are caused primarily by different instrumental peak profiles and different resolution $\sin\theta/\lambda$.

As a common tendency it was confirmed that the MEM map based on F_{obs}–constraints is the most biased by the model, and the MEM map based on F_{LeBail}+G–constraints is the least biased by the model. For the MEM maps calculated with procrystal density for known atoms, the value of the electron density of located metal atoms is increased in the order of maps based on F_{obs}–, F_{obs}+G–, and F_{LeBail}+G–constraints.

A strong advantage of the MEM is the possibility to use G–constraints for overlapping reflections, thus avoiding the model-bias for observed structure factors (F_{obs}) from Rietveld

refinement. The amplitudes of structure factors can be retrieved after a Le Bail fit (F_{LeBail}) without the need of any structural information. They also can be used as experimental data for MEM calculations for centrosymmetric structures in combination with phases from Rietveld refinement and *G*-constraints for overlapping reflections. Applying *G*–constraints for a sum of intensities of groups of overlapping reflections decreases the model bias through the absence of the model-biased partitioning of the overlapping intensities.

Another advantage of the MEM is the possibility to use prior information on the crystal structure. The procrystal prior electron density clearly reduces artifacts and MEM reconstructions with this prior allow the visualization of very fine features of the electron density. As an example, the experimental electron density distribution and the integrated ionic charges of $BaZnF_4$ and $BaMgF_4$ were determined by application of the MEM on high-resolution synchrotron X-ray powder diffraction data at 10 K. For the first time the MEM was successfully applied for the determination of accurate electron density distributions of heavy-atom compounds. The best electron density distribution was obtained by using *G*-constraints for strongly overlapping reflections (F_2+*G*-constraints) and by using prior-derived constraints (F_2+F_{PD}-constraints). The use of procrystal electron density in the form of IASM was necessary in both cases. The experimental atomic charges were in good agreement with the charges calculated by DFT.

Parametric refinement was established as a powerful tool to test different models of coupling between strain and order parameter during a structural phase transition. In the present PhD thesis, the high-temperature ferroelastic phase transitions $P\bar{1}$ <-> $P2_1/m$ of $LuF[SeO_3]$ and $Fm\bar{3}m$ –> $I4/m$ of Sr_2CoOsO_6 were analyzed in great detail. Using the distortion modes approach allowed to separate and quantify primary and secondary distortion mechanisms, which are responsible for the changing of crystal symmetry. These distortion mechanisms are related by group theory and their changes with temperature/pressure obey to Landau theory for structural phase transitions.

Strong lattice strain created during preliminary cooling of $LuF[SeO_3]$ possessed explicit temperature dependence and its variation on heating was described by biquadratic coupling between symmetry-adapted strain and order parameter with explicit temperature dependence of the strain, of which the underline theory was developed in the course of this work. It was

confirmed that different coupling mechanisms are responsible for the large hysteresis of the lattice parameters (and symmetry-adapted strains) during this phase transition.

The high-temperature phase transition $Fm\bar{3}m$ –> $I4/m$ in Sr_2CoOsO_6 was described using distortion modes and parametric refinement, based on classical distortion modes description, rigid body refinement, and rotational modes (rigid body distortion modes) refinement. The distortion modes approach allowed to separate three distortion modes, responsible for the changing of crystal symmetry in Sr_2CoOsO_6 during the phase transition. While the primary distortion mode describes the rotation of octahedra and acts as an order parameter, two secondary distortion modes describe de deformation of octahedra.

A systematic structural investigation of Kr and Xe adsorption sites in different types of MOFs, performed as part of the present PhD thesis, allows the analysis of relations between the crystal structure of a MOF and its ability to adsorb, store and separate noble gases. A highly flexible gas loading device was developed for this purpose. Different MOFs were investigated: CPO-27-Ni and CPO-27-Mg with 1D channel topology and abundant open metal sites, Zn-MFU-4*l* and Cu-MFU-4*l* with pore structure and non-abundant metal sites, and ZIF-8 with relatively small pores and inaccessible metal sites. It was found that two main factors influence noble gas adsorption by MOFs: pore's morphology and polarizability of adsorption sites. It was confirmed that open metal sites (which are the most polarizable part of the MOF structure) are the primary and strongest adsorption sites for noble gases, if there is no strong geometric confinement of intercalated atoms. The polarizability of C=O and C-O bonds is usually lower than for metal sites, and these bonds act as secondary adsorption sites. The less polarizable C=C bond is a major adsorption site for noble gases in ZIF-8 due to the absence of accessible metal sites and carbon-oxygen bonds in the crystal structure. The high isosteric heat of adsorption for noble gases in ZIF-8 is provided by the geometrical confinement of noble gases in small pores. A unique example of the influence of metal exchange on adsorption properties of MOFs was found for Cu-MFU-4*l*, possessing an extremely large adsorption capacity for Kr and Xe atoms (8 positions of Kr and 10 positions of Xe), which was not reported so far. This phenomenon is of technological importance and requires further investigations, which are outside the scope of the present PhD thesis.

6. Zusammenfassung

Auf Grund des reduzierten Informationsgehalts von Pulverbeugungsdaten im Vergleich mit der Einkristallbeugung, ist es von größter Wichtigkeit, die Genauigkeit der Pulverbeugung zu erhöhen. Im Zuge dieser Doktorarbeit wurden deshalb verschiedene Möglichkeiten untersucht, wie die Genauigkeit in der Pulverbeugung erhöht werden kann: Untersuchung der Möglichkeiten und Grenzen der Methode der Maximalen Entropie (MEM) mit welcher die Elektronendichte präzise aus hochauflösenden Labor- und Synchrotron-Röntgenpulverbeugungsdaten bestimmt werden kann; Anwendung der parametrisierten Verfeinerung um verschiedene Modelle der Kopplung zwischen Strain und Ordnungsparameter während eines strukturellen Phasenübergangs zu analysieren und Untersuchungen von Edelgasabsorption in MOFs mittels fortgeschrittener Labor- und Synchrotron-Pulverbeugung.

Eine Serie von 24 Apatiten mit interkalieren Atomen wurde mittels MEM untersucht. Es zeigte sich, dass konventionelle Fourierabbildungen basierend auf F_{obs}–Constraints (beobachtete Strukturfaktoren werden aus dem besten unvollständigen Modell berechnet) eine Menge unerwünschte Peaks mit hoher Elektronendichte beinhalten, welche es unmöglich machen, die eingelagerten Metallatome eindeutig zu lokalisieren. MEM-Abbildungen basierend auf F_{obs}–, F_{obs}+G– und F_{LeBail}+G–Constraints erlaubten dahingehend eine eindeutige Lokalisierung von Kupferatomen mit Besetzungsfaktoren bis zu 0.05 mittels Laborröntgenpulverbeugung, was ungefähr 1,4 Elektronen pro Position entspricht. Um die Zuverlässigkeit der erhaltenen Ergebnisse aus den hochauflösenden Laborröntgenpulverbeugungsdaten zu bestätigen, wurden zusätzlich hochauflösende Synchrotronröntgenpulverbeugungsdaten verwendet. Grundsätzlich bestätigten die Ergebnisse, dass MEM erfolgreich für die Bestimmung von akkuraten Elektronendichteverteilungen von hochauflösenden Laborröntgenpulverbeugungsdaten eingesetzt werden kann. Der Unterschied zwischen MEM-Abbildungen von Labor- und Synchrotronquellen ist primär durch verschiedene instrumentenabhängige Peakprofile und unterschiedlicher Auflösung $\sin\theta/\lambda$ verursacht.

Als allgemeine Tendenz wurde bestätigt, dass MEM-Abbildungen basierend auf F_{obs}–Constraints am meisten und dass MEM-Abbildungen basierend auf F_{LeBail}+G–Constraints am wenigsten vom zugrunde liegenden Modell beeinflusst werden. Für MEM-Abbildungen, berechnet aus den sogenannten Vorkristalldichten für bekannte Atome, wird der Wert der

Elektronendichte von lokalisierten Metallatomen im gleichen Maße angehoben wie für Abbildungen basierend auf F_{obs}–, F_{obs}+G–, and F_{LeBail}+G–Constraints.

Ein großer Vorteil von MEM ist die Möglichkeit, G-Constraints für überlappende Reflexe zu benutzen, was eine Beeinflussung für beobachtete Strukturfaktoren (F_{obs}) aus der Rietveld-Verfeinerung vermeidet. Die Amplitude der Strukturfaktoren kann aus einer Le Bail-Anpassung (F_{LeBail}) erhalten werden, ohne die Notwendigkeit die Kristallstruktur zu kennen. Ebenso können diese als experimentelle Daten für MEM-Berechnungen für zentrosymmetrische Strukturen in Kombination mit Phasen einer Rietveldverfeinerung und G-Constraints für überlappende Reflexe verwendet werden. Die Anwendung von G-Constraints auf eine Summe von Intensitäten einer Gruppe überlappender Reflektionen verringert die Modellbeeinflussung durch die Abwesenheit der modellbeeinflussenden Anteile der überlappenden Reflexe.

Ein weiterer Vorteil von MEM ist die Möglichkeit vorhandene Information über die Kristallstruktur zu nutzen. Die Vorkristallelektronendichte reduziert deutlich Artefakte und MEM-Rekonstruktionen mit dieser Vorelektronendichte erlauben die Visualisierung von sehr feinen Details der Elektronendichte. Als ein Beispiel wurden die experimentelle Elektronendichteverteilung und die integrierten ionischen Ladungen von $BaZnF_4$ und $BaMgF_4$ mittels Anwendung von MEM auf hochauflösende Synchrotronpulverbeugungsdaten bei 10 K bestimmt. Zum ersten Mal wurde damit erfolgreich die MEM auf die Bestimmung von akkuraten Elektronendichteverteilungen von Schweratomverbindungen angewendet. Die beste Elektronendichteverteilung wurde erhalten, indem G-Constraints für stark überlappende Reflexe (F_2+G-constraints) und vorab bestimmte Constraints (F_2+F_{PD}-constraints) verwendet wurden. Die Verwendung von Vorkristallelektronendichten in Form von IASM war in beiden Fällen notwendig. Die experimentellen Atomladungen waren in guter Übereinstimmung mit den Ladungen, die mittels DFT berechnet wurden.

Parametrische Verfeinerung wurden als mächtiges Werkzeug etabliert, um verschiedene Modelle der Kopplung zwischen Strain und Ordnungsparameter während eines strukturellen Phasenübergangs zu testen. In der vorliegenden Doktorarbeit, wurden die ferroelastischen Phasenübergange $P\bar{1}$ <-> $P2_1/m$ von $LuF[SeO_3]$ und $Fm\bar{3}m$ –> $I4/m$ von Sr_2CoOsO_6 bei hohen Temperaturen im Detail analysiert. Die Verwendung von Verzerrungs-Methoden erlaubte es, zwischen primären und sekundären Verzerrungsmechanismen zu separieren und zu quantifizieren, welche für die Veränderung der Kristallsymmetrie verantwortlich sind. Diese

Verzerrungs-Methoden sind an die Gruppentheorie gebunden und ihre Änderungen mit Temperatur/Druck folgen der Landau-Theorie für strukturelle Phasenübergänge.

Starke Gitterdeformationen, welche durch vorangegangenes Kühlen von $LuF[SeO_3]$ bezeugt wurden, zeigen eine explizite Temperaturabhängigkeit und ihre Variation mit dem Aufheizen konnte durch biquadratische Kopplung zwischen symmetrieadaptiertem Strain und einem Ordnungsparameter mit expliziter Temperaturabhängigkeit des Strain beschrieben werden, wobei die zugrundeliegende Theorie im Zuge dieser Arbeit entwickelt wurde. Es wurde bewiesen, dass unterschiedlich Kopplungsmechanismen für die große Hysterese der Gitterparameter (und der symmetrieadaptierten Verformungen) während des Phasenübergangs verantwortlich sind.

Der Hochtemperaturphasenübergang $Fm\bar{3}m$–>$I4/m$ in Sr_2CoOsO_6 wurde mittels Verzerrungsmoden und parametrischer Verfeinerung, basierend auf der klassischen Verzerrungsmodenbeschreibung, mittels starrer Körper-Verfeinerung und mittels Rotationsmodenverfeinerung (Verzerrungsmoden starrer Körper) beschrieben. Der Verzerrungsmodenansatz erlaubt es zwischen drei Verzerrungsmoden, welche verantwortlich für den Wechsel in der Kristallsymmetrie von Sr_2CoOsO_6 während des Phasenübergangs sind, zu separieren. Während die primäre Verzerrungsmode die Rotation des Oktaeders beschreibt und als Ordnungsparameter fungiert, beschreiben zwei sekundäre Verzerrungsmoden die Deformation des Oktaeders.

Eine systematische strukturelle Untersuchung von Kr und Xe Adsorptionspositionen in verschiedenen MOFs, durchgeführt als Teil der vorliegenden Doktorarbeit, erlaubt die Analyse von Beziehungen zwischen der Kristallstruktur eines MOFs und seiner Fähigkeit Edelgase zu adsorbieren, zu speichern und zu separieren. Für diesen Zweck wurden ein flexibles Gasladungsgerät entwickelt. Verschiedene MOFs wurde untersucht: CPO-27-Ni und CPO-27-Mg mit 1D-Kanaltopologie und vielen zugängliche Metallpositionen, Zn-MFU-4*l* und Cu-MFU-4*l* mit Porenstrukturen und zugängliche Metallpositionen und ZIF-8 mit relativ kleinen Poren und unzugänglichen Metallpositionen. Es wurde herausgefunden, dass zwei Hauptfaktoren die Edelgasadsoprtion von MOFs beeinflussen: die Morphologie der Poren und die Polarisierbarkeit von Adsorptionspositionen. Es konnte bestätigt werden, dass offene Metallpositionen (welche die am meisten polarisierbaren Teile der MOF-Struktur sind) die primären und am stärksten absorbierenden Positionen für Edelgase sind, falls es keinen starken

geometrischen Einfluss von eingeschobenen Atomen gibt. Die Polarisierbarkeit von C=O und C-O Bindungen ist für gewöhnlich niedriger als die von Metallpositionen und diese Bindungen agieren als sekundäre Absorptionsposition. Die weniger polarisierbare C=C Bindung ist eine Hauptadsorptionsposition für Edelgase in ZIF-8, auf Grund der Abwesenheit von erreichbaren Metallpositionen und Kohlenstoff-Sauerstoff-Bindungen in der Kristallstruktur. Die hohe isosterische Wärme der Adsorption für Edelgase in ZIF-8 hat ihren Ursprung im geometrischen Einschluss der Edelgase in kleinen Poren. Ein einzigartiges Beispiel des Einflusses eines Metallaustausches auf die Adsorptionseigenschaften von MOFs wurde für Cu-MFU-4*l* gefunden, welches eine extrem große Adsorptionskapazität für Kr- und Xe-Atome (8 Positionen von Kr und 10 Positionen von Xe) besitzt, was bislang unbekannt war. Dieses Phänomen ist von technologische Wichtigkeit und benötigt weitere Untersuchungen, die über den Umfang der hier vorgestellten Arbeit hinausgehen.

Abbreviations

DFT	density functional theory
IASM	Independent atomic spherical model
irrep	Irreducible representation
MAC	multi-analyzing crystal
MEM	maximum entropy method
MOF	metal-organic framework
MOFs	metal-organic frameworks
RT	room-temperature
WPPF	whole powder pattern fitting

List of Tables.

List of Figures.

Figure 2.15. Two-dimensional electron-density maps at *y=0* of the apatite $Sr_5(PO_4)_3Cu_{0.25}OH_{0.75-\delta}$ (sample SrA(0.25Cu)). Contour levels: from 1 to 50 e/Å^3, step 1 e/Å^3. High-resolution laboratory X-ray powder diffraction data.

Figure 2.16. Two-dimensional electron-density maps at *y=0* of apatite $Sr_5(PO_4)_3Ni_{0.2}OH_{0.8-\delta}$ (sample SrA(0.2Ni)). Contour levels: from 1 to 50 e/Å^3, step 1 e/Å^3. High-resolution laboratory X-ray powder diffraction data.

Figure 2.17. Two-dimensional electron-density maps at *y=0* of apatite $Sr_5(PO_4)_3Zn_{0.15}OH_{0.85-\delta}$ (sample SrA(0.15Zn)). Contour levels: from 1 to 50 e/Å^3, step 1 e/Å^3. High-resolution laboratory X-ray powder diffraction data.

Figure 2.18a. Two-dimensional electron-density maps at *y=0* of apatite $Sr_5(PO_4)_3Cu_{0.1}OH_{0.9-\delta}$ (sample SrA(0.1Cu-1), $\delta = 0.038$). Contour levels: from 1 to 50 e/Å^3, step 1 e/Å^3. High-resolution synchrotron X-ray powder diffraction data with $\sin\theta/\lambda = 0.55$ Å^{-1}.

Figure 2.18b. Two-dimensional electron-density maps at *y=0* of apatite $Sr_5(PO_4)_3Cu_{0.1}OH_{0.9-\delta}$ (sample SrA(0.1Cu-1), δ = 0.038). Contour levels: from 1 to 50 e/Å^3, step 1 e/Å^3. High-resolution synchrotron X-ray powder diffraction data with sinθ/λ = 0.65 Å^{-1}.

Figure 2.18c. Two-dimensional electron-density maps at *y=0* of apatite $Sr_5(PO_4)_3Cu_{0.1}OH_{0.9-\delta}$ (sample SrA(0.1Cu-1), δ = 0.038). Contour levels: from 1 to 50 e/Å^3, step 1 e/Å^3. High-resolution synchrotron X-ray powder diffraction data with sinθ/λ = 0.93 Å^{-1}.

Figure 2.19a. Two-dimensional electron-density maps at *y=0* of apatite $Sr_5(PO_4)_3Cu_{0.1}OH_{0.9-\delta}$ (sample SrA(0.1Cu-3), δ = 0.26). Contour levels: from 1 to 50 e/Å^3, step 1 e/Å^3. High-resolution synchrotron X-ray powder diffraction data with sinθ/λ = 0.55 Å^{-1}.

Figure 2.19b. Two-dimensional electron-density maps at *y=0* of apatite $Sr_5(PO_4)_3Cu_{0.1}OH_{0.9-\delta}$ (sample SrA(0.1Cu-3), $\delta = 0.26$). Contour levels: from 1 to 50 e/Å^3, step 1 e/Å^3. High-resolution synchrotron X-ray powder diffraction data with $\sin\theta/\lambda = 0.65$ Å^{-1}.

a) based on F_{obs} (with procrystal density for known atoms)

b) based on F_{obs} (with flat prior)

c) based on F_{obs}+G (with procrystal density for known atoms)

d) based on F_{LeBail}+G (with procrystal density for known atoms)……49

Figure 2.19c. Two-dimensional electron-density maps at *y=0* of apatite $Sr_5(PO_4)_3Cu_{0.1}OH_{0.9-\delta}$ (sample SrA(0.1Cu-3), $\delta = 0.26$). Contour levels: from 1 to 50 e/Å^3, step 1 e/Å^3. High-resolution synchrotron X-ray powder diffraction data with $\sin\theta/\lambda = 0.93$ Å^{-1}.

a) based on F_{obs} (with procrystal density for known atoms)

b) based on F_{obs} (with flat prior)

c) based on F_{obs}+G (with procrystal density for known atoms)

d) based on F_{LeBail}+G (with procrystal density for known atoms)……50

Figure 2.20a. Two-dimensional electron-density maps at *y=0* of apatite $Sr_5(PO_4)_3Cu_{0.1}OH_{0.9-\delta}$ (sample SrA(0.1Cu-4), $\delta > 0.26$). Contour levels: from 1 to 50 e/Å^3, step 1 e/Å^3. High-resolution synchrotron X-ray powder diffraction data with $\sin\theta/\lambda = 0.55$ Å^{-1}.

a) based on F_{obs} (with procrystal density for known atoms)

b) based on F_{obs} (with flat prior)

c) based on F_{obs}+G (with procrystal density for known atoms)

d) based on F_{LeBail}+G (with procrystal density for known atoms)……51

Figure 2.20b. Two-dimensional electron-density maps at *y=0* of apatite $Sr_5(PO_4)_3Cu_{0.1}OH_{0.9-\delta}$ (sample SrA(0.1Cu-4), $\delta > 0.26$). Contour levels: from 1 to 50 (from 3 to 50 – case d) e/Å^3, step 1 e/Å^3. High-resolution synchrotron X-ray powder diffraction data with $\sin\theta/\lambda = 0.65$ Å^{-1}.

a) based on F_{obs} (with procrystal density for known atoms)

Figure 2.20c. Two-dimensional electron-density maps at *y=0* of apatite $Sr_5(PO_4)_3Cu_{0.1}OH_{0.9-\delta}$ (sample SrA(0.1Cu-4), $\delta > 0.26$). Contour levels: from 1 to 50 (from 3 to 50 – case d) e/Å^3, step 1 e/Å^3. High-resolution synchrotron X-ray powder diffraction data with $\sin\theta/\lambda = 0.93$ Å^{-1}.

Figure 2.24. Two-dimensional electron-density maps based on F_{obs}+G–constraints (with procrystal density for complete structure) at *y=0* of Sr–apatites with different content of intercalated copper atoms. Contour levels: from 1 to 50 e/Å^3, step 1 e/Å^3. High-resolution laboratory X-ray powder diffraction data.

a) $Sr_5(PO_4)_3Cu_{0.3}OH_{0.7-\delta}$ (sample SrA(0.3Cu-2)),

b) $Sr_5(PO_4)_3Cu_{0.25}OH_{0.75-\delta}$ (sample SrA(0.25Cu)),

c) $Sr_5(PO_4)_3Cu_{0.125}OH_{0.875-\delta}$ (sample SrA(0.125Cu)),

d) $Sr_5(PO_4)_3Cu_{0.1}OH_{0.9-\delta}$ (sample SrA(0.1Cu-2)),

e) $Sr_5(PO_4)_3Cu_{0.05}OH_{0.95-\delta}$ (sample SrA(0.05Cu))

Figure 2.25. Two-dimensional electron-density maps based on F_{obs}+G–constraints (with procrystal density for complete structure) at $y=0$ of Ca–apatites:

a) $Ca_5(PO_4)_3Cu_{0.3}OH_{0.7-\delta}$ (sample CaA(0.3Cu))

b) $Ca_5(PO_4)_3Cu_{0.1}OH_{0.9-\delta}$ (sample CaA(0.1Cu)).

Contour levels: from 1 to 50 e/Å^3, step 1 e/Å^3. High-resolution laboratory X-ray powder diffraction data

Figure 2.26. Two-dimensional electron-density maps based on F_{obs}+G–constraints (with procrystal density for complete structure) at $y=0$ of apatites:

a) $Ca_5(PO_4)_3Cu_{0.1}O_{0.5}H_{0.4-\delta}F_{0.5}$ (sample CaA(0.1Cu_0.5F)),

b) $Ca_5(PO_4)_3Cu_{0.05}O_{0.5}H_{0.45-\delta}F_{0.5}$ (sample CaA(0.05Cu_0.5F)),

c) $Ca_5(PO_4)_3Cu_{0.02}O_{0.5}H_{0.48-\delta}F_{0.5}$ (sample CaA(0.02Cu_0.5F)),

d) $Ca_5(PO_4)_3Cu_{0.01}O_{0.5}H_{0.49-\delta}F_{0.5}$ (sample CaA(0.01Cu_0.5F)),

e) $Sr_5(PO_4)_3Cu_{0.05}O_{0.5}H_{0.45-\delta}F_{0.5}$ (sample SrA(0.05Cu_0.5F)).

Contour levels: from 1 to 50 e/Å^3, step 1 e/Å^3. High-resolution laboratory X-ray powder diffraction data. Dotted line – contour lever at 0.5 e/Å^3

Figure 2.27a. Two-dimensional electron-density maps based on F_{obs}+G–constraints (with procrystal density for complete structure) at $y=0$ of apatites $Sr_5(PO_4)_3Cu_{0.1}OH_{0.9-\delta}$ with different content δ of peroxide and copper ions in higher oxidation state. Contour levels: from 1 to 50 e/Å^3, step 1 e/Å^3. High-resolution laboratory X-ray powder diffraction data. Arrows show the distortion of the electron density near the copper atom.

a) $Sr_5(PO_4)_3Cu_{0.1}OH_{0.9-\delta}$ (sample SrA(0.1Cu-1), $\delta = 0.038$)

Figure 2.27b. Two-dimensional electron-density maps based on F_{obs}+G–constraints (with procrystal density for complete structure) at $y=0$ of apatites $Sr_5(PO_4)_3Cu_{0.1}OH_{0.9-\delta}$ with different content δ of peroxide and copper ions in higher oxidation state. Contour levels: from 1 to 50 e/Å^3, step 1 e/Å^3. High-resolution synchrotron X-ray powder diffraction data with $\sin\theta/\lambda = 0.93$ Å^{-1}. Arrows show the distortion of the electron density near the copper atom.

Figure 2.28. Two-dimensional electron-density maps based on F_{obs}+G–constraints (with procrystal density for complete structure) at $y=0$ of apatites $Sr_5(PO_4)_3Cu_{0.3}OH_{0.7-\delta}$ with different content δ of peroxide and copper ions in higher oxidation state. Contour levels: from 1 to 50 e/Å^3, step 1 e/Å^3. High-resolution laboratory X-ray powder diffraction data. Arrows show the distortion of the electron density near the copper atom.

Figure 2.29a. Two-dimensional electron-density maps based on F_{obs}+G–constraints (with procrystal density for complete structure) at $y=0$ of apatites $Sr_5(PO_4)_3Cu_{0.1}OH_{0.9-\delta}$ with different content of peroxide and copper ions in higher oxidation state. Contour levels: from 1 to 50 e/Å^3, step 1 e/Å^3. High-resolution synchrotron X-ray powder diffraction data with $\sin\theta/\lambda = 0.55$ Å^{-1}. Arrows show the distortion of the electron density near the copper atom.

Appendix 1.

Table A1. Crystallographic and refinement data (Rietveld refinement and Le Bail fit of incomplete crystal structures without intercalated metal atoms) for hydroxyapatites (space group $P6_3/m$ (176)) with different intercalated metal atoms from laboratory X-ray powder diffraction data (R_{Br}, *Rp, Rwp* and *GooF* as defined in Topas).

Sample	SrA(0.25Cu)	CaA(0.1Cu)	SrA(0.2Ni)	SrA(0.15Zn)
Molecular formula	$Sr_5(PO_4)_3Cu_{0.25}OH_{0.75-\delta}$	$Ca_5(PO_4)_3Cu_{0.1}OH_{0.9-\delta}$	$Sr_5(PO_4)_3Ni_{0.2}OH_{0.8-\delta}$	$Sr_5(PO_4)_3Zn_{0.15}OH_{0.85-\delta}$
Z	2	2	2	2
a / Å	9.7780(3)	9.4220(2)	9.7743(2)	9.7531(2)
c / Å	7.2942(2)	6.8871(2)	7.2977(2)	7.3088(2)
R_{Br}, % (Rietveld)	11.16	9.64	4.88	4.91
Rp, % (Rietveld)	11.11	10.60	5.74	5.58
Rwp, % (Rietveld)	17.71	15.84	7.63	7.62
GooF (Rietveld)	6.95	3.48	1.19	1.81
Rp, % (Le Bail)	4.42	5.89	3.79	3.53
Rwp, % (Le Bail)	6.94	7.95	5.33	4.74
GooF (Le Bail)	2.72	1.75	0.83	1.13
Temperature (K)	293	293	293	293
Wavelength (Å)	1.540596	1.540596	1.540596	1.540596
2θ – range (°)	10 – 120	10 – 120	15 – 100	15 – 100
Step width (° 2θ)	0.0079	0.0079	0.01	0.01

Sample	CaA(0.1Cu_0.5F)	CaA(0.05Cu_0.5F)	CaA(0.02Cu_0.5F)	CaA(0.01Cu_0.5F)
Molecular formula	$Ca_5(PO_4)_3Cu_{0.1}O_{0.5}H_{0.4-\delta}F_{0.5}$	$Ca_5(PO_4)_3Cu_{0.05}O_{0.5}H_{0.45-\delta}F_{0.5}$	$Ca_5(PO_4)_3Cu_{0.02}O_{0.5}H_{0.48-\delta}F_{0.5}$	$Ca_5(PO_4)_3Cu_{0.01}O_{0.5}H_{0.49-\delta}F_{0.5}$
Z	2	2	2	2
a / Å	9.3977(2)	9.3954(2)	9.3941(2)	9.3932(2)
c / Å	6.8930(2)	6.8890(2)	6.8855(2)	6.8846(2)
R_{Br}, % (Rietveld)	8.97	7.17	5.42	4.48
Rp, % (Rietveld)	9.76	8.46	7.62	6.10
Rwp, % (Rietveld)	15.56	12.59	11.05	8.62
GooF (Rietveld)	3.32	2.59	2.41	2.09
Rp, % (Le Bail)	4.83	5.18	4.96	4.40
Rwp, % (Le Bail)	6.54	7.05	7.11	6.10
GooF (Le Bail)	1.40	1.45	1.55	1.48
Temperature (K)	293	293	293	293
Wavelength (Å)	1.540596	1.540596	1.540596	1.540596
2θ – range (°)	10 – 120	10 – 120	10 – 120	10 – 120
Step width (° 2θ)	0.0079	0.0079	0.0079	0.0079

Sample	SrA(0.1Cu-1)	SrA(0.1Cu-3)	SrA(0.1Cu-4)
Molecular formula	$Sr_5(PO_4)_3Cu_{0.1}OH_{0.9-\delta}$	$Sr_5(PO_4)_3Cu_{0.1}OH_{0.9-\delta}$	$Sr_5(PO_4)_3Cu_{0.1}OH_{0.9-\delta}$
Z	2	2	2
a / Å	9.7689(3)	9.7599(3)	9.7559(3)
c / Å	7.2849(3)	7.2788(3)	7.2771(3)
R_{Br}, % (Rietveld)	5.19	5.03	6.34
Rp, % (Rietveld)	7.03	6.26	7.61
Rwp, % (Rietveld)	11.01	9.90	12.59
GooF (Rietveld)	4.92	4.21	5.85
Rp, % (Le Bail)	4.58	3.09	3.10
Rwp, % (Le Bail)	7.54	4.93	4.43
GooF (Le Bail)	3.37	2.10	2.06
Temperature (K)	293	293	293
Wavelength (Å)	1.540596	1.540596	1.540596
2θ – range (°)	10 – 120	10 – 120	10 – 120
Step width (° 2θ)	0.0079	0.0079	0.0079

Table A2. Crystallographic and refinement data (Rietveld refinement and Le Bail fit of incomplete crystal structures without intercalated metal atoms) for hydroxyapatites SrA(0.1Cu-1), SrA(0.1Cu-2), SrA(0.1Cu-3), SrA(0.1Cu-4) from synchrotron powder diffraction data (R_{Br}, *Rp, Rwp* and *GooF* as defined in Topas).

Sample	SrA(0.1Cu-1)	SrA(0.1Cu-3)	SrA(0.1Cu-4)
Molecular formula	$Sr_5(PO_4)_3Cu_{0.1}OH_{0.9-\delta}$	$Sr_5(PO_4)_3Cu_{0.1}OH_{0.9-\delta}$	$Sr_5(PO_4)_3Cu_{0.1}OH_{0.9-\delta}$
Z	2	2	2
a / Å	9.7696(3)	9.7626(3)	9.7584(3)
c / Å	7.2855(3)	7.2821(3)	7.2782(3)
R_{Br}, % (Rietveld)	5.76	5.73	4.78
Rp, % (Rietveld)	8.07	6.57	6.20
Rwp, % (Rietveld)	11.12	9.61	9.07
GooF (Rietveld)	3.24	3.24	2.69
Rp, % (Le Bail)	6.18	4.04	3.78
Rwp, % (Le Bail)	8.01	5.39	5.01
GooF (Le Bail)	2.33	1.81	1.49
Temperature (K)	293	293	293
Wavelength (Å)	0.8264	0.8264	0.8264
2θ – range (°)	2 – 100	2 – 100	2 – 100
Step width (° 2θ)	0.001	0.001	0.001

Table A3. Crystallographic and refinement data (Rietveld refinement of complete crystal structures) for hydroxyapatites (space group $P6_3/m$ (176)) with different intercalated metal atoms from laboratory X-ray powder diffraction data (R_{Br}, *Rp, Rwp* and *GooF* as defined in Topas).

Sample	SrA(0.25Cu)	SrA(0.125Cu)	SrA(0.05Cu)	SrA(0.05Cu_0.5F)
Molecular formula	$Sr_5(PO_4)_3Cu_{0.25}OH_{0.75-\delta}$	$Sr_5(PO_4)_3Cu_{0.125}OH_{0.875-\delta}$	$Sr_5(PO_4)_3Cu_{0.05}OH_{0.95-\delta}$	$Sr_5(PO_4)_3Cu_{0.05}O_{0.5}H_{0.45-\delta}F_{0.5}$
Z	2	2	2	2
a / Å	9.7780(3)	9.7635(2)	9.7602(2)	9.7382(2)
c / Å	7.2942(2)	7.2810(2)	7.2763(2)	7.2844(2)
R_{Br}, %	3.36	3.26	3.93	4.13
Rp, %	5.74	5.22	5.56	6.50
Rwp, %	8.89	8.34	8.18	9.72
GooF	3.50	3.31	2.70	3.11
Temperature (K)	293	293	293	293
Wavelength (Å)	1.540596	1.540596	1.540596	1.540596
2θ – range (°)	10 – 120	10 – 120	15 – 100	15 – 100
Step width (° 2θ)	0.0079	0.0079	0.0079	0.0079

Sample	CaA(0.3Cu)	CaA(0.1Cu)	SrA(0.2Ni)	SrA(0.15Zn)
Molecular formula	$Ca_5(PO_4)_3Cu_{0.3}OH_{0.7-\delta}$	$Ca_5(PO_4)_3Cu_{0.1}OH_{0.9-\delta}$	$Sr_5(PO_4)_3Ni_{0.2}OH_{0.8-\delta}$	$Sr_5(PO_4)_3Zn_{0.15}OH_{0.85-\delta}$
Z	2	2	2	2
a / Å	9.4319 (3)	9.4220(2)	9.7743(2)	9.7531(2)
c / Å	6.9081 (2)	6.8871(2)	7.2977(2)	7.3088(2)
R_{Br}, %	3.34	4.55	2.35	4.67
Rp, %	6.94	7.80	4.53	5.29
Rwp, %	10.01	10.78	6.09	7.05
GooF	2.18	2.37	0.95	1.68
Temperature (K)	293	293	293	293
Wavelength (Å)	1.540596	1.540596	1.540596	1.540596
2θ – range (°)	10 – 120	10 – 120	15 – 100	15 – 100
Step width (° 2θ)	0.0079	0.0079	0.01	0.01

Sample	CaA(0.1Cu_0.5F)	CaA(0.05Cu_0.5F)	CaA(0.02Cu_0.5F)	CaA(0.01Cu_0.5F)
Molecular formula	$Ca_5(PO_4)_3Cu_{0.1}O_{0.5}H_{0.4-\delta}F_{0.5}$	$Ca_5(PO_4)_3Cu_{0.05}O_{0.5}H_{0.45-\delta}F_{0.5}$	$Ca_5(PO_4)_3Cu_{0.02}O_{0.5}H_{0.48-\delta}F_{0.5}$	$Ca_5(PO_4)_3Cu_{0.01}O_{0.5}H_{0.49-\delta}F_{0.5}$
Z	2	2	2	2
a / Å	9.3977(2)	9.3954(2)	9.3941(2)	9.3932(2)
c / Å	6.8930(2)	6.8890(2)	6.8855(2)	6.8846(2)
R_{Br}, %	6.58	4.93	4.86	4.30
Rp, %	6.84	7.17	7.23	5.99
Rwp, %	9.92	10.05	10.41	8.41
GooF	2.12	2.07	2.27	2.04
Temperature (K)	293	293	293	293
Wavelength (Å)	1.540596	1.540596	1.540596	1.540596
2θ – range (°)	10 – 120	10 – 120	10 – 120	10 – 120
Step width (° 2θ)	0.0079	0.0079	0.0079	0.0079

Sample	SrA(0.1Cu-1)	SrA(0.1Cu-2)	SrA(0.1Cu-3)	SrA(0.1Cu-4)
Molecular formula	$Sr_5(PO_4)_3Cu_{0.1}OH_{0.9-\delta}$	$Sr_5(PO_4)_3Cu_{0.1}OH_{0.9-\delta}$	$Sr_5(PO_4)_3Cu_{0.1}OH_{0.9-\delta}$	$Sr_5(PO_4)_3Cu_{0.1}OH_{0.9-\delta}$
Z	2	2	2	2
a / Å	9.7689(3)	9.7647(3)	9.7599(3)	9.7559(3)
c / Å	7.2849(3)	7.2827(3)	7.2788(3)	7.2771(3)
R_{Br}, %	4.20	4.41	3.96	4.48
Rp, %	6.42	6.42	5.30	5.77
Rwp, %	9.35	9.67	8.04	9.20
GooF	4.17	3.78	3.42	4.28
Temperature (K)	293	293	293	293
Wavelength (Å)	1.540596	1.540596	1.540596	1.540596
2θ – range (°)	10 – 120	10 – 120	10 – 120	10 – 120
Step width (° 2θ)	0.0079	0.0079	0.0079	0.0079

Sample	SrA(0.3Cu-1)	SrA(0.3Cu-2)	SrA(0.3Cu-3)
Molecular formula	$Sr_5(PO_4)_3Cu_{0.3}OH_{0.7-\delta}$	$Sr_5(PO_4)_3Cu_{0.3}OH_{0.7-\delta}$	$Sr_5(PO_4)_3Cu_{0.3}OH_{0.7-\delta}$
Z	2	2	2
a / Å	9.7768(3)	9.7760(3)	9.7662(3)
c / Å	7.2916(3)	7.2926(3)	7.2882(3)
R_{Br}, %	6.71	6.05	5.61
Rp, %	9.99	8.60	7.52
Rwp, %	15.11	12.24	10.47
GooF	3.91	3.40	2.50
Temperature (K)	293	293	293
Wavelength (Å)	1.540596	1.540596	1.540596
2θ – range (°)	10 – 120	10 – 120	10 – 120
Step width (° 2θ)	0.0079	0.0079	0.0079

Table A4. Crystallographic and refinement data (Rietveld refinement of complete crystal structures) for hydroxyapatites SrA(0.1Cu-1), SrA(0.1Cu-2), SrA(0.1Cu-3), SrA(0.1Cu-4) from synchrotron powder diffraction data (R_{Br}, *Rp, Rwp* and *GooF* as defined in Topas).

Sample	SrA(0.1Cu-1)	SrA(0.1Cu-2)	SrA(0.1Cu-3)	SrA(0.1Cu-4)
Molecular formula	$Sr_5(PO_4)_3Cu_{0.1}OH_{0.9-\delta}$	$Sr_5(PO_4)_3Cu_{0.1}OH_{0.9-\delta}$	$Sr_5(PO_4)_3Cu_{0.1}OH_{0.9-\delta}$	$Sr_5(PO_4)_3Cu_{0.1}OH_{0.9-\delta}$
Z	2	2	2	2
a / Å	9.7696(3)	9.7665(3)	9.7626(3)	9.7584(3)
c / Å	7.2855(3)	7.2851(3)	7.2821(3)	7.2782(3)
R_{Br}, %	4.41	4.06	4.48	3.55
Rp, %	7.55	5.70	5.78	5.28
Rwp, %	9.80	7.50	7.63	7.07
GooF	2.85	2.23	2.57	2.10
Temperature (K)	293	293	293	293
Wavelength (Å)	0.8264	0.8264	0.8264	0.8264
2θ – range (°)	2 – 100	2 – 100	2 – 100	2 – 100
Step width (° 2θ)	0.001	0.001	0.001	0.001

Table A5. Details about maximum-entropy calculations for incomplete crystal structures (without intercalated metal atoms) of investigated apatites from laboratory X-ray powder diffraction data (R_F, R_{wF}, R_G and R_{wG} as defined in BayMEM).

Sample	SrA(0.25Cu)	CaA(0.1Cu)	SrA(0.2Ni)	SrA(0.15Zn)
The grid / pixels	96×96×72			
Resolution / Å^3	0.1×0.1×0.1			
F(0 0 0)	693.48	505.40	690.39	688.38
Lagrange multiplier, λ_{FG}	50	140	100	100
MEM calculations based on F_{obs} (procrystal density for known atoms)				
χ^2_{aim}	3.0	1.8	0.4	0.3
R_F / R_{wF}, %	2.05 / 2.18	1.73 / 1.80	1.19 / 1.10	0.76 / 0.76
MEM calculations based on F_{obs} (flat prior)				
χ^2_{aim}	6.0	2.7	0.7	0.4
R_F / R_{wF}, %	2.81 / 3.08	1.99 / 2.20	1.42 / 1.46	0.89 / 0.87
MEM calculations based on F_{obs} + G and F_{LeBail} + G				
χ^2_{aim} (F_{obs}+G)	1.4	0.4	0.1	0.2
R_F / R_{wF}, % (F_{obs}+G)	2.52 / 2.56	1.73 / 1.62	1.22 / 1.03	1.30 / 1.00
R_G / R_{wG}, % (F_{obs}+G)	1.10 / 1.31	0.53 / 0.66	0.59 / 0.50	0.66 / 0.70
χ^2_{aim} (F_{LeBail}+G)	1.0	0.4	0.1	0.1
R_F / R_{wF}, % (F_{LeBail}+G)	1.99 / 2.40	1.65 / 1.51	1.87 / 1.38	0.87 / 0.62
R_G / R_{wG}, % (F_{LeBail}+G)	0.93 / 0.99	0.57 / 0.74	0.09 / 0.10	0.75 / 0.85
No. of unique reflections	54	47	37	18
No. of overlapping reflections	222	198	190	192
No. of groups of the overlapping reflections	86	75	64	60

Sample	CaA(0.1Cu_0.5F)	CaA(0.05Cu_0.5F)	CaA(0.02Cu_0.5F)	CaA(0.01Cu_0.5F)
The grid / pixels	96×96×72			
Resolution / Å^3	0.1×0.1×0.1			
F(0 0 0)	505.40	502.69	501.07	500.54
Lagrange multiplier, λ_{FG}	50	50	50	50
MEM calculations based on F_{obs} (procrystal density for known atoms)				
χ^2_{aim}	0.5	0.6	0.1	0.1
R_F / R_{wF}, %	0.96 / 1.05	0.99 / 1.13	0.37 / 0.45	0.36 / 0.40
MEM calculations based on F_{obs} (flat prior)				
χ^2_{aim}	2.0	0.9	1.0	1.0
R_F / R_{wF}, %	1.83 / 2.11	1.17 / 1.39	1.17 / 1.43	1.05 / 1.20
MEM calculations based on F_{obs} + G and F_{LeBail} + G				
χ^2_{aim} (F_{obs}+G)	0.5	0.2	0.1	0.1
R_F / R_{wF}, % (F_{obs}+G)	1.60 / 1.72	0.96 / 1.01	0.73 / 0.78	0.70 / 0.71
R_G / R_{wG}, % (F_{obs}+G)	0.70 / 0.84	0.44 / 0.60	0.30 / 0.37	0.35 / 0.44
χ^2_{aim} (F_{LeBail}+G)	0.5	0.3	0.1	0.1
R_F / R_{wF}, % (F_{LeBail}+G)	1.55 / 1.57	1.38 / 1.29	0.79 / 0.79	0.83 / 0.76
R_G / R_{wG}, % (F_{LeBail}+G)	0.77 / 0.97	0.60 / 0.71	0.30 / 0.38	0.34 / 0.41
No. of unique reflections	58	56	54	55
No. of overlapping reflections	187	189	191	190
No. of groups of the overlapping reflections	82	79	79	79

Sample	SrA(0.1Cu-1)	SrA(0.1Cu-3)	SrA(0.1Cu-4)
The grid / pixels	96×96×72		
Resolution / Å^3	0.1×0.1×0.1		
F(0 0 0)	685.38	685.38	685.38
Lagrange multiplier, λ_{FG}	50	50	50
MEM calculations based on F_{obs} (procrystal density for known atoms)			
χ^2_{aim}	1.0	0.9	0.4
R_F / R_{wF}, %	1.14 / 1.22	1.09 / 1.17	0.64 / 0.73
MEM calculations based on F_{obs} (flat prior)			
χ^2_{aim}	1.5	1.3	1.6
R_F / R_{wF}, %	1.32 / 1.50	1.23 / 1.40	1.24 / 1.45
MEM calculations based on F_{obs} + G and F_{LeBail} + G			
χ^2_{aim} (F_{obs}+G)	0.2	0.2	0.2
R_F / R_{wF}, % (F_{obs}+G)	0.87 / 0.93	0.96 / 0.97	0.70 / 0.79
R_G / R_{wG}, % (F_{obs}+G)	0.40 / 0.44	0.39 / 0.44	0.44 / 0.50
χ^2_{aim} (F_{LeBail}+G)	0.3	0.3	6.0
R_F / R_{wF}, % (F_{LeBail}+G)	1.00 / 1.17	1.19 / 1.17	3.15 / 3.72
R_G / R_{wG}, % (F_{LeBail}+G)	0.49 / 0.55	0.51 / 0.55	2.83 / 3.17
No. of unique reflections	60	56	51
No. of overlapping reflections	216	220	225
No. of groups of the overlapping reflections	90	91	84

Table A6. Details about maximum-entropy calculations for incomplete crystal structures (without intercalated metal atoms) of investigated apatites from synchrotron powder diffraction data with resolution $\sin\theta/\lambda = 0.93$ Å^{-1} (R_F, R_{wF}, R_G and R_{wG} as defined in BayMEM).

Sample	SrA(0.1Cu-1)	SrA(0.1Cu-3)	SrA(0.1Cu-4)
The grid / pixels	96×96×72		
Resolution / Å^3	0.1×0.1×0.1		
F(0 0 0)	685.38	685.38	685.38
Lagrange multiplier, λ_{FG}	50	50	50
MEM calculations based on F_{obs} (procrystal density for known atoms)			
χ^2_{aim}	1.0	0.9	0.2
R_F / R_{wF}, %	1.34 / 0.16	1.33 / 1.55	0.63 / 0.69
MEM calculations based on F_{obs} (flat prior)			
χ^2_{aim}	3.5	2.8	2
R_F / R_{wF}, %	2.22 / 2.99	2.05 / 2.74	1.63 / 2.20
MEM calculations based on F_{obs} + G and F_{LeBail} + G			
χ^2_{aim} (F_{obs}+G)	0.2	0.2	0.1
R_F / R_{wF}, % (F_{obs}+G)	1.40 / 1.49	1.30 / 1.45	1.17 / 1.13
R_G / R_{wG}, % (F_{obs}+G)	0.63 / 0.73	0.66 / 0.75	0.44 / 0.51
χ^2_{aim} (F_{LeBail}+G)	1.3	0.7	1.5
R_F / R_{wF}, % (F_{LeBail}+G)	2.77 / 3.31	2.03 / 2.46	2.63 / 2.57
R_G / R_{wG}, % (F_{LeBail}+G)	1.67 / 1.99	1.20 / 1.48	2.35 / 2.49
No. of unique reflections	89	99	71
No. of overlapping reflections	1324	1314	1341
No. of groups of the overlapping reflections	351	375	306

Table A7. Details about maximum-entropy calculations for incomplete crystal structures (without intercalated metal atoms) of investigated apatites from synchrotron powder diffraction data with resolution $\sin\theta/\lambda = 0.65$ Å^{-1} (R_F, R_{wF}, R_G and R_{wG} as defined in BayMEM).

Sample	SrA(0.1Cu-1)	SrA(0.1Cu-3)	SrA(0.1Cu-4)
The grid / pixels	96×96×72		
Resolution / Å^3	0.1×0.1×0.1		
F(0 0 0)	685.38	685.38	685.38
Lagrange multiplier, λ_{FG}	50	50	50
MEM calculations based on F_{obs} (procrystal density for known atoms)			
χ^2_{aim}	0.6	0.1	0.2
R_F / R_{wF}, %	0.93 / 1.02	0.40 / 0.43	0.55 / 0.58
MEM calculations based on F_{obs} (flat prior)			
χ^2_{aim}	2.0	1.5	1.6
R_F / R_{wF}, %	1.57 / 1.87	1.39 / 1.67	1.37 / 1.64
MEM calculations based on F_{obs} + G and F_{LeBail} + G			
χ^2_{aim} (F_{obs}+G)	0.1	0.2	0.1
R_F / R_{wF}, % (F_{obs}+G)	0.77 / 0.69	1.05 / 0.99	0.81 / 0.74
R_G / R_{wG}, % (F_{obs}+G)	0.34 / 0.40	0.49 / 0.58	0.35 / 0.39
χ^2_{aim} (F_{LeBail}+G)	0.4	0.2	0.4
R_F / R_{wF}, % (F_{LeBail}+G)	1.41 / 1.40	0.89 / 1.00	0.75 / 0.75
R_G / R_{wG}, % (F_{LeBail}+G)	0.63 / 0.79	0.49 / 0.56	0.77 / 1.02
No. of unique reflections	79	79	62
No. of overlapping reflections	416	416	433
No. of groups of the overlapping reflections	160	159	142

Table A8. Details about maximum-entropy calculations for incomplete crystal structures (without intercalated metal atoms) of investigated apatites from synchrotron powder diffraction data with resolution $\sin\theta/\lambda = 0.55$ Å^{-1} (R_F, R_{wF}, R_G and R_{wG} as defined in BayMEM).

Sample	SrA(0.1Cu-1)	SrA(0.1Cu-3)	SrA(0.1Cu-4)
The grid / pixels	96×96×72		
Resolution / Å^3	0.1×0.1×0.1		
F(0 0 0)	685.38	685.38	685.38
Lagrange multiplier, λ_{FG}	50	50	50
MEM calculations based on F_{obs} (procrystal density for known atoms)			
χ^2_{aim}	0.1	0.1	0.1
R_F / R_{wF}, %	0.39 / 0.40	0.40 / 0.42	0.38 / 0.40
MEM calculations based on F_{obs} (flat prior)			
χ^2_{aim}	1.0	0.8	1.0
R_F / R_{wF}, %	1.10 / 1.28	0.99 / 1.17	1.06 / 1.25
MEM calculations based on F_{obs} + G and F_{LeBail} + G			
χ^2_{aim} (F_{obs}+G)	0.1	0.1	0.1
R_F / R_{wF}, % (F_{obs}+G)	0.73 / 0.63	0.72 / 0.63	0.72 / 0.63
R_G / R_{wG}, % (F_{obs}+G)	0.31 / 0.36	0.33 / 0.37	0.33 / 0.38
χ^2_{aim} (F_{LeBail}+G)	0.2	0.2	3.3
R_F / R_{wF}, % (F_{LeBail}+G)	0.86 / 0.94	0.76 / 0.85	1.62 / 2.39
R_G / R_{wG}, % (F_{LeBail}+G)	0.44 / 0.48	0.48 / 0.54	1.99 / 2.69
No. of unique reflections	66	65	54
No. of overlapping reflections	253	252	266
No. of groups of the overlapping reflections	107	108	102

Table A9. Details about maximum-entropy calculations (based on F_{obs}+G) for complete crystal structures of investigated apatites from laboratory X-ray powder diffraction data (R_F, R_{wF}, R_G and R_{wG} as defined in BayMEM).

Sample	SrA(0.25Cu)	SrA(0.125Cu)	SrA(0.05Cu)	SrA(0.05Cu_0.5F)
The grid / pixels	96×96×72			
Resolution / Å^3	0.1×0.1×0.1			
F(0 0 0)	693.48	685.28	682.68	690.68
Lagrange multiplier, λ_{FG}	50	40	40	40
χ^2_{aim}	0.4	0.4	0.4	0.2
R_F / R_{wF}, %	1.13/1.14	0.97/1.02	0.77/0.96	0.54/0.65
R_G / R_{wG}, %	0.69/0.81	0.73/0.87	0.79/0.88	0.54/0.62
No. of unique reflections	54	54	44	46
No. of overlapping reflections	222	220	238	230
No. of groups of the overlapping reflections	86	85	91	80

Sample	CaA(0.3Cu)	CaA(0.1Cu)	SrA(0.2Ni)	SrA(0.15Zn)
The grid / pixels	96×96×72			
Resolution / Å^3	0.1×0.1×0.1			
F(0 0 0)	516.19	505.40	690.39	688.38
Lagrange multiplier, λ_{FG}	130	140	100	100
χ^2_{aim}	0.3	0.3	0.2	0.2
R_F / R_{wF}, %	1.37/1.22	1.42/1.29	1.42/1.30	1.54/1.16
R_G / R_{wG}, %	0.65/0.74	0.54/0.68	0.93/0.77	0.61/0.68
No. of unique reflections	51	47	37	18
No. of overlapping reflections	195	198	190	192
No. of groups of the overlapping reflections	80	75	64	60

Sample	CaA(0.1Cu_0.5F)	CaA(0.05Cu_0.5F)	CaA(0.02Cu_0.5F)	CaA(0.01Cu_0.5F)
The grid / pixels	96×96×72			
Resolution / Å^3	0.1×0.1×0.1			
F(0 0 0)	505.40	502.69	501.07	500.54
Lagrange multiplier, λ_{FG}	50	50	50	50
χ^2_{aim}	0.2	0.2	0.2	0.2
R_F / R_{wF}, %	0.88/0.95	1.11/1.06	0.57/0.68	0.48/0.67
R_G / R_{wG}, %	0.51/0.60	0.48/0.52	0.45/0.52	0.41/0.45
No. of unique reflections	58	56	54	55
No. of overlapping reflections	187	189	191	190
No. of groups of the overlapping reflections	82	79	79	79

Sample	SrA(0.3Cu-1)	SrA(0.3Cu-2)	SrA(0.3Cu-3)
The grid / pixels	96×96×72		
Resolution / Å^3	0.1×0.1×0.1		
F(0 0 0)	696.18	696.18	696.18
Lagrange multiplier, λ_{FG}	50	50	50
χ^2_{aim}	0.4	0.4	0.4
R_F / R_{wF}, %	0.95/1.05	1.01/1.08	1.06/1.16
R_G / R_{wG}, %	0.82/0.99	0.78/0.92	0.88/0.90
No. of unique reflections	42	44	40
No. of overlapping reflections	234	232	236
No. of groups of the overlapping reflections	86	90	81

Sample	SrA(0.1Cu-1)	SrA(0.1Cu-2)	SrA(0.1Cu-3)	SrA(0.1Cu-4)
The grid / pixels	96×96×72			
Resolution / Å^3	0.1×0.1×0.1			
F(0 0 0)	685.38	685.38	685.38	685.38
Lagrange multiplier, λ_{FG}	50	50	50	50
χ^2_{aim}	0.4	0.4	0.4	0.4
R_F / R_{wF}, %	0.90/1.01	1.22/1.29	0.96/1.09	0.93/1.03
R_G / R_{wG}, %	0.66/0.79	0.62/0.70	0.67/0.77	0.69/0.76
No. of unique reflections	60	55	56	51
No. of overlapping reflections	216	221	220	225
No. of groups of the overlapping reflections	90	91	91	84

Table A10. Details about maximum-entropy calculations (based on $F_{obs}+G$) for complete crystal structures of investigated apatites from synchrotron powder diffraction data with resolution $\sin\theta/\lambda = 0.93$ Å^{-1} (R_F, R_{wF}, R_G and R_{wG} as defined in BayMEM).

Sample	SrA(0.1Cu-1)	SrA(0.1Cu-2)	SrA(0.1Cu-3)	SrA(0.1Cu-4)
The grid / pixels	96×96×72			
Resolution / Å^3	0.1×0.1×0.1			
F(0 0 0)	685.38	685.38	685.38	685.38
Lagrange multiplier, λ_{FG}	50	50	50	50
χ^2_{aim}	0.4	0.4	0.4	0.4
R_F / R_{wF}, %	1.38/1.86	1.37/1.84	1.26/1.67	1.38/1.76
R_G / R_{wG}, %	0.96/1.10	0.97/1.16	0.99/1.17	0.99/1.14
No. of unique reflections	89	104	99	71
No. of overlapping reflections	1324	1309	1314	1341
No. of groups of the overlapping reflections	351	381	375	306

Table A11. Details about maximum-entropy calculations (based on $F_{obs}+G$) for complete crystal structures of investigated apatites from synchrotron powder diffraction data with resolution $\sin\theta/\lambda = 0.65$ Å^{-1} (R_F, R_{wF}, R_G and R_{wG} as defined in BayMEM).

Sample	SrA(0.1Cu-1)	SrA(0.1Cu-2)	SrA(0.1Cu-3)	SrA(0.1Cu-4)
The grid / pixels	96×96×72			
Resolution / Å^3	0.1×0.1×0.1			
F(0 0 0)	685.38	685.38	685.38	685.38
Lagrange multiplier, λ_{FG}	50	50	50	50
χ^2_{aim}	0.4	0.4	0.4	0.4
R_F / R_{wF}, %	0.97/1.20	1.05/1.24	1.00/1.16	1.07/1.17
R_G / R_{wG}, %	0.74/0.87	0.79/0.91	0.79/0.92	0.80/0.90
No. of unique reflections	79	81	79	62
No. of overlapping reflections	416	414	416	433
No. of groups of the overlapping reflections	160	163	159	142

Table A12. Details about maximum-entropy calculations (based on F_{obs}+G) for complete crystal structures of investigated apatites from synchrotron powder diffraction data with resolution $\sin\theta/\lambda = 0.55$ Å^{-1} (R_F, R_{wF}, R_G and R_{wG} as defined in BayMEM).

Sample	SrA(0.1Cu-1)	SrA(0.1Cu-2)	SrA(0.1Cu-3)	SrA(0.1Cu-4)
The grid / pixels	96×96×72			
Resolution / Å^3	0.1×0.1×0.1			
F(0 0 0)	685.38	685.38	685.38	685.38
Lagrange multiplier, λ_{FG}	50	50	50	50
χ^2_{aim}	0.4	0.4	0.4	0.4
R_F / R_{wF}, %	0.81 / 1.04	0.86 / 1.03	0.91 / 1.03	0.95 / 1.00
R_G / R_{wG}, %	0.72 / 0.83	0.79 / 0.90	0.74 / 0.87	0.75 / 0.87
No. of unique reflections	66	65	65	54
No. of overlapping reflections	253	252	252	266
No. of groups of the overlapping reflections	107	108	108	102

Appendix 2.

Table A1. Crystallographic and refinement data for $BaZnF_4$ and $BaMgF_4$ (s.g. $Cmc2_1$) from synchrotron powder diffraction data (R_{Br}, *Rp*, *Rwp* and *GooF* as defined in Topas).

Sample	$BaZnF_4$	$BaMgF_4$
Temperature (K)	10	10
Z	4	4
a / Å	4.1908(3)	4.1193(2)
b / Å	14.5137(3)	14.4636(7)
c / Å	5.8361(3)	5.8119(3)
R_{Br}, %	9.86	6.53
Rp, %	16.09	17.82
Rwp, %	23.72	24.30
Rexp, %	11.43	10.69
GooF	2.075	2.27
Wavelength (Å)	0.3995	0.3995
2θ – range (°)	2 – 31	2 – 31
Step width (° 2θ)	0.002	0.002

Table A2. Details about maximum-entropy calculations for $BaZnF_4$ and $BaMgF_4$ (R_F, R_{wF}, R_G and R_{wG} as defined in BayMEM).

Sample	$BaZnF_4$	$BaMgF_4$
Temperature (K)	10	10
The grid / pixels	48×144×128	
Resolution / Å^3	0.09×0.1×0.05	
F(0 0 0)	488.1877	416.0000
Total No. of reflections	219	223
MEM calculations based on F_{obs} (procrystal density), n=2		
Lagrange multiplier, λ_{FG}	50	50
χ^2_{aim}	1.3	1.3
R_F / R_{wF}, %	1.88 / 1.81	2.38 / 2.05
MEM calculations based on F_{obs} (procrystal density), n=4		
Lagrange multiplier, λ_{FG}	8	10
χ^2_{aim}	1.1	1.2
R_F / R_{wF}, %	2.01 / 1.83	2.62 / 2.11
MEM calculations based on F_{obs} (procrystal density), n=6		
Lagrange multiplier, λ_{FG}	AUTO	AUTO
χ^2_{aim}	0.9	1.0
R_F / R_{wF}, %	2.12 / 1.96	2.75 / 2.24
MEM calculations based on F_{obs} (flat prior), n=2		
Lagrange multiplier, λ_{FG}	50	50
χ^2_{aim}	3.0	2.0
R_F / R_{wF}, %	2.62 / 2.75	3.07 / 2.55
MEM calculations based on F_{obs} + G, n=2		
Lagrange multiplier, λ_{FG}	50	50
χ^2_{aim} (F_{obs}+G)	1.3	1.0
R_F / R_{wF}, % (F_{obs}+G)	2.10 / 2.09	2.02 / 1.86
R_G / R_{wG}, % (F_{obs}+G)	2.17 / 2.74	4.16 / 3.05
MEM calculations based on F_{obs} + G, n=4		
Lagrange multiplier, λ_{FG}	10	10
χ^2_{aim} (F_{obs}+G)	1.4	1.0
R_F / R_{wF}, % (F_{obs}+G)	2.15 / 1.88	2.38 / 2.02
R_G / R_{wG}, % (F_{obs}+G)	2.25 / 2.80	1.04 / 2.98
MEM calculations based on F_{obs} + G + F_{PD} (2.0 Å^{-1}), n=2		
Lagrange multiplier, λ_{FG}	AUTO	AUTO
χ^2_{aim} (F_{obs}+G)	2.0	2.5
R_F / R_{wF}, % (F_{obs}+G)	2.65 / 2.63	3.44 / 3.51
R_G / R_{wG}, % (F_{obs}+G)	2.44 / 3.16	4.33 / 3.16
No. of unique reflections	125	179
No. of overlapping reflections	94	44
No. of groups of the overlapping reflections	41	21

Appendix 3.

Example of an input file for program Topas 4 which was used for the sequential Rietveld fit of the strain modes for $LuF[SeO_3]$.

```
macro Out_file(file)
{
   out file append
      Out(Get(r_wp), "    \n %11.5f" ) ' _Rwp
      Out(Get(a), "%15.5f", "%9.5f") ' cell_length_a
      Out(Get(b), "%15.5f", "%9.5f") ' cell_length_b
      Out(Get(c), "%15.5f", "%9.5f") ' cell_length_c
      Out(Get(al), "%15.5f", "%9.5f") ' cell_angle_alpha
      Out(Get(be), "%15.5f", "%9.5f") ' cell_angle_beta
      Out(Get(ga), "%15.5f", "%9.5f") ' cell_angle_gamma
      Out(s1, "%12.5f", "%9.5f")
      Out(s2, "%12.5f", "%9.5f")
      Out(s3, "%12.5f", "%9.5f")
      Out(s4, "%12.5f", "%9.5f")
      Out(s5, "%12.5f", "%9.5f")
      Out(s6, "%12.5f", "%9.5f")
      Out(pe1, "%12.5f", "%9.5f")
      Out(pe2, "%12.5f", "%9.5f")
      Out(pe3, "%12.5f", "%9.5f")
      Out(pe4, "%12.5f", "%9.5f")
      Out(pe5, "%12.5f", "%9.5f")
      Out(pe6, "%12.5f", "%9.5f")
}

'{{{macros for calculations involving the lattice parameters

      'Takes non-refinable undistorted cell parameters, and variable strains
as input.
      'Returns strained cell parameters
      macro straincell(pa0, pb0, pc0, pal0, pbe0, pga0)
      {
            prm  !radian  57.2957795
            prm  palpha0 = pal0/radian;
            prm  pbeta0  = pbe0/radian;
            prm  pgamma0 = pga0/radian;
            'distorted parent-cell parameters
            prm  pa = pa0*(pe1 + 1);:  6.44848
            prm  pb = pb0*(pe2 + 1);:  6.84409
            prm  pc = pc0*(pe3 + 1);:  4.27980
            prm  palpha = palpha0 - pe4*Sin(palpha0);
            prm  pbeta  = pbeta0  - pe5*Sin(pbeta0);
            prm  pgamma = pgamma0 - pe6*Sin(pgamma0);
            prm  pal = palpha*radian;: 90.07091
            prm  pbe = pbeta*radian ;: 95.61740
            prm  pga = pgamma*radian;: 90.03307
      }

      'Use basis-transformation matrix to transform from parent-cell to
supercell parameters
      macro celltransform(t11, t12, t13, t21, t22, t23, t31, t32, t33)
      {
```

```
            prm  !radian  57.2957795

            'parent-lattice basis vectors in cartesian coords
            prm  zzz  = (Cos(palpha) - Cos(pbeta)*Cos(pgamma))/Sin(pgamma);
            prm  pv11 = pa;
            prm  !pv21  0
            prm  !pv31  0
            prm  pv12 = pb*Cos(pgamma);
            prm  pv22 = pb*Sin(pgamma);
            prm  !pv32  0
            prm  pv13 = pc*Cos(pbeta);
            prm  pv23 = pc*zzz;
            prm  pv33 = pc*Sqrt(1 - Cos(pbeta)^2 - zzz^2);

            'supercell basis vectors in cartesian coords
            prm  sv11 = t11*pv11 + t12*pv12 + t13*pv13;
            prm  sv21 = t11*pv21 + t12*pv22 + t13*pv23;
            prm  sv31 = t11*pv31 + t12*pv32 + t13*pv33;
            prm  sv12 = t21*pv11 + t22*pv12 + t23*pv13;
            prm  sv22 = t21*pv21 + t22*pv22 + t23*pv23;
            prm  sv32 = t21*pv31 + t22*pv32 + t23*pv33;
            prm  sv13 = t31*pv11 + t32*pv12 + t33*pv13;
            prm  sv23 = t31*pv21 + t32*pv22 + t33*pv23;
            prm  sv33 = t31*pv31 + t32*pv32 + t33*pv33;

            'distorted supercell parameters
            prm  sa = Sqrt(sv11^2+sv21^2+sv31^2);
            prm  sb = Sqrt(sv12^2+sv22^2+sv32^2);
            prm  sc = Sqrt(sv13^2+sv23^2+sv33^2);
            prm  salpha = ArcCos((sv12*sv13+sv22*sv23+sv32*sv33)/(sb*sc));
            prm  sbeta  = ArcCos((sv11*sv13+sv21*sv23+sv31*sv33)/(sa*sc));
            prm  sgamma = ArcCos((sv11*sv12+sv21*sv22+sv31*sv32)/(sa*sb));
            prm  sal = salpha*radian;
            prm  sbe = sbeta*radian;
            prm  sga = sgamma*radian;
      }
'}}}

iters 300
do_errors
XYE(FileName)
bkg @  11753.9469`_14.7944678 -7130.01235`_25.1300073  1935.93213`_23.0003751
561.944125`_21.3053992 -368.916997`_20.9094482  35.1972098`_19.8681934 -
24.8299646`_19.7882956  149.933676`_18.4599147  119.144117`_18.3542657
90.609349`_15.9106356 -52.0456283`_15.1624355
      start_X  4
      finish_X  30
      LP_Factor( 90)
      Zero_Error(, -0.0138)
      convolution_step 5
      Rp 217.5
      Rs 217.5
      Simple_Axial_Model( 0.001)
      lam
            ymin_on_ymax  0.0001
            la  1 lo  0.826401 lh  0.0001
```

```
      x_calculation_step 0.001
      str
            LVol_FWHM_CS_G_L( 1, 371.24214`_52.84462, 0.89,
358.49782`_45.08627,@, 411.79449`_49.86917,@, 9999.99999`_20342.19111)
            e0_from_Strain( 0.04488`_12.28008,lg, 0.17951`_0.00427,lg,
0.17951`_0.00427)
            r_bragg  6.55700305
            phase_name "Structure"
            MVW( 641.847, 187.946784`_0.00573257063, 100.000`_0.000)
            scale @  0.000567754063`_6.89e-006
            Phase_LAC_1_on_cm( 531.89653`_0.01622)
            Phase_Density_g_on_cm3( 5.67082`_0.00017)

            space_group P-1

            #define refine_strain_modes  'comment out this line for a
traditional supercell-parameter refinement.

      '     #ifdef refine_strain_modes
            prm  s1     -0.00230`_0.00002 min  -0.50 max  0.50
'P2_1/m[0,0,0]GM1+(a)strain_1(a)
            prm  s2     -0.01046`_0.00005 min  -0.50 max  0.50
'P2_1/m[0,0,0]GM1+(a)strain_2(a)
            prm  s3     -0.00231`_0.00002 min  -0.50 max  0.50
'P2_1/m[0,0,0]GM1+(a)strain_3(a)
            prm  s4     -0.00080`_0.00001 min  -0.50 max  0.50
'P2_1/m[0,0,0]GM1+(a)strain_4(a)
            prm  s5     -0.02823`_0.00004 min  -0.50 max  0.50
'P2_1/m[0,0,0]GM2+(a)strain_1(a)
            prm  s6     -0.06016`_0.00006 min  -0.50 max  0.50
'P2_1/m[0,0,0]GM2+(a)strain_2(a)

            'unitless parent cell strains (in lattice rather than orthogonal
coords)
            prm  pe1      = +  1.00000*s1;: -0.00230`_0.00002
            prm  pe2      = +  1.00000*s3;: -0.00231`_0.00002
            prm  pe3      = +  1.00000*s4;: -0.00080`_0.00001
            prm  pe4      = +  1.00000*s6;: -0.06016`_0.00006
            prm  pe5      = +  1.00000*s2;: -0.01046`_0.00005
            prm  pe6      = +  1.00000*s5;: -0.02823`_0.00004

            straincell(6.47340,6.87020,4.28430,90.00000,95.60200,90.00000)
            celltransform(1,0,0,0,1,0,0,0,1)

                  a  = sa;:    6.45854`_0.00013
                  b  = sb;:    6.85435`_0.00012
                  c  = sc;:    4.28088`_0.00007
                  al = sal;:  93.44678`_0.00326
                  be = sbe;:  96.19830`_0.00258
                  ga = sga;:  91.61764`_0.00237

'{{{mode definitions
            prm  !a1     -0.01000 min  -1.41 max  1.41
'P2_1/m[0,0,0]GM1+(a)[Lu1:e]A'_1(a)
            prm  !a2     -0.01291 min  -1.41 max  1.41
'P2_1/m[0,0,0]GM1+(a)[Lu1:e]A'_2(a)
```

```
            prm  a3     -0.02820`_0.01233 min  -1.41 max  1.41
'P2_1/m[0,0,0]GM2+(a)[Lu1:e]A''(a)
            prm  !a4     -0.02302 min  -1.41 max  1.41
'P2_1/m[0,0,0]GM1+(a)[F1:e]A'_1(a)
            prm  !a5     -0.06958 min  -1.41 max  1.41
'P2_1/m[0,0,0]GM1+(a)[F1:e]A'_2(a)
            prm  a6      0.07997`_0.07392 min  -1.41 max  1.41
'P2_1/m[0,0,0]GM2+(a)[F1:e]A''(a)
            prm  !a7     -0.00079 min  -1.41 max  1.41
'P2_1/m[0,0,0]GM1+(a)[Se1:e]A'_1(a)
            prm  !a8      0.03442 min  -1.41 max  1.41
'P2_1/m[0,0,0]GM1+(a)[Se1:e]A'_2(a)
            prm  a9      0.18568`_0.02063 min  -1.41 max  1.41
'P2_1/m[0,0,0]GM2+(a)[Se1:e]A''(a)
            prm  !a10    -0.03090 min  -1.41 max  1.41
'P2_1/m[0,0,0]GM1+(a)[O1:e]A'_1(a)
            prm  !a11    -0.04852 min  -1.41 max  1.41
'P2_1/m[0,0,0]GM1+(a)[O1:e]A'_2(a)
            prm  a12     0.23911`_0.05407 min  -1.41 max  1.41
'P2_1/m[0,0,0]GM2+(a)[O1:e]A''(a)
            prm  !a13    -0.06769 min  -2.00 max  2.00
'P2_1/m[0,0,0]GM1+(a)[O2:f]A_1(a)
            prm  !a14    -0.00842 min  -2.00 max  2.00
'P2_1/m[0,0,0]GM1+(a)[O2:f]A_2(a)
            prm  !a15    -0.02061 min  -2.00 max  2.00
'P2_1/m[0,0,0]GM1+(a)[O2:f]A_3(a)
            prm  a16    -0.44042`_0.04677 min  -2.00 max  2.00
'P2_1/m[0,0,0]GM2+(a)[O2:f]A_1(a)
            prm  a17    -0.24993`_0.04396 min  -2.00 max  2.00
'P2_1/m[0,0,0]GM2+(a)[O2:f]A_2(a)
            prm  a18     0.18712`_0.08173 min  -2.00 max  2.00
'P2_1/m[0,0,0]GM2+(a)[O2:f]A_3(a)
'}}}

'{{{mode-amplitude to delta transformation
            prm  Lu1_dx   = +  0.10923*a2;: -0.00141
            prm  Lu1_dy   = +  0.10292*a3;: -0.00290`_0.00127
            prm  Lu1_dz   = +  0.16505*a1;: -0.00165
            prm  F1_dx    = +  0.10923*a5;: -0.00760
            prm  F1_dy    = +  0.10292*a6;:  0.00823`_0.00761
            prm  F1_dz    = +  0.16505*a4;: -0.00380
            prm  Se1_dx   = -  0.10923*a8;: -0.00376
            prm  Se1_dy   = -  0.10292*a9;: -0.01911`_0.00212
            prm  Se1_dz   = -  0.16505*a7;:  0.00013
            prm  O1_dx    = +  0.10923*a11;: -0.00530
            prm  O1_dy    = +  0.10292*a12;:  0.02461`_0.00557
            prm  O1_dz    = +  0.16505*a10;: -0.00510
            prm  O2_dx    = +  0.07724*a14 +  0.07724*a17;: -0.01995`_0.00340
            prm  O2_dy    = +  0.07278*a15 +  0.07278*a18;:  0.01212`_0.00595
            prm  O2_dz    = +  0.11671*a13 +  0.11671*a16;: -0.05930`_0.00546
            prm  O3_dx    = +  0.07724*a14 -  0.07724*a17;:  0.01865`_0.00340
            prm  O3_dy    = -  0.07278*a15 +  0.07278*a18;:  0.01512`_0.00595
            prm  O3_dz    = +  0.11671*a13 -  0.11671*a16;:  0.04350`_0.00546
 '}}}

'{{{distorted parameters
            prm  Lu1_x    =    0.36836 + Lu1_dx;:  0.36695
```

```
            prm  Lu1_y    = 1/4 + Lu1_dy;:  0.24710`_0.00127
            prm  Lu1_z    =    0.46083 + Lu1_dz;:  0.45918
            prm  F1_x     =    0.35790 + F1_dx;:  0.35030
            prm  F1_y     = 1/4 + F1_dy;:  0.25823`_0.00761
            prm  F1_z     =   -0.03820 + F1_dz;: -0.04200
            prm  Se1_x    =    0.14630 + Se1_dx;:  0.14254
            prm  Se1_y    = 3/4 + Se1_dy;:  0.73089`_0.00212
            prm  Se1_z    =    0.32170 + Se1_dz;:  0.32183
            prm  O1_x     =    0.02340 + O1_dx;:  0.01810
            prm  O1_y     = 1/4 + O1_dy;:  0.27461`_0.00557
            prm  O1_z     =    0.41130 + O1_dz;:  0.40620
            prm  O2_x     =    0.32160 + O2_dx;:  0.30165`_0.00340
            prm  O2_y     =    0.92560 + O2_dy;:  0.93772`_0.00595
            prm  O2_z     =    0.45060 + O2_dz;:  0.39130`_0.00546
            prm  O3_x     =    0.32160 + O3_dx;:  0.34025`_0.00340
            prm  O3_y     =    0.57440 + O3_dy;:  0.58952`_0.00595
            prm  O3_z     =    0.45060 + O3_dz;:  0.49410`_0.00546

            prm !Lu1_occ  = 1;:  1.00000
            prm !F1_occ   = 1;:  1.00000
            prm !Se1_occ  = 1;:  1.00000
            prm !O1_occ   = 1;:  1.00000
            prm !O2_occ   = 1;:  1.00000
            prm !O3_occ   = 1;:  1.00000
'}}}

'{{{mode-dependent sites
            site Lu1  x = Lu1_x;  y = Lu1_y;  z = Lu1_z;  occ Lu = Lu1_occ;
beq reflu   3.0577`_0.1879 min =0.2 ;
            site F1   x = F1_x;   y = F1_y;   z = F1_z;   occ F  = F1_occ;
beq reff    0.2000`_0.8350 min =0.2 ;
            site Se1  x = Se1_x;  y = Se1_y;  z = Se1_z;  occ Se = Se1_occ;
beq refse   5.5362`_0.4056 min =0.2 ;
            site O1   x = O1_x;   y = O1_y;   z = O1_z;   occ O  = O1_occ;
beq refo   0.2000`_0.6530 min =0.2 ;
            site O2   x = O2_x;   y = O2_y;   z = O2_z;   occ O  = O2_occ;
beq refo   0.2000`_0.6530 min =0.2 ;
            site O3   x = O3_x;   y = O3_y;   z = O3_z;   occ O  = O3_occ;
beq refo   0.2000`_0.6530 min =0.2 ;
'}}}
```

Example of an input file for program Topas 4 which was used for the sequential Le Bail fit of the strain modes for $LuF[SeO_3]$.

```
macro Out_file(file)
{
   out file append
      Out(Get(r_wp), "    \n %11.5f" ) ' _Rwp
      Out(Get(a), "%15.5f", "%9.5f") ' cell_length_a
      Out(Get(b), "%15.5f", "%9.5f") ' cell_length_b
      Out(Get(c), "%15.5f", "%9.5f") ' cell_length_c
      Out(Get(al), "%15.5f", "%9.5f") ' cell_angle_alpha
      Out(Get(be), "%15.5f", "%9.5f") ' cell_angle_beta
      Out(Get(ga), "%15.5f", "%9.5f") ' cell_angle_gamma
      Out(pe1, "%15.5f", "%9.5f")
      Out(pe2, "%15.5f", "%9.5f")
      Out(pe3, "%15.5f", "%9.5f")
      Out(pe4, "%15.5f", "%9.5f")
      Out(pe5, "%15.5f", "%9.5f")
      Out(pe6, "%15.5f", "%9.5f")
}
      macro straincell(pa0, pb0, pc0, pal0, pbe0, pga0)
      {
            prm  !radian  57.2957795
            prm  palpha0 = pal0/radian;
            prm  pbeta0  = pbe0/radian;
            prm  pgamma0 = pga0/radian;
            'distorted parent-cell parameters
            prm  pa = pa0*(pe1 + 1);:  6.44848
            prm  pb = pb0*(pe2 + 1);:  6.84409
            prm  pc = pc0*(pe3 + 1);:  4.27980
            prm  palpha = palpha0 - pe4*Sin(palpha0);
            prm  pbeta  = pbeta0  - pe5*Sin(pbeta0);
            prm  pgamma = pgamma0 - pe6*Sin(pgamma0);
            prm  pal = palpha*radian;: 90.07091
            prm  pbe = pbeta*radian ;: 95.61740
            prm  pga = pgamma*radian;: 90.03307
      }
      macro celltransform(t11, t12, t13, t21, t22, t23, t31, t32, t33)
      {
```

```
            prm  !radian  57.2957795
            'parent-lattice basis vectors in cartesian coords
            prm  zzz  = (Cos(palpha) - Cos(pbeta)*Cos(pgamma))/Sin(pgamma);
            prm  pv11 = pa;
            prm  !pv21  0
            prm  !pv31  0
            prm  pv12 = pb*Cos(pgamma);
            prm  pv22 = pb*Sin(pgamma);
            prm  !pv32  0
            prm  pv13 = pc*Cos(pbeta);
            prm  pv23 = pc*zzz;
            prm  pv33 = pc*Sqrt(1 - Cos(pbeta)^2 - zzz^2);
            'supercell basis vectors in cartesian coords
            prm  sv11 = t11*pv11 + t12*pv12 + t13*pv13;
            prm  sv21 = t11*pv21 + t12*pv22 + t13*pv23;
            prm  sv31 = t11*pv31 + t12*pv32 + t13*pv33;
            prm  sv12 = t21*pv11 + t22*pv12 + t23*pv13;
            prm  sv22 = t21*pv21 + t22*pv22 + t23*pv23;
            prm  sv32 = t21*pv31 + t22*pv32 + t23*pv33;
            prm  sv13 = t31*pv11 + t32*pv12 + t33*pv13;
            prm  sv23 = t31*pv21 + t32*pv22 + t33*pv23;
            prm  sv33 = t31*pv31 + t32*pv32 + t33*pv33;
            'distorted supercell parameters
            prm  sa = Sqrt(sv11^2+sv21^2+sv31^2);
            prm  sb = Sqrt(sv12^2+sv22^2+sv32^2);
            prm  sc = Sqrt(sv13^2+sv23^2+sv33^2);
            prm  salpha = ArcCos((sv12*sv13+sv22*sv23+sv32*sv33)/(sb*sc));
            prm  sbeta  = ArcCos((sv11*sv13+sv21*sv23+sv31*sv33)/(sa*sc));
            prm  sgamma = ArcCos((sv11*sv12+sv21*sv22+sv31*sv32)/(sa*sb));
            prm  sal = salpha*radian;
            prm  sbe = sbeta*radian;
            prm  sga = sgamma*radian;
      }
iters 100
do_errors
continue_after_convergence
XYE(FileName)
```

```
      bkg @  11209.8127` -7332.04118`  2248.66707`  312.4385` -446.151343`
48.9687557`  92.0060604`  62.5305514` -97.8755136` -150.174412`  40.1732165`
      start_X  4
      LP_Factor( 90)
      Zero_Error(, -0.0138)
      convolution_step 5
      Rp 217.5
      Rs 217.5
      Simple_Axial_Model( 0.001)
      lam
            ymin_on_ymax  0.0001
            la  1 lo  0.826401 lh  0.0001
      x_calculation_step 0.001
      hkl_Is
            lebail  1
            LVol_FWHM_CS_G_L( 1, 317.8518953, 0.89, 306.0315349,@,
350.4475805,@, 10000_LIMIT_MIN_0.3)
            e0_from_Strain( 0.06714911244,lg, 0.1637203233,lg, 0.1637203233)
            r_bragg  0.462166152
            phase_name "hkl_P-1"
            space_group "P-1"
            hkl_m_d_th2 0 1 0 2 6.83792591 6.92873144 I  0.03167503434
            hkl_m_d_th2 1 0 0 2 6.41686535 7.38399029 I  3.883647208
            hkl_m_d_th2 1 -1 0 2 4.76291418 9.95375633 I  1.968085691
            hkl_m_d_th2 1 1 0 2 4.59972572 10.3078327 I  1.666087449
            hkl_m_d_th2 0 0 1 2 4.24731684 11.1657076 I  35.1017308
            hkl_m_d_th2 1 0 -1 2 3.73559332 12.7011623 I  14.973385
            hkl_m_d_th2 0 -1 1 2 3.71510625 12.7714939 I  0.5720678465
            hkl_m_d_th2 0 1 1 2 3.50958157 13.5227985 I  0.3002439841
            hkl_m_d_th2 0 2 0 2 3.41896296 13.8829575 I  41.48216495
            hkl_m_d_th2 1 0 1 2 3.37526488 14.0635958 I  0.02639934675
            hkl_m_d_th2 1 1 -1 2 3.32830381 14.263052 I  0.03559812789
            hkl_m_d_th2 1 -1 -1 2 3.2304616 14.6973915 I  0.05614762095
            hkl_m_d_th2 2 0 0 2 3.20843267 14.7988653 I  0.6354186041
            hkl_m_d_th2 1 -1 1 2 3.11277413 15.2563143 I  5.681631878
            hkl_m_d_th2 1 -2 0 2 3.0620892 15.5103836 I  3.931344037
            hkl_m_d_th2 1 2 0 2 2.97459078 15.9695597 I  0.2948419239
            hkl_m_d_th2 1 1 1 2 2.94725585 16.1186523 I  4.110764447
```

```
hkl_m_d_th2 2 -1 0 2 2.94439578 16.1344128 I  31.8610824
hkl_m_d_th2 2 1 0 2 2.86635399 16.5767517 I  21.50942402
hkl_m_d_th2 0 -2 1 2 2.74983549 17.28442 I  10.92717352
hkl_m_d_th2 2 0 -1 2 2.70705819 17.5596905 I  0.2522461304
hkl_m_d_th2 0 2 1 2 2.58443761 18.399889 I  5.025544893
hkl_m_d_th2 1 2 -1 2 2.56783724 18.5198841 I  4.494602893
hkl_m_d_th2 2 1 -1 2 2.5264852 18.8257408 I  10.55444544
hkl_m_d_th2 2 -1 -1 2 2.50760698 18.968771 I  8.191734326
hkl_m_d_th2 1 -2 1 2 2.48906946 19.1113625 I  0.625480755
hkl_m_d_th2 1 -2 -1 2 2.4787128 19.191967 I  6.415372667
hkl_m_d_th2 2 0 1 2 2.43472695 19.5420589 I  0.01653932826
hkl_m_d_th2 2 -2 0 2 2.38145709 19.9836235 I  0.1609160045
hkl_m_d_th2 2 -1 1 2 2.34062719 20.3358898 I  15.29571802
hkl_m_d_th2 1 2 1 2 2.32342339 20.4880867 I  0.2304624266
hkl_m_d_th2 2 2 0 2 2.29986286 20.7002735 I  0.6435761287
hkl_m_d_th2 0 3 0 2 2.27930856 20.8890305 I  2.133650791
hkl_m_d_th2 2 1 1 2 2.24942732 21.1696987 I  2.537921561
hkl_m_d_th2 1 -3 0 2 2.17188907 21.9346733 I  5.45092177
hkl_m_d_th2 3 0 0 2 2.13895512 22.2766914 I  13.74680978
hkl_m_d_th2 2 2 -1 2 2.13375187 22.3317127 I  1.011896311
hkl_m_d_th2 1 3 0 2 2.12456274 22.4295502 I  4.910475903
hkl_m_d_th2 0 0 2 2 2.12365842 22.4392262 I  14.32599399
hkl_m_d_th2 2 -2 -1 2 2.11111546 22.5742931 I  5.095830096
hkl_m_d_th2 1 0 -2 2 2.08558846 22.8542938 I  8.260360785
hkl_m_d_th2 0 -1 2 2 2.06554317 23.0791206 I  0.08161570324
hkl_m_d_th2 0 -3 1 2 2.06365323 23.1005478 I  0.6368514118
hkl_m_d_th2 3 -1 0 2 2.06203032 23.1189785 I  4.78373099
hkl_m_d_th2 2 -2 1 2 2.04490328 23.3153172 I  3.571661755
hkl_m_d_th2 1 1 -2 2 2.02383375 23.5615063 I  0.6194230323
hkl_m_d_th2 3 1 0 2 2.02139831 23.5903015 I  6.838058186
hkl_m_d_th2 3 0 -1 2 2.00067735 23.8381939 I  2.138912158
hkl_m_d_th2 0 1 2 2 1.99262273 23.9359741 I  0.05554895191
hkl_m_d_th2 1 3 -1 2 1.97712755 24.1263771 I  0.6722031757
hkl_m_d_th2 1 -1 -2 2 1.96710289 24.251194 I  1.284730243
hkl_m_d_th2 0 3 1 2 1.95733178 24.3741112 I  0.2216940918
hkl_m_d_th2 1 0 2 2 1.95315433 24.4270458 I  2.875062992
hkl_m_d_th2 1 -3 1 2 1.95222831 24.4388103 I  2.043713098
hkl_m_d_th2 2 2 1 2 1.92684615 24.7658138 I  0.02774018865
```

hkl_m_d_th2 3 -1 -1 2 1.92162049 24.8342361 I 16.54722922
hkl_m_d_th2 3 1 -1 2 1.91873336 24.8722019 I 9.05852093
hkl_m_d_th2 1 -3 -1 2 1.91575527 24.9114876 I 0.01173116786
hkl_m_d_th2 1 -1 2 2 1.91320658 24.9452057 I 23.60225578
hkl_m_d_th2 2 -3 0 2 1.88956165 25.2624798 I 29.56832132
hkl_m_d_th2 2 0 -2 2 1.86779666 25.5618095 I 0.05974077687
hkl_m_d_th2 0 -2 2 2 1.85755312 25.7051773 I 4.36158894
hkl_m_d_th2 1 1 2 2 1.84475112 25.8866501 I 6.38744074
hkl_m_d_th2 3 -2 0 2 1.84248817 25.9189968 I 8.95762995
hkl_m_d_th2 1 3 1 2 1.83143497 26.0781727 I 9.407112421
hkl_m_d_th2 3 0 1 2 1.8312993 26.0801392 I 10.03115965
hkl_m_d_th2 2 3 0 2 1.828251 26.1243916 I 25.89582379
hkl_m_d_th2 1 2 -2 2 1.82220745 26.2125778 I 13.62178355
hkl_m_d_th2 2 1 -2 2 1.81824589 26.27071 I 16.46117778
hkl_m_d_th2 3 -1 1 2 1.79481769 26.6198902 I 9.352267211e-005
hkl_m_d_th2 2 -1 -2 2 1.7857691 26.7572727 I 1.220059406
hkl_m_d_th2 3 2 0 2 1.78551149 26.7612057 I 2.084311552
hkl_m_d_th2 0 2 2 2 1.75479078 27.2386513 I 0.1200195344
hkl_m_d_th2 2 3 -1 2 1.75305951 27.2660713 I 20.78355162
hkl_m_d_th2 1 -2 2 2 1.74865687 27.3360519 I 2.077151171
hkl_m_d_th2 3 1 1 2 1.74418604 27.4074879 I 2.388976308
hkl_m_d_th2 1 -2 -2 2 1.74147427 27.4510002 I 8.668837292
hkl_m_d_th2 2 -3 -1 2 1.73423302 27.5678806 I 11.94817054
hkl_m_d_th2 3 -2 -1 2 1.72886372 27.6551952 I 0.8972588613
hkl_m_d_th2 3 2 -1 2 1.72466445 27.723875 I 0.2418645551
hkl_m_d_th2 2 -3 1 2 1.71871519 27.8217678 I 12.65468874
hkl_m_d_th2 0 4 0 2 1.70948148 27.9750957 I 38.6924784
hkl_m_d_th2 2 0 2 2 1.68763244 28.3447971 I 0.003445217182
hkl_m_d_th2 1 -4 0 2 1.66640663 28.7135372 I 5.179661842
hkl_m_d_th2 2 -1 2 2 1.66532505 28.7325859 I 6.513869393
hkl_m_d_th2 2 2 -2 2 1.66415191 28.7532768 I 1.521876791
hkl_m_d_th2 3 -2 1 2 1.65420151 28.9299927 I 10.34876388
hkl_m_d_th2 1 2 2 2 1.6476984 29.0466785 I 0.05979760466
hkl_m_d_th2 1 4 0 2 1.63770437 29.227869 I 2.089787806
hkl_m_d_th2 0 -4 1 2 1.62187767 29.5195274 I 18.25260649
hkl_m_d_th2 2 -2 -2 2 1.6152308 29.6437836 I 3.296554867
hkl_m_d_th2 2 3 1 2 1.6141026 29.664978 I 0.8524039247
hkl_m_d_th2 2 1 2 2 1.61287057 29.6881599 I 2.74473682

```
            hkl_m_d_th2 0 -3 2 2 1.60537469 29.8299904 I  26.96598698
            hkl_m_d_th2 4 0 0 2 1.60421634 29.8520298 I  3.543460163
            hkl_m_d_th2 3 0 -2 2 1.59728301 29.9846439 I  0.001599724206
            hkl_m_d_th2 3 -3 0 2 1.58763802 30.1711159 I  0.06687685381
            hkl_m_d_th2 1 3 -2 2 1.57924962 30.3352146 I  0.2402028967
            hkl_m_d_th2 3 2 1 2 1.5771724 30.3761311 I  0.3127680431
            hkl_m_d_th2 1 4 -1 2 1.5757283 30.4046421 I  0.3293136094
            hkl_m_d_th2 4 -1 0 2 1.57408154 30.4372196 I  0.3341454992
            MVW( 0.000, 187.982346`, 0.000)
            prm  s1     -0.00385 min  -0.50 max  0.50
'P2_1/m[0,0,0]GM1+(a)strain_1(a)
            prm  s2     -0.01547 min  -0.50 max  0.50
'P2_1/m[0,0,0]GM1+(a)strain_2(a)
            prm  s3     -0.00380 min  -0.50 max  0.50
'P2_1/m[0,0,0]GM1+(a)strain_3(a)
            prm  s4     -0.00105 min  -0.50 max  0.50
'P2_1/m[0,0,0]GM1+(a)strain_4(a)
            prm  s5     -0.03307 min  -0.50 max  0.50
'P2_1/m[0,0,0]GM2+(a)strain_1(a)
            prm  s6     -0.07091 min  -0.50 max  0.50
'P2_1/m[0,0,0]GM2+(a)strain_2(a)
            prm  pe1      = +  1.00000*s1;: -0.00385
            prm  pe2      = +  1.00000*s3;: -0.00380
            prm  pe3      = +  1.00000*s4;: -0.00105
            prm  pe4      = +  1.00000*s6;: -0.07091
            prm  pe5      = +  1.00000*s2;: -0.01547
            prm  pe6      = +  1.00000*s5;: -0.03307
            straincell(6.47340,6.87020,4.28430,90.00000,95.60200,90.00000)
            celltransform(1,0,0,0,1,0,0,0,1)
                  a  = sa;:    6.44848
                  b  = sb;:    6.84409
                  c  = sc;:    4.27980
                  al = sal;:  94.06284
                  be = sbe;:  96.48413
                  ga = sga;:  91.89477
Out_file(hkl.txt)
```

Example of an input file for program Topas 4 which was used for the parametric Le Bail fit of the strain modes for $LuF[SeO_3]$.

```
macro Out_file(file)
{
   out file append
      Out(Get(r_wp), "    \n %11.5f" ) ' _Rwp
      Out(Get(a), "%15.5f", "%9.5f") ' cell_length_a
      Out(Get(b), "%15.5f", "%9.5f") ' cell_length_b
      Out(Get(c), "%15.5f", "%9.5f") ' cell_length_c
      Out(Get(al), "%15.5f", "%9.5f") ' cell_angle_alpha
      Out(Get(be), "%15.5f", "%9.5f") ' cell_angle_beta
      Out(Get(ga), "%15.5f", "%9.5f") ' cell_angle_gamma
      Out(pe1, "%15.5f", "%9.5f")
      Out(pe2, "%15.5f", "%9.5f")
      Out(pe3, "%15.5f", "%9.5f")
      Out(pe4, "%15.5f", "%9.5f")
      Out(pe5, "%15.5f", "%9.5f")
      Out(pe6, "%15.5f", "%9.5f")
}
      '{{{macros for calculations involving the lattice parameters
      'Takes non-refinable undistorted cell parameters, and variable strains
as input.
      'Returns strained cell parameters
      macro straincell(pa0, pb0, pc0, pal0, pbe0, pga0)
      {
            prm  !radian  57.2957795
            local  palpha0 = pal0/radian;
            local  pbeta0  = pbe0/radian;
            local  pgamma0 = pga0/radian;
            'distorted parent-cell parameters
            local  pa = pa0*(pe1 + 1);:  6.44848
            local  pb = pb0*(pe2 + 1);:  6.84409
            local  pc = pc0*(pe3 + 1);:  4.27980
            local  palpha = palpha0 - pe4*Sin(palpha0);
            local  pbeta  = pbeta0  - pe5*Sin(pbeta0);
            local  pgamma = pgamma0 - pe6*Sin(pgamma0);
            local  pal = palpha*radian;: 90.07091
            local  pbe = pbeta*radian ;: 95.61740
```

```
            local  pga = pgamma*radian;: 90.03307
      }
      'Use basis-transformation matrix to transform from parent-cell to
supercell parameters
      macro celltransform(t11, t12, t13, t21, t22, t23, t31, t32, t33)
      {
            prm  !radian  57.2957795
            'parent-lattice basis vectors in cartesian coords
            local  zzz  = (Cos(palpha) - Cos(pbeta)*Cos(pgamma))/Sin(pgamma);
            local  pv11 = pa;
            local  !pv21  0
            local  !pv31  0
            local  pv12 = pb*Cos(pgamma);
            local  pv22 = pb*Sin(pgamma);
            local  !pv32  0
            local  pv13 = pc*Cos(pbeta);
            local  pv23 = pc*zzz;
            local  pv33 = pc*Sqrt(1 - Cos(pbeta)^2 - zzz^2);
            'supercell basis vectors in cartesian coords
            local  sv11 = t11*pv11 + t12*pv12 + t13*pv13;
            local  sv21 = t11*pv21 + t12*pv22 + t13*pv23;
            local  sv31 = t11*pv31 + t12*pv32 + t13*pv33;
            local  sv12 = t21*pv11 + t22*pv12 + t23*pv13;
            local  sv22 = t21*pv21 + t22*pv22 + t23*pv23;
            local  sv32 = t21*pv31 + t22*pv32 + t23*pv33;
            local  sv13 = t31*pv11 + t32*pv12 + t33*pv13;
            local  sv23 = t31*pv21 + t32*pv22 + t33*pv23;
            local  sv33 = t31*pv31 + t32*pv32 + t33*pv33;
            'distorted supercell parameters
            local  sa = Sqrt(sv11^2+sv21^2+sv31^2);
            local  sb = Sqrt(sv12^2+sv22^2+sv32^2);
            local  sc = Sqrt(sv13^2+sv23^2+sv33^2);
            local  salpha = ArcCos((sv12*sv13+sv22*sv23+sv32*sv33)/(sb*sc));
            local  sbeta  = ArcCos((sv11*sv13+sv21*sv23+sv31*sv33)/(sa*sc));
            local  sgamma = ArcCos((sv11*sv12+sv21*sv22+sv31*sv32)/(sa*sb));
            local  sal = salpha*radian;
            local  sbe = sbeta*radian;
            local  sga = sgamma*radian;
```

```
      }
 '}}}
bootstrap_errors 100
approximate_A

prm !t_kr 120

prm pA_e1  0.049`
prm pB_e1  757.51398`
prm pA_e2  0.02951`
prm pB_e2  750.70520`
prm pA_e3  0.00188`
prm pB_e3  1611.79064`
prm pA_e4  0.68113`
prm pB_e4  113.43002`
prm pA_e5  0.90131`
prm pB_e5  317.62995`
prm pA_e6  0.94034`
prm pB_e6  221.29718`
prm up_beta  0.40009`

macro parametric {
      local Tdiff = (t_kr - t_cur) / t_kr;
      local ppA_e1 = pA_e1 * 0.00001;
      local ppA_e2 = pA_e2 * 0.00001;
      local ppA_e3 = pA_e3 * 0.00001;
      local ppA_e4 = pA_e4 * 0.001;
      local ppA_e5 = pA_e5 * 0.00001;
      local ppA_e6 = pA_e6 * 0.0001;

      local  s1 =  0.000052109 + t_cur * 0.00000733868 -
((ppA_e1*Tdiff)^(up_beta)) * (1- (2/ (Exp(2*Tdiff*pB_e1*
((ppA_e1*Tdiff)^(up_beta)) )+1 ) ) ) ;
      local  s3 = -0.000470013 + t_cur * 0.00000495331 -
((ppA_e2*Tdiff)^(up_beta)) * (1- (2/ (Exp(2*Tdiff*pB_e2*
((ppA_e2*Tdiff)^(up_beta)) )+1 ) ) ) ;
```

```
      local  s4 = -0.000280688 + t_cur * 0.00000131401 -
((ppA_e3*Tdiff)^(up_beta)) * (1- (2/ (Exp(2*Tdiff*pB_e3*
((ppA_e3*Tdiff)^(up_beta)) )+1 ) ) ) ;
      local  s6 = 0 - ((ppA_e4*Tdiff)^(up_beta)) * (1- (2/
(Exp(2*Tdiff*pB_e4* ((ppA_e4*Tdiff)^(up_beta)) )+1 ) ) ) ;
      local  s2 = -0.00239     + t_cur * 0.0000240263  -
((ppA_e5*Tdiff)^(up_beta)) * (1- (2/ (Exp(2*Tdiff*pB_e5*
((ppA_e5*Tdiff)^(up_beta)) )+1 ) ) ) ;
      local  s5 = 0 - ((ppA_e6*Tdiff)^(up_beta)) * (1- (2/
(Exp(2*Tdiff*pB_e6* ((ppA_e6*Tdiff)^(up_beta)) )+1 ) ) ) ;

      local  pe1      = +  1.00000*s1;: -0.00385
      local  pe2      = +  1.00000*s3;: -0.00380
      local  pe3      = +  1.00000*s4;: -0.00105
      local  pe4      = +  1.00000*s6;: -0.07091
      local  pe5      = +  1.00000*s2;: -0.01547
      local  pe6      = +  1.00000*s5;: -0.03307
      straincell(6.47340,6.87020,4.28430,90.00000,95.60200,90.00000)
      celltransform(1,0,0,0,1,0,0,0,1)
      a  = sa;
      b  = sb;
      c  = sc;
      al = sal;
      be = sbe;
      ga = sga;
}
do_errors
XYE(FileName)
      bkg @  11709.2632` -7270.52638`  1807.12667`  559.698689` -327.151394`
59.2198455` -27.9445084`  134.076664`  129.903703`  104.599382` -82.3954619`
      start_X  4
      LP_Factor( 90)
      Zero_Error(, -0.0138)
      convolution_step 5
      Rp 217.5
      Rs 217.5
      Simple_Axial_Model( 0.001)
      lam
```

```
            ymin_on_ymax  0.0001
            la  1 lo  0.826401 lh  0.0001
      x_calculation_step 0.001

      local !t_cur 26.4

      hkl_Is
            lebail  1
            LVol_FWHM_CS_G_L( 1, 371.73081`, 0.89, 358.97949`,@,
412.35940`_LIMIT_MIN_0.3,@, 10000.00000`_LIMIT_MIN_0.3)
            e0_from_Strain( 0.04225`,lg32, 0.16898`,lg32, 0.16898`)
            r_bragg  0.391664467
            phase_name "hkl_P-1"
            space_group "P-1"
            load hkl_m_d_th2 I
            {
                  0  1  0  2   6.83805     6.92861  0.024746976
                  1  0  0  2   6.41715     7.38367  3.91833743
                  1 -1  0  2   4.76305     9.95348  1.95279846
                  1  1  0  2   4.59989    10.30747  2.19829103
                  0  0  1  2   4.24747    11.16532  35.4301596
                  1  0 -1  2   3.73571    12.70076  15.0139436
                  0 -1  1  2   3.71500    12.77186  0.514215051
                  0  1  1  2   3.50987    13.52167  0.301598166
                  0  2  0  2   3.41902    13.88271  41.7200628
                  1  0  1  2   3.37541    14.06300  0.00965341159
                  1  1 -1  2   3.32825    14.26329  0.015741823
                  1 -1 -1  2   3.23069    14.69633  0.0622192814
                  2  0  0  2   3.20857    14.79821  0.783841376
                  1 -1  1  2   3.11276    15.25639  6.2565887
                  1 -2  0  2   3.06215    15.51007  3.94958044
                  1  2  0  2   2.97467    15.96912  0.262972008
                  1  1  1  2   2.94748    16.11742  0.682246278
                  2 -1  0  2   2.94450    16.13383  35.3165712
                  2  1  0  2   2.86647    16.57605  21.2494837
                  0 -2  1  2   2.74972    17.28512  11.0410951
                  2  0 -1  2   2.70715    17.55908  0.287663831
                  0  2  1  2   2.58465    18.39836  5.03708848
```

1	2	-1	2	2.56776	18.52045	4.52744489
2	1	-1	2	2.52650	18.82560	10.5987918
2	-1	-1	2	2.50775	18.96768	8.29112031
1	-2	1	2	2.48901	19.11184	0.714758468
1	-2	-1	2	2.47890	19.19052	8.70722257
2	0	1	2	2.43484	19.54117	0.0045915165
2	-2	0	2	2.38152	19.98307	0.115084831
2	-1	1	2	2.34067	20.33554	15.3077497
1	2	1	2	2.32361	20.48646	0.203657649
2	2	0	2	2.29994	20.69953	0.654754332
0	3	0	2	2.27935	20.88865	2.14257628
2	1	1	2	2.24957	21.16830	3.8556419
1	-3	0	2	2.17193	21.93427	5.47330838
3	0	0	2	2.13905	22.27571	13.4310804
2	2	-1	2	2.13374	22.33188	1.59925821
1	3	0	2	2.12461	22.42902	2.29348514
0	0	2	2	2.12373	22.43843	17.0513902
2	-2	-1	2	2.11125	22.57285	5.01758677
1	0	-2	2	2.08566	22.85355	10.8027288
0	-1	2	2	2.06554	23.07919	0.0270627272
0	-3	1	2	2.06358	23.10133	0.546757305
3	-1	0	2	2.06211	23.11806	4.94936706
2	-2	1	2	2.04490	23.31537	3.63708017
1	1	-2	2	2.02383	23.56159	0.246170742
3	1	0	2	2.02149	23.58926	7.08766494
3	0	-1	2	2.00075	23.83729	2.21456699
0	1	2	2	1.99276	23.93434	0.0381457235
1	3	-1	2	1.97707	24.12703	0.884439619
1	-1	-2	2	1.96723	24.24963	1.59091136
0	3	1	2	1.95747	24.37234	0.290096333
1	0	2	2	1.95323	24.42607	1.49976884
1	-3	1	2	1.95218	24.43945	3.7225812
2	2	1	2	1.92698	24.76405	0.0357697151
3	-1	-1	2	1.92172	24.83298	15.3702146
3	1	-1	2	1.91878	24.87165	10.5021546
1	-3	-1	2	1.91588	24.90979	0.000554760994
1	-1	2	2	1.91322	24.94506	23.8592822

2	-3	0	2	1.88960	25.26190	29.9266132
2	0	-2	2	1.86786	25.56098	0.0611182032
0	-2	2	2	1.85750	25.70593	4.5347546
1	1	2	2	1.84487	25.88488	6.23538139
3	-2	0	2	1.84255	25.91813	9.53611491
1	3	1	2	1.83156	26.07629	10.3017915
3	0	1	2	1.83138	26.07892	6.34041753
2	3	0	2	1.82831	26.12359	29.0195537
1	2	-2	2	1.82216	26.21331	14.5588336
2	1	-2	2	1.81825	26.27061	15.8913536
3	-1	1	2	1.79487	26.61911	6.28905689e-006
2	-1	-2	2	1.78587	26.75572	1.35247204
3	2	0	2	1.78558	26.76012	1.94795434
0	2	2	2	1.75494	27.23635	0.00078025157
2	3	-1	2	1.75304	27.26639	21.2171818
1	-2	2	2	1.74862	27.33659	1.66479242
3	1	1	2	1.74429	27.40586	1.67610647
1	-2	-2	2	1.74161	27.44878	9.36480741
2	-3	-1	2	1.73434	27.56618	11.9615474
3	-2	-1	2	1.72896	27.65365	1.35138474
3	2	-1	2	1.72468	27.72359	0.239750293
2	-3	1	2	1.71870	27.82206	12.735513
0	4	0	2	1.70951	27.97458	39.181141
2	0	2	2	1.68770	28.34357	0.00092284731
1	-4	0	2	1.66644	28.71302	4.26644262
2	-1	2	2	1.66535	28.73210	8.31600931
2	2	-2	2	1.66412	28.75377	0.716769313
3	-2	1	2	1.65422	28.92959	10.6894532
1	2	2	2	1.64783	29.04427	0.0229028229
1	4	0	2	1.63774	29.22722	2.86629758
0	-4	1	2	1.62184	29.52029	18.6687268
2	-2	-2	2	1.61535	29.64162	3.37294527
2	3	1	2	1.61421	29.66295	0.617988899
2	1	2	2	1.61297	29.68622	2.88230491
0	-3	2	2	1.60531	29.83119	29.1986885
4	0	0	2	1.60429	29.85070	1.49953387
3	0	-2	2	1.59734	29.98363	0.000422094507

```
                    3 -3  0  2   1.58768     30.17026  0.0319418927
                    1  3 -2  2   1.57919     30.33638  0.163447899
                    3  2  1  2   1.57727     30.37417  0.210912489
                    1  4 -1  2   1.57570     30.40529  0.235003204
                    4 -1  0  2   1.57415     30.43595  0.26096073
               }
               MVW( 0.000, 188.005031`, 0.000)
parametric

Out_file(hkl_param.txt)
```

Appendix 4.

For calculations of the lattice strains the following formulas were used (Carpenter *et al.*, 1998a):

$$e_1 = \frac{a}{a_0}\sin\gamma - 1$$

$$e_2 = \frac{b}{b_0} - 1$$

$$e_3 = \frac{c\sin\alpha\sin\beta^*}{c_0\sin\beta_0^*} - 1$$

$$e_4 = \frac{c\cos\alpha}{c_0\sin\beta_0^*} + \frac{a\cos\beta_0^*\cos\gamma}{a_0\sin\beta_0^*}$$

$$e_5 = \frac{a\sin\gamma\cos\beta_0^*}{a_0\sin\beta_0^*} - \frac{c\sin\alpha\cos\beta^*}{c_0\sin\beta_0^*}$$

$$e_6 = \frac{a}{a_0}\cos\gamma$$

Asterics (*) refers to the reciprocal lattice angles, a_0, b_0, c_0, α_0, β_0, γ_0 – lattice parameters of high-symmetry phase, a, b, c, α, β, γ – lattice parameters of low-symmetry phase,

Acknowledgements

I would like to thank my supervisor Prof. Dr. Robert E. Dinnebier for the opportunity to join his team, as well as his continuous support and motivation throughout this work. I am really very thankful for his guidance and his numerous advices given throughout my work and this thesis, and also for his patience and readiness to help.

My sincere thanks to my Ph.D. examination committee members Prof. Dr. Thomas Schleid and Prof. Dr. Frank Gießelmann for accepting being my examiners, reading thoroughly the thesis and giving valuable comments and remarks.

Also I would like to thank to:

Prof. Sander van Smaalen for his help with the program BayMEM and for explanation of many difficult questions about maximum entropy method.

Mr. Frank Adams for constant and invaluable technical support in laboratory and at synchrotrons.

Prof. Dr. Martin Jansen for many scientific advises and support with PhD work.

Prof. Pavel E. Kazin for synthesis of many wonderful apatites and many invaluable discussions.

Dr. Christian Lipp and Prof. Dr. Thomas Schleid for synthesis of $LuF[SeO_3]$.

Dr. Avijit K. Paul for samples of double perovskites.

Mr. Dmytro Denysenko and Prof. Dr. Dirk Volkmer for synthesis and adsorption measurements of Zn-MFU-4*l* and Cu-MFU-4*l*.

Dr. Michael Hirscher, Mr. Ali Soleimani-Dorcheh, and Ms. Ingrid Weinrauch for thermal desorption measurements, and many fruitful discussions.

Dr. Ulrich Wedig for DFT calculations.

Dr. Jürgen Nuss and Dr. Hanne Nuss for their help with single crystal service.

All peoples at synchrotrons which helped me to perform many measurement for my work and for work of my colleagues: Mr. Frank Adams, Dr. Julia E. Parker, Dr. Chiu Tang, Dr. Ann-Christin Dippel, Dr. Hans-Peter Liermann, Dr. Manuel Hinterstein, Dr. Joseph Bednarcik, Dr. Christina Drathen, Dr. Yves Watier, Dr. Thomas Buslaps, Dr. Simon A.J. Kimber, Dr. Antonio Cervellino, Mr. T. Runcevski, Mr. M. Etter, Ms. Mueller.

Mr. Martin Etter for translation of summary of my PhD thesis.

Dr. Vyacheslav Saltykov and Dr. Vanya Todorova for their help during my first months in Germany.

Ms. Sabine Paulsen and Ms. Birgit King for invaluable assistance in general administrative matters.

Erklärung über die Eigenständigkeit der Dissertation

Ich versichere, dass ich die vorliegende Arbeit mit dem Titel
„Increasing accuracy in powder diffraction"
selbständig verfasst und keine anderen als die angegebenen Quellen und Hilfsmittel benutzt habe; aus fremden Quellen entnommene Passagen und Gedanken sind als solche kenntlich gemacht.

Declaration of Authorship

I hereby certify that the dissertation entitled
„Increasing accuracy in powder diffraction"
is entirely my own work except where otherwise indicated. Passages and ideas from other sources have been clearly indicated.

Name/Name: Oxana Magdysyuk

Unterschrift/Signed: _____

Datum/Date: _____